Microstructural and Mechanical Property Development in Metastable Beta Titanium Alloys

Mark David Richardson

Department of Materials Science and Engineering

The University of Sheffield

Thesis submitted for the degree of Doctor of Philosophy

April 2016

Note to the reader:

For easier interpretation of certain pairs of Figures in Chapter 4, it is recommended that this document be printed and bound such that this page is a left hand page.

If viewing in Adobe Acrobat Reader with 'Two Page Scrolling' enabled (or 'Two Page View'), these pairs of Figures will not appear opposite one another. Select 'Show Cover Page in Two Page View' under 'View' → 'Page Display' to allow this.

Abstract

Titanium alloys represent an ever increasing proportion of the materials employed in aerostructural applications. Metastable beta alloys in particular, offer high specific strength and good corrosion resistance that allow them to compete with steels. Ti-5Al-5Mo-5V-3Cr and Ti-10V-2Fe-3Al are two such alloys used in the main landing gear of large commercial aircraft. Thermomechanical processing of metastable beta alloys is critical in obtaining the desired microstructure, which in turn governs the mechanical properties. This therefore demands a thorough understanding of the relationship between processing, microstructure and mechanical properties in order to optimise the final product and process route.

This project characterises the microstructural and mechanical property variation within forged Ti-5553. Microstructural variables are quantified in order to examine their relative influence on mechanical properties. This reaffirmed the importance of microstructural control during materials processing. Gradual changes in primary alpha morphology, beta volume fraction and grain structure were observed throughout the forgings. However, it was also found that the size of secondary alpha precipitates could fluctuate rapidly over relatively short distances. The effect on mechanical properties was significant enough to completely reverse the general trends exhibited over the entire forging. It was also found that the heat treatment response varied with orientation. It would appear that unspecified microstructural variables limited the maximum achievable properties in certain orientations, preventing the heat treatment from further affecting them. However, changes in work hardening behaviour were observed which increased the proof stress while leaving the tensile strength essentially unchanged.

The influence of subtransus thermomechanical processing on the microstructural evolution of Ti-10-2-3 was also investigated. Flow curves exhibited an initial peak at low strain followed by extensive flow softening. Microstructural analysis would suggest that the fragmentation and globularisation of acicular alpha particles is at least partially responsible for this softening effect. The use of torsion tests demonstrated that non-linear strain paths may not represent an efficient means of globularising primary alpha. The Burger's Orientation Relationship (BOR) was found to break down at a linear strain of about 0.5. However, the process of 'strain reversal' could partially restore this up to an original linear strain of around 0.8. Solution treatment and ageing revealed that more highly strained regions were less responsive to age hardening.

Contents

Acknowledgements

List of Figures

7

List of Tables

Chapter 1 Introduction

Titanium and its alloys are a highly prized group of materials, exhibiting a range of properties that make them very attractive to many areas of industry. With its high strength, low density, good creep properties (up to 500°C) and excellent corrosion resistance, titanium is the ideal candidate for many demanding applications, particularly in the aerospace sector. The element itself makes up approximately 0.6% of the earth's crust, most of this in the form of ilmenite ($FeTiO_3$) and rutile (TiO_2), making it the 4th most abundant structural metal in the world [1].

However, the price of metallic titanium does not reflect this prevalence due to the high costs incurred during extraction and processing. These costs are the result of its high reactivity with oxygen, making these operations difficult and expensive. Ironically it is this characteristic that also gives it such good corrosion resistance since it causes the rapid formation of a stable oxide on any exposed surfaces, thus preventing any further reaction. Due to this high cost, commercial success of titanium requires applications where its superior properties set it apart from other engineering materials [2]. This has led to increasing usage in the aerospace industry where the low density of titanium provides a key advantage (Figure 1.1) [3][4].
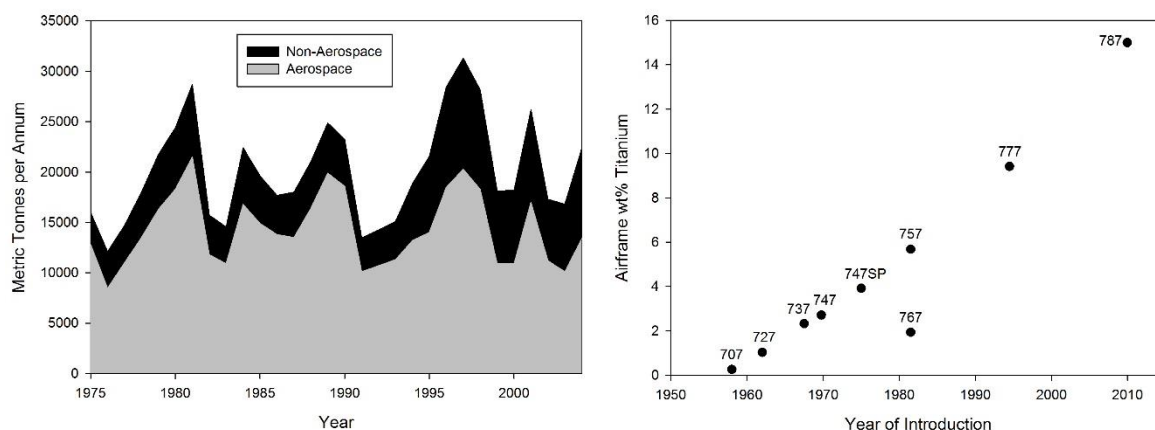
Figure 1.1: Industrial trends of titanium: annual US titanium sponge consumption by end use and titanium usage in Boeing aircraft [3][4]

Beta titanium alloys represent a growing segment of this demand. The high specific strength of β alloys is one factor driving this expansion. This allowed the metastable β titanium alloy Ti-10-2-3 to replace high strength steel in large parts of the Boeing 777 main landing gear, resulting in significant weight savings [5]. In addition, the corrosion resistance of β alloys extends the lifetime of components and reduces the frequency of maintenance intervals [6]. A further advantage of titanium alloys generally is their compatibility with polymer matrix composites [5]. However, as mentioned above, the cost of titanium inhibits its wider use, and as Figure 1.2 illustrates, this is not solely due to the issues with extraction. It can be seen that thermomechanical processing (TMP) accounts for nearly half of the cost of a semi-finished

product [7]. This processing is necessary to ensure that the properties offered by titanium alloys justify the price tag. In order to ensure the cost-competitiveness of titanium alloys it is therefore critical to balance the property requirements against the cost of TMP. Optimisation of this requires a comprehensive understanding of the relationship between processing, microstructure and properties.
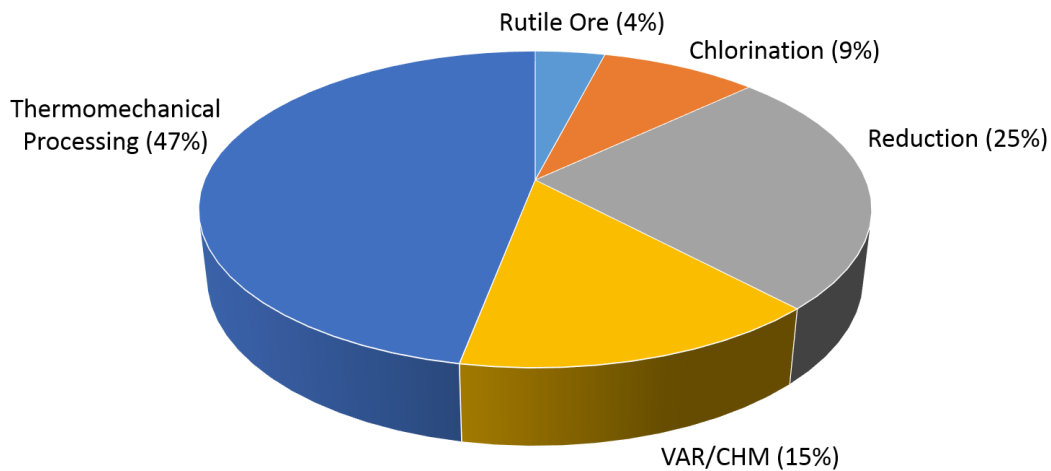
Figure 1.2: Breakdown of the costs involved in the fabrication of titanium alloy plate [7].

Ti-5553 is a metastable β titanium alloy developed in the 1990s to provide easier processing and property improvements over the older alloy Ti-10-2-3. It has been selected for use in airframe and landing gear applications on the Boeing 787 [8]. However, as with all titanium alloys it is still a costly material to work with. There have also been difficulties with obtaining the required ductility for landing gear applications [9]. This thesis seeks to address these issues and further investigate thermomechanical processing of β titanium alloys. Through an improved understanding of process-microstructure-property relationships, the intention is to aid in the optimisation of processing in order to maximise the benefit that these alloys offer.

Chapter 2 provides an overview of titanium metallurgy with a specific focus upon β alloys. Given the different approaches taken in Chapters 4 and 5, the relevant methodologies are included at the beginning of each respective chapter. However, in order to avoid unnecessary repetition, the characterisation techniques common to both chapters are detailed in Chapter 3. The microstructural and mechanical property variation within a forged Ti-5553 component is examined in Chapter 4. By studying the correlations between the microstructure and properties, the aim was to identify key microstructural variables that could improve ductility. Chapter 5 investigates the influence of subtransus forging upon microstructural evolution of Ti-10-2-3. The original intention was to carry out this work on Ti-5553, but material supply issues necessitated the use of the more established β alloy Ti-10-2-3. The main findings of this project are then summarised in Chapter 6, and finally, recommendations for further work are made in Chapter 7.

Chapter 2 Literature Review

2.1 Fundamental Aspects of Titanium

2.1.1 Structure and Properties

At room temperature, pure unalloyed titanium exists as a hexagonal close packed (hcp) structure known as the 'α' phase. Upon heating it will undergo an allotropic phase transformation at 882 °C to a body centred cubic (bcc) structure referred to as the 'β' phase (Figure 2.1). The presence of other elements can strongly influence this transformation temperature, leading to significant variation of the 'β transus' (T_β) between alloys. At room temperature, the lattice parameters of the hcp unit cell (α phase) are 0.295 nm for the 'a-axis' and 0.468 nm for the 'c-axis'. This gives a c/a ratio of 1.587, smaller than that of the ideal hcp structure (1.633). The β phase does not exist at room temperature without extensive alloying. However, the lattice parameter of β titanium at 900 °C has been determined as 0.332 nm. Figure 2.1 also illustrates the families of lattice planes with the densest packing. For the hcp α unit cell these are the basal plane, (0002), the three prismatic planes, $\{10\bar{1}0\}$, and the six pyramidal planes, $\{10\bar{1}1\}$. The close packed directions, $<11\bar{2}0>$, fall along the three axes a_1, a_2 and a_3. For the β phase, being body centred cubic, the most densely packed planes are the six $\{110\}$ lattice planes. The closest packed directions are the four $<111>$ directions [2].
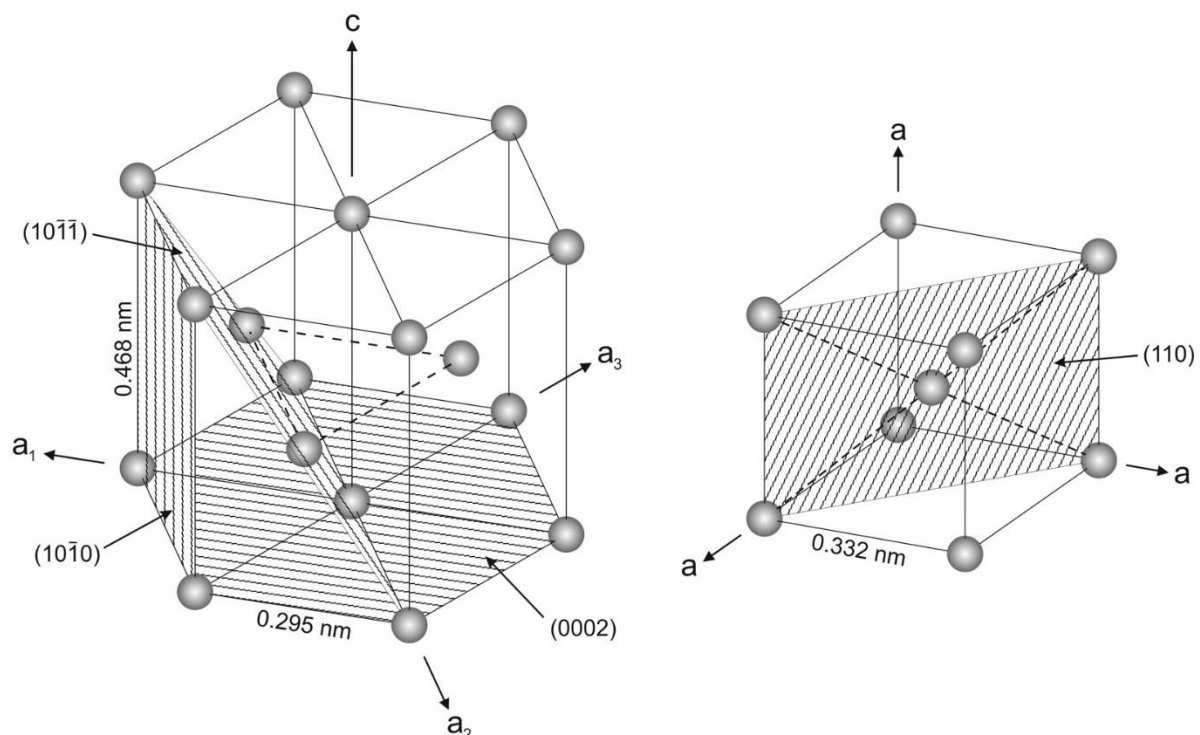
Figure 2.1: Unit cells for the low temperature α phase (left) and the high temperature β phase (right). Redrawn from [2].

The use of a four index system for the hcp unit cell is necessary to ensure that equivalent planes and directions have the same indices. This system is known as the Miller-Bravais coordinate system. Converting between the three and four index systems is achieved through the use of Equation 2.1 for planes, and Equations 2.2-2.5 for directions [10].

For Plane $(hkl) \rightarrow (hkil)$

$$i = -(h + k) \tag{2.1}$$

For Direction $[u'v'w'] \rightarrow [uvtw]$

$$u = \frac{1}{3}(2u' - v') \tag{2.2}$$

$$v = \frac{1}{3}(2v' - u') \tag{2.3}$$

$$t = -(u + v) \tag{2.4}$$

$$w = w' \tag{2.5}$$

As a result of the lower symmetry of the hcp unit cell, the elastic properties of the α phase display significant anisotropy. A study of single crystals of α titanium found the elastic modulus varied from 100 GPa (loaded perpendicular to the c-axis) to 145 GPa (loaded parallel to the c-axis). While this phenomenon is at its most pronounced in single crystals, the formation of crystallographic textures in polycrystalline α titanium can still cause a significant degree of anisotropy. It is therefore important to take these effects into account when processing titanium alloys with a high volume fraction of α phase [2].

2.1.2 Mechanisms of Deformation

Deformation of titanium is accommodated through the movement of dislocations and the activation of mechanical twins. The occurrence of twins is most prevalent in pure titanium and some α rich alloys, particularly when deformed at low temperatures. Twinning is suppressed in two phase (α+β) alloys, and although it can occur in the β phase, it is entirely suppressed in age hardened β alloys. Figure 2.2 illustrates the slip planes and directions in the hcp α unit cell. Since the close packed directions are all of the type $< 11\bar{2}0 >$, these constitute the major slip directions. The slip planes which incorporate this type of 'basal' Burgers vector are the basal plane itself, (0002), the three prismatic planes of the type $\{10\bar{1}0\}$ and the six pyramidal planes of the type $\{10\bar{1}1\}$. Combining these slip planes and directions gives a total of 12 slip systems (Table *2.1*) [2][11][12].

However, only four of these are truly independent, whereas the Von Mises criterion states that a minimum of five are required for homogeneous plastic deformation of a polycrystalline material. This may force slip in the $< 11\bar{2}3 >$ direction on one of the $\{11\bar{2}2\}$ planes (second order pyramidal planes). While these types of dislocation have been observed, the Critical Resolved Shear Stress (CRSS) for them is much higher than for other slip systems [12]. However, when stress is applied parallel to the c-axis, this is the only viable form of slip since the Schmidt factor for the other directions is zero. Consequently, this gives rise to further anisotropy in the mechanical properties of α rich alloys. The difficulties experienced with slip in the α phase also help explain the greater propensity for deformation induced twinning [2].

Concerning deformation of the β phase, the greater symmetry of the bcc unit cell provides much more freedom to deform plastically. In common with most other bcc metals, the slip systems for the β phase all involve the <111> direction on one of the following types of plane: {110}, {112} and {123} [13]. As a result, the β phase is not as prone to anisotropic behaviour as the α phase. However, due to the orientation relationship between the α and β phases, any texture in the β phase is likely to influence the α phase and exacerbate the anisotropy of mechanical properties [14][4][15][16]. If the β phase is retained down to room temperature, certain alloys may also accommodate some deformation through the formation of stress induced martensite [17].
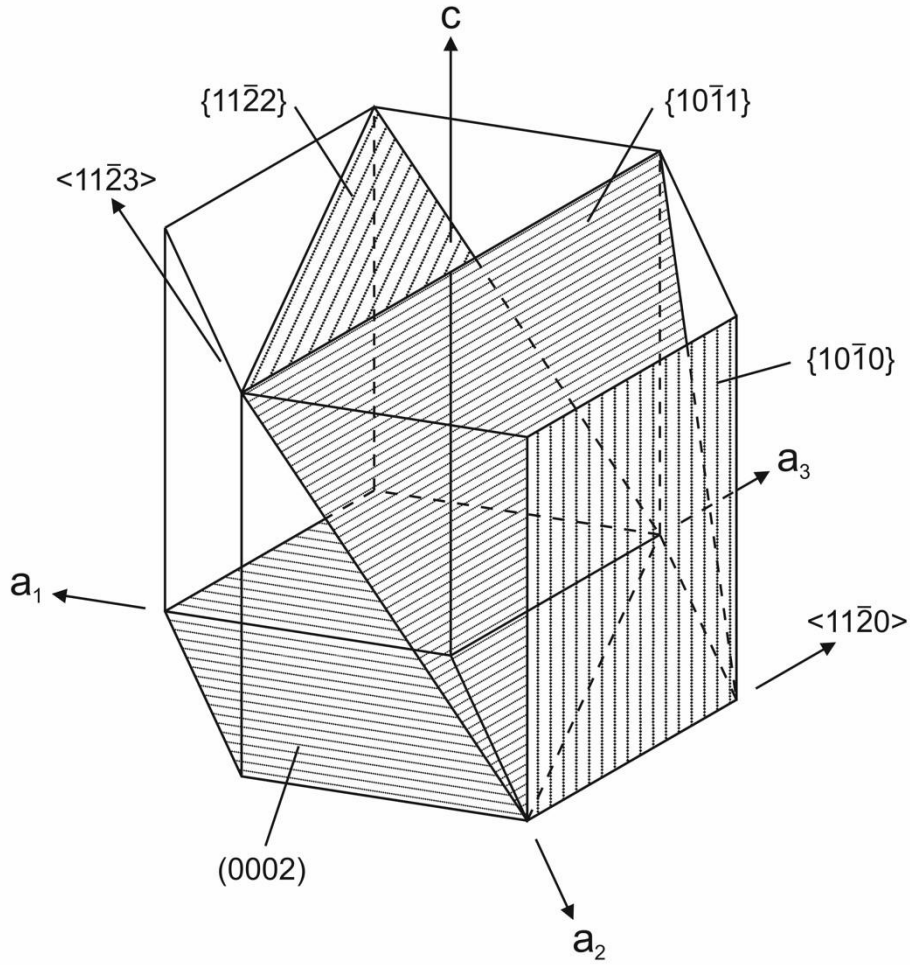
Figure 2.2: Slip planes and directions in the hcp α phase. Redrawn from [2].

Table 2.1: Slip systems in the hcp α phase [2][11][12].

Slip System Type	Burgers Vector Type	Slip Direction	Slip Plane	Number of Slip Systems
1	$\vec{a}$	$< 11\bar{2}0 >$	(0002)	3
2	$\vec{a}$	$< 11\bar{2}0 >$	$\{10\bar{1}0\}$	3
3	$\vec{a}$	$< 11\bar{2}0 >$	$\{10\bar{1}1\}$	6
4	$\vec{c} + \vec{a}$	$< 11\bar{2}3 >$	$\{11\bar{2}2\}$	6

2.1.3 Alloying

The alloying additions made in titanium are usually classified according to their effect on the β transus (T_β) (Figure 2.3) [2][1]. Those which lower the T_β are referred to as β stabilisers, while those that raise it are known as α stabilisers. There are some which have little or no effect, and these are classified as neutral elements. Strong α stabilisers include the substitutional element Al, along with the interstitial additions O, N and C. Aluminium is a popular choice for alloying as it has good solid solubility in both phases and is readily available. However, the intermetallic compound Ti_3Al (α_2) leads to embrittlement. As a result, the concentration of aluminium in conventional alloys is usually kept below 6 wt% in order to minimise Ti_3Al formation. Oxygen can be used to increase strength, although its presence is tightly controlled. At elevated temperatures, oxygen diffusion into the surface of components can lead to the formation of an α rich layer near the surface, known as 'α case'. The brittle nature of this layer can compromise fatigue performance, and thus precludes titanium from use in the hotter parts of gas turbine engines. The rare earth elements, along with B, Ga and Ge are also α stabilisers, though much less soluble than Al and rarely used [2].

The β stabilisers can be categorised as either β isomorphous or β eutectoid forming elements (Figure 2.3). At sufficiently high concentrations, the β isomorphous elements are capable of retaining the β phase down to room temperature, whereas the β eutectoid formers will produce some form of intermetallic phase under equilibrium conditions. The solubility of β stabilisers in the α phase is generally quite low, encouraging partitioning to the β phase if time and temperature permit. Of the isomorphous elements, V, Mo and Nb are the most common additions. While Ta and Re also belong to this group they are rarely used due to their effects upon the alloy density (a particularly important factor in aerospace alloys). Mo and Nb are similar in their influence of the T_β, lowering it to around 750 °C at concentrations of 15 wt% (down from 882 °C in pure titanium). V is more potent, bringing the T_β down to 700 °C at about 15wt%, while also maintaining greater solubility in the α phase than Mo [2].

Common β eutectoid formers are Cr, Fe and Si, with less popular elements including Ni, Cu, Mn, W, Pd and Bi. There are numerous others which have never found use, likely due to cost or impracticality (e.g. Pt, U). H is also a β eutectoid forming element, but induces such brittleness that its presence is generally kept to a minimum (typically no more than 125-150 ppm). Cr and Fe are even more effective β stabilisers than the isomorphous element V. The eutectoid temperature of Cr is 667 °C and situated at approximately 15 wt%. Fe is more potent still, with a eutectoid lying around 600 °C. However, the intermetallic compounds that form below the eutectoid are very detrimental to ductility. For this reason the concentration of Cr in conventional alloys is typically kept below 5 wt%. This slows the eutectoid decomposition enough to prevent $TiCr_2$ formation. The exception to this practice is Si, where the intermetallic Ti_5Si_3 is intentionally formed to improve creep properties. The eutectoid forming elements also

tend to exhibit very low solubility in the α phase (<0.5 wt% in the case of Cr) leading to their partitioning almost completely to the β phase [18]. It should also be noted that the diffusivity of Fe in α titanium is not only very high, but can also increase the diffusion rate of other elements that are present [2]. This has important implications in alloy design when considering creep properties and aging kinetics [8].
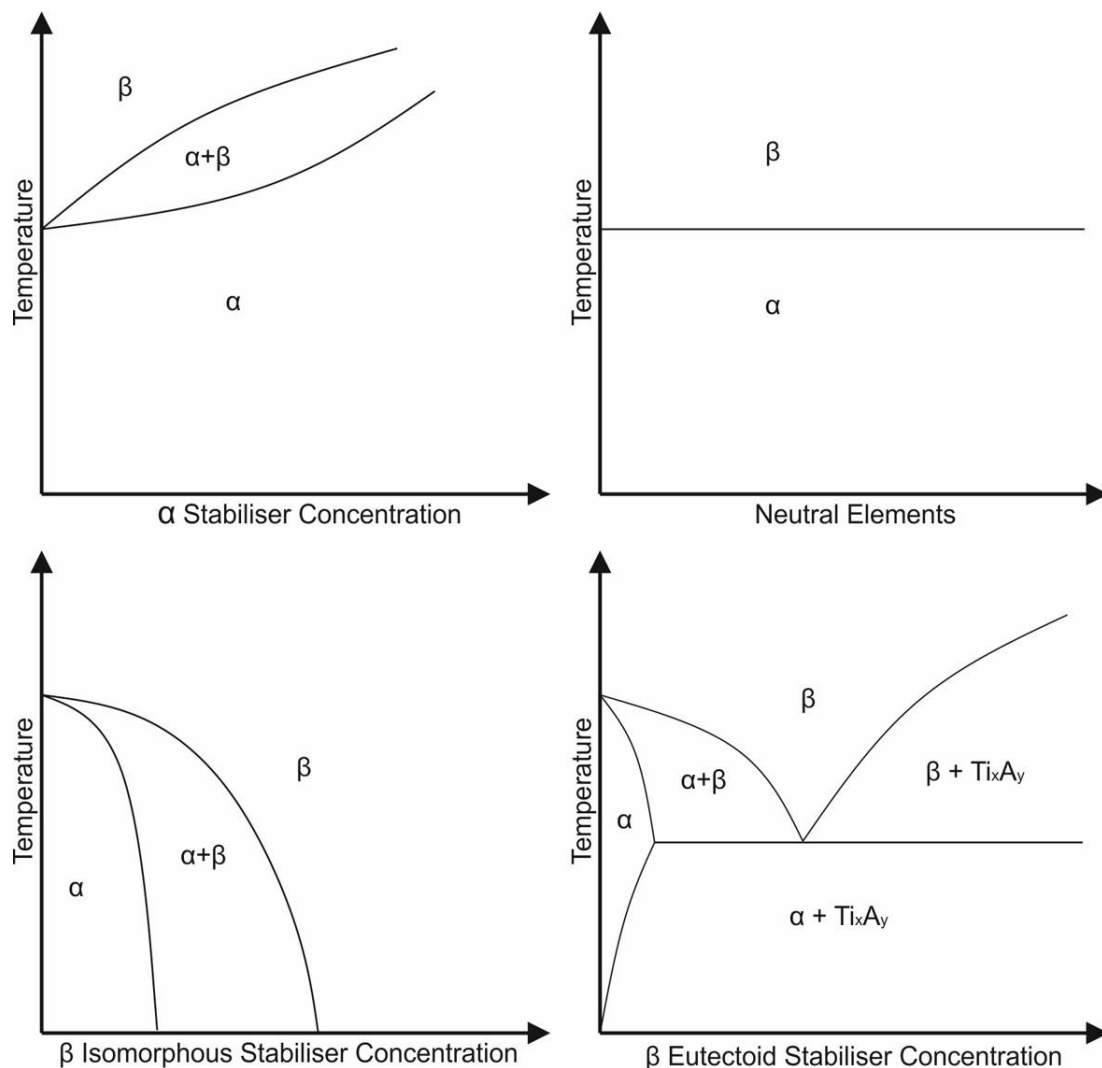
Figure 2.3: Clockwise from top left, the effect of α stabilisers, neutral elements, β eutectoid stabilisers and β isomorphous stabilisers on the Ti-X phase diagram. Redrawn from [2].

Amongst the neutral elements, Zr and Hf are isomorphous with Titanium, possessing the same α/β transformation and being completely soluble in both phases. They may have some influence on T_β, but the effect is small and varies with concentration (small amounts lower T_β slightly, while higher concentrations raise it). Sn is a β eutectoid forming element, although it has almost no effect on T_β. However, in the presence of Al, it will act as an α stabiliser and can substitute for Al in the Ti_3Al phase (α_2) [2]. In order to better understand the alloying behaviour of Titanium, attempts have been made to represent multicomponent alloys as binary Ti-X

systems. For heavily α stabilised systems, an equivalent concentration of Al is often used to represent the net effect of alloying. The result is termed the 'Al equivalence', and Equation 2.6 is that developed by Rosenburg for determination of this value [19].

$$[Al]_{eq} = [Al] + 0.17[Zr] + 0.33[Sn] + 10[O] \tag{2.6}$$

2.1.4 Alloy Classification

Titanium alloys can be classified into five broad categories depending on their constitution. This is best illustrated with a pseudo-binary isomorphous phase diagram (Figure 2.4) [2][20]. This shows qualitatively the effects of increasing β stabilisation. Although eutectoid forming elements would be expected to alter this diagram, the sluggish nature of the eutectoid reactions can lead to behaviour similar to a β isomorphous model [21]. Figure 2.4 also illustrates the martensitic start/finish (dashed line labelled $M_{s/f}$). Compositions to the left of this line will transform martensitically when cooled rapidly to room temperature. The α alloys are those which sit on the very far left of the phase diagram. These contain very little or no β phase at room temperature, and all the grades of commercially pure titanium (CP-Ti) lie here. The excellent corrosion resistance and good weldability of the α alloys makes them a popular choice in the chemical industry. Typical applications include heat exchangers and piping. Pressure vessels are another possibility, although strength is a more significant consideration in these roles. This may warrant the use of stronger alloys such as those in the α+β range [22].

Between the α transus and the $M_{s/f}$ lie the α+β alloys. These contain an appreciable quantity of β and represent a compromise between competing properties. Increasing the β volume fraction enables higher strengths to be achieved but reduces corrosion resistance. Precipitation of secondary α within the β phase provides significant strengthening. In addition, where the Al content exceeds 5%, coherent particles of Ti_3Al can be precipitated within the α phase, providing further strength. The incredibly popular Ti-6Al-4V alloy falls into the α+β category. This alloy dominates the market thanks to its excellent balance of properties and finds a great deal of use in the aerospace industry [2]. Applications often include structural components within both airframes and engines [14]. However, Ti-64 is unsuitable for use at temperatures above about 350 °C on account of its creep performance. In a gas turbine, this prevents the use of Ti-64 towards the rear of the high pressure compressor. In order to improve creep properties, so-called 'near-α' alloys such as Ti-834 are employed. Technically, these are α+β alloys too, but are situated closer to the α transus, possessing only a small volume fraction of β phase under equilibrium. Since diffusion in the β phase is 2-3 orders of magnitude faster than in the α phase, the near α alloys exhibit superior creep properties due to the lower volume fraction of

β. In addition, since Fe is a fast diffuser and can enhance the diffusivity of other elements (including the self diffusion of α titanium) its presence is minimised in such alloys [2][23]. The term β alloy and metastable β alloy are often used interchangeably to describe the latter, since truly stable β alloys are not very common. The metastable β alloys are situated between the $M_{s/f}$ and T_β. If cooled sufficiently quickly, this permits retention of the β phase to room temperature while avoiding the formation of martensite. Since the retained β phase is not thermodynamically stable, it is then possible to precipitate a uniform dispersion of very fine secondary α (so-called in order to distinguish it from any α phase which existed prior to cooling, known as primary α). The strengthening effect of the secondary α is such that the metastable β alloys are responsible for the highest achievable strengths among all the commercial titanium alloys. In addition, the corrosion resistance of metastable β alloys is equal to, if not better than α+β alloys [6]. The β-isomorphous stabiliser Mo has been shown to significantly enhance general corrosion resistance at concentrations above 3 wt%. Metastable β alloys also exhibit less susceptibility to hydrogen embrittlement. However, it should be noted that this effect will be reduced in the aged condition as more α will be present [2].
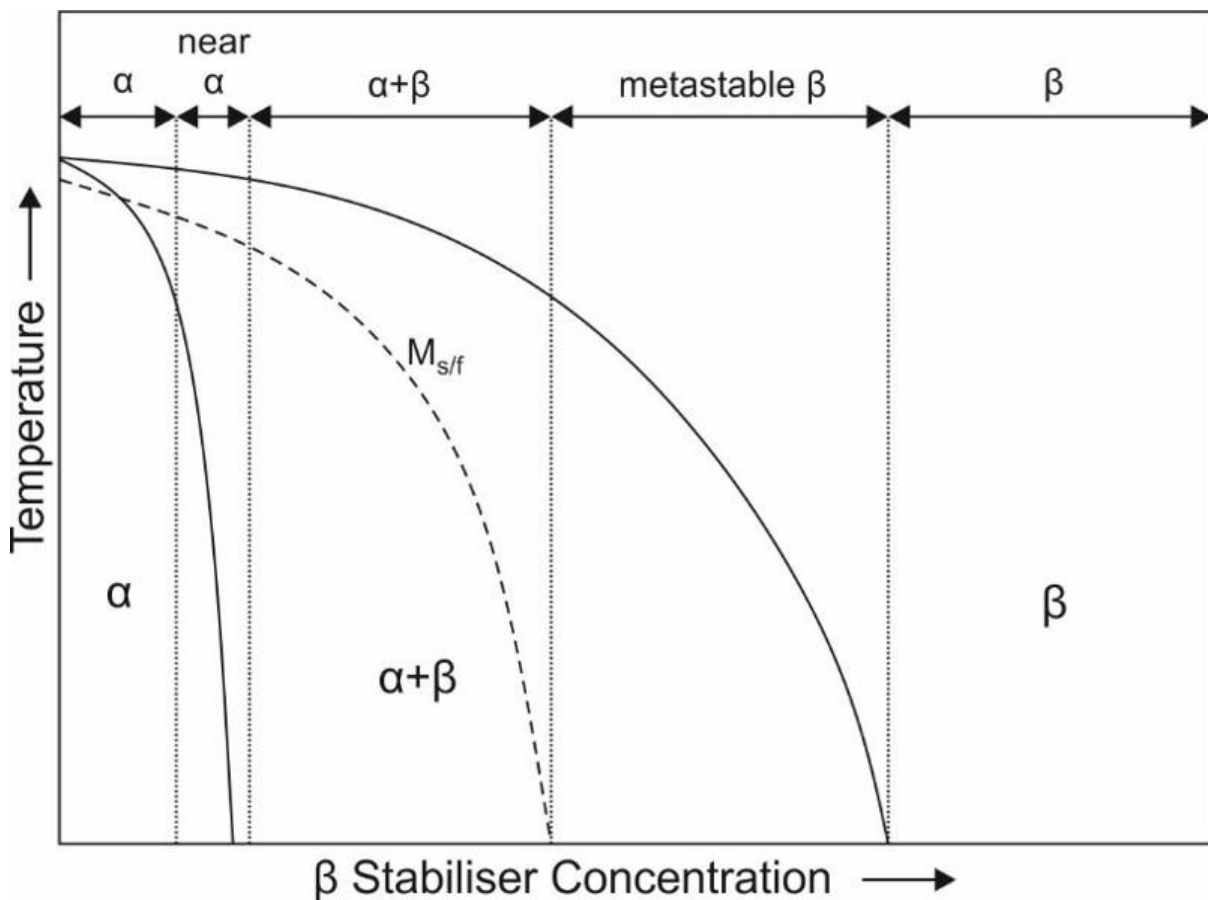
Figure 2.4: Pseudo-binary isomorphous phase diagram of β stabilised titanium. Redrawn from [2][20].

The dependence of the yield stress upon composition gives rise to a further subdivision of the metastable β alloys into 'high strength' and 'heavily stabilised' alloys. The high strength alloys are those lying closest to the $M_{s/f}$. These alloys are the least stable, and readily decompose upon aging to produce the greatest volume fraction of secondary α. This provides the greater strength associated with alloys such as Ti-10-2-3 and Ti-5553. The more heavily stabilised alloys sit further to the right of the pseudo binary phase diagram, closer to the $T_β$. These alloys offer greater formability and a lower modulus of elasticity. This makes them ideal for use in applications such as springs and fasteners. Examples include Beta C, Ti-15-3 and Beta 21S. They are also suitable for casting, which offers economic advantages due to nearer net shape processing [8][6][24][25]. Table 2.2 lists the concentrations of some elements required to suppress the $M_{s/f}$ line below room temperature. Just as Al is used as a reference element for the degree of α stabilisation, Mo is often employed to describe the extent of β stabilisation. Equation 2.7 determines the Mo equivalence (wt%) based upon the data in Table 2.2 [26].

Table 2.2: Concentrations of individual elements required to suppress $M_{s/f}$ below room temperature [26].

	Mo	Ta	Nb	W	V	Cr	Ni	Mn	Co	Fe
Wt%	10	50	36	25	15	8	8	6	6	4
At%	5.2	20.9	22.5	8	14.2	7.4	6.6	5.3	4.9	3.4

$$[Mo]_{eq} = [Mo] + 0.2[Ta] + 0.28[Nb] + 0.4[W] + 0.67[V] + 1.25[Cr] + 1.25[Ni] + 1.7[Mn] + 1.7[Co] + 2.5[Fe] \tag{2.7}$$

As mentioned earlier, the term β alloy is often used to describe both stable and metastable β alloys. In Figure 2.4, metastable alloys have been explicitly labelled as such, so in this context the term β alloy refers to the stable alloys towards the right hand side of the phase diagram. There also exists the term 'near β alloy', to describe alloys left of, but very close to the $M_{s/f}$. These are often included under the classification of β alloys even though they don't meet the exact definition of a true β alloy. However, for the sake of brevity, in this thesis the term β alloy may be used to describe all of those above. To avoid confusion, the near β alloys and stable β alloys will be identified as such. Like the metastable alloys, the stable β alloys can retain the β phase down to room temperature. In addition, the cooling rate is less critical for β retention since there is little/no tendency for decomposition. Retention of the β phase makes these alloys very formable, even cold workable, but due to their stability they are unable to precipitate secondary α. As a result, their strength is limited and they find very little use on an industrial scale [2].

The classification of titanium alloys in the aforementioned manner helps clarify and explain their general behaviour. However, it is important to realise that these boundaries aren't always precise, and can be misleading. For example, despite the name, most α alloys will usually contain a small amount of β phase (this helps control the α grain size and improves hydrogen tolerance) [2]. The $M_{s/f}$ line also becomes nearly vertical below about 400 °C. It is therefore possible for an alloy with a bulk composition near the $M_{s/f}$ to contain martensite and retained β due to local variations in chemistry. This matter is further complicated by the formation of stress induced martensite. In some metastable β alloys, the application of a stress will cause the retained β to undergo a transformation to α" martensite. The stress necessary to induce this transformation can be as low as 150 MPa. This may be exceeded when quenching thick sections, or even just mechanically polishing a specimen. Electrolytic polishing avoids this issue, and limitations on component dimensions can reduce quenching stresses [17]. Care should also be exercised with the use of Al and Mo equivalence values. They are a useful guide, but the exact behaviour of a multicomponent alloy may vary [2]. It should be noted that the relative influence of an element on the $M_{s/f}$ may differ from its influence upon the T_β.

2.2 Phase Transformations

The transformation between the bcc and hcp phases of titanium has been shown to follow a crystallographic orientation relationship of the form:

$$(110)_\beta \parallel (0002)_\alpha$$

$$[1\bar{1}1]_\beta \parallel [11\bar{2}0]_\alpha$$

This was first demonstrated by Burgers for Zirconium, and later confirmed in titanium [27][28]. Figure 2.5 illustrates how the atoms within the (110) plane of the bcc β phase shift in order to make the transformation to the parallel (0002) basal plane of the hcp α phase (and vice versa for the transformation back to β) [1]. Refer to Figure 2.1 for the orientation of these planes in their respective phases. In accordance with the Burger's relationship there are twelve hexagonal variants which can form from a parent bcc crystal. However, some variants may be unintentionally favoured as a result of prior deformation of the β phase. During cooling, selective nucleation of these variants can lead to an intense texture in the α phase [14][16].
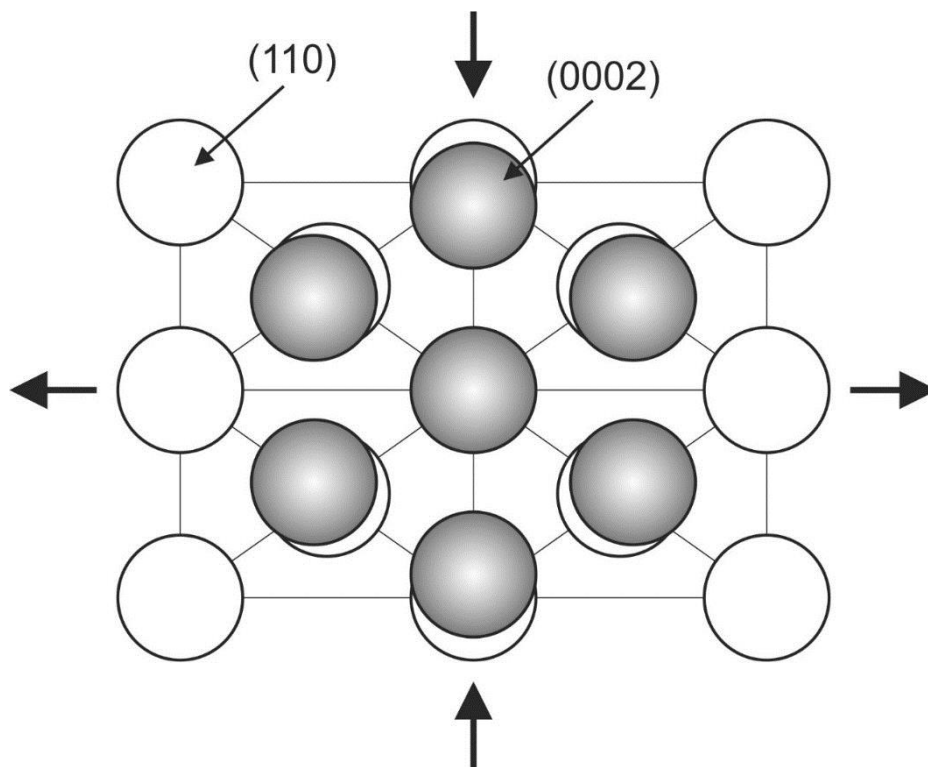
Figure 2.5: Illustration of β transformation to the α phase [1].

2.2.1 Nucleation and Diffusional Growth

Under slow cooling, the transformation from β to α occurs through a diffusion based nucleation and growth process. The α phase first nucleates at the β grain boundaries and rapidly forms a continuous layer. As cooling continues, colonies of parallel α plates nucleate at this layer and grow into the β grains. Within a colony, all plates will share the same variant of the Burgers relationship. These colonies grow into the grain interior until they impinge on each other, giving rise to a characteristic lamellar structure (Figure 2.6(a)) [2][20]. The α plates are separated by a thin layer of solute enriched, retained β. Despite this layer, easy slip transfer occurs between parallel plates, and therefore each colony effectively acts as a larger microstructural unit. However, there can still be some difference in the relative ease with which dislocations in the α phase transfer to the β phase. This is caused by variation in the alignment of slip systems between the two phases [4].

If the cooling rate is increased, the colony size and the width of individual α plates are both reduced. Colonies begin to nucleate upon the boundaries of other colonies, increasing the number of variants within each prior β grain (Figure 2.6(b)). In order to minimise the elastic strains, α plates that nucleate on the broad face of existing plates tend to grow roughly perpendicular to them. With more rapid cooling, this selective mechanism of nucleation and growth, combined with the smaller colony size yields a 'basket weave' type of microstructure (Figure 2.6(c)). Further increase in the cooling rate will nucleate even more α variants until a 'Widmanstätten' microstructure is achieved (Figure 2.6(d)) [2][20]. The greater number of variants and finer precipitation provide a much smaller effective microstructural unit than the colony microstructures. The tendency to form a more interwoven microstructure increases with greater β stabilisation [2].
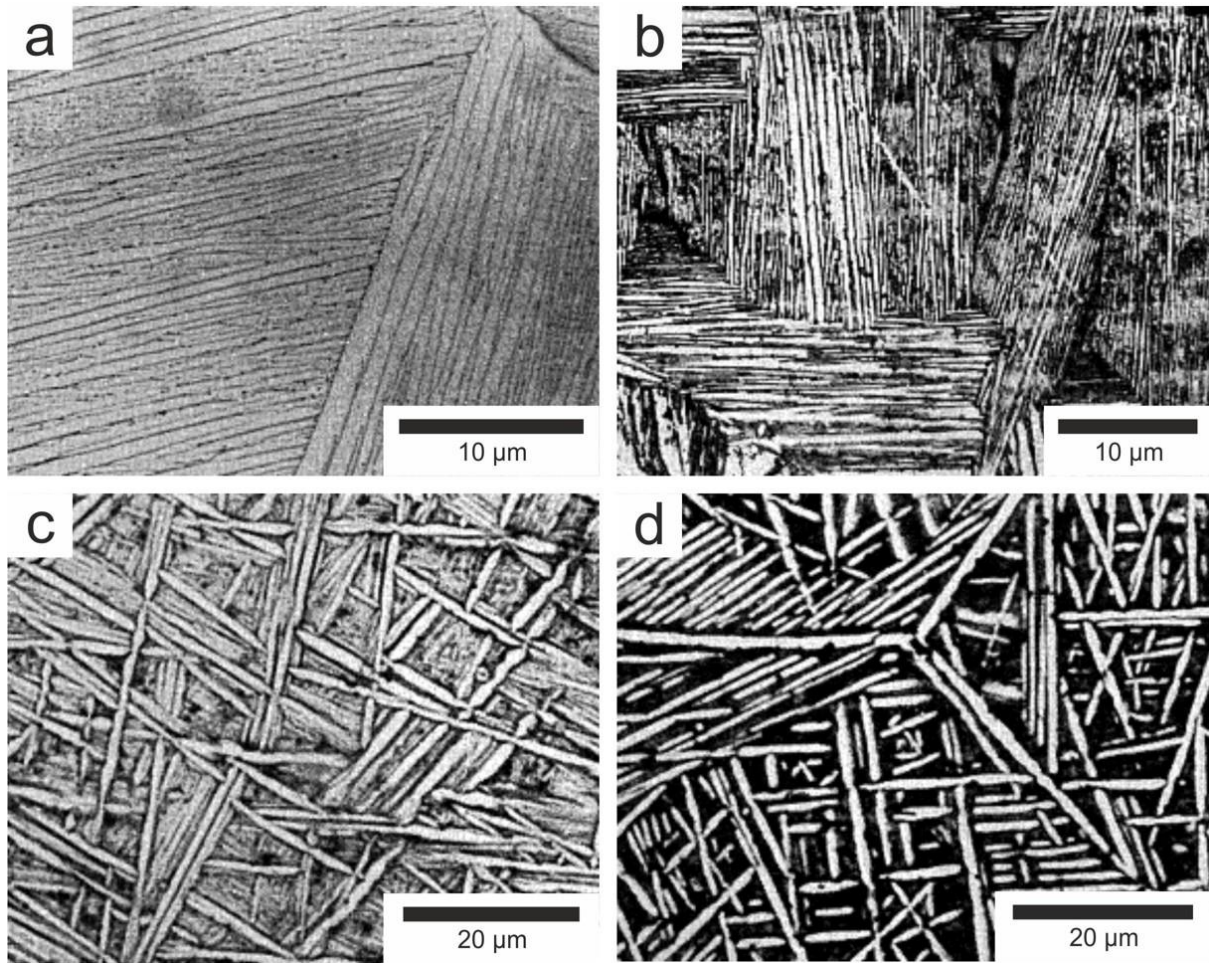
Figure 2.6: The effect of cooling rate on microstructural development. (a) was furnace cooled, whereas (b)-(d) were cooled at progressively faster rates. Adapted from [20].

2.2.2 Metastable Phases

At sufficiently high cooling rates, the β phase will undergo a martensitic transformation. This occurs when the cooling rate reaches the point that diffusional processes can no longer accommodate the phase change rapidly enough. In this case a diffusionless transformation takes place involving the cooperative movement of atoms through a shearing mechanism. The specific shear systems activated in this process are $[111]_\beta$ $(11\bar{2})_\beta$ and $[111]_\beta$ $(\bar{1}01)_\beta$, or in four-axis (hexagonal) notation $[2\bar{1}\bar{1}3]_\alpha$ $(\bar{2}112)_\alpha$ and $[2\bar{1}\bar{1}3]_\alpha$ $(\bar{1}011)_\alpha$ [29]. This transformation also obeys the Burger's relationship, and the resulting hexagonal martensite is known as α' [4]. The morphology of α' is dependent upon the solute content, occurring as either 'massive' or 'acicular' martensite. 'Massive' martensite, also known as lath, or packet martensite, occurs in pure titanium and those alloys with relatively high martensitic transformation temperatures ($M_{s/f}$). As such, these alloys are very dilute with respect to β stabilising elements, although α stabilisers may be present since they raise the $M_{s/f}$. Massive martensite itself presents as large, irregular regions approximately 50-100 μm across, containing small packets of parallel α plates

32

(or laths) around 0.5-1 µm thick. The plates within each packet all share the same Burgers variant. 'Acicular' martensite occurs in alloys with a lower $M_{s/f}$ (higher solute content), forming a tightly mixed distribution of α plates with Burgers variants differing between them. The dislocation density is typically high within martensitic plates, and twinning may also be present in order to accommodate the transformation [30]. Subsequent annealing of α' in the α+β phase field leads to decomposition into the two equilibrium phases through the precipitation of β at dislocations and plate interfaces [2]. As solute content rises, a distortion of the hexagonal lattice takes place, giving rise to martensite with an orthorhombic crystal structure known as α''. Decomposition of this martensite appears to begin in a spinodal fashion across regions of high and low solute content [30]. While the microstructures detailed previously refer to cooling from above $T_β$, they also apply to cooling regimes from the α+β phase field. The α phase present during hot working will remain upon cooling, and is referred to as primary α. Depending on the cooling rate, the β phase fraction will transform to one of the microstructures mentioned above [20].

With enough alloying of β stabilisers, martensite formation can be suppressed entirely and the β phase retained down to room temperature. However, as Figure 2.7 indicates, there are a number of other phases which may form under certain conditions [17][8]. Of the metastable alloys, many of the leaner ones exhibit ω phase formation during decomposition of the β phase. This phase presents as a uniform distribution of extremely fine particles. It can form upon quenching, or, as in more heavily stabilised alloys, during subsequent ageing (in the region of 300-500 °C). The ω formed during quenching is known as athermal ω, while that induced through aging is referred to as isothermal ω. Formation of the athermal type occurs through a diffusionless transformation that involves the periodic displacement of [111] planes in the <111> direction (these being perpendicular to one another) [17]. The particles formed are of the order of 2-4 nm in diameter and therefore require the use of transmission electron microscopy (TEM) to resolve them.

Of the alloys which form athermal ω, the leaner compositions yield a hexagonal structure (though not hcp), while richer alloys exhibit a trigonal symmetry. The transition between the two is a continuous function of composition [2]. In more heavily stabilised alloys, so-called isothermal ω can form during ageing. Localised segregation creates solute lean regions in the β phase which then transform through the same shear displacement mechanism as the athermal ω particles [31]. These particles can grow in a compositionally invariant manner, but will subsequently stabilise through solute rejection [32]. The resulting particles are larger than the athermal type (up to 200 nm across) and their shape is dependent upon the precipitate/matrix misfit [17]. In low misfit systems (e.g. Ti-Mo and Ti-Nb), they form ellipsoids, aligning their long axis with one of the <111> directions of the β phase. In high misfit systems (e.g. Ti-V, Ti-Cr and Ti-Fe) they take on a cuboidal appearance, oriented such that their flat faces are

parallel to the {100} planes of the β phase. Isothermal ω can also form through aging of the athermal type [2][33]. In alloys with even greater β stabilisation, another solute lean phase known as β' may form during low-medium temperature ageing (Figure 2.7). This occurs through a phase separation reaction, as short range diffusion creates solute lean regions (β') within a solute rich matrix (β phase) [4][34]. The crystal structure of β' is that of a slightly distorted bcc lattice. The resulting precipitates are extremely fine and exhibit a number of different shapes including spheres, cuboids and plates, depending on misfit and coherency strains [2]. Decomposition of the β phase into β+β' is particularly important in alloys where the formation of ω is suppressed [34]. This can be achieved through alloying and/or the use of appropriate heat treatments. Direct ageing (quenching straight to the ageing temperature) and the presence of Al, Zr, Sn and O are known to suppress ω formation [17][35].
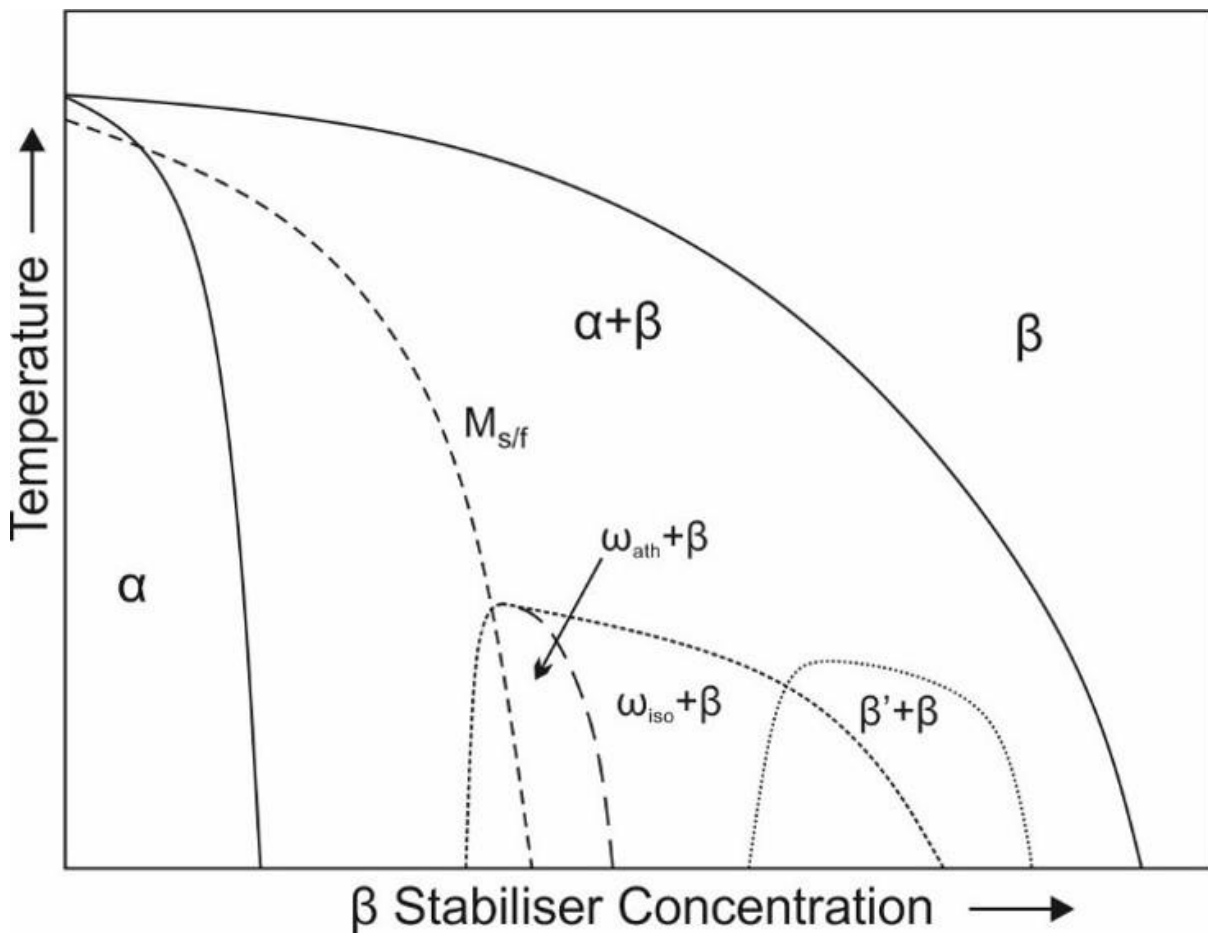
Figure 2.7: Pseudo-binary isomorphous phase diagram of β stabilised titanium, illustrating metastable phases [17][8]

2.3 Mechanical Influence of Metastable Phases

Metastable phases can affect the mechanical properties of β alloys in a number of ways. While the athermal ω phase is not believed to have much direct influence on mechanical properties, the isothermal form has a significant effect upon strength and ductility [36][37][38]. Deformation of the β phase occurs through slip in the <111> direction on the {110}, {112} and {123} planes. For a dislocation moving in the parent β phase, only one of the four ω variants will provide a slip direction that coincides, while the other three act as barriers. Isothermal ω particles thus provide a significant strengthening effect through the hindrance of dislocation movement [37]. However, it has been shown that the stress required for a by-pass mechanism is generally higher than that required for shear. Therefore, at sufficiently high stresses it is possible for dislocations to shear ω particles, and in so doing their resistance to further shearing is reduced, giving rise to strain localisation. This creates intense slip bands, leading to void formation and early crack nucleation [38]. The macroscopic effect of this is a severe embrittlement [39].

The extent of this influence would appear to depend upon the size, morphology and volume fraction of ω particles. For a given volume fraction, larger ω particles lead to greater embrittlement. This is thought to be caused by the interaction of more slip systems with larger particles, combined with the greater difficulty of cross-slip. As a result, dislocations pile up more rapidly and voids are formed earlier, at lower strains [40][41]. However, if the volume fraction of ω phase is kept below 0.6, it has been found that substantial improvements in yield strength can be achieved without unacceptable loss of ductility [42]. In addition, studies of the metastable β alloy Ti-10-2-3 revealed that grain size refinement could significantly improve ductility with only a relatively minor reduction in yield strength [43]. Despite this progress, the ω phase is still generally regarded as deleterious to ductility and avoided in commercial applications [2][44].

However, industrial thermal regimes often employ ω precipitation as a 'precursor' phase in order to nucleate a more homogenous distribution of intragranular secondary α. The preferential nucleation of α at grain boundaries and other discontinuities would otherwise lead to a very non-uniform distribution [6]. Developments in this area have raised the prospect of utilising the ω phase to engineer the secondary α and thus optimise mechanical properties [45][46]. The exact mechanism by which ω phase assists α nucleation is unclear, with some reports of nucleation within ω precipitates, and other studies indicating nucleation on or immediately adjacent to the ω/β interface [45][35][47]. It would appear though, that the level of misfit has some influence. In the case of high misfit systems such as Ti-V, α precipitates are believed to nucleate on ledges and dislocations at ω/β interfaces. For lower misfit systems, the mechanism is less well understood. It has been proposed that solute rejection from ω particles creates Al rich zones in the immediate vicinity of the ω/β interface. Since Al is an α stabiliser,

this would encourage nucleation of α precipitates close to, but not directly upon, the ω particles. Others have reported α nucleation within the core of ω particles [35]. However, regardless of the exact mechanism, there is little doubt that the ω phase can assist with α nucleation [17]. Figure 2.8 illustrates the effect of different thermal histories upon α phase formation in Beta 21S, an alloy that is known to form isothermal ω [48]. Both samples were solution treated above $T_β$, then cooled to room temperature and subsequently aged at 600 °C for 8 hours. However, the cooling rate from solution treatment was varied between the two samples. While one was air cooled all the way to room temperature (Figure 2.8(a)), the other sample was only air cooled part way, being furnace cooled from about 400 °C (Figure 2.8(b)). It can be seen that Figure 2.8(a) exhibits much coarser α laths that nucleated at the grain boundaries and grew into the grain interiors. These laths were unable to fill entire grains, leaving regions of retained β at the grain centres. On the other hand, Figure 2.8(b) displays much finer α precipitates distributed more uniformly throughout the grains.

This microstructural variation can be explained by consulting the time temperature transformation (TTT) diagram of Beta 21S (Figure 2.9) [49]. Air cooling and the subsequent rate of heating provided insufficient time for ω formation. This resulted in heterogeneous nucleation and growth of α at grain boundaries. However, furnace cooling from 400 °C was slow enough to allow homogenous nucleation of isothermal ω, followed by heterogenous nucleation of α on these ω particles, yielding a much finer, more uniform distribution of α precipitates [6][49].
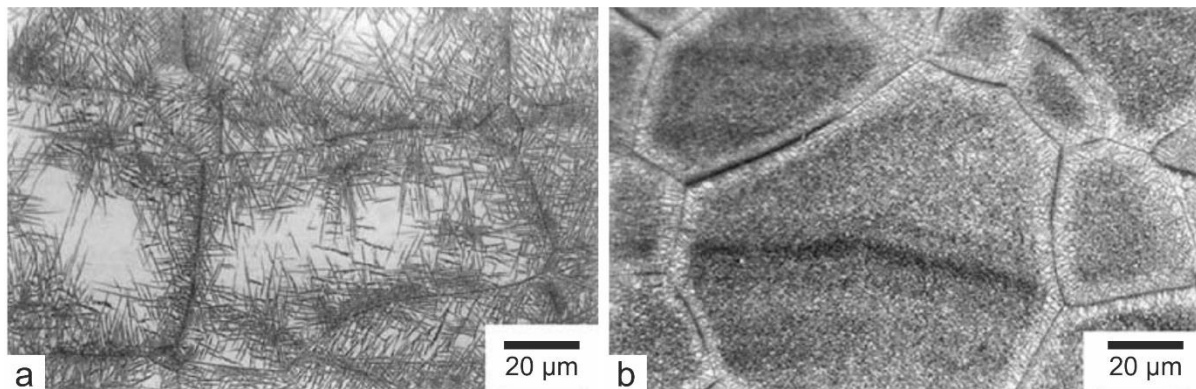
Figure 2.8: Micrographs illustrating the effect of different thermal histories on Beta21S. (b) experienced a slower cooling rate prior to ageing. Adapted from [6][48].
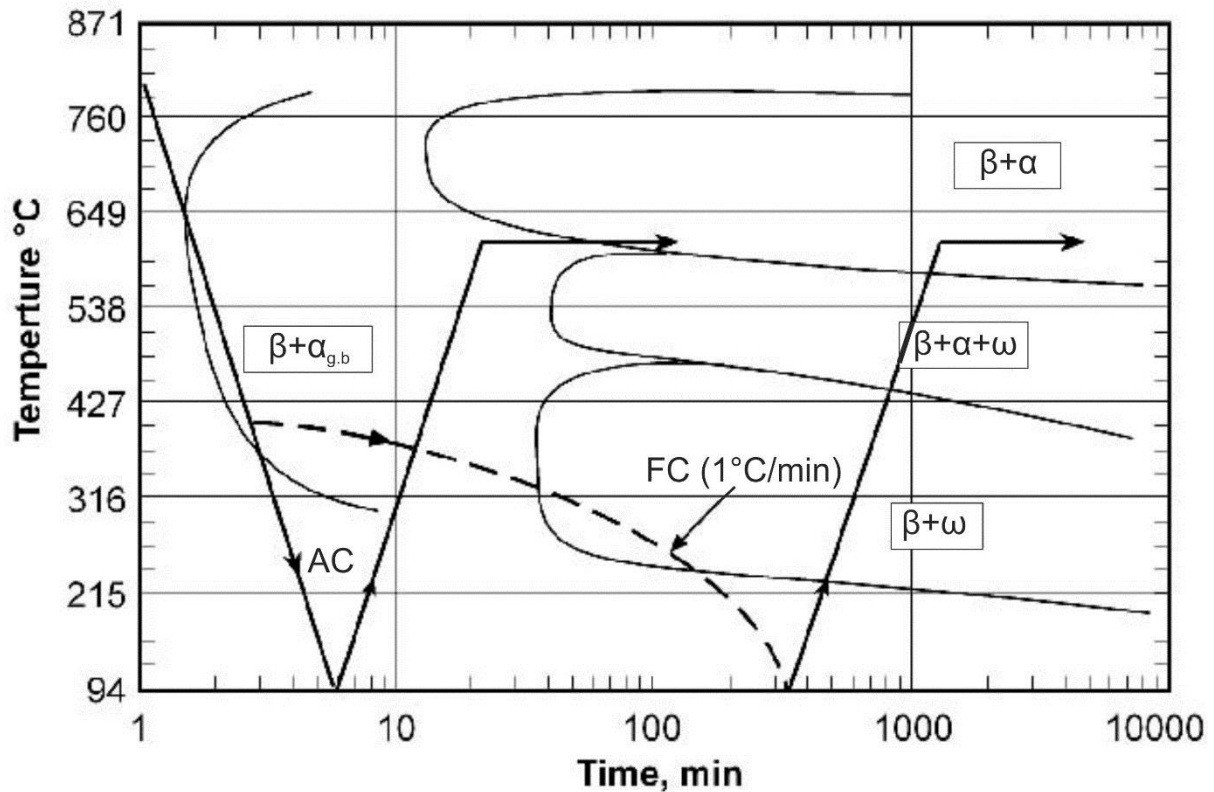
Figure 2.9: TTT diagram for Beta21S. Adapted from [6][49].

Heavily stabilised β alloys such as Beta 21S display this type of behaviour because the kinetics of ω formation are more sluggish than the leaner β alloys. Table 2.1 illustrates the improvements in yield stress and high cycle fatigue strength conferred by the finer, more uniform microstructure [6][48]. An alternative way to encourage a more homogenous distribution of secondary α is to employ a two step ageing treatment. The first, lower temperature age is designed to use ω particles as precursors to nucleate a uniform distribution of α precipitates. The second, higher temperature age then grows these precipitates to the desired size. Such 'pre-ageing' is less important for leaner β alloys as the ω phase forms more rapidly, allowing nucleation during heating to the ageing temperature [6]. However, quenching to the ageing temperature (direct ageing) may suppress or avoid ω formation, leading to a coarse, non-uniform microstructure [17][49]. The mechanical influence of the β' phase is similar to that of the ω phase. Like ω, it also maintains a coherent interface with the β matrix, providing strength but compromising ductility [2][50]. β' is also used as a 'precursor phase' to aid α nucleation and promote a more uniform, homogeneous α distribution [2][51]. This is particularly important for the heavily stabilised β alloys given their slower precipitation kinetics (see above) [17].

Table 2.3: Mechanical properties of the microstructures exhibited in Figure 2.8. HCF is at 10^7 cycles and R = 1. From [6][48].

Condition	$\sigma_{0.2}$ (MPa)	HCF Strength (MPa)
Air Cool Only	985	350
Air Cool + Furnace Cool	1120	500

The influence of titanium martensite upon mechanical properties is somewhat different to that of the Fe-C system. While α' provides some strengthening of titanium alloys, it is less significant than that provided by martensite in steels. This is due to the smaller elastic distortion of the hexagonal lattice compared to the severe straining of the bcc lattice in ferrous martensite [2]. The orthorhombic α'' martensite that forms in richer titanium alloys generally has little or no direct effect on strength [52]. However, martensite can significantly influence the elastic modulus of titanium alloys. Figure 2.10 illustrates this effect in the Ti-V system under rapid cooling (solid line). With increasing vanadium content, the modulus drops sharply, reaching a minimum at around 10% V. This behaviour is characteristic of titanium martensite as the concentration of β stabilisers increases [2][53]. The transition from α' to α'' occurs at 9.4% V [54]. However, the competing ω phase causes a sharp spike in the modulus at about 15% V. The modulus then drops again, reaching another minimum at 20% V, where rapid cooling can retain the β phase down to room temperature. The modulus of the β phase then rises with solute content, but is generally lower than that of the α phase. Annealing in the α+β phase field removes these fluctuations and creates a tie line in accordance with the rule of mixtures (dashed line) [2][53].

As mentioned earlier, the orthorhombic α'' martensite can also be stress induced in some alloys. This can give rise to superelastic and shape memory effects. Superelastic properties arise where large strains are accommodated by the reversible formation of stress assisted martensite. This phenomenon gives two yield points in a stress-strain curve, with the lower one being the 'trigger stress' at which martensite formation begins. Upon removal of a load, the transformation from α'' back to the β phase allows recovery of a relatively large strain [55][56]. In the case of 'permanent' deformation induced martensite, this strain can sometimes be recovered by heating the material above it's A_s temperature, whereupon the martensite transformation reverses. This effect is known as 'shape memory' [57][58]. Formation of stress assisted martensite appears to be influenced by the stability of the β phase, with increasing stabilisation suppressing stress induced transformations. Thus, the occurrence of deformation induced martensite is affected not only by the nominal alloy composition, but also its thermal history. Solution treating in the α+β phase field allows partitioning of solutes between the two phases, stabilising them and inhibiting the formation of stress induced martensite [55][59]. Although α'' provides little in the way of strength, the low modulus of martensite and the β

phase does make β alloys potentially useful in orthopaedic implants [4]. A low modulus is desirable in these applications in order to ensure sufficient load transfer to the surrounding bone. Failure to do so is believed to cause bone resorption and associated loosening of the prosthesis. This 'stress shielding' effect is minimised in β alloys since the modulus is much closer to that of bone [60]. While titanium itself is relatively biocompatible, concerns over the toxicity of some β stabilising elements (e.g. V, Cr, Ni etc) has lead to a search for safer alloying additions [4][58]. Other work has looked at inducing martensite through deformation. In addition, despite the embrittling effect of the ω phase, some studies have attempted to induce a controlled amount to improve strength without an unacceptable increase in modulus. Success will require careful microstructural control in order to balance these competing properties [60][61].
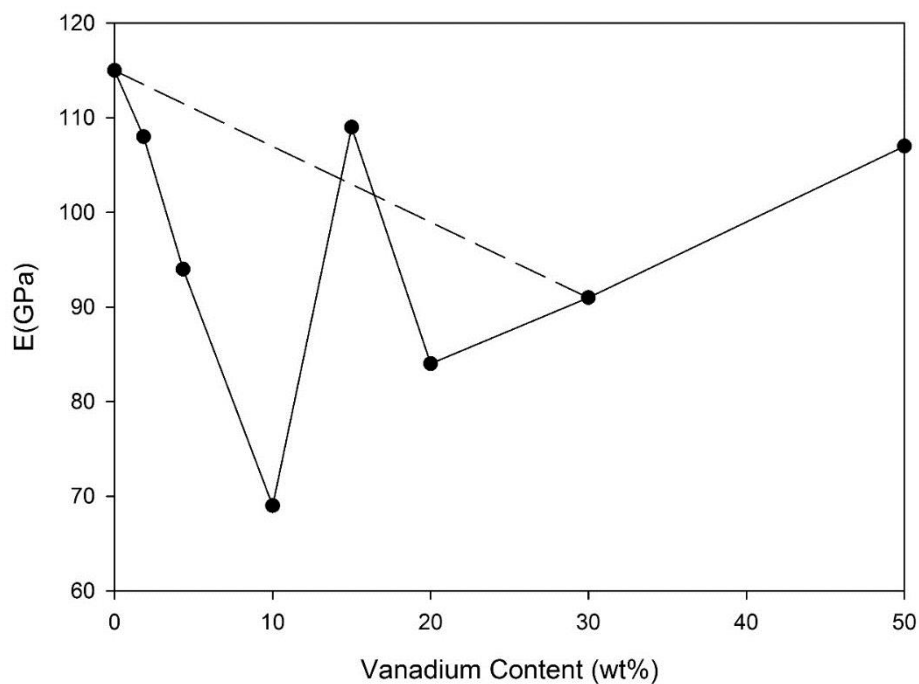
Figure 2.10: Variation in elastic modulus (E) with vanadium content in Ti-V system. Solid line represents 24 hrs at 900 °C followed by water quenching. Dashed line represents modulus after annealing at 600 °C. Adapted from [2][53].

Like the other metastable phases, martensite can also influence subsequent microstructural development, and thus have further, indirect effects upon mechanical properties. This has important implications for thick sections where there is the possibility of quenching stresses inducing α''. A study of the β alloys Ti-10-2-3 and Transage 134 demonstrated that age hardening of stress assisted α'' was more effective than ageing the retained β of slower cooled specimens. Therefore, careful attention should be paid to quenching stresses when trying to ensure uniform properties throughout large components [17].

2.4 Process Metallurgy of Titanium Alloys

As mentioned earlier, the major obstacle hindering the widespread application of titanium alloys is the high cost of extraction and processing. This is due in part to its high reactivity, which makes extraction difficult, and complicates subsequent processing [2]. In addition, the temperature sensitivity of microstructural development often requires the use of isothermal or near-isothermal forging practices, adding further cost and complexity [62]. Today, the Kroll process remains the predominant method for extraction of metallic titanium, although there are ongoing efforts to develop more efficient production routes [63]. The Kroll process itself involves the reduction of $TiCl_4$ by Mg. This is a batch process that has to be conducted under an inert atmosphere and therefore incurs substantial cost. The resulting product is porous and sponge-like in appearance. In order to produce a solid, homogeneous ingot, several further melting operations are required. These are carried out through vacuum arc re-melting (VAR) or cold hearth melting (CHM). Care must be taken to prevent the introduction of defects at this stage, as they are difficult to remove through subsequent processing.

Of particular concern for segregation prone alloys such as Ti-10-2-3 and Ti-17 is a defect known as 'beta fleck'. This occurs where segregation leads to regions over enriched in β stabilisers. These regions do not harden adequately in response to ageing, as the driving force for α precipitation is lower. Fatigue performance is compromised by this, as the strength mismatch between these soft 'beta flecks' and the harder surrounding material leads to strain localisation and early crack nucleation. Alloys containing β eutectoid stabilisers tend to solidify over a relatively wide temperature range, exacerbating segregation during solidification. As a result, alloys such as Ti-10-2-3 are more susceptible to 'beta fleck'. Improvements in melt practice, such as the use of smaller diameter ingots and lower melt rates help reduce these segregation problems. However, this only adds to the already high cost of production, particularly since VAR is already a batch (ingot) operation. Recycling scrap is an obvious way to lower costs, but great care must be taken to avoid contamination, as the cost of removing defects later is considerable [2].

Melting is carried out multiple times in order to minimise the presence of defects. Once these steps are complete, an ingot is subjected to thermomechanical processing in order to achieve a suitably shaped product with the required microstructure (and hence properties). This stage can be subdivided into primary and secondary processing [62][64][65]. Primary processing is intended to break down the coarse ingot microstructure and produce a uniform, equiaxed microstructure that will respond to subsequent thermomechanical processing in the desired manner. Secondary processing focuses on optimising the microstructure and achieving a shape that is as near to that of the final component as practical. This latter point helps minimise machining losses [2].

2.4.1 Primary Processing

Typically, an as cast ingot is first given a homogenisation treatment in the β phase field. The initial hot working is also carried out in the β phase field through a process known as cogging. This involves feeding the ingot/billet through an open die press while rotating it about its long axis between forging steps. In this way the ingot is transformed into a longer, narrower billet [66]. Since segregation prone alloys are typically cast as smaller diameter ingots, they may also require an upsetting operation to ensure sufficient strain can be applied during cogging. Following initial deformation, rapid cooling is employed to minimise the formation of grain boundary α, either through water quenching (Ti-64) or aggressive fan cooling (Ti-10-2-3) [2]. Alpha alloys will be further worked in the α phase field, while α+β and metastable β alloys can be worked in the two phase (α+β) phase field [4].

The presence of primary α phase at the forging temperature helps pin β grain boundaries and prevents excessive grain growth during subsequent thermal treatments [17]. Care must also be taken when forging in the β phase field, as selective recrystallization can introduce a mixed grain structure of widely differing sizes. Once formed, thermal treatments alone cannot remove such a non-uniform microstructure. The use of processing maps helps illustrate the 'window' through which working must be conducted to avoid such problems. The exact temperatures and processing routes will vary between alloys. Some metastable β alloys such as Beta-C are processed entirely within the β phase field, while others begin with super transus forging and finish with subtransus work (e.g. Ti-6246) [2][62].

In recent years, it has become clear that the ingot breakdown can have significant influence beyond that which is observable by conventional microscopy. This has come about due to the development of Electron Backscatter Diffraction (EBSD), which has permitted a more comprehensive analysis of texture evolution. Davies [67] investigated the textures formed during production of a Ti-834 billet, and demonstrated that secondary working was not an efficient means of removing them. The persistence of such textures in a final product has implications for fatigue performance. Similar results of texture variation were reported by Nasseri [68] in a Ti-6246 billet. Crawforth [69] also showed how billet texture could affect machinability further downstream in the production route (with possible implications for fatigue life).

2.4.2 Secondary Processing

Secondary processing consists of forging/shaping operations that convert a billet into a part with the desired final microstructure, ideally with a shape as close to the final component dimensions as possible [62]. For β alloys this is often carried out in the (α+β) phase field, where a specific volume fraction of primary α will be required to achieve the desired microstructure. This is due to the direct and indirect effects that the primary α phase can have on the resulting mechanical properties [6]. The presence of primary α can also influence evolution of the β phase substructure [70]. However, given the temperature sensitivity of the α volume fraction, these requirements often result in a very narrow temperature range in which to operate. In addition, the flow stress can vary markedly with only minor fluctuations in temperature. The effect of die chill can therefore lead to strain localisation, and corresponding microstructural variation throughout the workpiece [64].

Adiabatic heating can also complicate matters, compounded by the low thermal conductivity of titanium. This is of particular concern when forging near the β transus, when such temperature fluctuations could exceed the transus and transform the microstructure completely. Strain localisation can also result from minor temperature variations due to the temperature sensitivity of the flow stress. A compromise must also be made between energy input and dimensional accuracy. Higher temperatures provide lower flow stresses, whereas better dimensional accuracy is achieved at lower temperatures [20]. Temperature and flow stress will also have an effect upon die life that will need to be accounted for. The difficulties associated with microstructural control of titanium alloys thus make the use of isothermal forging an attractive option. This involves maintaining the dies and workpiece at the same temperature during forming. With a constant temperature maintained throughout the forging operation, slower strain rates can be employed (10^{-5} - 10^{-1} s^{-1}). This in turn keeps flow stresses low and minimises adiabatic heating, resulting in a uniform microstructure throughout the workpiece.

The cost of isothermal forging equipment is substantial, but the process control that it offers can justify the expense for high value products. It is also capable of achieving nearer net shape than conventional forging processes. This helps offset some of the expense through material savings, in addition to reducing the time and tooling costs of machining excess material away [71].The use of computer software to model complex forging operations now permits the rapid and cost effective development of production plans by reducing the need for expensive, time consuming trials [72]. Common programs employed in this process are DEFORM and ABAQUS, providing significant modelling capabilities coupled with user friendly interfaces. Currently, much of this modelling is empirical, relying on curve fitting of process variables (strain, strain rate, temperature) with microstructural evolution. While this can provide accurate results within a given range of process variables, it can struggle to deal with variations that encompass multiple modes of deformation. In order to overcome this, a more fundamental,

micromechanistic approach is required, based upon a deeper understanding of the actual deformation processes taking place. Much work on high temperature deformation during the two phase (α+β) field aims to address this matter [20][73]. However, despite advances in forming technology, there are still significant limitations to the final shapes that can be attained through forging processes. This can result in the need to remove substantial quantities of material when machining the forged part to its final dimensions. It is not uncommon for complex, forged aerospace components to possess a 'buy-to-fly' ratio of 10:1 (where 90% of the original forging is machined away). This adds significant cost to production, but also represents an opportunity for significant saving through better process modelling.

Unfortunately, there are factors beyond the forging process itself that can limit the final shape. The use of ultrasonic inspection to detect defects often requires forgings to possess a rectilinear shape. Improvements in forging processes may not be fully realised while the component shape is limited in this way. Although powder metallurgy offers the potential for near net shape forming, at present it cannot match the properties of forged components in high performance applications [73]. Therefore, with cost continuing to be a significant hurdle, the successful application of titanium will require a thorough understanding of process-microstructure-property relationships in order to maximise performance [2].

2.4.3 Microstructural Development of β Titanium Alloys

As mentioned previously, in addition to the forming objectives of secondary processing, it is also necessary to achieve the required microstructure. The defining characteristic of metastable β alloys is their ability to achieve much higher aged strengths compared to α+β alloys [6]. While this is accomplished through the precipitation of secondary α, careful process control is able to obtain a wide range of microstructures in order to optimise other mechanical properties such as ductility and toughness [62]. The exact process will depend upon the specific alloy and intended use, but a distinction can be made between the high strength β alloys and the more heavily stabilised ones. The lower transus of the more heavily stabilised alloys permits deformation at lower temperatures, and in some cases even cold work [6]. Of the various different processing routes available, Figure 2.11 illustrates what is known as the 'β annealed' condition. This microstructure is achieved through a recrystallization heat treatment in the β phase field prior to ageing. Low magnification micrographs reveal the presence of continuous layers of α along the β grain boundaries. At higher magnification, transmission electron microscopy (TEM) shows the fine scale secondary α platelets precipitated during age hardening. Figure 2.11(b) also reveals the so-called 'precipitate free zone' (PFZ) adjacent to the grain boundary α layer. In this region, α precipitation is suppressed due to rejection of β stabilisers by the grain boundary α. This lack of age hardening leads to localised deformation

along the grain boundaries and early crack nucleation. While it is possible to encourage more uniform nucleation of α particles within β grains through the use of 'precursor' phases such as ω and β', the formation of continuous α layers along the β grain boundaries is unavoidable due to preferential nucleation of α at these locations. As a result, the β annealed condition is unsuitable for high strength β alloys, where the strength mismatch between the aged matrix and grain boundaries is most pronounced. On the other hand, heavily stabilised β alloys such as Beta 21S, Beta C and Ti-15-3 employ similar processing in the manufacture of various products including strip, springs and nut clips. The grain size of β annealed microstructures is also typically smaller for β alloys than α+β alloys. This is because the rate of grain growth above the β transus is exponentially dependent upon absolute temperature. As such, the lower transus of β alloys slows this process considerably. Typical grain sizes for high strength β alloys might be 400 μm compared to 600 μm for α+β alloys, and as small as 40-50 μm for heavily stabilised β alloys [6].
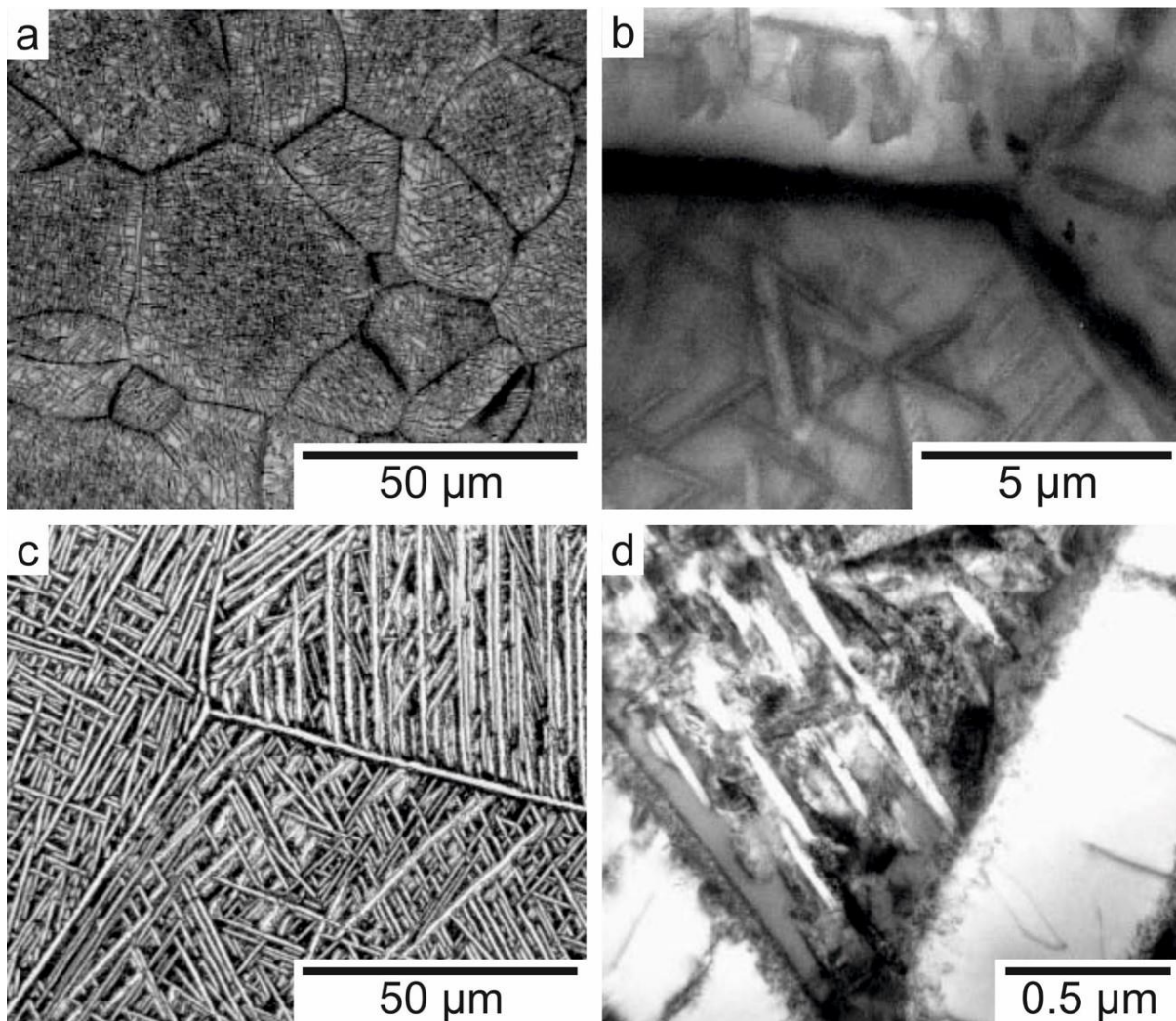
Figure 2.11: Beta annealed microstructures in Beta21S (a)-(b), and β-CEZ (c)-(d). Left hand images are light micrographs, right hand images are TEM micrographs. Adapted from [6][74].

44

Since the β annealed condition is unsuitable for high strength β alloys, alternative processing routes have been developed in an attempt to address the problems with grain boundary α. The first two of these (β processing and through-transus processing) focus upon minimisation of grain boundary α formation. The third option (α+β processing) is intended to produce a bimodal microstructure which mitigates the effect of these layers on final mechanical properties. Figure 2.12 provides an example of a β processed microstructure. For this condition, deformation is carried out in the β phase field, followed by sufficiently rapid cooling to prevent recrystallization and minimise the growth of grain boundary α. This results in a microstructure consisting of unrecrystallised β grains with highly deformed boundaries. The α layers which form on these grain boundaries adopt their deformed shape, leading to a discontinuous wavy appearance, with some side plates growing into the grain interior. The length of these side plates can vary but is limited by the width of the deformed β grains (Figure 2.12(a)). An annealing step is used to control the size and volume fraction of these 'coarse' α plates, before an ageing step precipitates a distribution of finer α platelets between them (Figure 2.12(b)). The size and volume fraction of these fine α platelets dictates the strengthening effect they provide. The asymmetrical shape of the unrecrystallised β grains also leads to anisotropic behaviour in mechanical properties influenced by the grain boundary α. This must be accounted for during the design phase of a component [6].
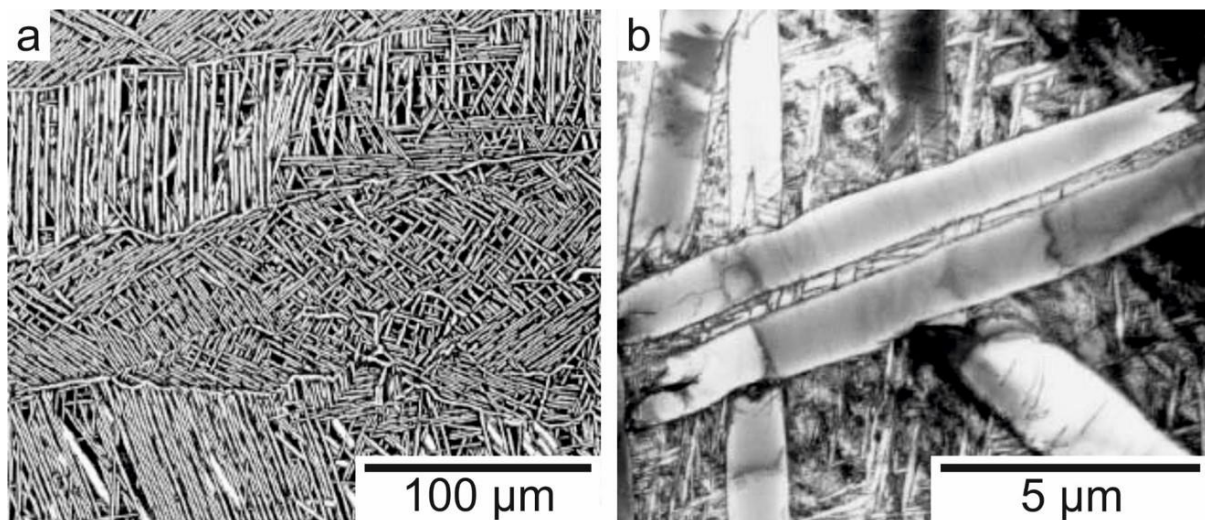
Figure 2.12: Beta processed microstructure of Ti-6246, under light microscopy (a), and TEM (b). Adapted from [6]

The intention of through-transus processing is to break up and globularise the grain boundary α as it forms. This is achieved by beginning deformation above the β transus and finishing in the (α+β) phase field. If successful, the resulting microstructure should consist of deformed β grains, decorated by separate globular α particles (Figure 2.13(a)) [6][75]. Work by CEZUS on β-CEZ led to their naming this a 'necklace' microstructure on account of its appearance [76].

As with the β processed microstructure, an annealing step is used to control the size and volume fraction of α particles, before ageing produces a dispersion of intragranular α platelets (Figure 2.13(b)) [6]. Careful control of the deformation time within the β phase field is required to avoid recrystallization of β grains (Figure 2.13(c)). In addition, it is also important to limit the time spent within the (α+β) phase field to prevent formation and globularisation of intragranular α (Figure 2.13(d)) [77].
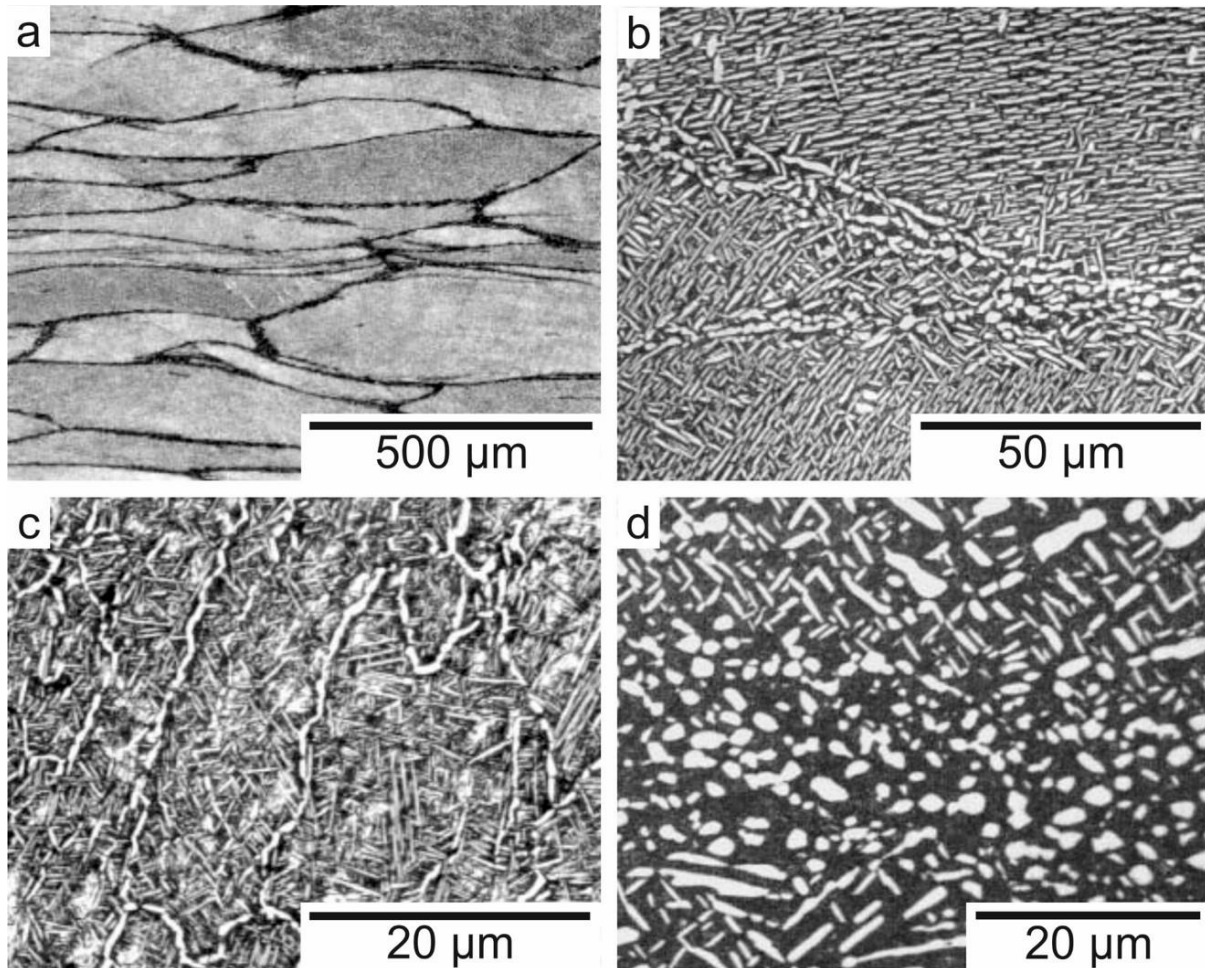
Figure 2.13: Through-transus processed microstructures. (a) and (b) are Ti-6246. (c) and (d) illustrate possible complications (in this case, for β-CEZ), where β recrystallization has begun (c) and intragranular α has formed during deformation (d). Adapted from [6][77].

The creation of a bimodal microstructure is intended to minimise the detrimental effect of grain boundary α by reducing the β grain size (Figure 2.14). The process route for such a microstructure begins with a homogenisation treatment in the β phase field. The cooling rate from this heat treatment determines the thickness of the grain boundary α layer. Deformation then takes place in the (α+β) phase field to break up and recrystallize the grain boundary α, producing isolated, globular α particles. Following deformation, a recrystallisation anneal then produces a new set of small, equiaxed β grains, the size of which is determined by the spacing between the globular α particles. Like the previous two conditions, an annealing step is

employed to set the size and volume fraction of coarse α particles, before an ageing treatment induces precipitation of fine scale α platelets (Figure 2.14(b)). An important issue at the beginning of the process route is the cooling rate from the β homogenisation treatment. Slower cooling rates lead to thicker layers of grain boundary α. Once formed, these are more difficult to break up and globularise in the deformation step [6]. Figure 2.15 shows a remnant α layer on a prior β grain boundary that persisted into the final microstructure [77]. This can only be removed by repeating the deformation step and all the treatments that followed it, adding extra time and cost to production [6].
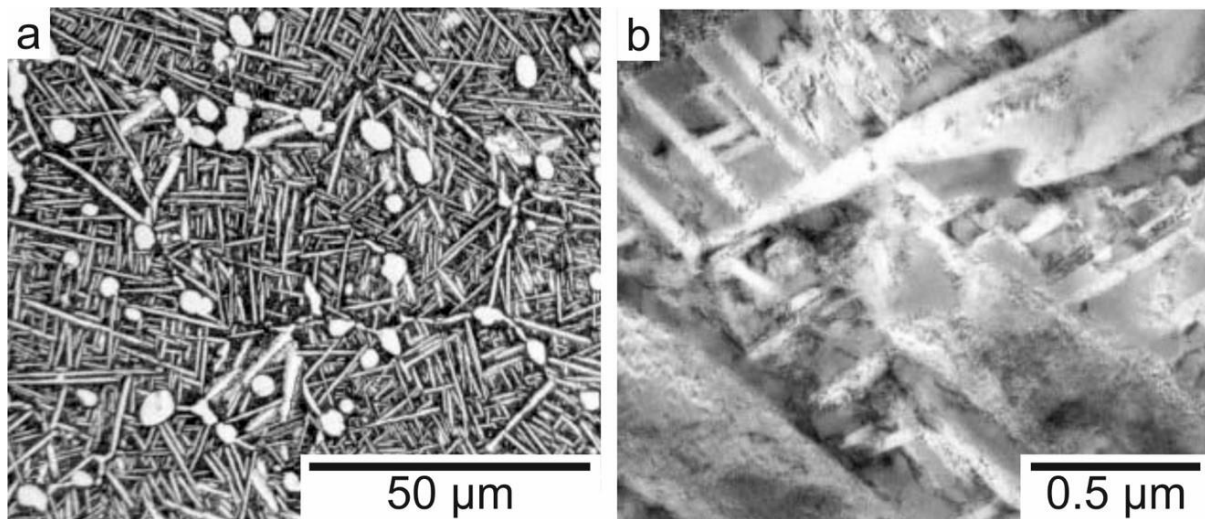
Figure 2.14: Bimodal microstructure in β-CEZ, under light microscopy (a), and TEM (b). Adapted from [6].
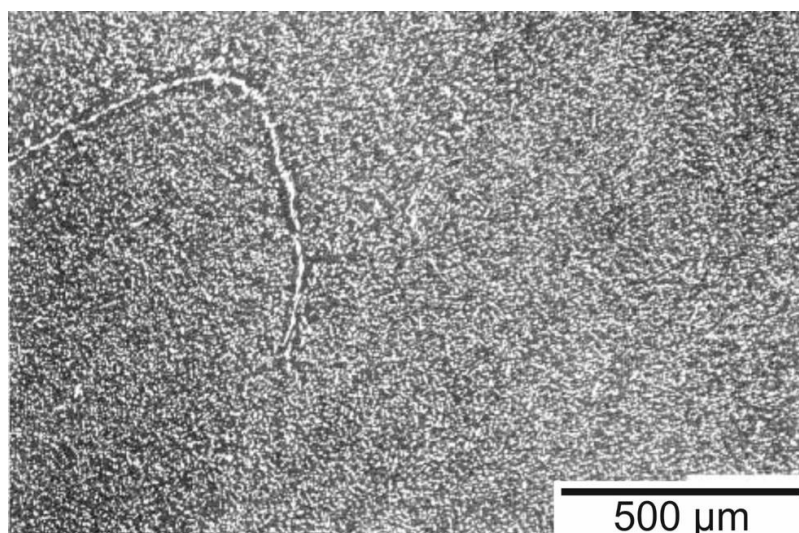
Figure 2.15: A remnant α layer at a prior β grain boundary in a heat treated bimodal microstructure (β-CEZ). Adapted from [6][77].

2.4.4 Microstructural Influence of Mechanical Properties in β Alloys

The ability to manipulate the microstructure of β alloys through thermomechanical processing provides the opportunity to fine tune mechanical properties for specific applications. However, in order to capitalise on this, a thorough understanding of the relationship between microstructure and properties is required. As mentioned previously, the high strength of β alloys is achieved through the precipitation of fine scale α platelets. These act as hard, undeformable particles that impede the movement of dislocations, and thus strengthen the material. The resistance of these particles to deformation appears to be related to their small size. For a given volume fraction, a smaller particle size results in a higher particle density. This reduces the interparticle spacing, and thus the slip length in the β matrix. Consequently, it is more difficult to reach the critical stress concentration for slip to penetrate a small α particle. It should also be noted that the dislocation density in the β matrix rises during α precipitation. This lends further strength through dislocation hardening [17][78][79][80]. Since the strength provided by α/β interfaces is derived from obstructing dislocation movement, the hardening effect is found to be inversely proportional to the interparticle spacing (Orowan relationship). It is therefore possible to estimate the yield strength of β alloys with formulae such as Equation 2.8 [8][81]:

$$TYS = 850 + 70d^{-1} \qquad (2.8)$$

Where TYS is the tensile yield strength (MPa) and d is the interparticle spacing (μm). The level of strengthening provided by second phase particles is also dependent upon their shape. While a distribution of spherical particles will improve strength, the hardening effect of particles adopting a needle or plate-like morphology can be an order of magnitude greater [82]. Thermal treatments are utilised to control the distribution of secondary α. The choice of ageing temperature is critical in achieving the desired size, with lower temperatures generally producing a finer distribution. The cooling and heating rates during solution treatment and ageing can also affect the size and morphology of secondary α particles. As discussed in Section 2.3, the homogeneous precipitation of precursor phases (ω and β') help produce a finer, more uniform distribution of secondary α. Depending upon kinetics of formation, the cooling/heating rates involved in thermal treatments will influence the formation of these precursor phases, and by extension, the final distribution of secondary α [6]. The solution treatment is also used as a means to manipulate strength. By solution treating in the α+β phase field, a controlled volume fraction of coarse primary α particles is produced. Since these particles are too large to provide any significant strength, they can be used to control the volume fraction of retained β that is available for hardening during ageing. Therefore, a decrease in the

solution treatment temperature will generally lead to a lower aged strength, since the volume fraction of coarse primary α will be greater, and thus the volume fraction of secondary α will be lower. In addition, partitioning of stabilising elements during solution treatment leads to greater stability of the β phase. This in turn will reduce the equilibrium volume fraction of secondary α leading to a lower aged strength. However, where a decrease in solution treatment temperature prevents recrystallization, it is possible to see an increase in aged strength since this can enhance α phase nucleation enough to counteract the influence of increased β phase stability [17].

Given that the primary α particles provide little strength, changes in the solution treatment temperature will have little effect on the ultimate tensile strength (UTS) in the unaged condition. However, the yield strength and work hardening behaviour can be affected if changes in the β phase stability influence the propensity for stress assisted phases to form (such as α'' and ω) [83]. For example, in Ti-10-2-3, higher solution treatment temperatures can reduce the β phase stability to the point that stress assisted martensite will form during deformation. This leads to a reduction in yield strength and improved work hardening, but almost no effect on UTS [84]. Similar behaviour has been observed in the newer β alloy Ti-7333, where changes in solution treatment altered the yield strength to a far greater extent than the UTS, prior to ageing [85].

In addition to strength, other mechanical properties can also be optimised through microstructural control. However, it is often the case that these properties compete with each other, and thus a compromise must be reached for a given application. For example, as with many alloys, ageing to a higher strength will generally lead to a decrease in ductility. However, for a given strength level, it may be possible to improve ductility by altering thermomechanical processing. For equivalent strength levels, the bimodal microstructure (produced through α+β processing) provides far superior ductility than the β annealed condition. The improvement in ductility comes about as a result of the reduction in β grain size. Deformation of high strength β alloys leads to strain localisation within the soft grain boundary α layers. This results in stress concentrations at grain boundary triple points, leading to early crack nucleation. By reducing the β grain size, the effective slip length (distance between grain boundary triple points) is reduced, lowering the stress concentrations and thereby improving ductility. Consequently, the true fracture strain has been found to be proportional to D^{-1} (where D is the grain boundary length) [6].

Unfortunately, improvements in ductility brought about through thermomechanical processing often lead to a reduction in fracture toughness [62]. In β alloys, the high strength of the aged matrix results in a tendency for cracks to follow grain boundaries. This actually confers greater fracture toughness to microstructures with larger β grains, as they present a geometrically less favourable route for cracks to grow (greater deviation from the macroscopic direction of crack

growth). Furthermore, when a crack does enter a grain, acicular α particles provide greater crack deflection than globular α particles. As a result, the β annealed microstructure, with its large β grains and acicular α particles, offers superior fracture toughness compared to the bimodal (α+β worked) microstructure with its smaller grain size and globular α [17][6]. However, an improvement in toughness does not necessarily translate to better fatigue performance, since this is dependent upon other factors such as crack initiation [20]. The rate of fatigue crack growth (FCG) may also vary depending upon length scale. Studies of β-CEZ showed that the propagation of small fatigue cracks (microcracks) was slower in the bimodal microstructure than the β annealed condition. On the other hand, macrocracks propagated more rapidly in the bimodal microstructure, but despite this it was still capable of delivering greater fatigue strength [6]. Interestingly, microstructures aged in the ω phase field exhibit significantly lower FCG rates than α aged samples of equal strength. This has been attributed to enhanced slip reversibility reducing the accumulation of damage at the crack tip, and therefore slowing its advance. However, the greater reversibility is a consequence of deformation through coarse planar slip, which increases the rate of crack nucleation and ultimately leads to a shorter fatigue life [17][86].

In the case of unrecrystallised microstructures with elongated β grains, there can be significant anisotropy in the tensile properties. Generally, the best ductility is found when testing parallel to the working direction (longitudinal axis). However, there is a substantial reduction in both ductility and yield strength when tested at 45° to the longitudinal and short transverse directions. The drop in yield strength arises from the crystallographic texture of the β matrix, whereas the ductility is compromised because the broad faces of β grains are oriented in the position of maximum shear stress (45° from the applied stress axis). This exacerbates the stress concentrations at grain boundary triple points, and promotes early crack nucleation. There is also a drop in ductility (relative to the working direction) when tested in the short transverse direction, though not as severe as at 45°. The normal stress acting upon a grain boundary crack will be greater when the elongated β grains are oriented perpendicular to the tensile axis. This leads to faster crack propagation and a reduction in ductility [6].

With a relatively low elastic modulus and density, titanium is well suited for spring related applications in aerospace. The weight savings of such springs can be as much as 70% when compared to their steel counterparts. This substantial reduction in weight is a result of the combined effects of low modulus and density, since half as many coils can be used (i.e. half the volume) at 60% of the density of steel. In addition, the corrosion resistance of titanium springs is superior to that of steel, reducing the frequency of maintenance and replacement [24][5]. As mentioned in Section 2.3, the room temperature β phase has a lower modulus than the α phase, making β alloys the logical choice for use in springs. Further reductions in modulus are achievable in near β alloys through the formation of martensite. If higher strength is

required, ageing may be necessary, but since the α phase has a higher modulus, there will be a corresponding increase in the bulk modulus [6].

It is obvious that understanding the microstructural influence of mechanical properties is a prerequisite for successful manipulation of these properties. Unsurprisingly though, given the difficulty in separating the effects of individual variables there is still much confusion. For example, despite the apparent advantages of the bimodal microstructure, some studies have found conflicting results, with reports of inferior ductility under certain conditions (but at equivalent strength levels) [87]. However, given the number of competing microstructural variables, it is possible there exist differences that are unaccounted for. This also illustrates the difficulty encountered with optimisation of mechanical properties, and underscores the need for a deeper understanding of the fundamental mechanisms that govern such properties in β titanium alloys.

2.5 Ti-10V-2Fe-3Al

Ti-10-2-3 is a high strength metastable β alloy which sits very close to the $M_{s/f}$ [8]. It exhibits excellent forgeability and can be heat treated to a wide range of strength levels in order to tailor properties to specific applications [84]. It has good hardenability, although water quenching from solution treatment is required to ensure a sufficient response to ageing. In the high strength condition, this limits the section size at heat treatment to 76 mm [8]. This can also impose considerable residual stress that can affect dimensional accuracy when machining. Such residual stress should be closely monitored as Ti-10-2-3 is also known to form stress assisted martensite [17]. However, Ti-10-2-3 offers greater tensile strength than the ubiquitous $\alpha+\beta$ alloy, Ti-6Al-4V. At a section thickness of 76 mm, Ti-10-2-3 can reach 1193 MPa, compared to 965 MPa for similarly sized Ti-6Al-4V components [88][89]. This allows it to compete with steels in aerostructural applications [84]. One notable application is the Boeing 777 main landing gear, where it replaced 4340M. This resulted in weight savings of approximately 270 kg per aircraft [5].

Thermomechanical processing is necessary to achieve the correct balance of properties for a specific application. Globularisation of the primary α improves ductility, but this must be weighed against the toughness requirements, which benefit from a more acicular morphology [8]. Hot deformation in the $\alpha+\beta$ phase field is characterised by an initial peak in flow stress at low strain, followed by extensive flow softening. The observed softening is believed to be caused by break-up of acicular primary α particles into a more globular morphology [90]. At low strain rates, deformation is dominated by dynamic recovery [91]. The microstructural evolution during subtransus forging is very temperature sensitive, exhibiting a relatively narrow 'processing window' in which to operate. Segregation issues were initially reported as a result of the iron content, although improvements in melt practice are now capable of dealing with these issues [8].

2.6 Ti-5Al-5Mo-5V-3Cr

Ti-5553 was developed in the 1990s by VSMPO to address some of the issues with Ti-10-2-3. It combines marginally superior mechanical properties with improved processing characteristics. It is based upon the older Russian alloy, VT-22, exhibiting deeper hardenability than both Ti-10-2-3 and its predecessor, VT-22. The lower iron content reduces segregation issues. This allows higher melt rates and an accelerated production schedule. Homogenisation of ingots is not required, saving time and improving yield. Air cooling from solution treatment can be employed up to a section thickness of 150 mm. Further, the aged strength exceeds that of Ti-10-2-3 and VT-22. It also exhibits a shallower β approach curve, providing a wider processing window [8].

The Boeing 787 main landing gear features Ti-5553 extensively, making up the Bogie beam and inner cylinder [24]. The deformation behaviour is reported to be similar to that of Ti-10-2-3, with dynamic recovery being the dominating mechanism. The microstructural evolution is also more stable with respect to forming variables, in particular temperature and strain rate, allowing for easier processing [92]. It has also been confirmed that Ti-5553 exhibits athermal formation of the ω phase, raising the possibility of engineering the secondary α distribution [93]. However, as with all titanium alloys, it remains an expensive choice for manufacturers, which remains a barrier to wider use.

2.7 Summary

Beta titanium alloys represent a growing fraction of the materials employed in aerostructural applications on account of their high specific strength and good corrosion resistance. Ti-10-2-3 and Ti-5553 are two such alloys that have found use in the main landing gear of large commercial aircraft. However, the high cost of these alloys demands exceptional performance. This places a great deal of emphasis on microstructural development to ensure the mechanical properties meet such standards. Thermomechanical processing (TMP) is critical in the achievement of these objectives, and therefore a thorough understanding of the relationship between processing and microstructure is required. This is particularly important given the costly nature of TMP itself. Redundant work that achieves marginal refinement of the microstructure only adds to the cost of production with little improvement in properties.

In addition to this, the influence of microstructure on mechanical properties must be understood in order to guide the microstructural objectives of the forger. Ti-5553 represented an improvement in processability over Ti-10-2-3. However, these alloys are operating at the upper limit of their capabilities in such demanding applications as aircraft landing gear. This requires consistency in mechanical properties, and although Ti-5553 can meet the strength requirements, there have been difficulties with obtaining the required ductility. This thesis intends to examine these issues by investigating the process-microstructure-property relationships in metastable β alloys.

Chapter 3 Characterisation Methods

The specific methodologies employed in Chapters 4 and 5 are included at the beginning of each respective chapter. However, to avoid repetition, the characterisation techniques employed in both are detailed here.

3.1 Microscopy

3.1.1 Light Microscopy

Reflected light microscopy was carried out with a Nikon microscope on etched specimens. Sample preparation began with mounting of the specimen in Bakelite. Specimens were then ground flat using p800 SiC paper under 30 Newtons of force and water lubrication (platen rotation was 150RPM). A plane surface could be achieved in 3-4 minutes. Once flat, specimens were ground on p1200 SiC paper under the same conditions for 5 minutes. Fine grinding was carried out with 9µm diamond suspension on an MD-Largo composite disc for 6 minutes. The force and platen speed were also 30 Newtons and 150 RPM respectively. However, additional lubrication was unnecessary since the diamond suspension is water based. An MD-Chem polishing cloth was employed for the final step, together with 0.06 µm colloidal silica. As with the fine grinding, water lubrication was unnecessary while polishing. The duration was 10 minutes, with a 1 minute break in the middle (11 minutes in total).

The break employs water lubrication in the absence of colloidal silica. A 5 minute water-only step is also included at the beginning and end to clean the disc and specimens. It is imperative that all specimens and holders are washed between stages to prevent coarser grinding media contaminating finer abrasives. Etching was carried out via immersion in Kroll's reagent for 8-10 seconds. The etchant was made up using standard laboratory concentrations of the acids in question. This consisted of 6 vol% hydrofluoric acid and 12 vol% nitric acid with the balance being water. Mechanical polishing of Ti-10-2-3 has been known to induce stress-assisted martensite [2]. However, none was observed in this study (possibly due to the stability that the α phase offered) so electro-polishing was unnecessary.

3.1.2 Electron Microscopy

Electron microscopy was carried out with an FEI InspectF Field Emission Gun Scanning Electron Microscope (FEG SEM). The sample preparation procedure was very similar to that for light microscopy. The key differences were the lack of etching and removal of specimens from Bakelite at the end. This ensured electrical conductivity was maintained with the specimen holder in the SEM chamber. Etching was not required, since imaging was carried out under backscattered mode. This is also known as 'Z-contrast' as the reflected signal depends upon the atomic number of the elements present. Given the partitioning of elements between the two phases in β titanium alloys (α and β), this generates significant contrast and improves consistency between samples.

3.2 Quantitative Metallography

In order to provide consistent microstructural information, analysis of micrographs was necessary to quantify the features present. Various techniques are available, with advantages and disadvantages to each. The primary α volume fraction was of particular interest. Determination of this parameter can be carried out via several methods, including point counting, lineal analysis and areal analysis. For details on the specifics of each of these techniques, the reader is referred to Higginson et al [94]. These are all based on the assumption that the volume fraction is independent of the plane and orientation in which it is measured [94]. Relative to point counting, lineal analysis can provide a more reliable figure per micrograph. However, it is not necessarily the most efficient means of acquiring such data since the speed of point counting allows analysis of more micrographs in a given time. On the other hand, this advantage is only fully realised if the number of available micrographs permits a large enough area to be covered.

A further consideration was the analysis of particle morphology within micrographs. Both point counting and lineal analysis can only provide volume fraction measurements. However, the use of software such as ImageJ to perform areal analysis also provides the ability to quantify particle shape. For this reason, analysis was carried out with ImageJ in order to provide both volume fraction measurements and information on particle morphology. However, as Figure 3.1 illustrates, this presented the problem of distinguishing between microconstituents when they exhibited similar grayscale values. Figure 3.1(a) presents an example micrograph of aged Ti-10-2-3. The large primary α particles are visible, set in a matrix of retained β that is permeated with secondary α. When thresholded (Figure 3.1(b)), it can be seen that the secondary α forms a dense, interconnected array of fine particles (note that although the secondary α appears grey, this is due to the resolution of the image; all dark pixels are actually the same shade). This array contacts the large primary α particles, preventing separation by

'filling' the latter with another shade (since this fills/highlights large tracts of the secondary α as well). Manually altering the threshold would compromise the consistency of area fraction measurements. The only satisfactory way to resolve this issue was to delineate the boundaries manually, as in Figure 3.1(c). After thresholding, ImageJ can then produce an accurate depiction of the primary α phase (Figure 3.1(d)). These particles can then be analysed to provide information about their size, area and morphology. The minimum and maximum feret diameter were chosen as the 'shape descriptors'. These are defined as the minimum and maximum dimensions of each particle [95][96]. However, the data was not normally distributed, so results were presented as the median feret min and median feret max. This was considered to be a more reliable measure of central tendency than the mean. The combined volume fraction of retained β and secondary α was also calculated by subtracting the primary α volume fraction from the whole.
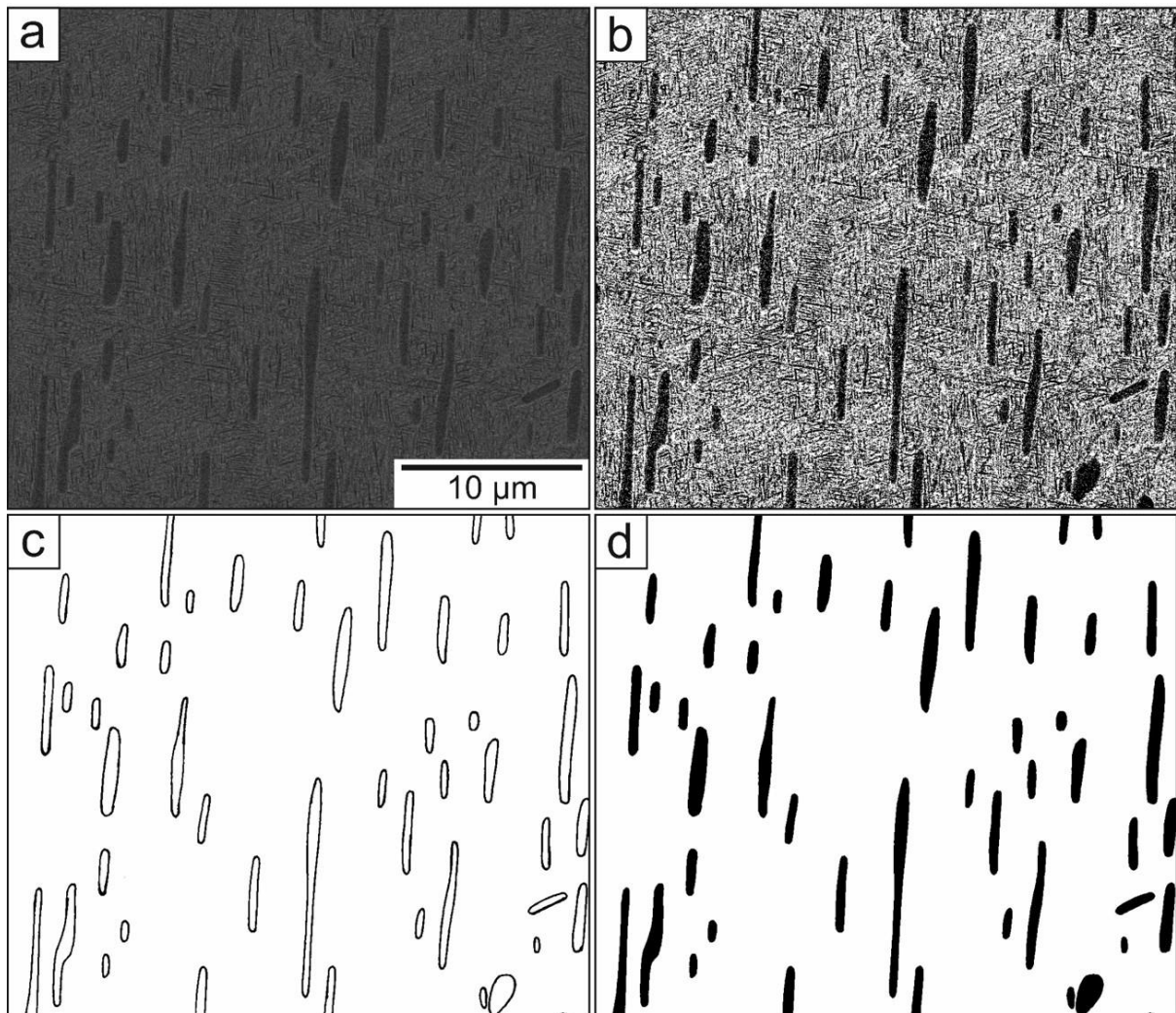
Figure 3.1: Aged Ti-10-2-3 micrograph under BSEI conditions. Original image (a), thresholded (b), manually delineated (c) and after 'filling' of the latter (d).

Quantification of secondary α proved difficult, given its fine scale. However, attempts were made to determine the mean interparticle spacing. This can be determined by first placing a series of lines over a micrograph. These should be spaced such that no particle is in contact with two lines. The number of second phase particles which intersect each line is then counted up. Dividing the length of each line by the number of intersections per line gives the mean linear interparticle spacing (or *d* as it is known). Combining the means of many lines from multiple micrographs improves the statistical reliability of the result. However, a problem arises when the second phase particles are not spherical (or circular, as they would appear in a 2D plane such as a micrograph). One approach is to place lines at random orientations on the micrographs so that, given a large enough sample, all directions are measured. Another approach is to use circles, instead of lines, as was done here (Figure 3.2). In principle, this effectively ensures all angles/directions are also sampled, but covers a greater distance per micrograph, which it was assumed would improve the reliability of results. It is important to bear in mind though, that the circumferential distance between particles will deviate from the linear displacement. It is therefore advisable to ensure the circles are as large as possible to minimise this source of error [94].
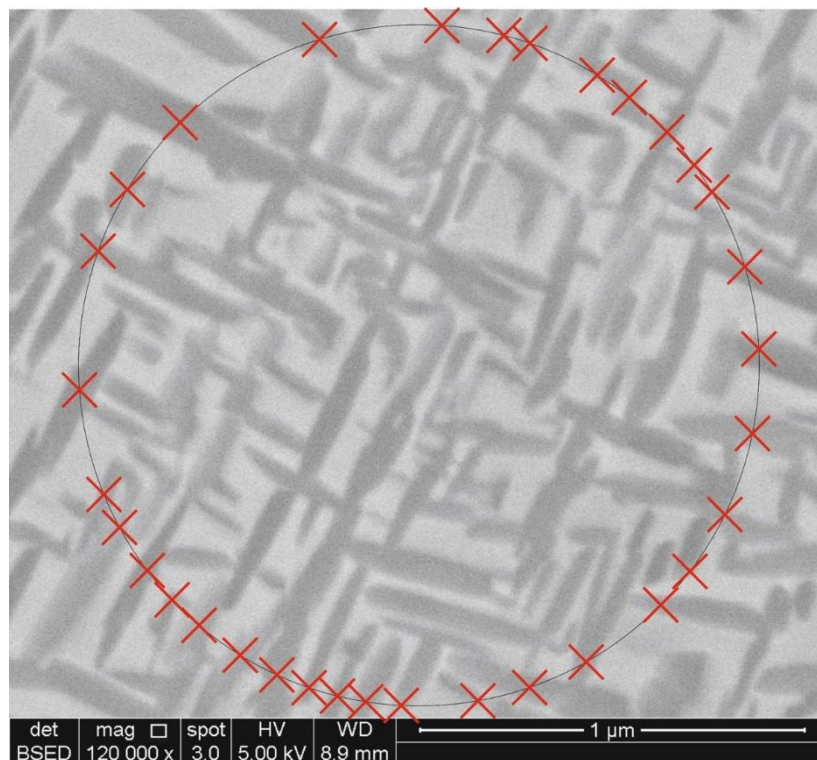
Figure 3.2: Backscattered electron micrograph of Ti-5553 secondary α. Illustrating the procedure for measuring interparticle spacing over all directions.

3.3 Electron Backscatter Diffraction

Electron Backscatter Diffraction (EBSD) was employed throughout this investigation to provide orientation information about the microstructures examined. This was carried out using an FEI Sirion FEG SEM. Most data acquisition was performed by Oxford Instruments HKL Channel 5 Flamenco software, although some large maps were obtained using fast acquisition software. Post-processing of results was conducted by the Channel 5 suite of programs. The EBSD process itself relies upon the diffraction of backscattered electrons to produce a 'Kikuchi pattern' on an appropriately positioned detector. Tilting of the specimen is required to lower the absorption of backscattered electrons, producing a clearer diffraction pattern [97]. This pattern is then used to determine the orientation of the crystal lattice at the point beneath the electron beam. By scanning the surface of a sample, a 'map' of orientations can be constructed. This can then be represented with the use of a colour scheme that illustrates the orientation at each indexed point.

In this project, these maps are presented in IPF (Inverse Pole Figure) colouring. This allows easy interpretation of orientation information by eye. However, it does not identify rotation around the reference plane normal which can obscure some changes in orientation (e.g. grain boundaries and lattice rotation). The 'All Euler' colour scheme contains all of the orientation information. However, it is harder to interpret by eye since the colour of each pixel is based on three separate scales defining each Euler angle. It is also susceptible to 'wrap-around' errors, which appear to overstate the misorientation between grains [67]. For this reason, the IPF colour scheme was used in combination with the grain boundary delineation function in HKL Tango. This required a near-contiguous map in order to calculate the misorientations between adjacent points. However, indexing deteriorates at grain boundaries, so it was necessary to apply noise reduction to the data. This function removes 'wild spikes' and fills in missing points based on the orientations of neighbours. This feature should be used with caution as it may mask unknown phases or indicate surface contamination [98]. Application of noise reduction here was based on 3-4 nearest neighbours.

An accelerating voltage of 20 kV and spot size of 5 was used in EBSD data acquisition. The step size varied depending upon the scale of the features of interest. The number of bands (min-max) was set at 5-7 for most maps. This balances reliability/accuracy of the data against the indexing rate. A small number of maps were indexed at 4-6 bands to improve the indexing rate. This proved to be a false economy, as the presence of pseudo-symmetry compromised the reliability of the data. This occurs where different orientations that present similar Kikuchi patterns confuse the acquisition system. Two adjacent points with similar/identical orientations can then end up being recorded with very different orientations. Including additional bands in the diffraction pattern helps avoid such errors.

Contoured pole figures are also used to present the aggregate orientation data of some maps using HKL Mambo. Determination of a pole figure begins by considering the orientation of an indexed point at the centre of a sphere. Selected plane normals (poles) are extended until they intersect with the sphere surface. Points of intersection can then be projected onto a reference plane. Repeating this procedure for all indexed points produces one figure that represents all orientations in the map. However, interpretation is likely to be difficult given the amount of data presented. The application of contouring to illustrate the pole density allows for easier identification of preferred orientations. The colour contour scale employed presents this data as Multiples of Uniform Density (MUD). The projection method can be stereographic or equal area. Stereographic projection maintains angular truth. However, a random orientation distribution presented in this manner will result in a higher pole density near the centre of the figure. For this reason, equal area projection is used for all pole figures presented here [99]. For more information on EBSD and texture analysis in general, the reader is referred to Engler and Randle [97]. Sample preparation for EBSD is essentially identical to that for SEM, although the specimen size and shape is restricted by the specific holder employed.

3.4 Hardness Testing

Preliminary Vickers hardness testing was carried out with a manual Mitutoyo hardness tester. However, towards the end of the project, a Durascan-80 automated hardness tester became available (courtesy of R. Goodall). This fully automated device allowed the rapid acquisition of a much larger quantity of data. This includes the hardness maps in Chapter 4, and is the reason for the slightly illogical order of their presentation (since it would have been preferable to carry them out first). Therefore, in order to ensure consistency, all manually tested specimens were retested with the Durascan. Only these values are reported in this thesis. Sample preparation was identical to that for light microscopy, except etching was omitted. A polished surface provides a more sharply defined indent. The load employed was 0.5 kg (4.905 N), with a dwell time of 3 seconds. The short dwell time was used as the Durascan relies on a load cell to control the indentor force. Where indents were placed in close proximity (as in the hardness traverses in Chapter 5) a minimum spacing of three times the indent width was maintained to prevent work hardening distorting adjacent measurements [100].

Chapter 4 Microstructure-Property Study of Forged Ti-5553

As outlined earlier, this chapter examines the microstructural and mechanical property variation within a forged Ti-5553 component. By analysing such variation, the intention was to identify and quantify the influence of microstructural variables on key mechanical properties, with a specific focus on strength and ductility. The component under investigation was the inner cylinder of a Boeing 787 Dreamliner main landing gear (MLG), an example of which is illustrated in Figure 4.1. Although this shows the component in service, the actual study was carried out on semi-finished components in the as-forged and rough machined condition. In this state, the forging is solid and would have been subjected to further machining, heat treatment and other finishing operations before final assembly of the MLG. However, machining operations will not affect the bulk microstructure, and this condition provided the flexibility to study the influence of heat treatment on the as-received material. Messier-Bugatti-Dowty kindly supplied material for this project in the form of sections removed from two separate forgings, one of which is shown in Figure 4.2.

The contents of this chapter begins with the methodology employed to assess the microstructure and mechanical properties of the material provided (4.1 Experimental Method). This is specific to this chapter and may refer to characterisation techniques described in Chapter 3 that are common to both Chapters 4 and 5. As Section 4.1 outlines, the results begin with the macrostructural and microstructural analysis of the two forging sections. This includes the effect of heat treatment on the second forging. Following this is the mechanical property assessment of the second forging, before the first forging is revisited for hardness mapping. A review of the observed relationships between microstructure and mechanical properties is then presented, and finally a summary of the main findings in this chapter. These results have been presented in this order to more accurately reflect the order in which the characterisation was carried out, and clarify the evolving experimental methodology. As will be explained in greater detail later, an unexpected finding during hardness mapping prompted re-analysis of some initial results.

Figure 4.1: Right-hand main landing gear of a Boeing 787. Arrow indicates the inner cylinder. Photograph by Julian Herzog, taken at the Paris airshow, 19th June 2013 and shared under a creative commons license (4.0). Image has been cropped to fit.

4.1 Experimental Method

Material for this investigation was supplied by Messier-Bugatti-Dowty (MBD), having been sourced from their forging supplier, VSMPO-AVISMA. This material took the form of sections removed from cylindrical forgings of Ti-5553 (Figure 4.2). For this study, two forging cross-sections were examined, both approximately 320 mm in diameter and 100 mm deep, as indicated in Figure 4.3. From this point forward, where it is necessary to distinguish between these two sections, they will be referred to as 'forging 1' and 'forging 2' in accordance with the order of their delivery. Their compositions are as specified in Table 4.1. Taking these and applying Equation 2.7, it is possible to determine a molybdenum equivalence for each forging (using the mean % where a range is given). These work out as 12.95wt% and 12.93wt% for forging 1 and 2 respectively. Since Mo equivalence is intended as a guide rather than an exact rule, a more sensible figure would perhaps be 13wt% for both.
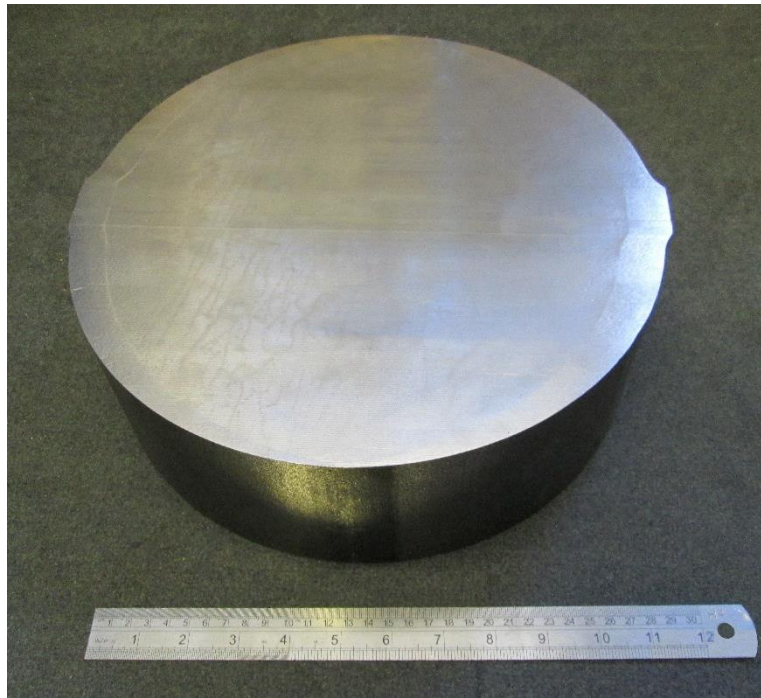
Figure 4.2: As-received material. Section of Ti-5553 inner cylinder forging, provided by MBD (305 mm ruler).

An approximate outline of the final component is also overlaid in Figure 4.3 [101]. Since forging was complete by this stage, it is clear that a significant quantity of material is subsequently machined away in order to reach the final component shape. At the narrowest point in the cylinder wall, only 13% of the original material remains in the final product (a 'buy to fly' ratio of almost 8:1 for that area). Rough machining would be carried out prior to heat treatment, while finish machining would be completed post-heat treatment to ensure dimensional accuracy. In practice the heat treatment would have involved a solution treatment

63

approximately 40°C below T_β for 4 hours followed by air cooling. Ageing is carried out at approximately 600-620°C for 8 hours and also followed by air cooling. This is in accordance with MBD's own internal specification, MTL-3103. Full details cannot be disclosed for reasons of confidentiality but the basic requirements are included in Table 4.1. MBD also stated that changes were made to the process route between delivery of the two forgings. The exact details of these changes, and the process routes themselves were regarded as commercially sensitive information, and cannot be clarified. As a result, although analysis of the two forgings showed many similarities between them, caution must be exercised when generalising about both. This also presented the opportunity to investigate the effect of such process variation on the final microstructure and mechanical properties.
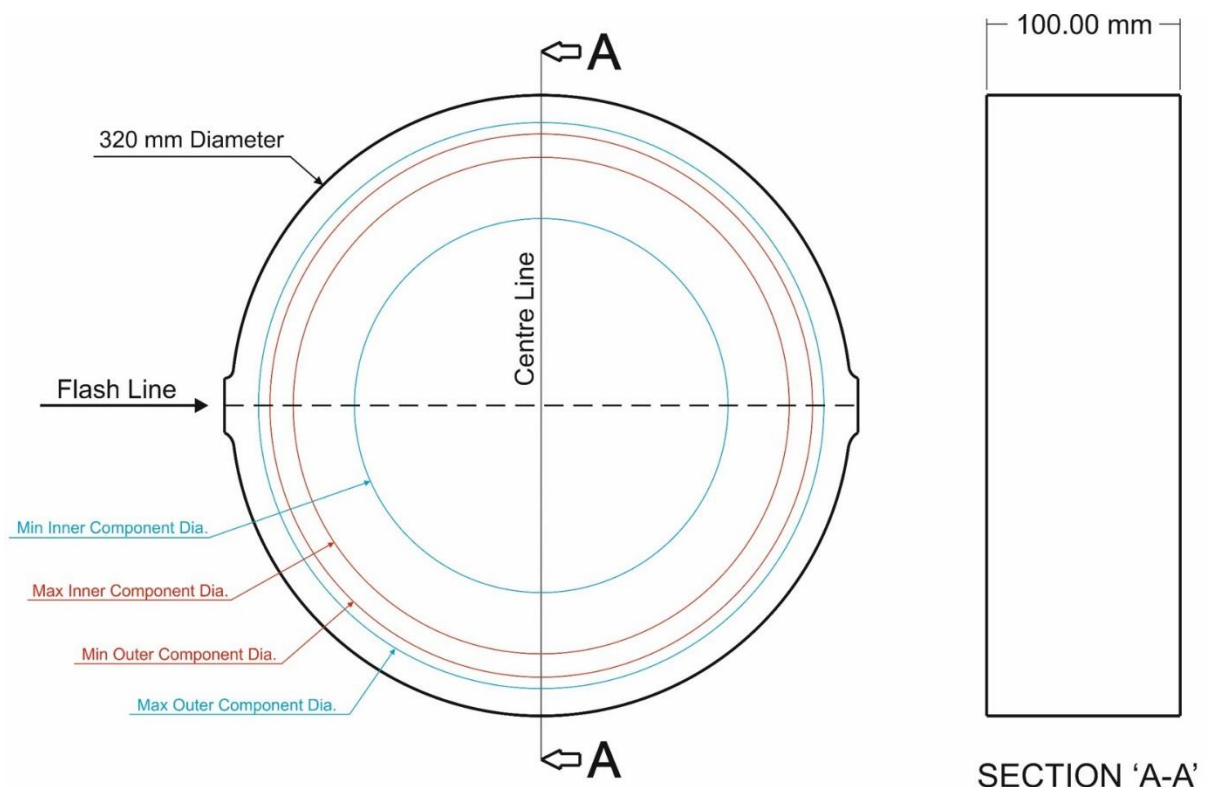
Figure 4.3: Forging cross-section with final component outline overlaid. The flash line may also be referred to as the transverse direction and the centre line as the short transverse.

As Figure 4.3 illustrates, the two protuberances on either side of the forgings correspond to the excess material, or 'flash', that was forced out during closed die operations. These flat facets (having been trimmed back between forging steps) have been used to orient the as-received material and relate sample locations back to the original forging. In order to clarify orientation, the cylinder axis may be referred to as the axial direction or longitudinal axis, while the direction perpendicular to this and connecting the two flash edges, will be known as the 'flash line' (or 'transverse' direction). At right angles to both of these is the direction labelled 'centre line' (vertical in the diagram). The 'centre line' may also be referred to as the 'short transverse' direction despite it being of equal length to the transverse direction in order to distinguish

between the two. No defining feature could be found on either forging to differentiate between each face. It therefore had to be assumed that the forgings were symmetrical either side of the centre line and flash line. However, despite their cylindrical shape, it would seem unwise to extend this assumption to one of an axisymmetric forging on account of the flash line.

Table 4.1: Composition, β transus (T_β) and mechanical properties of as-received material.

	T_β (°C)	0.2% PS (MPa)	UTS (MPa)	Elong. (%)	Al (wt%)	Mo (wt%)	V (wt%)	Cr (wt%)	Fe (wt%)
MTL-3103 Spec.	n/a	>1170	1240-1410	>4	4.4-5.7	4.0-5.5	4.0-5.5	2.5-3.5	0.30-0.50
Forging 1	843	1225	1308	6.9	4.95-5.00	5.16-5.23	5.16-5.21	2.71-2.72	0.36
Forging 2	848	1232	1308	6.9	4.90-4.92	5.19-5.25	4.94-4.96	2.68-2.72	0.41-0.42

Macrostructural and microstructural characterisation began with forging 1. Figure 4.4 illustrates the shape, location and orientation of the samples removed for examination. The large, hatched slices are positioned perpendicular to one another in order to elucidate any axial or radial variation in the macrostructure. One rectangular slice was situated along the flash line, while another was positioned perpendicular to this, along the centre line. Between these two right angled slices, a 'quarter' cross section slice was removed in order to identify any circumferential variation. A carbide tipped bandsaw was employed to bisect the forging along the centre line, before a cut was made along the flash line to yield a quarter block. From the three perpendicular surfaces were cut the actual sample faces.

These slices were then polished and etched in a similar manner to that mentioned in Chapter 3, the major difference being their size, and consequently the lack of mounting in Bakelite. Due to the uneven surface of the slices, they had to initially be ground flat. This was carried out with the coarsest silicon carbide paper available, p120 grit. A slower progression up the grit scale, through p240, p400, p600, p800 and p1200 then followed. Unlike the Bakelite mounted specimens, the 9 µm diamond suspension step was substituted with two fine grinding steps using p2400 and p4000 papers. Polishing was completed with 0.06 µm colloidal silica and water on an MD Chem polishing cloth. As with the Bakelite mounted specimens, etching was carried out by immersing in Kroll's reagent, although the concentration was halved in order to slow the rate of etching. This facilitated easier handling during the etching process. Imaging of the etched surface was carried out with a high resolution scanner at 1200 dpi. Higher resolution settings were available, but due to the file size, these were not practicable to use. In addition to

the macroetch samples, extra slices were removed adjacent to these, from which smaller microscopy specimens could be removed. These took the form of small cubes approximately 10 mm along each edge. They were prepared for light and electron microscopy in accordance with the procedures set out in Chapter 3. Electron backscatter diffraction (EBSD) was also employed on some specimens. Hardness tests were carried out with a Durascan-80 automated indenter using a Vickers indenter tip. Due to the inherent scatter in hardness data, bulk hardness values were determined from the mean of 25 indents per specimen face. These were placed in a 5x5 square grid with a spacing of 1-2 mm. The specimen surfaces were tested in the polished and un-etched condition for easier and more consistent measurement. The Durascan-80 automated indenter was also employed to create hardness maps of the macroetch slices (in the polished, un-etched condition). The grid spacing for these varied, and was informed by earlier results. These had shown greater microstructural variation radially compared to the axial/longitudinal direction. It was therefore decided to increase the axial spacing (4 mm) relative to the radial spacing (2 mm).
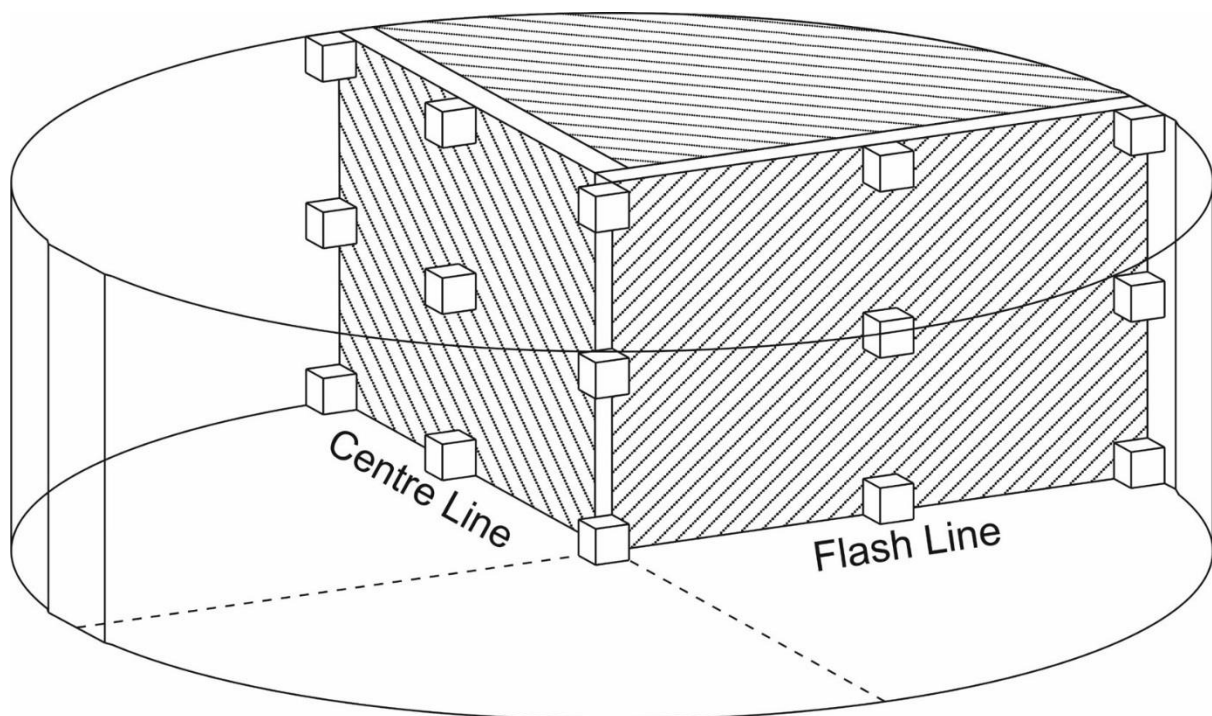
Figure 4.4: Forging1 sample layout. Hatched slices for macro-etching and hardness mapping. Cube samples for microscopy, EBSD and hardness testing.

Tensile testing was carried out upon forging 2, along with microstructural analysis in order to examine the influence on mechanical properties and make a comparison with forging 1. Testing was carried out by Element Materials Technology, an MBD approved supplier. Cylindrical samples, 80 mm in length and 12 mm in diameter were removed via Electrical Discharge Machining (EDM) by Electrotech EDM Services Ltd. Tensile testpieces were then machined

from these cylinders. Testing was carried out in accordance with BS EN ISO 6892-1:2009. Figure 4.5 (a) shows one of the testpieces, the dimensions of which conform to this standard.
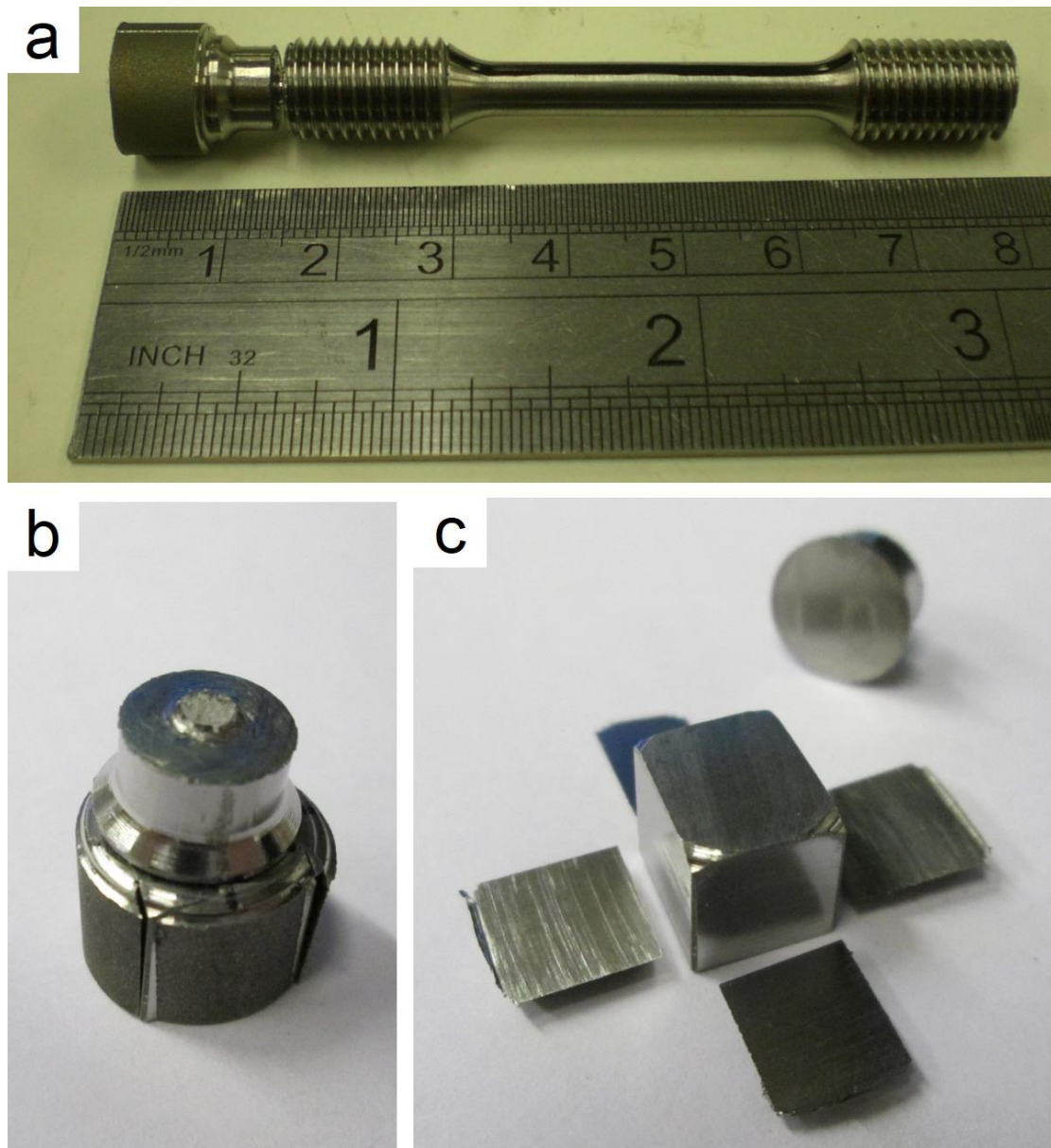
Figure 4.5: (a) Tensile specimen from forging 2, (b) and (c) illustrate removal of microscopy specimens.

Figure 4.6 provides a plan view of the sample layout in forging 2. The purple rectangles represent the cylinders from which tangentially oriented testpieces were removed, and the blue/red circles represent the cylinders from which axially oriented testpieces were removed (viewed end on). The layout was chosen based upon the symmetry elements of the forging, and in light of the observed microstructural variation in forging 1. By spacing tests at regular intervals across the flash line and down the centre line, the intention was to highlight any variation throughout the forging, both radially and circumferentially (the latter by comparing the flash edge with the bottom edge). Although the centre material would largely be removed during subsequent machining operations, any variation within the forging could be used to examine the relationship between microstructure and mechanical properties. It should be noted that Figure 4.6 shows the opposite sides of forging 2 being tested compared to the microstructural examination of forging 1. This was chosen in order to allow comparison with preliminary mechanical tests conducted on forging 1. These had to be positioned on opposite sections due to the removal of microstructural specimens as indicated in Figure 4.4. However, due to the symmetry of the forgings, it is assumed that either side of the flash line is equivalent, as is the 'top' and 'bottom' sections of the centre line. It is important though, to bear in mind this reversal of position when consulting results figures.

It can be seen in Figure 4.6 that the axial specimens (blue/red circles) have been arranged in pairs. This allowed one specimen from each radial location to be tested in the as-received condition (blue circles) and the other in the heat treated condition (red circles). This heat treatment was carried out in accordance with MBD internal specification MTL-3103 (see above) at their Gloucester site. Samples were heat treated as 80 mm x 12 mm diameter cylinders, before machining into testpieces. The tangential specimens (purple rectangles) were also arranged in pairs, one in the as-received condition and the other heat treated. This is not immediately apparent in Figure 4.6 as they are situated one above each other. The arrangement was such that the seeming impingement of specimens at the forging centre was not actually the case (for a more detailed view, see appendix).

The testpiece image in Figure 4.5(a) also shows excess material leftover from the machining operation. This was left on until immediately prior to testing as it had sample ID and orientation information inscribed on the end. It is also possible to see the mark formed by EDM during removal of the sample cylinders (horizontal white line at left-hand end). This was used to orient the specimens since there were corresponding marks on the forging. The black line drawn along the specimen coincides with this EDM mark, allowing orientation of the tensile specimen after the excess material was removed completely. This excess material was also utilised to provide microstructural information. As Figure 4.5 illustrates, this material could be cut into small, cube shaped specimens suitable for microscopy.
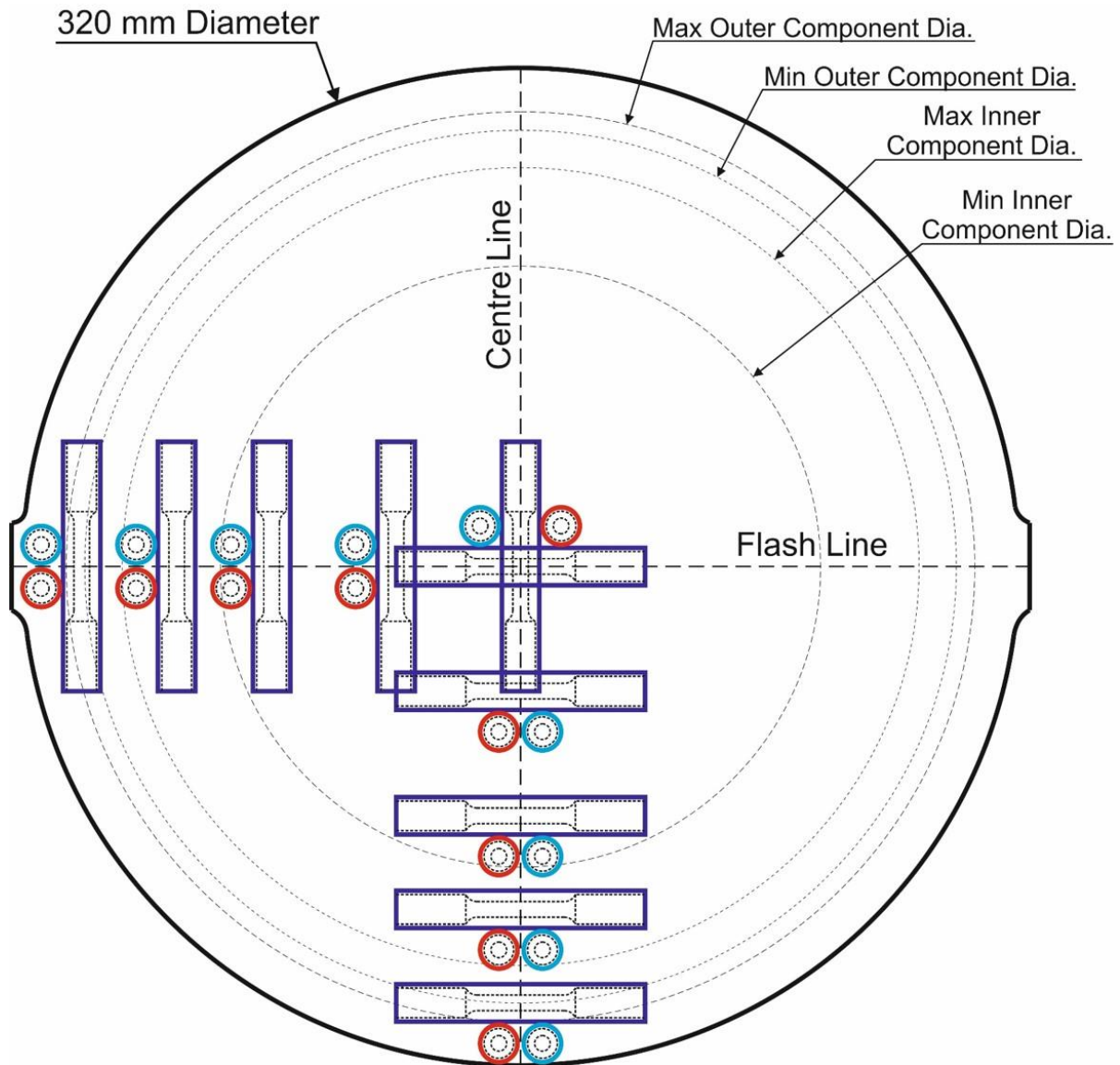
Figure 4.6: Forging 2 specimen layout for tensile testing. Blue and red circles represent axially oriented specimens in the as-received and heat treated condition, respectively. Purple rectangles represent tangentially oriented specimens, stacked two deep, one as-received and one heat treated at each location.

The layout of tensile specimens as in Figure 4.6 was intended to position the specimen gauge lengths as close to the flash line and centre line as possible. Since the tangential specimens displace the excess material (microscopy sample) some way from the flash line/centre line, it was only axial specimens that were used for microstructural examination. However, the excess material could be situated at either end of a testpiece, so the axial microscopy specimens could be displaced along the longitudinal forging axis by 70-80 mm. It was assumed though, that (as found in forging 1) the axial variation in microstructure was much less significant than radial variation. Therefore, for simplicity, any axial displacement was ignored, and all microscopy specimens were depicted in the same plane, as in Figure 4.7. It should be noted however, that when comparing microstructures with the tangential mechanical properties, there is a radial

displacement of about 15 mm between the microscopy sample and the testpiece gauge length. The significance of this will depend on the degree of microstructural variation between the two, and the consistency of this variation. As with forging 1, the microscopy specimens were also used to collect hardness data. This was carried out in a similar manner, using a Durascan-80 automated indenter with a Vickers indenter tip making 25 indents per specimen face.
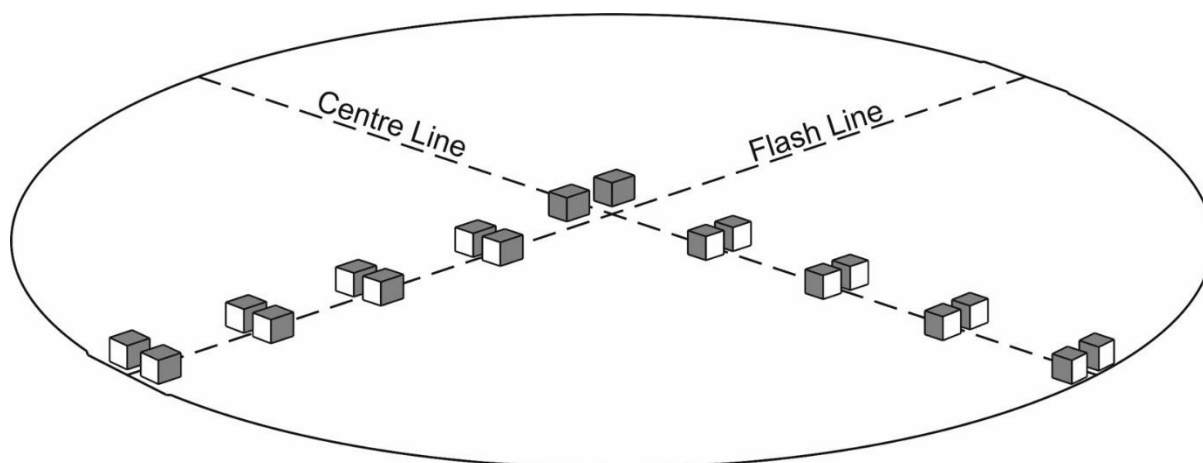
Figure 4.7: Forging 2 layout of microscopy samples from the excess material of axially oriented tensile specimens. All samples shown in the same plane for clarity. Grey faces are those subject to examination.

4.2 Macrostructural Examination

Figure 4.8-4.9 reveal the etched macrostructure of the centre line and flash line slices. For clarity, the scanned images were edited to remove dust and scratches, and the intensity increased by 95% to better match what can be seen with the naked eye (see appendix for unedited versions of these images). From Figure 4.8-4.9 it can clearly be seen that the observed features exhibit a significant degree of directionality. Changes in colour and shade create the appearance of bands that run almost parallel to the forging axis. What appear to be very large β grains or macrozones are visible in the darker, outer half/third of the two slices. The boundary between these two regions does not quite lie parallel to the forging axis, shifting slightly outwards towards the top of each slice.

Within the lighter, central region, the macrostructure appears finer, whilst also exhibiting some isolated β grains or macrozones that are larger even than those in the darker, outer region. These are more obvious in the flash line slice, where two, very large β grains/macrozones sit next to each other. In the outer third of the two slices (darker region), the β grains appear elongated parallel to the forging axis, but also larger and wider in the flash line. There is also a narrow light band near the outer edge of both slices that runs parallel to the forging axis. Referring to

the quarter cross-section (Figure 4.10), this band, along with the others, appears to extend around the forging, between the two perpendicular slices. This is most clearly illustrated by the 3D stitch of all three macro-etches (Figure 4.11). It can also be seen that the path of the light band maintains a near constant displacement from the forging edge, tracing a quarter of an almost circular path. However, the boundary between the central, lighter region, and the outer, darker region, does not. Its shape is reminiscent of a rounded corner, suggesting this was induced by imposed strains during forging from a non-circular cross-section. The slightly off-axis nature of this boundary in the rectangular slices, when viewed three-dimensionally, implies that the central, lighter region varied in cross section along the forging axis. This may indicate that the imposed strains varied along the forging length.

The uniform displacement of the light band from all edges however, suggests that this may be the result of a thermal effect after forging (or at least, in the final stages, as finishing steps produce only minor shape changes). Compared to the grain structure of the rectangular slices, the quarter cross-section appears finer and possibly more equiaxed, depending upon location. This would make sense given the morphology of grains in the other two orientations (slices). The elongated nature of the β grains in the axial direction would produce a more equiaxed appearance when viewed end on (as in the quarter cross-section). In the lower right corner of the quarter slice, the grain structure appears 'swept' towards the flash edge, elongating the grains laterally. This may account for the wider β grains in the flash line slice compared to the centre line. Around the forging edge, the grains may also be elongated circumferentially. Both of these phenomena are presumably the result of material flow during hot forming.
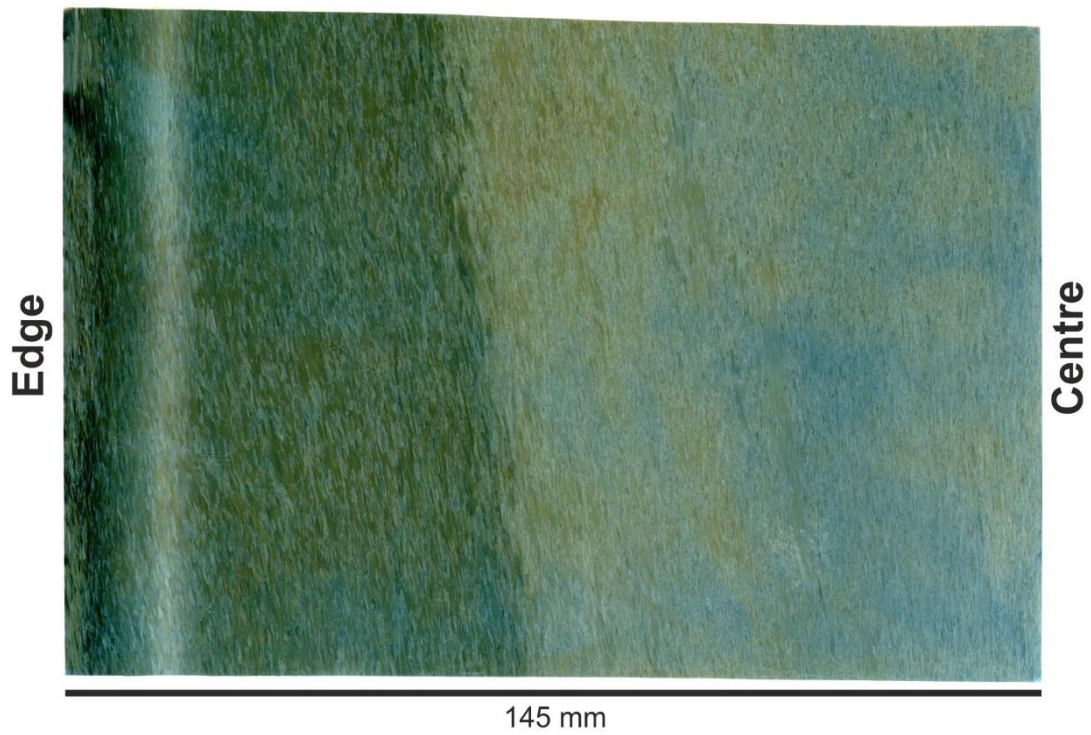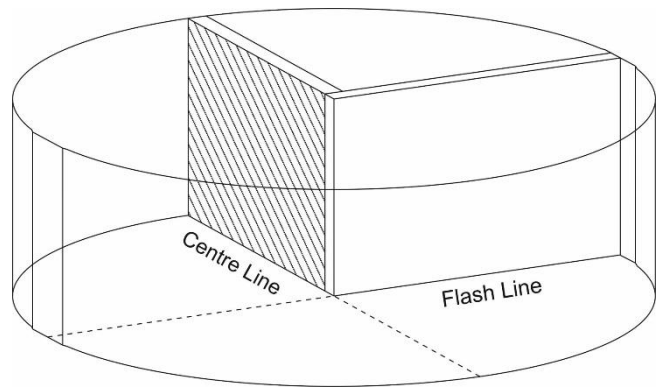
Figure 4.8: Scanned macro-etch of centre line slice. Intensity increased (+95%) and edited to remove dust and scratches (see appendix for original image).
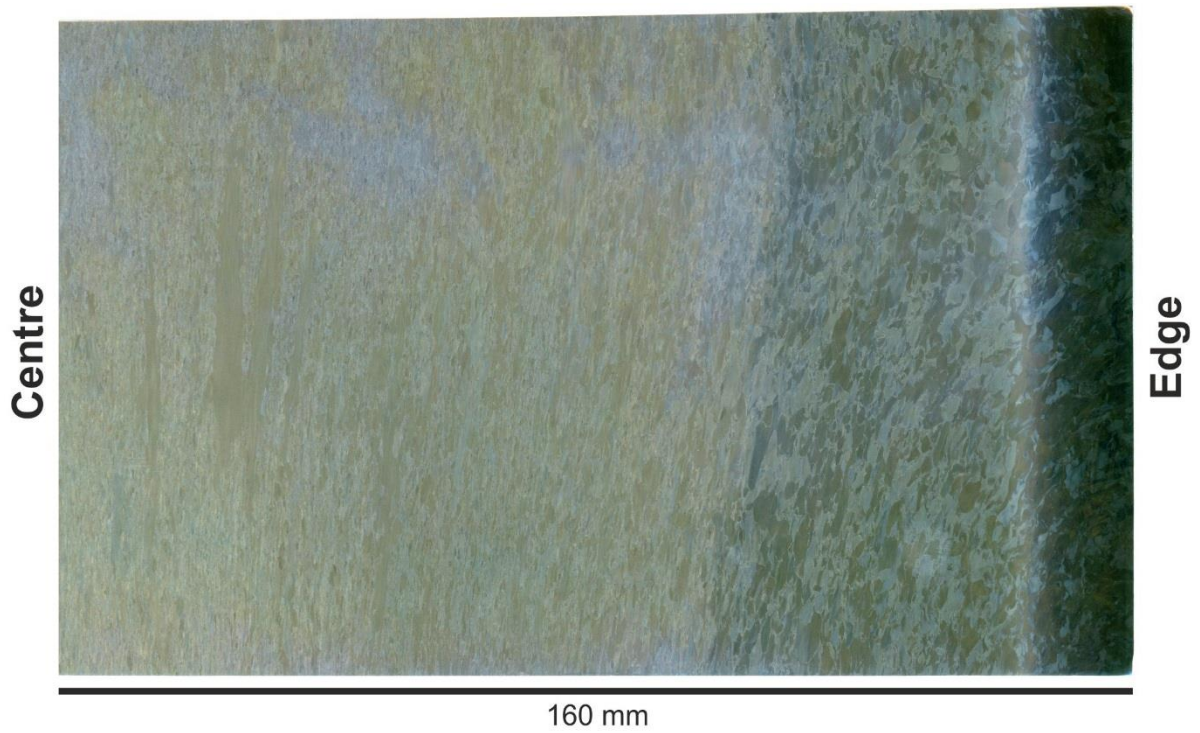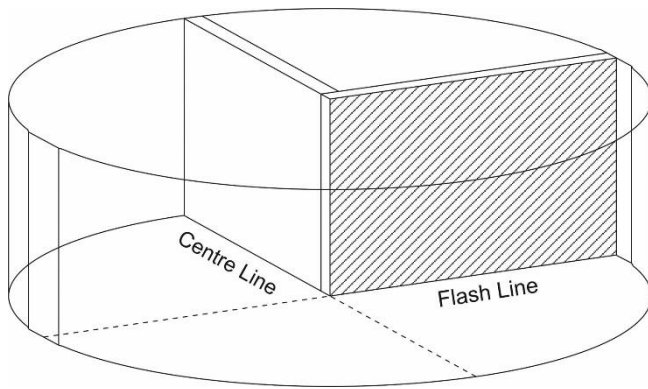
Figure 4.9: Scanned macro-etch of flash line slice. Intensity increased (+95%) and edited to remove dust and scratches (see appendix for original image).
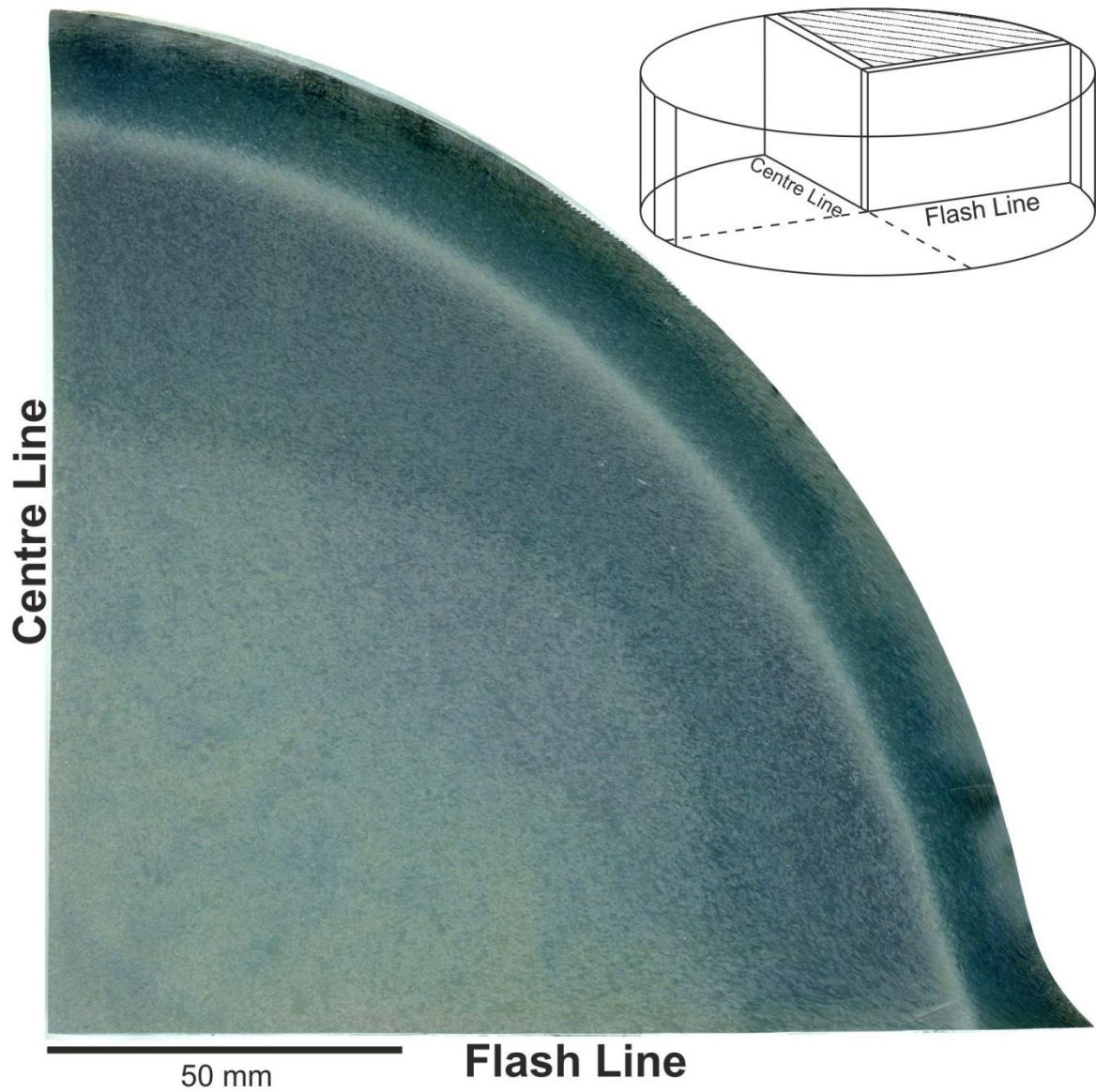
Figure 4.10: Scanned macro-etch of quarter cross-section. Intensity increased (+95%) (see appendix for original image).
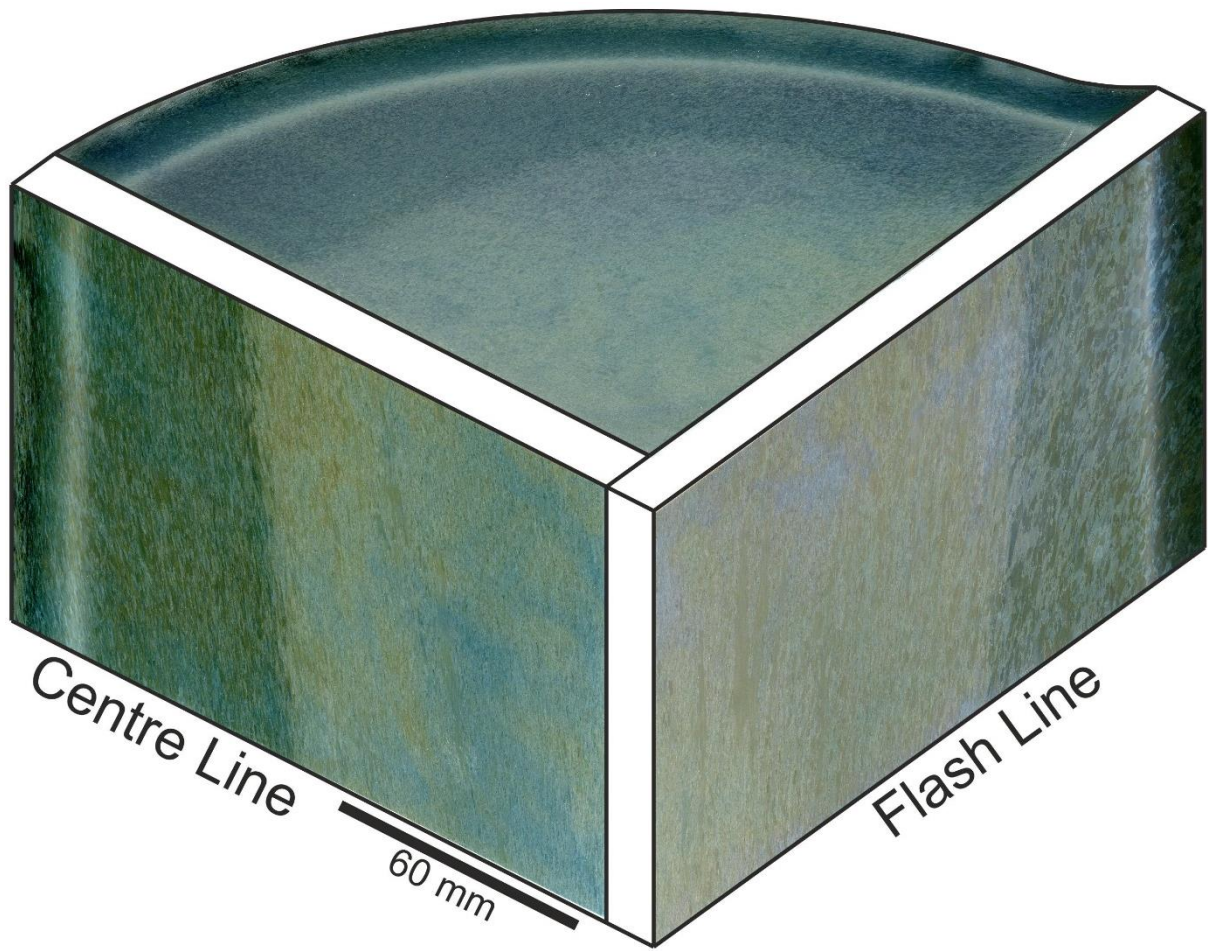
Figure 4.11: Three dimensional stitch of Figures 4.8-4.10.

4.3 Microstructural Examination:

4.3.1 Light Microscopy

Figure 4.12-4.18 depict a range of light micrographs taken from various samples across forging 1. These have been subdivided by magnification and orientation. Those micrographs taken in the same orientation as the two rectangular slices (Figure 4.12-4.14, and Figure 4.16-4.17) will be referred to as tangentially oriented images since the viewing direction is tangential to the forging circumference. Those micrographs oriented perpendicular to these (Figure 4.15 and 4.18) will be referred to as being axially oriented since the viewing direction is parallel to the forging's longitudinal axis. The micrographs are intended to be representative, and were adjusted to improve clarity for the reader (brightness, contrast, sharpness). While they do not provide quantitative analysis, they serve as a qualitative guide to the microstructural variation observed throughout the forging.

Referring to the low magnification, tangential micrographs of Figure 4.12 and 4.13, one can see similar directionality to that observed in the macro-etches. With the exception of Figure 4.12(a), the β grains appear elongated in the axial direction. Although Figure 4.12(a) appears to be the odd one out, further examination reveals it not to be as dissimilar as first appears. Figure 4.14 presents a wider view of the area in Figure 4.12(a), and it can be seen that the β grains become much more elongated only slightly further from the edge. Under higher magnification (Figure 4.16(a)), the region in Figure 4.12(a) appears to consist of finer, more equiaxed β grains. This band of finer grains extends most of the way up the edge of the microscopy specimen. This may be an indication of localised deformation near the die-wall interface producing low angle subgrains, or a new set of recrystallized grains.

While the β grains appear elongated in the axial direction in most regions, this effect was greatest near the forging edge. Here, the aspect ratio became very high, producing narrow bands of light and dark grains (Figure 4.12-4.13). At the forging mid radius, the tangentially oriented micrographs exhibit the widest β grains. The central micrographs in these figures typically show narrower, higher aspect ratio grains, though not quite as elongated as those near the forging edge. In agreement with the macro-etches, the radial variation of the microstructure within the forging appears much more significant than the axial variation. Due to time constraints and equipment availability, this led to a compromise between the number of samples examined and the characterisation techniques employed. As such, only one set of micrographs were taken in the axial orientation, and it was assumed that these were representative of each radial location along the forging axis (Figure 4.15 and 4.18). Consulting the low magnification axial micrographs (Figure 4.15), it can be seen that the β grains may adopt an elongated-equiaxed, or pancaked shape depending on location. This is likely due in part to the variation in deformation history throughout the forging. Material in the 'upper section' of the centre line may have experienced less strain and therefore produced an equiaxed

β grain morphology (when viewed end-on, but elongated in the axial direction) (Figure 4.15(a) and (b)). However, along the flash line the strain may have been considerably higher, and resulted in greater lateral flow of material. This could account for the pancaked nature of these β grains, elongating them in the transverse (and longitudinal) direction. This effect appears greatest at the flash edge, where the strain is presumably at a maximum (Figure 4.15(e)). Thus, although it is possible that some recrystallization may have occurred near the forging edge, it can be said that the β grain structure largely consists of deformed, unrecrystallised grains, oriented parallel to the longitudinal axis of the forging.

It can also be seen at the forging centre and mid-radius that the β grain boundaries are delineated with layers of primary α, which are noticeably absent at the forging edge. This is more visible in the high magnification light micrographs (Figure 4.16 and 4.17). These micrographs also help illustrate the morphology and distribution of the primary α particles within the retained β matrix. It can be seen that there are both intergranular and intragranular particles, and that the morphology of these varies across the forging. Near the edge, these particles are of a more equiaxed or 'globular' morphology, whereas towards the forging centre they appear elongated.

It is notable that the thickness of the more elongated α particles is similar to the diameter of the globular α particles. This alludes to the mechanism by which the globular particles form. Although α particles preferentially form as high aspect ratio plates parallel to the {110} planes of the β matrix, hot working will break these up, producing a distribution of more equiaxed, globular particles [17]. This provides another indication of strain distribution throughout the forging. The more globular appearance of α particles near the flash edge would support the conclusion that strain was higher there than at the forging centre (Figure 4.17 and 4.18). However, it would appear that the strain was also high enough at the top of the centre line to globularise the α phase (Figure 4.16 and 4.18). Extended time at temperature will also spheroidise α plates, but this process is quite slow as the acicular morphology is still reasonably stable [17]. In addition, it seems unlikely that the edge of a forging of this size would remain hotter for longer than the centre.
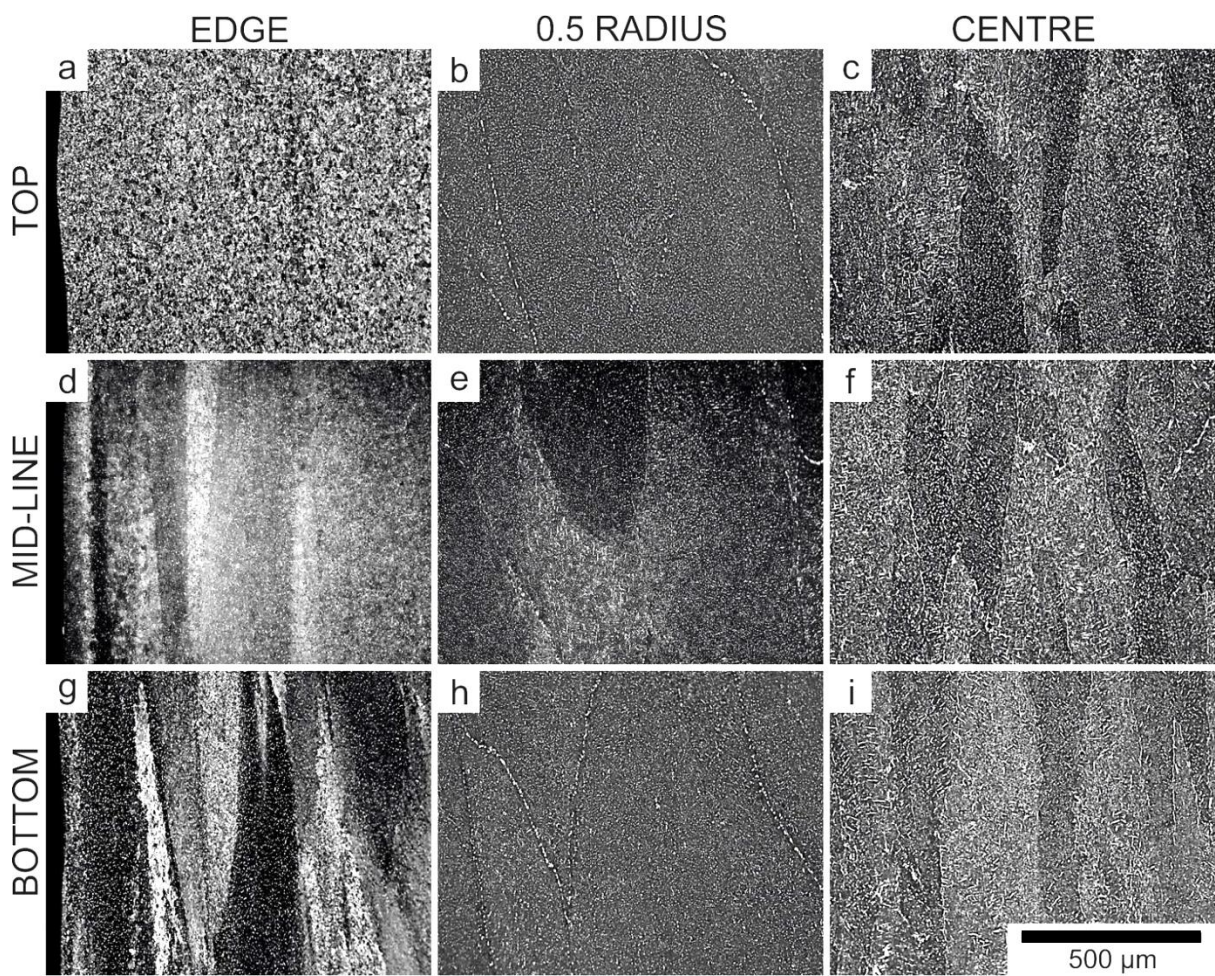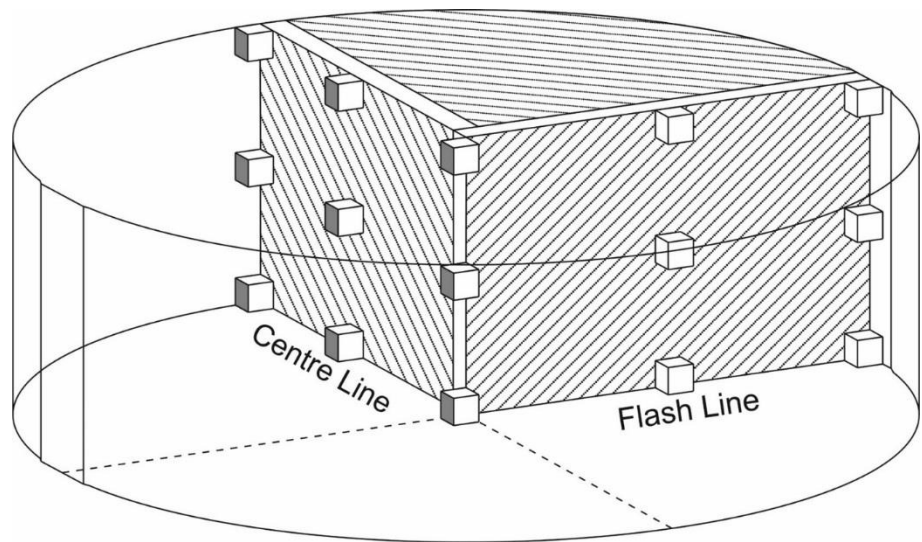
Figure 4.12: Low magnification light micrographs taken from the centre line samples.
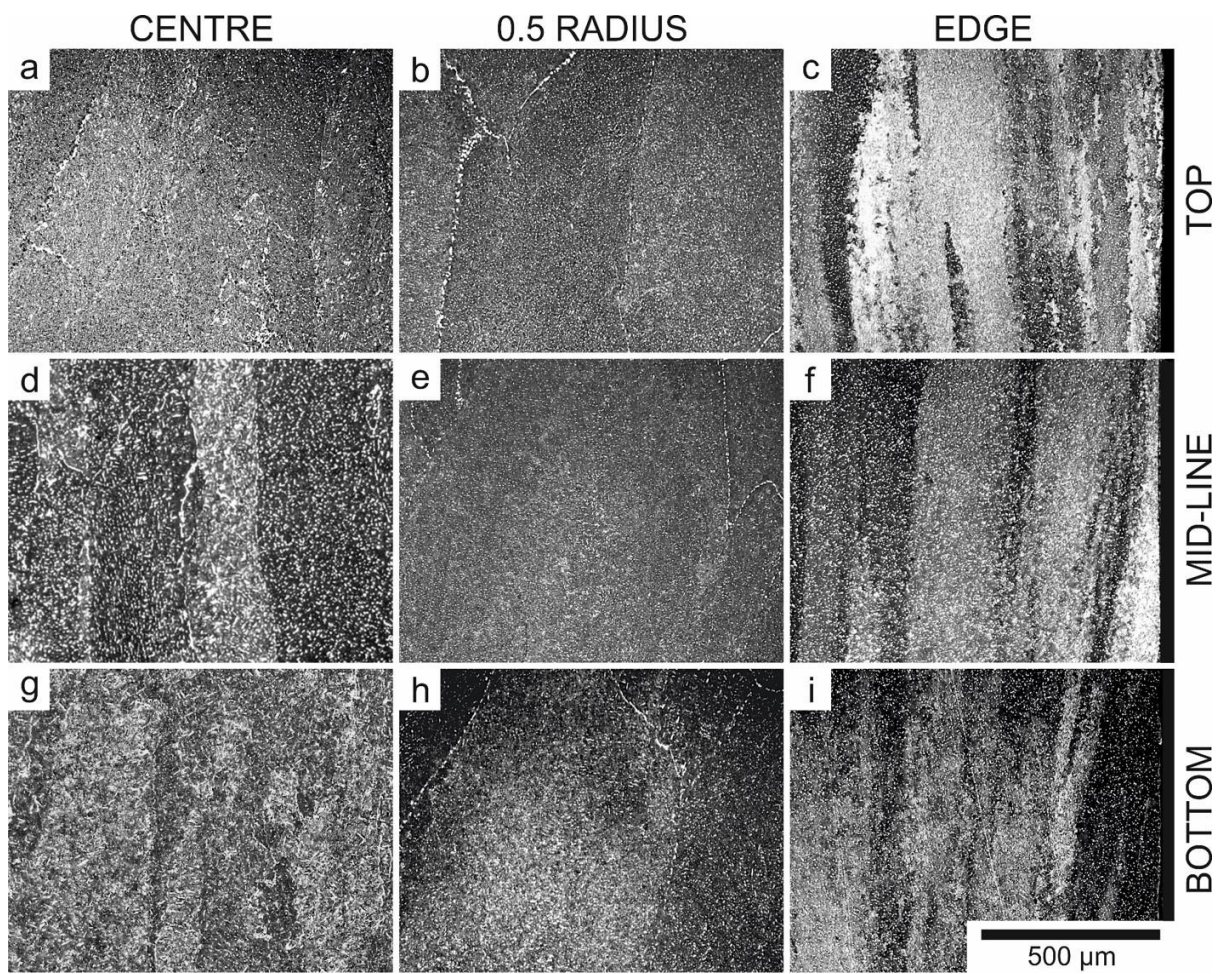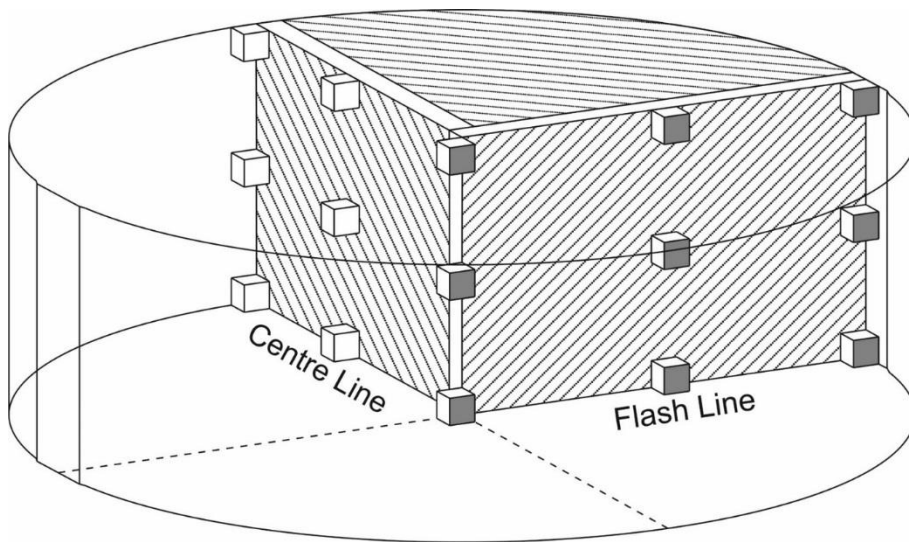
Figure 4.13: Low magnification light micrographs taken from the flash line samples.
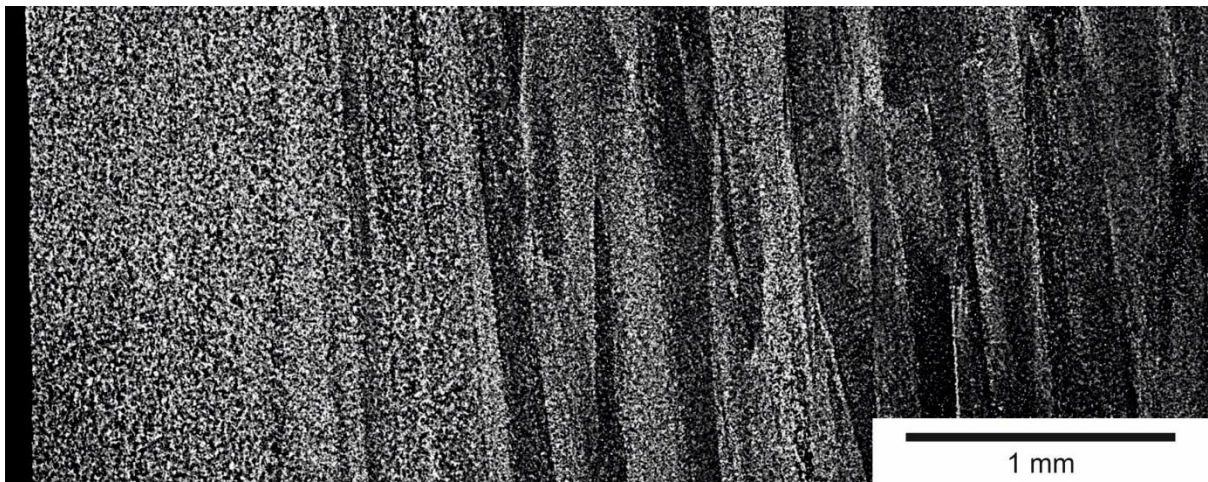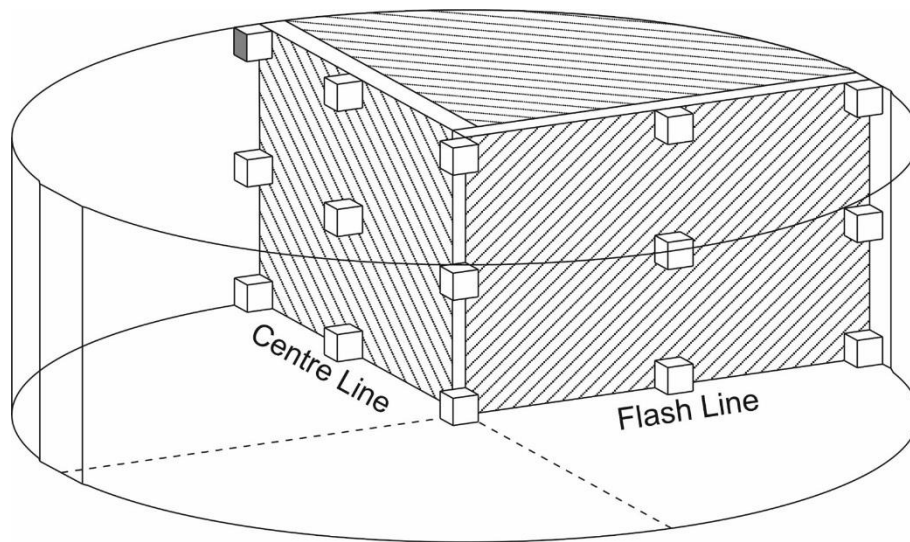
Figure 4.14: Stitched image showing the microstructure further from the edge in Figure 4.12(a).
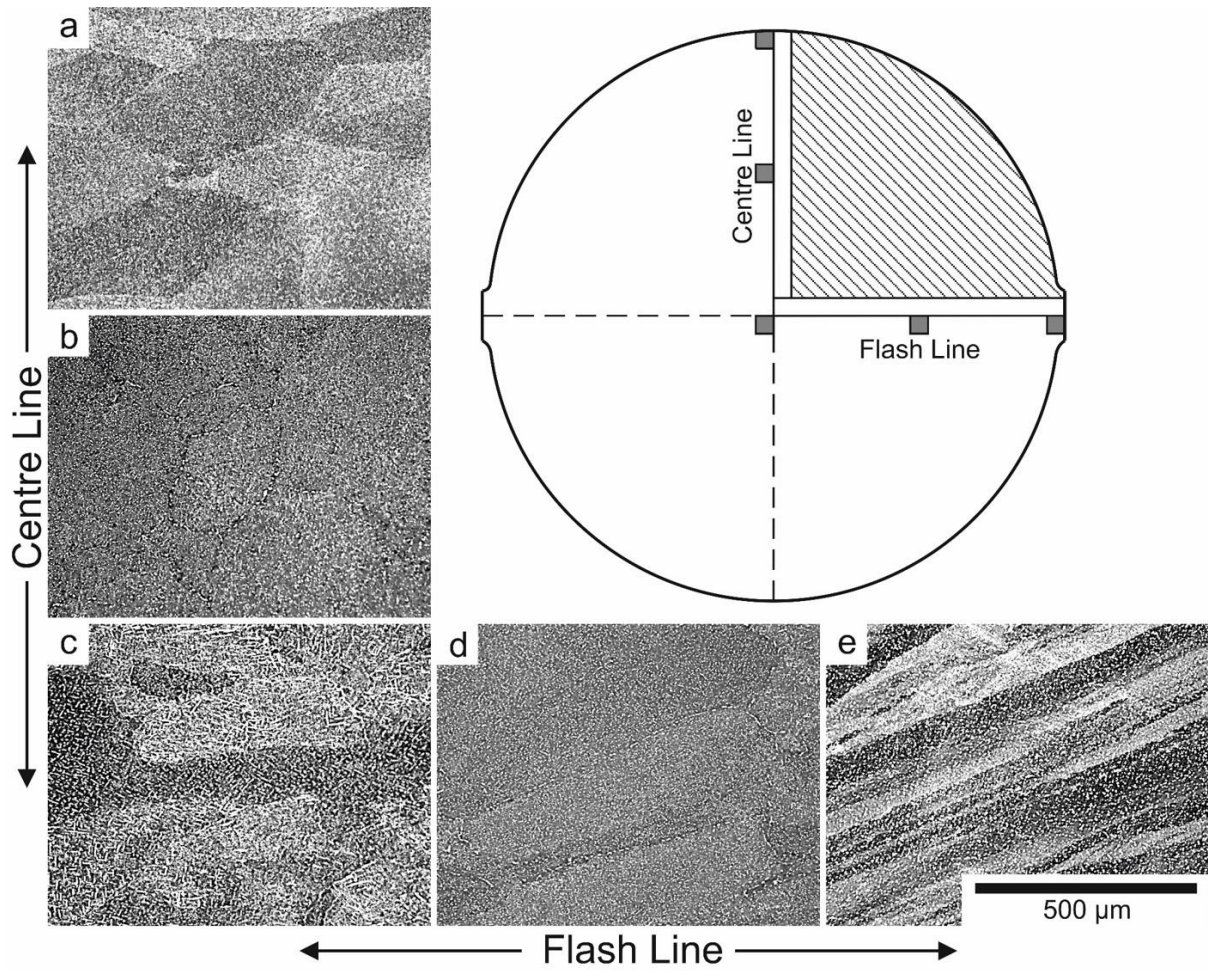
Figure 4.15: Low magnification light micrographs taken perpendicular to the longitudinal axis of the forging.
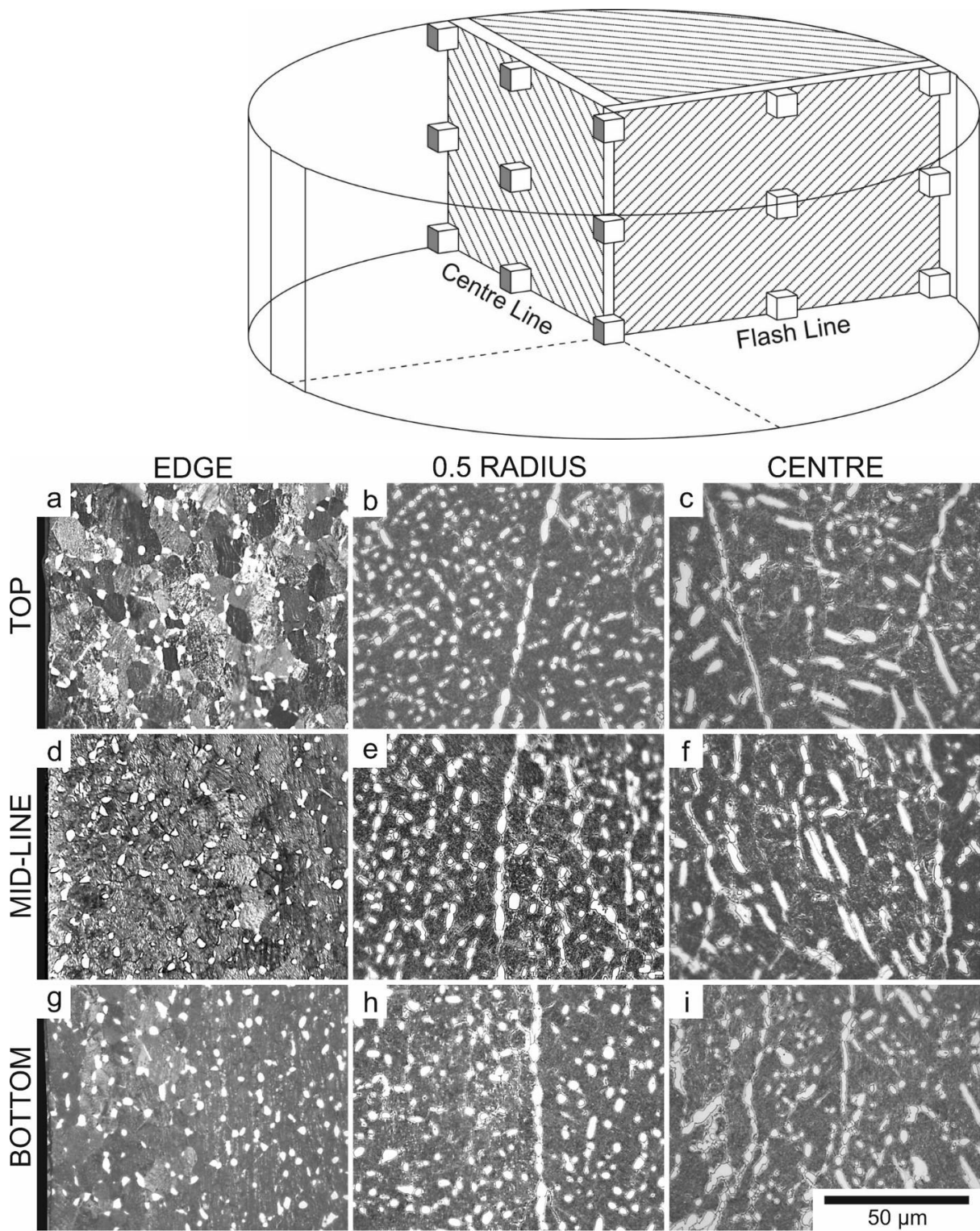
Figure 4.16: High magnification light micrographs taken from the centre line samples. Light phase is primary α, dark phase is the retained β matrix.
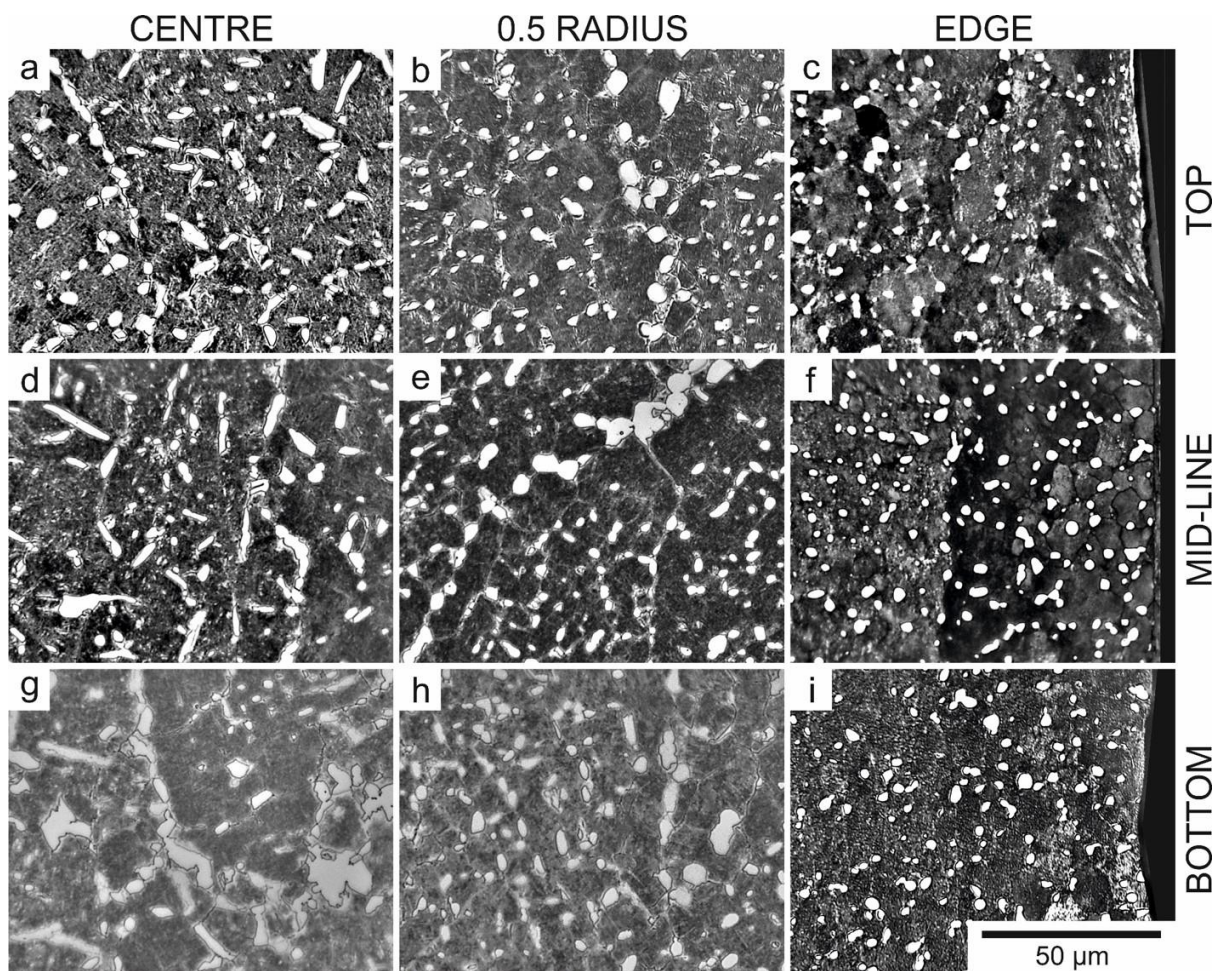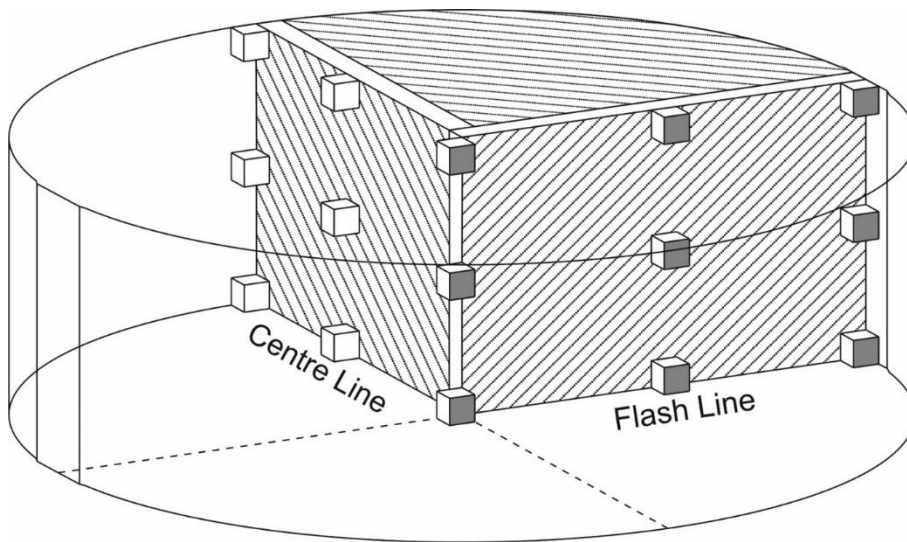
Figure 4.17: High magnification light micrographs taken from the flash line samples. Light phase is primary α, dark phase is the retained β matrix.
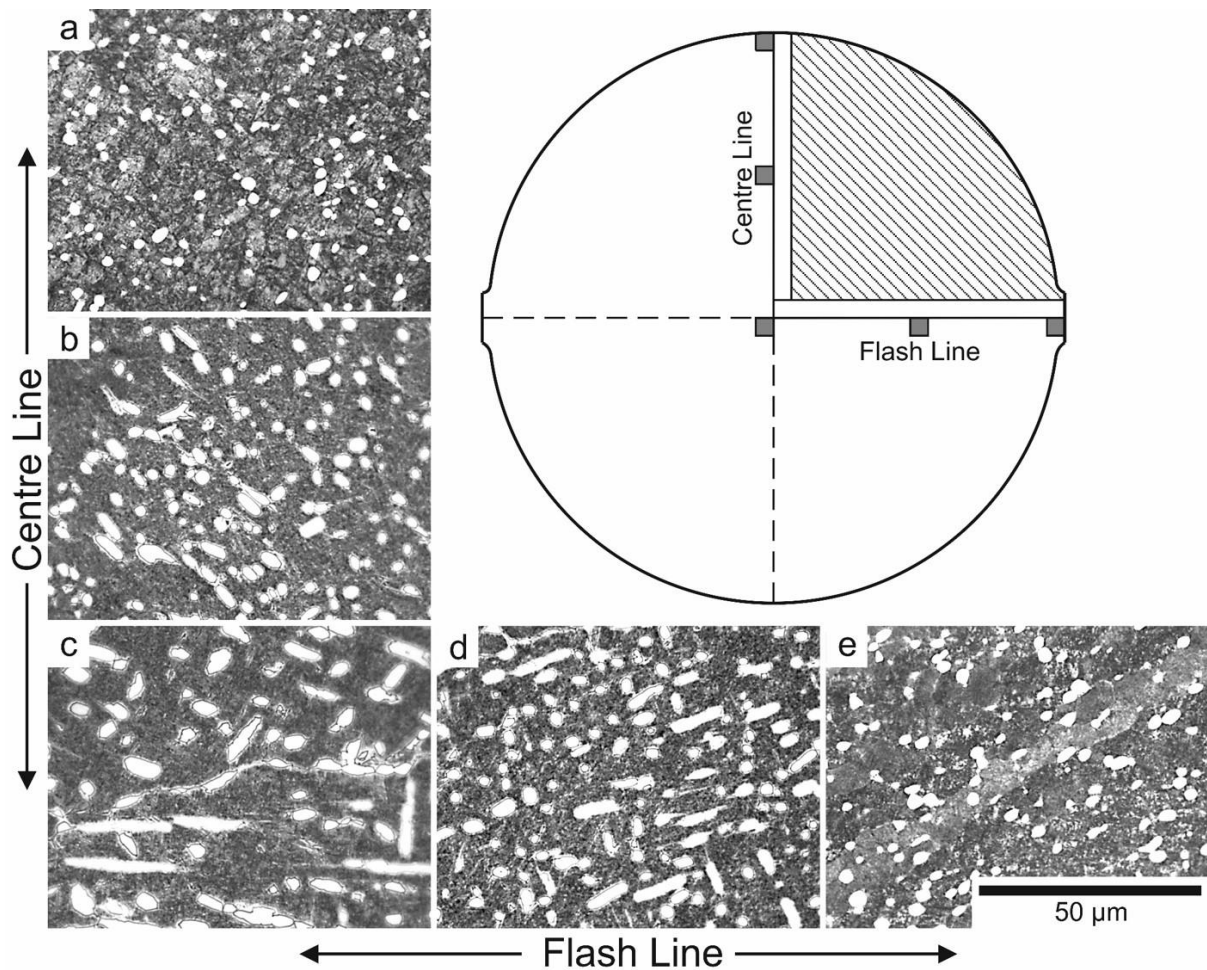
Figure 4.18: High magnification light micrographs taken perpendicular to the longitudinal axis of the forging. Light phase is primary α, dark phase is the retained β matrix.

4.3.2 Electron Microscopy

Figure 4.19-4.22 illustrate the microstructure of forging 1 as depicted through backscattered electron imaging (BSEI). As mentioned earlier, a compromise had to be made between thoroughness and practicality due to restrictions on time and equipment availability. Therefore, as with the axial light micrographs, only one set of electron micrographs was taken, and assumed to be representative of the microstructure along the forging axis. The low magnification electron micrographs of Figure 4.19-4.21 paint a similar picture to that of the light micrographs. The primary α particles appear more globular towards the edge, adopting a more elongated morphology nearer the forging centre. The near-continuous layers of grain boundary α are also in evidence towards the centre. The strain penetration was presumably insufficient to break up these features, but since the final component is hollow, this microstructure should be removed by machining anyway. However, care must be exercised when balancing microstructural requirements in the finished product against the economic

consequences of unnecessary hot work. Unlike the etched, light micrographs, the BSEI micrographs do not clearly illustrate the β grain boundaries except where demarcated by primary α phase. However, channelling contrast provides some indication of the presence of subgrains near the forging edge (Figure 4.19(a) and 4.20(c)). The high magnification electron micrographs also reveals the secondary α, which was not previously visible under light microscopy. This takes the form of a fine distribution of α particles within the β matrix (Figure 4.19-4.20 and 4.22). Although they appear needle shaped in a 2D micrograph, these particles are often referred to as platelets since this more accurately reflects their true 3D shape [66]. As one might expect, the size and morphology of these particles varies throughout the forging. This is likely due to differences in thermal history within the workpiece, since cooling/heating rates and time at temperature both influence the formation and growth of secondary α (see Section 2.3).

It can be seen that the finest secondary α exists near the flash edge, where the particles are so small as to be almost unresolvable (Figure 4.20(f)). Towards the forging centre, they become coarser and increase in aspect ratio. Exact measurements are difficult due to the resolution limit of scanning electron microscopy. It would probably require transmission electron microscopy (TEM) to resolve the finest particles properly. However, it can be said that the particles are sub-micron in size, and that the variation does not appear linearly dependant upon the radius. That is to say, qualitatively, the change in particle size appears greater between the flash edge and mid-radius, than between the mid-radius and centre. This variation does not seem as clear along the centre line (Figure 4.19 and 4.22). Indeed, while there may be some morphological change, the secondary α size appears more consistent across this region.

Given that this forging is in the un-heat treated condition, it is presumably during cooling that the secondary α particles formed. It would therefore seem possible that variations in cooling rate led to the observed variation in particle size and morphology. If the centre of the forging cooled more slowly than the edge, a coarser distribution would be expected towards the centre. This agrees with the findings along the flash line. However, considering the geometrical symmetry of the forging, one might expect the centre line to display the same trend, which doesn't appear to be the case. It might seem reasonable to assume that the temperature of the dies and surrounding environment led to non-axisymmetric cooling profiles. However, the author would caution the reader against drawing any firm conclusions about the secondary α at this stage. It had been assumed that significant microstructural variation within a forging of this size would only occur over relatively large distances. Within individual microscopy specimens (10 mm x 10 mm) it was expected that the microstructure would be reasonably consistent. While this may be true with respect to the primary α, later work, particularly on forging 2, suggested this may not be the case with the secondary α (see 4.6 Microstructure-Property Analysis).
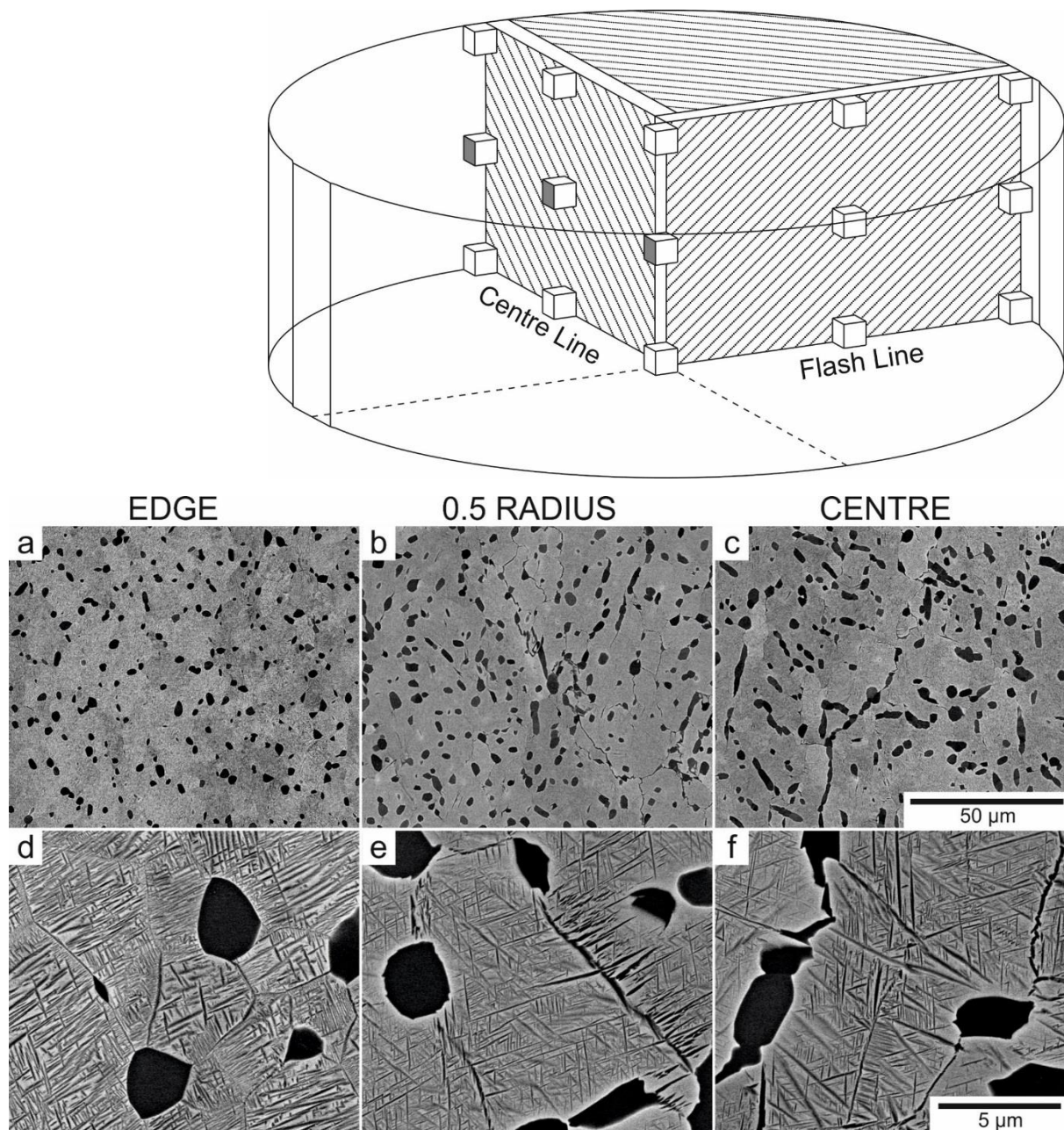
Figure 4.19: BSEI micrographs taken across the centre line at low magnification (a), (b), (c), and high magnification (d), (e), (f). The α phase now appears dark and the β phase appears light (in contrast to etched light microscopy).

The high magnification micrographs do however provide an indication of the primary α size and shape. Although this can vary, the globular particles are generally on the order of 2-3 µm in diameter, while the elongated particles are of similar thickness. In addition to the thick grain boundary α present at the forging centre and mid-radius, there is also the formation of thinner films of α phase along the β subgrain boundaries (Figure 4.19(e)-(f), 4.20(d)-(e) and 4.22(b)-(d)). In the thick grain boundary α layers it is also possible in some places to see slight variations in shade, creating the impression of a string of interconnected particles (Figure 4.20(d)).
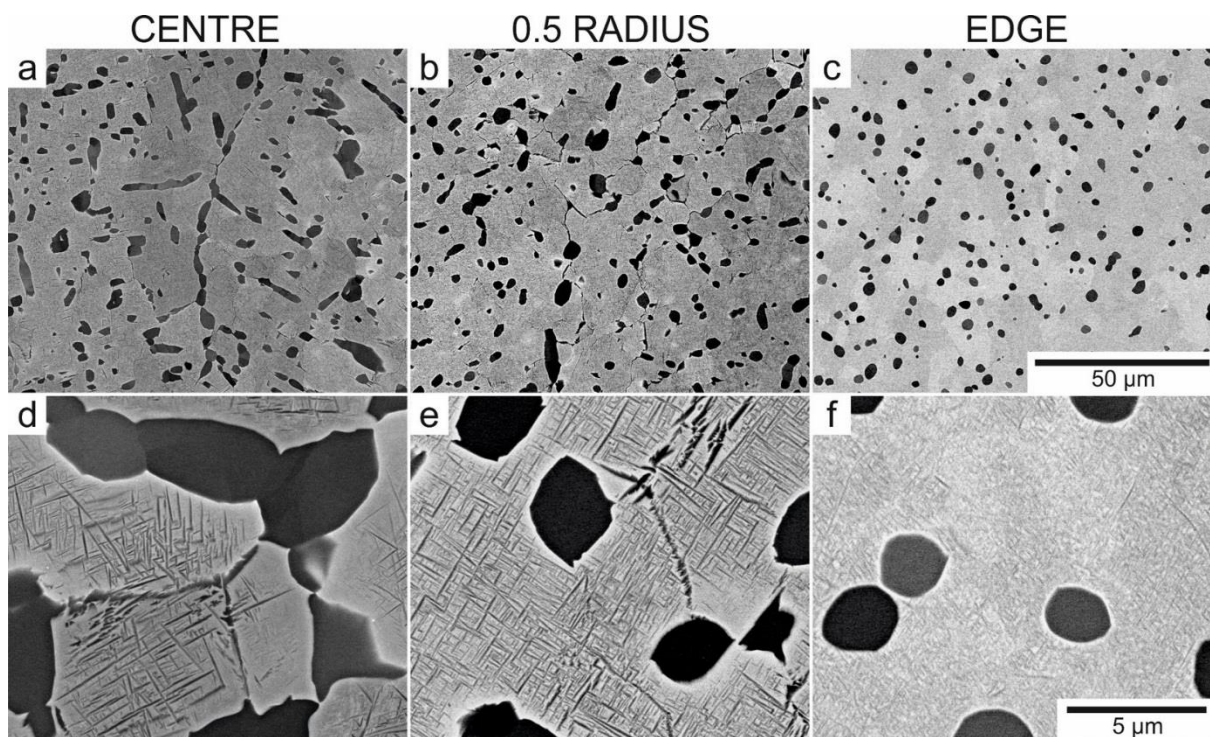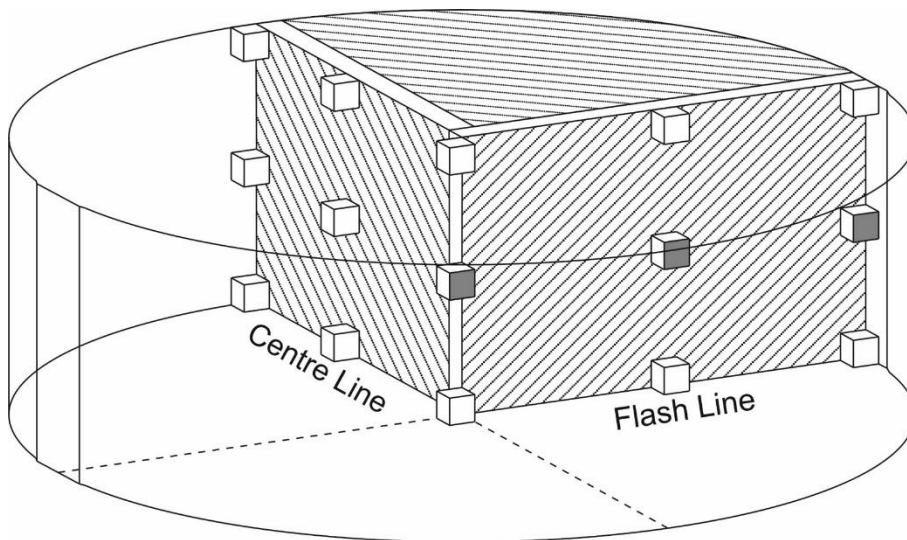
Figure 4.20: BSEI micrographs taken across the flash line at low magnification (a), (b), (c), and high magnification (d), (e), (f). The α phase now appears dark and the β phase appears light (in contrast to etched light microscopy).

This may be due to channelling contrast, indicating the presence of orientation boundaries, or merely compositional fluctuations due to segregation. Towards the forging centre, the primary α particles also exhibit a 'precipitate free zone' (PFZ). This is a layer of β phase immediately adjacent to the α/β interface where the rejection of β stabilisers by the α particle leaves the region devoid of any secondary α particles (precipitates). These precipitate free layers are relatively soft and deform preferentially, giving rise to ductility and fatigue issues [6]. The thickness of the PFZ appears to increase towards the forging centre, probably due to a slower cooling rate.
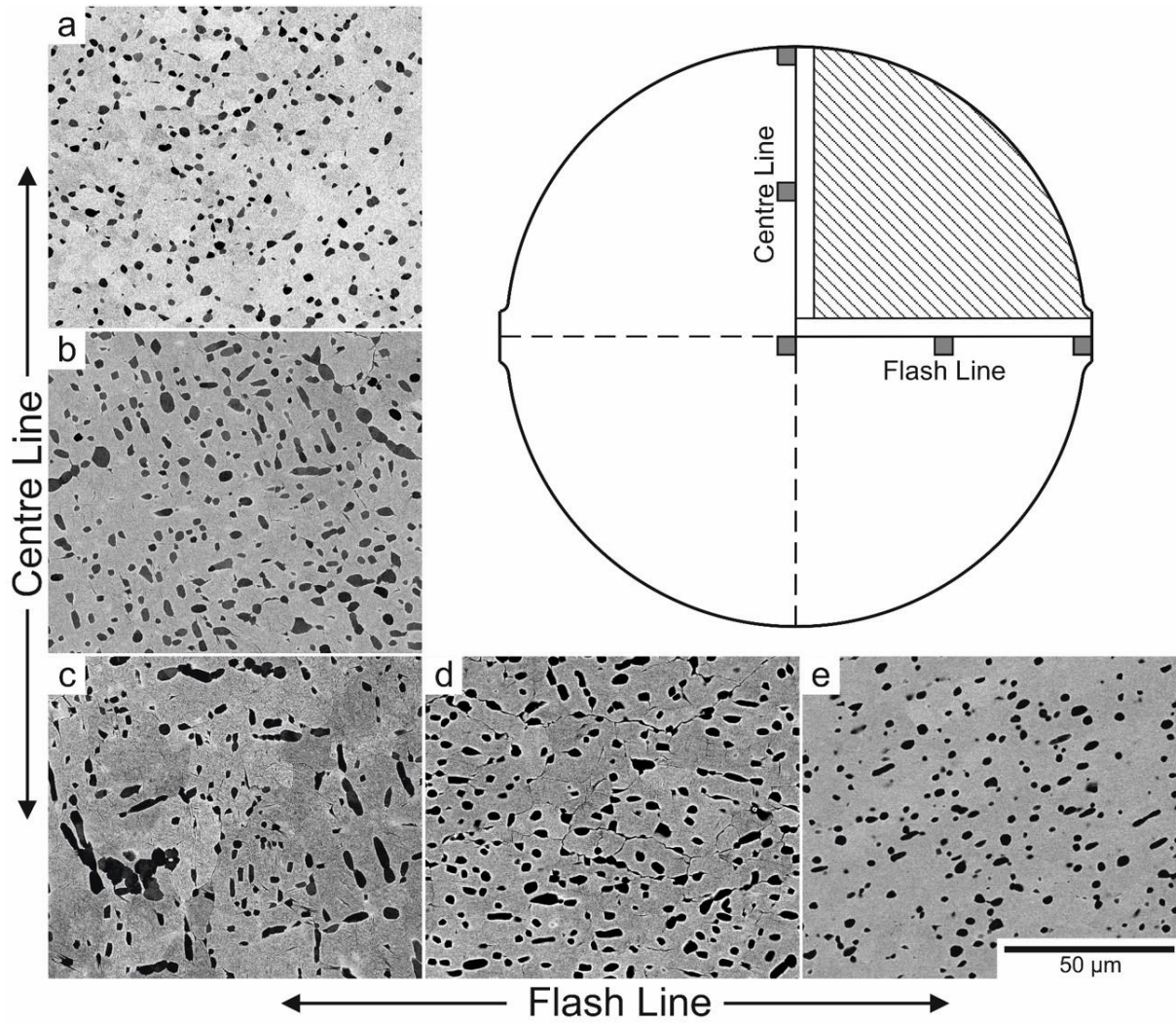
Figure 4.21: Low magnification BSEI micrographs taken perpendicular to the longitudinal axis of the forging.
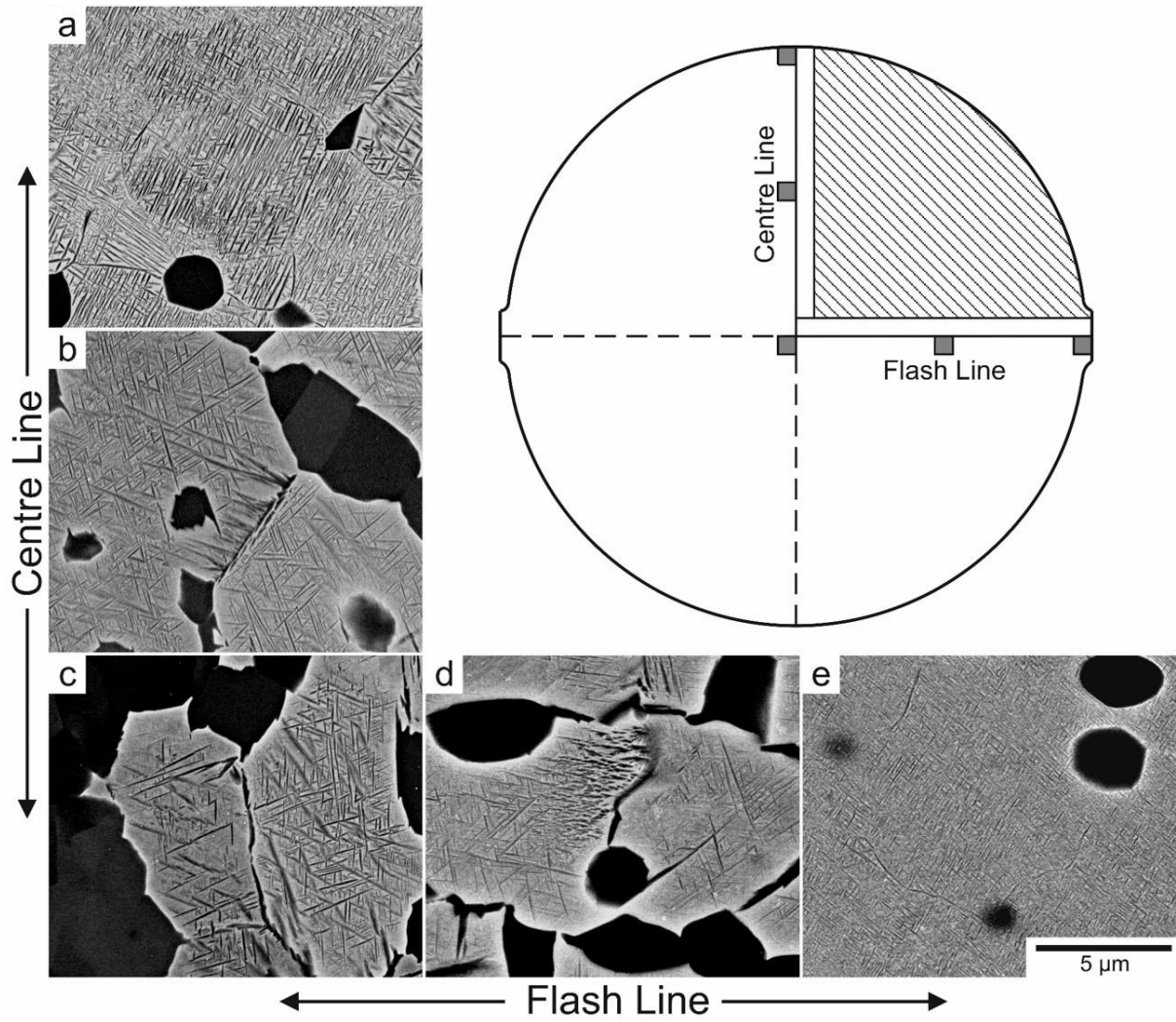
Figure 4.22: High magnification BSEI micrographs take perpendicular to the longitudinal axis of the forging.

4.3.3 Electron Backscatter Diffraction (EBSD)

Figure 4.23-4.29 describe the microstructure of forging 1 with the use of EBSD data. As with the light and electron microscopy, only selected specimens and planes were analysed to avoid excessive redundancy where little microstructural variation was expected. Unsurprisingly, the directionality observed with previous characterisation techniques is also evident in the EBSD maps of Figure 4.23-4.24. The IPF colour scheme allows for easy interpretation of some orientation information by eye. However, it does not show rotation of a crystal around the pole of the reference plane. This can obscure the presence of orientation (grain) boundaries. For this reason, the grain boundaries of the β phase were demarcated in HKL Tango. In the low magnification maps (step size of 1 µm), the high angle β grain boundaries (HAGB, >15°) have been marked with thick black lines, while the high magnification maps (step size of 0.06 µm) also include low angle boundaries (LAGB, $2°>θ>15°$) delineated with thin black lines.

It was quickly established that the secondary α was too fine to be resolved/indexed through EBSD, even with the smallest step size (0.06 µm). This means that the microstructure between the primary α phase generally appears as β phase alone. Because of the fine scale of the secondary α, the interaction volume of the electron beam when it passed over the aged matrix probably included both retained β and secondary α. This presumably complicated the process of interpreting the EBSP (diffraction pattern) since it would contain Kikuchi bands for both phases, and may have reduced the indexing rate as a result. In some cases, the α reflection within the aged matrix was evidently strong enough for a point to be indexed as hexagonal. This would sometimes lead to 'specks' of individual α points within the β matrix of the high magnification EBSD maps.

The elongation of the β grains in the longitudinal direction is readily apparent in Figure 4.23-4.24, in broad agreement with the light micrographs (Figure 4.12-4.13). However, although the β grains at the forging edge do appear elongated, they also appear slightly wider than those in the light micrographs. This may simply be due to random variation in the area examined. Another possible cause could be the grain boundary threshold (>15°) overlooking lower angle boundaries that are visible under etched light microscopy. For example, in Figure 4.23(a) there is a grain containing both a green/yellow region and a red/purple region without a grain boundary between them. There is also the occurrence of lattice rotation. Referring to Figure 4.23(a) again, the large (wide), green grain shows a transition across it. The specific shade of colour changes from a blueish green to a yellowy green, indicating a gradual rotation of the crystal lattice. This deviation from the mean orientation of the grain is sufficient to alter the colour slightly, but too gradual for any clear boundary to be drawn. This illustrates the difficulty with precisely defining grain boundaries. In addition, a much larger area would be required for reliable quantitative measurements about grain size. However, it is clear that they can exceed hundreds of microns in the transverse directions, and extend well over a millimetre in the axial

direction. It should also be noted that the EBSD maps were positioned more centrally on the specimen surfaces, whereas the light micrographs at the forging edge overlapped the outer edge of the forging. At this extreme location, the material immediately adjacent to the die wall may have experienced greater deformation, producing more elongated grains than those at the specimen centre (five millimetres from the forging edge). This perhaps illustrates the potential for significant microstructural variability over relatively short distances. As with the light micrographs, the grains at the forging centre appear narrower than those at the mid-radius. However, it is important to bear in mind the limited coverage of these maps.

The β grains at the forging centre also appear wider in the flash line direction than the centre line direction. Closer examination of the light micrographs of Figure 4.12-4.13 and 4.15 also suggests this may be the case. While the axially oriented EBSD maps (Figure 4.25-4.26) clearly show the transverse elongation of the β grains at the flash edge, it is also possible to discern some deviation from an elongated-equiaxed structure elsewhere. The most equiaxed grains (viewed end-on) appear at the mid-radius and edge (top) of the forging centre line (Figure 4.25 (a) and (b)). Along the flash line, the β grains may have been elongated in both the axial and transverse directions, to form 'pancaked' grains, with the most pronounced effect at the flash edge (Figure 4.25(c)-(e)). For a three dimensional representation of this, Figure 4.27 combines the low magnification axial, tangential and radial EBSD maps at the forging centre and edges.

Despite the elongated nature of the β grains, it can be seen in the tangential EBSD maps that there exist some small, equiaxed grains with high angle boundaries near the centre of the forging (Figure 4.24 (a)). These may be evidence of partial recrystallization along the deformed β grain boundaries. If the forging centre remained warmer for longer than the edge, this may have provided sufficient time for selective recrystallization to begin, yielding a bi-modal grain size/shape distribution. Some β grains also contain small black specks, indicating the presence of high angle grain boundaries. These are most likely the result of misindexed points, possibly as a result of pseudo-symmetry. In an attempt to improve the indexing rate for the EBSD maps in Figure 4.24(e) and (f), the min/max number of bands was reduced from 5-7 to 4-6. This proved to be a false economy, providing more data but compromising its reliability in the process. The greater prevalence of misindexed points then produced the black speckled appearance of Figure 4.24(e) and (f) when the grain boundary delineation was applied. Fortunately, the general grain structure is still discernible.
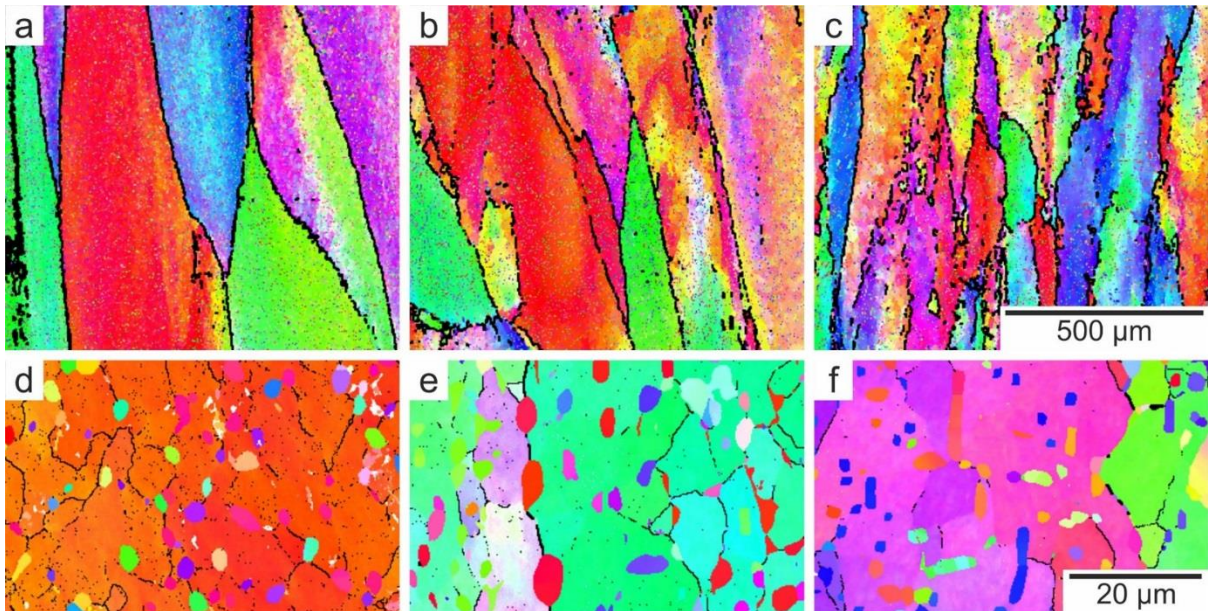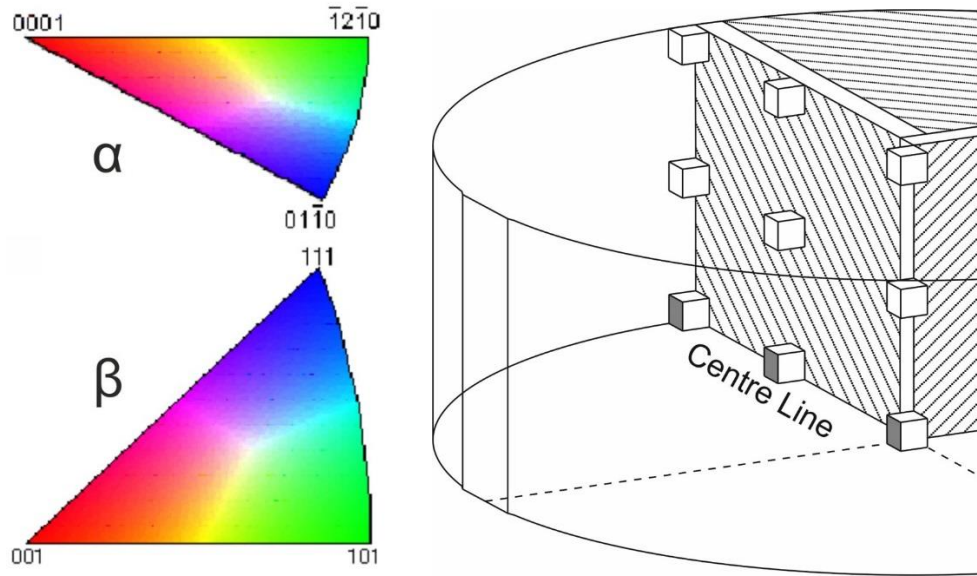
Figure 4.23: EBSD maps taken at low magnification (a), (b), (c) and high magnification (d), (e), (f). High angle grain boundaries (>15°) are marked by thick black lines. Low angle grain boundaries (2°>θ>15°) are also marked in the high magnification maps (thin black lines).

The high magnification EBSD maps of Figure 4.23-4.24 and 4.26 also include low angle grain boundaries (thin black lines, 2°>θ>15°), indicating the presence of subgrains within the large, deformed β grains. These are particularly prevalent at the forging edge (Figure 4.23(d), 4.24(f) and 4.26(a) and (f)). This would suggest that the small equiaxed grains near the forging edge in the high magnification light micrographs are actually subgrains, rather than new, recrystallized grains. This is characteristic of Ti-5553, where high temperature deformation is typically dominated by dynamic recovery [92]. The subgrain size also appears to be of the order of the primary α particle spacing. This would suggest that the α particles influenced deformation of the β matrix and subgrain formation.
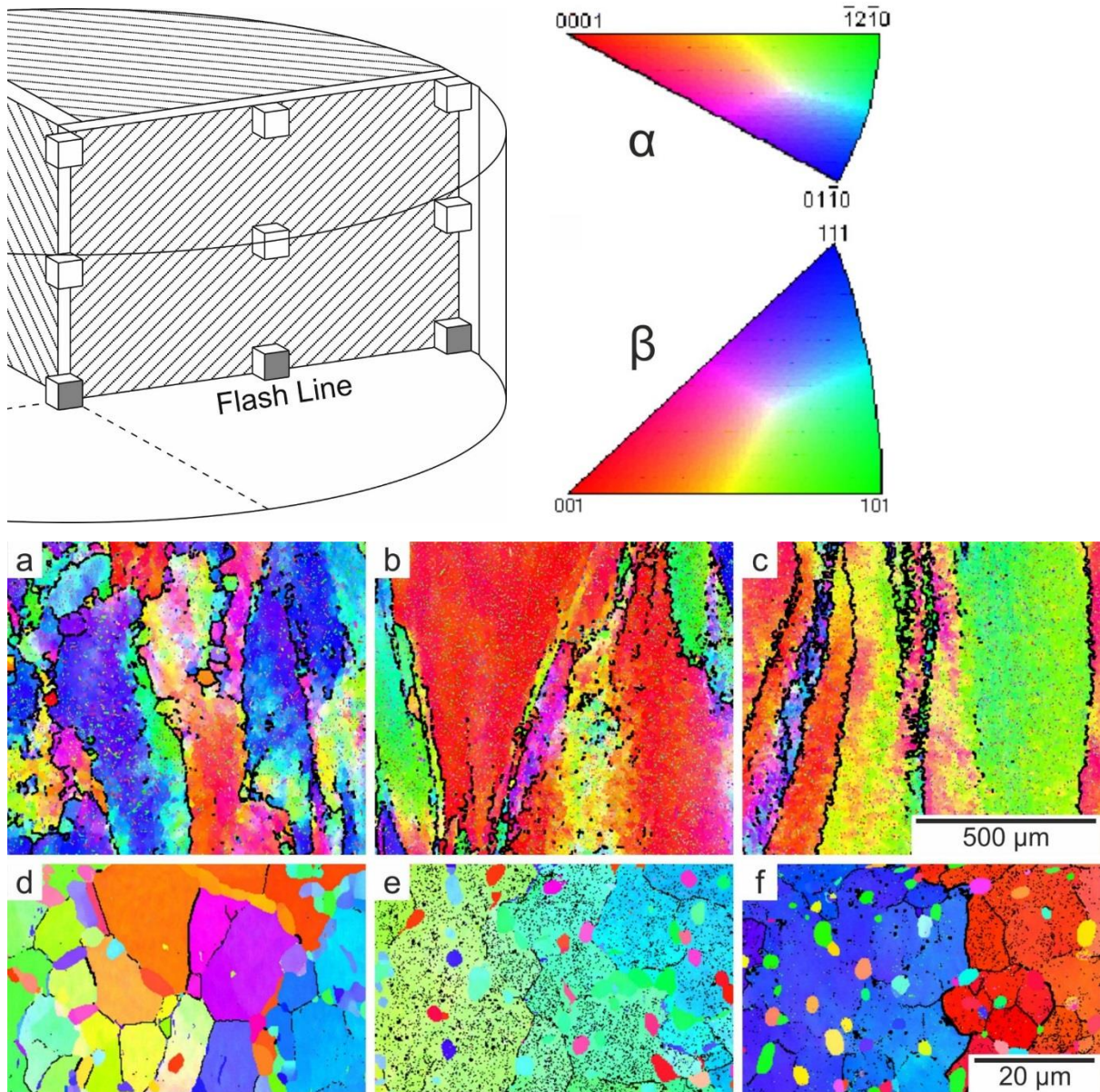
Figure 4.24: EBSD maps taken at low magnification (a), (b), (c) and high magnification (d), (e), (f). High angle grain boundaries (>15°) are marked by thick black lines. Low angle grain boundaries (2°>θ>15°) are also marked in the high magnification maps (thin black lines).

Along high angle β grain boundaries, where continuous α layers have been avoided, it can still be seen that individual primary α particles 'decorate' these boundaries, as in Figure 4.23(e).
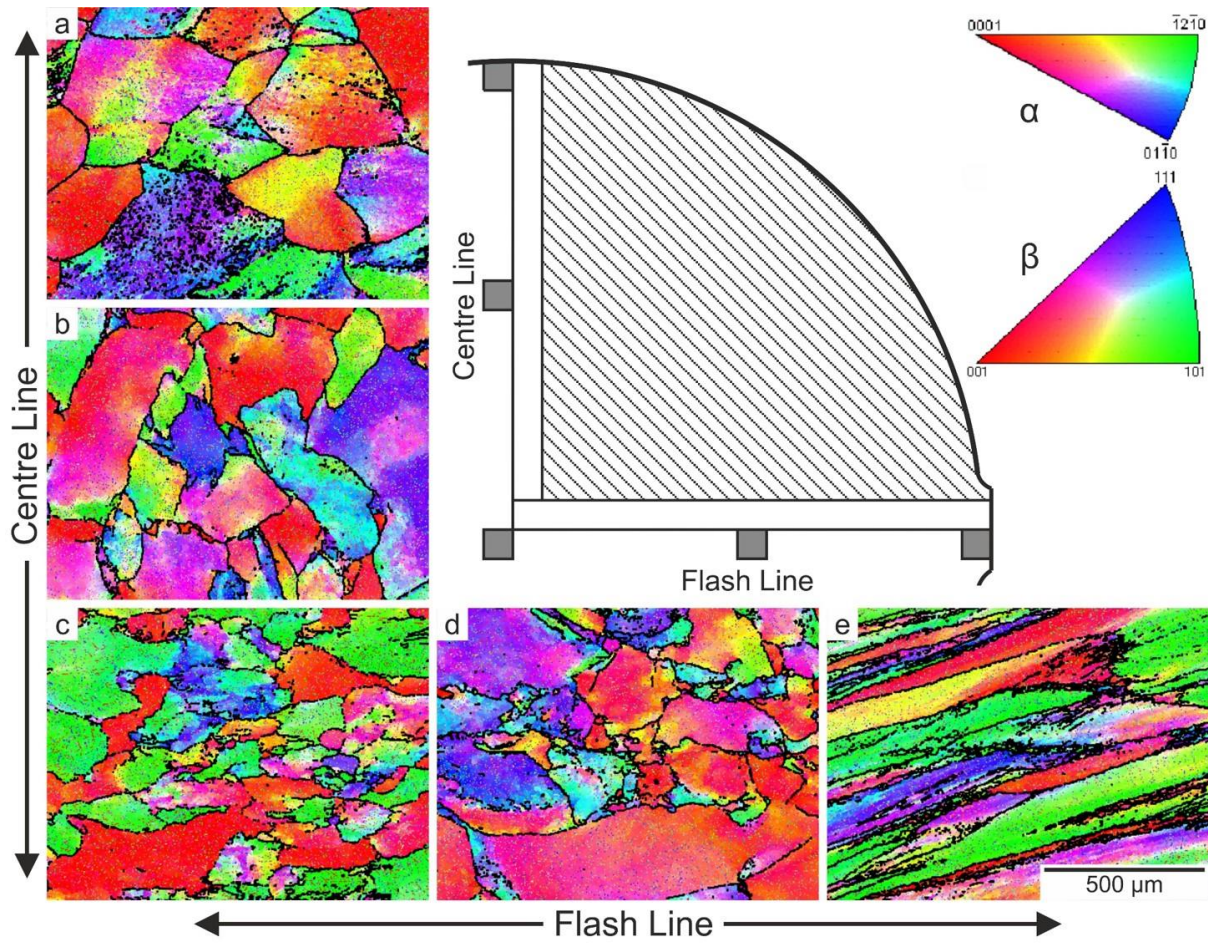
Figure 4.25: Low magnification EBSD maps oriented perpendicular to the longitudinal axis of the forging. High angle grain boundaries (>15°) delineated with thick black lines.
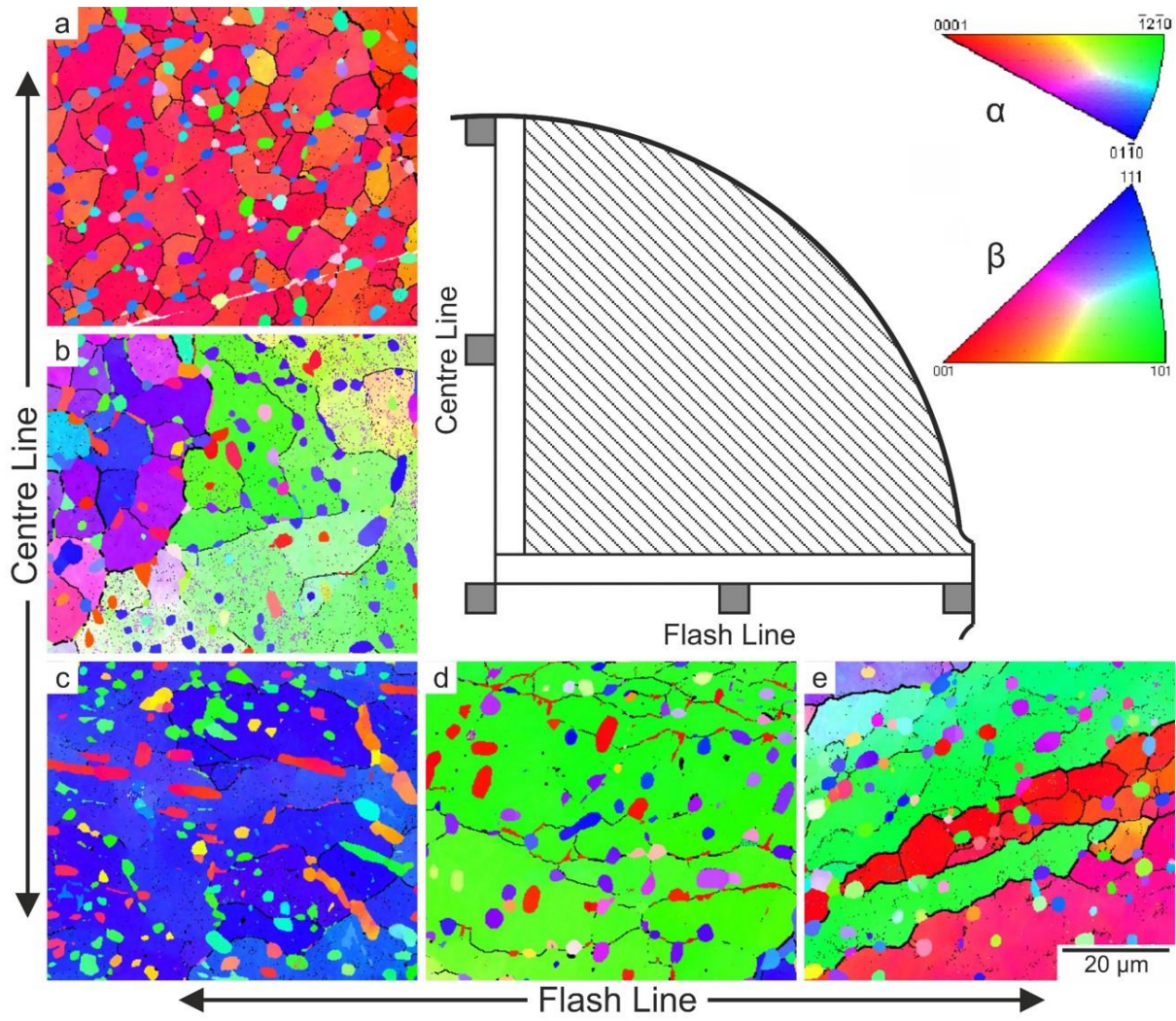
Figure 4.26: High magnification EBSD maps oriented perpendicular to the longitudinal axis of the forging. High angle grain boundaries (>15°) delineated with thick black lines, and low angle boundaries (2°>θ>15°) by thin black lines.

95
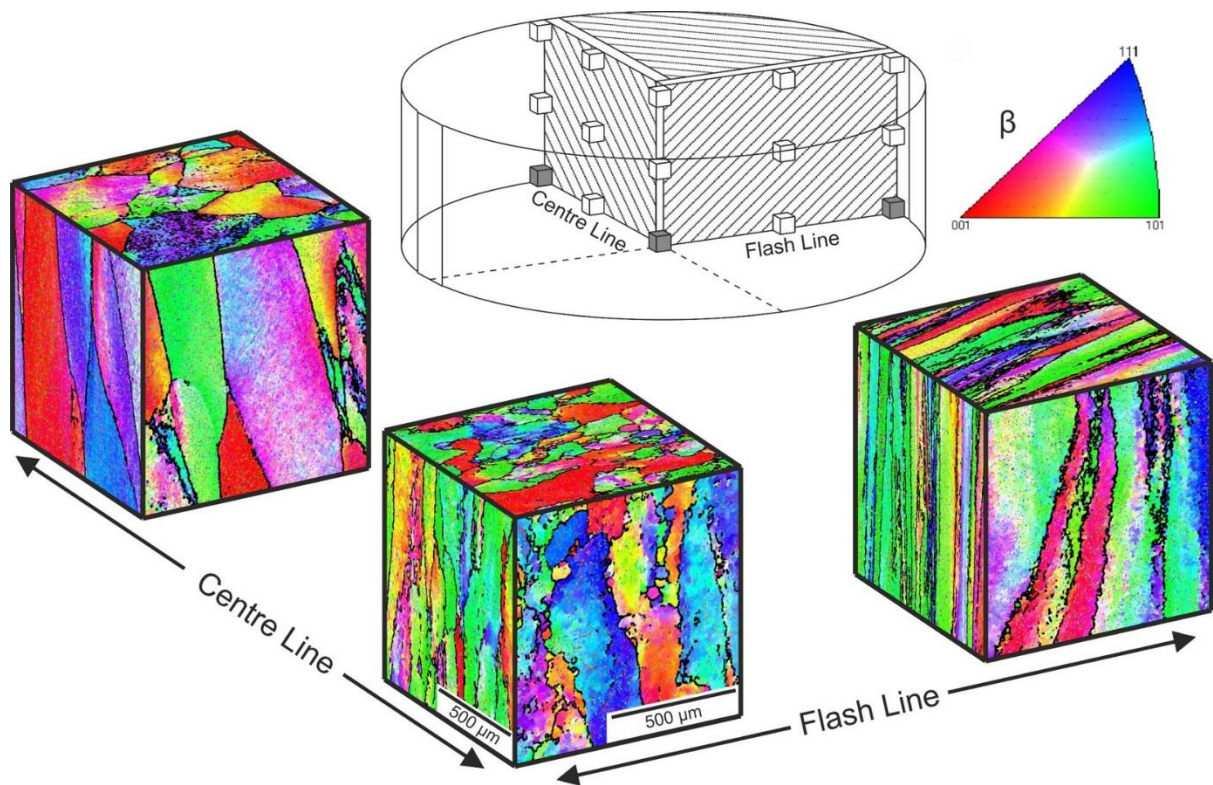
Figure 4.27: 3D stitch of low magnification EBSD maps, with high angle grain boundaries (>15°) marked (thick black lines). IPF reference plane is perpendicular to the longitudinal axis of the forging (cylinder axis). Note that grey faces indicate the planes analysed, not the scale.

The EBSD data was also reviewed as to its suitability for texture analysis. However, it became apparent that the area covered by the maps was insufficient to provide a reliable description of the macrotexture [97]. The use of EBSD to provide macrotexture information has been successfully carried out before, but this required sampling a much larger number of orientations (grains) than was available in the low magnification maps presented here [67]. One option was to increase the step size beyond 1 µm in order to map a larger area. However, in order to examine the consistency of the Burger's Orientation Relationship (BOR) it was necessary to capture the α orientation data as well. Therefore, given the size of the primary α particles (2-3 µm), it seemed unwise to increase the step size any further.

Figure 4.28 presents pole figures of the basal plane {0001} for the α phase and {110} plane for the β phase. These pairs of pole figures were produced from the raw data of the low magnification axially oriented EBSD maps. The BOR states that the hexagonal {0001} plane and cubic {110} plane should be parallel, giving rise to coincidence of these plane normals on the pole figures. If the distribution of orientations were entirely random, this would not be noticeable in the figures. However, since individual β grains produce areas of greater pole density on a figure (as indicated by the colour scale), these regions should coincide with the pole density peaks of the {0001} plane of the α phase.
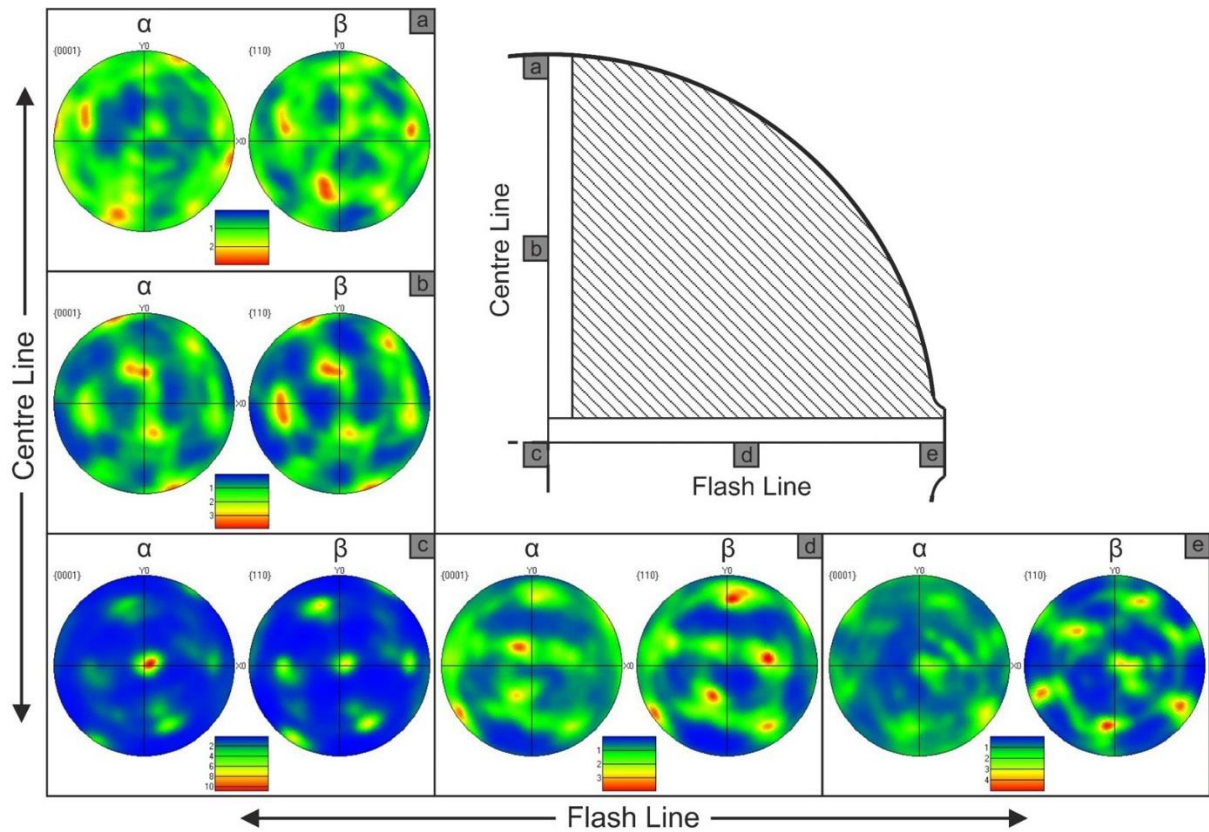
Figure 4.28: Equal area, upper hemisphere pole figures for the hexagonal {0001} plane and cubic {110} plane. Z-axis is parallel to the forging's longitudinal axis. Colour contour scale illustrates pole density in Multiples of Uniform Density (MUD).

In confirming adherence to BOR, it is less significant that the 'intensity' of these points match than their location, since variant selection can increase the frequency of some orientations at the expense of others. With this in mind, it can be seen that there is reasonable agreement between the pole figures across all samples. This would suggest that the level of strain experienced during the forging operations was insufficient to break down the BOR, even at the flash edge. This would agree with studies of other alloys, which could tolerate very high levels of strain before any significant deviation occurred [102][68].

Within the EBSD maps, assuming the BOR holds, the variation in colour of the intragranular α particles indicates multiple variants are present in each 'parent' β grain. If no particular orientation were favoured, all twelve possible variants should nucleate with equal probability within each grain. However, this is unlikely since variant selection is known to occur during the formation of both intergranular and intragranular α [4]. Figure 4.29 would appear to confirm this, showing the relevant pole figures for the high magnification axially oriented EBSD map from Figure 4.26(a). Because this covers a much smaller area, the pole figures are less 'busy'. This makes it much easier to see the six {110} poles of the single β orientation (β grain) that constitutes most of the EBSD map (seven points appear because one overlaps the edge of the figure). Comparison with the α {0001} pole figure shows that one variant (the one which

97

overlaps the edge) is favoured over the others. Conversely, three of the variants are so unfavourable that they are almost completely omitted from the α pole figure. In addition, the coincidence of points on these pole figures also illustrates the strict adherence to the BOR even after substantial deformation.
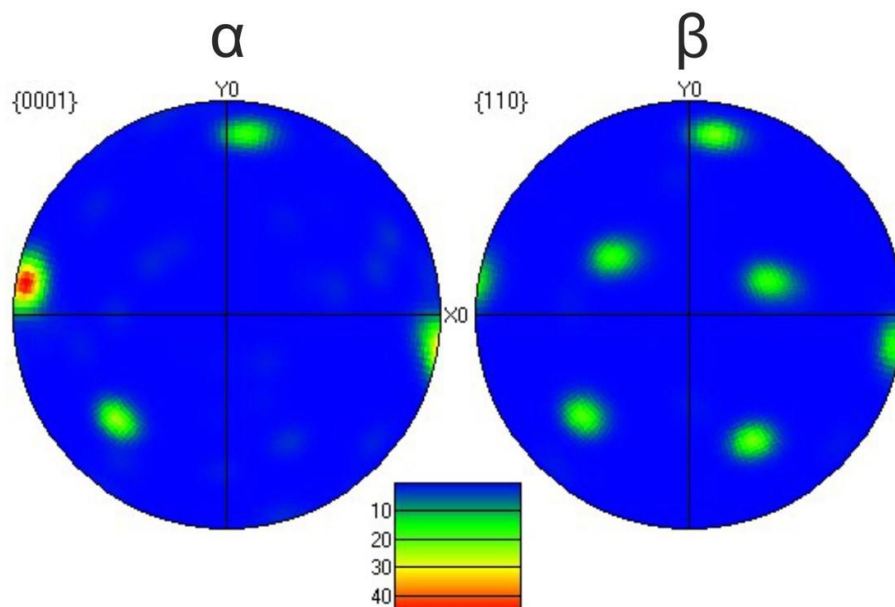
Figure 4.29: Equal area, upper hemisphere pole figures of the hexagonal {0001} plane and cubic {110} plane for the high magnification, axially oriented EBSD map of Figure 4.26(a). Colour contour scale illustrates pole density in Multiples of Uniform Density (MUD).

4.4 Effect of Heat Treatment

Forging 2 was used to investigate the effect of heat treatment upon microstructure and mechanical properties. Given the limited axial variation in forging 1, examination of forging 2 was restricted to analysis of only radial variation along the flash line and centre line. Microscopy specimens are pictured in a common plane perpendicular to the longitudinal axis for the same reason. Also note that diagrams of forging 2 place the flash line on the left hand side and the centre line on the right hand side. This reversal was necessary to allow comparison with mechanical tests carried out on forging 1. These had to be on the opposite halves of the forging due to the microscopy specimens (unlike forging 2, where microscopy specimens were removed from the tensile testpieces). Figure 4.30 and 4.31 compare the as-received and heat treated microstructures of forging 2 at low magnification. The as-received material can be seen to follow the same general trends as forging 1. Towards the forging edge the primary α particles are more globular and grain boundary α layers are absent. The heat treatment consisted of a solution treatment approximately 40°C below T_β for 4 hours followed by ageing at approximately 600-620°C for 8 hours. The solution treatment is intended to set the volume fraction of primary α, and therefore dictate the volume fraction of retained β available for

strengthening during ageing (through precipitation of secondary α). For a given ageing temperature, increasing the solution temperature will provide more retained β for ageing, and thus a higher strength. For a constant solution temperature, lowering the ageing temperature will produce finer secondary α, and therefore increase the final strength. From Figure 4.30 and 4.31 it would appear that the solution treatment had little effect on the morphology of the primary α, with the same morphological trends across the forging after heat treatment. The process of spheroidisation at high temperature is a slow one, and the duration of the solution treatment was presumably too short for any significant change to occur [17].

Figure 4.32 illustrates the primary α volume fraction across forging 2 in the as-received and heat treated condition. Given that the flash line and centre line are normal to one another, representing these directions on a 2D graph presented some difficulty. It is therefore important for the viewer to bear in mind that each half of the X-axis is effectively perpendicular to the other. The measurements themselves were taken on the tangential faces under the assumption that the area fraction of a second phase is equal to the volume fraction of that phase and independent of the plane in which it is measured [94]. While this may be true in principle, there was a discrepancy between the two tangential faces of the as-received sample at the forging centre. However, since the 95% confidence limits overlapped, this was assumed to be a random fluctuation and the two values were averaged to provide a single quantity.

It can be seen in Figure 4.32 that there exists a significant variation in the primary α volume fraction across the forging in the as-received condition. At both edges, the volume fraction is around 10.5%, rising to about 17% near the forging centre. The increase may (initially) be more rapid from the bottom edge than the flash edge, although it is difficult to say this with any degree of certainty. The solution treatment largely removes this variation, bringing the primary α volume fraction down to about 10-12%. These levels are similar to that originally present at the forging edge. This may explain the lack of nucleation of new primary α particles during the solution treatment, since the driving force will have been towards dissolution (or nearly static at the forging edge). The original variation is likely caused by variation in the cooling rate across the forging. If the forging centre cooled more slowly, this would have provided extra time for primary α to form/grow.
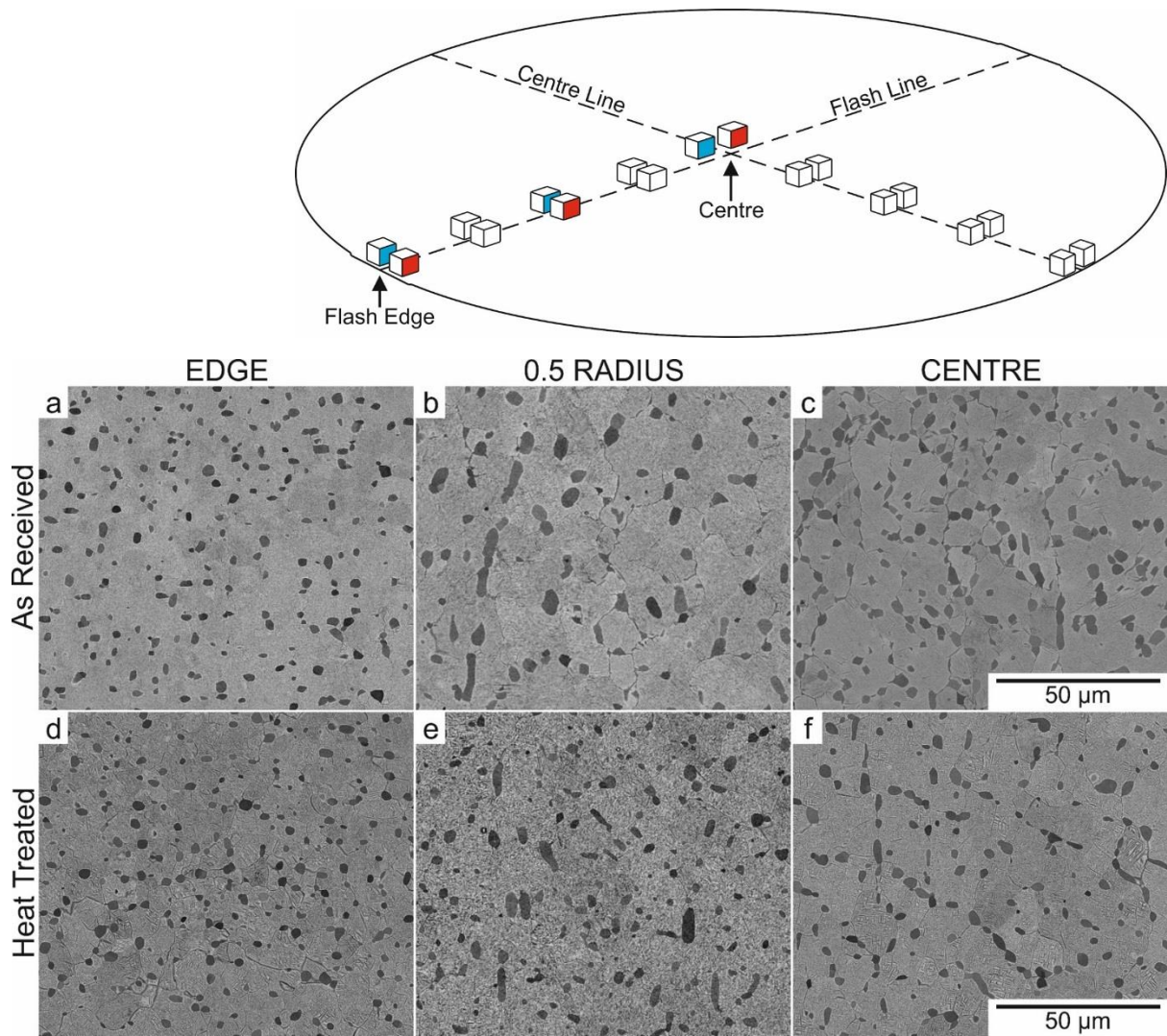
Figure 4.30: Forging 2, low magnification BSEI micrographs taken across the flash line in the as-received condition (blue faces) (a), (b), (c), and in the heat treated condition (red faces) (d), (e), (f). When comparing with forging 1, note that flash line samples are now on the left.
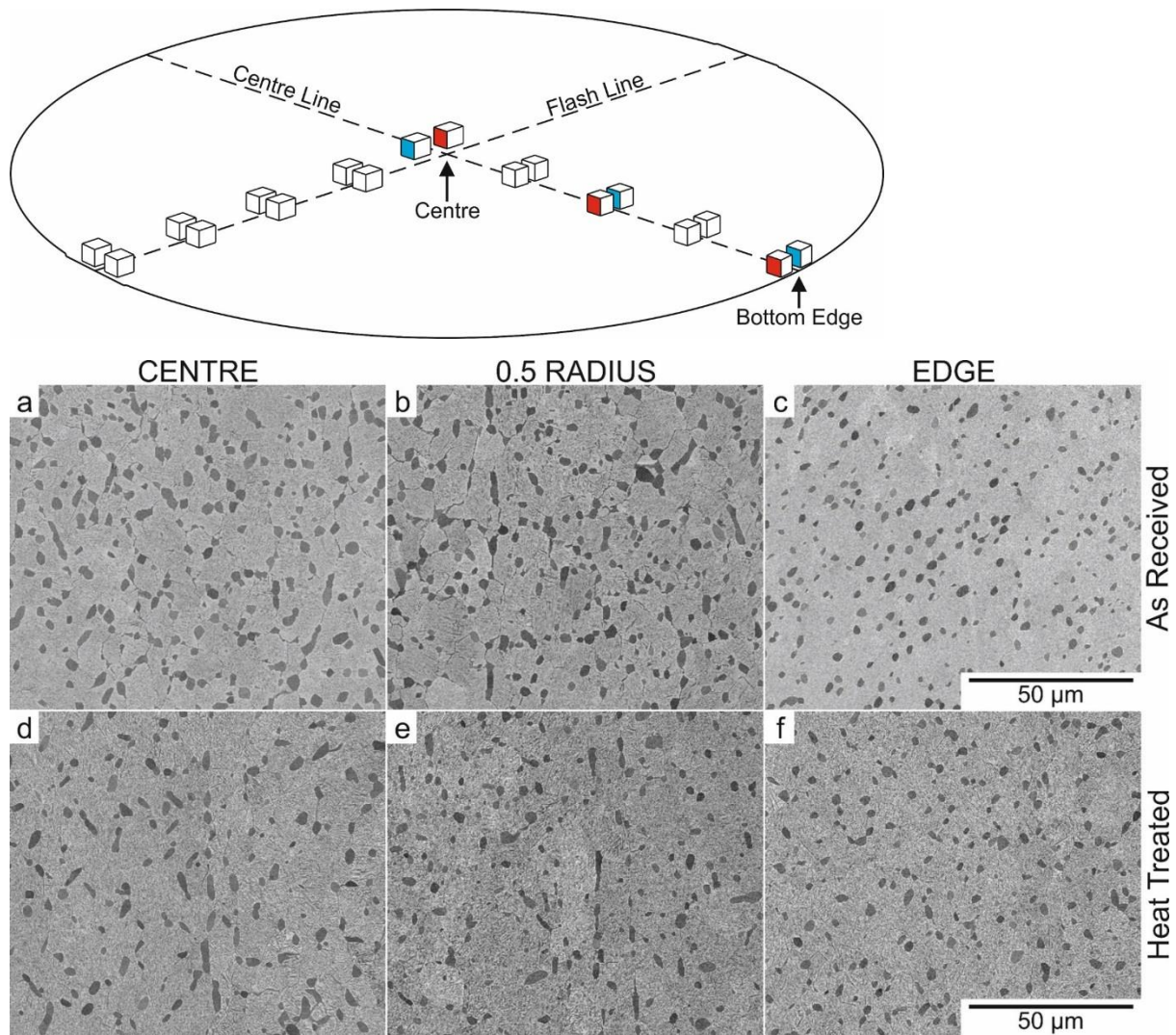
Figure 4.31: Forging 2, low magnification BSEI micrographs taken across the centre line in the as-received condition (blue faces) (a), (b), (c), and in the heat treated condition (red faces) (d), (e), (f). When comparing with forging 1, note that centre line samples are now on the right. Micrograph (d) provided courtesy of A. Cox.
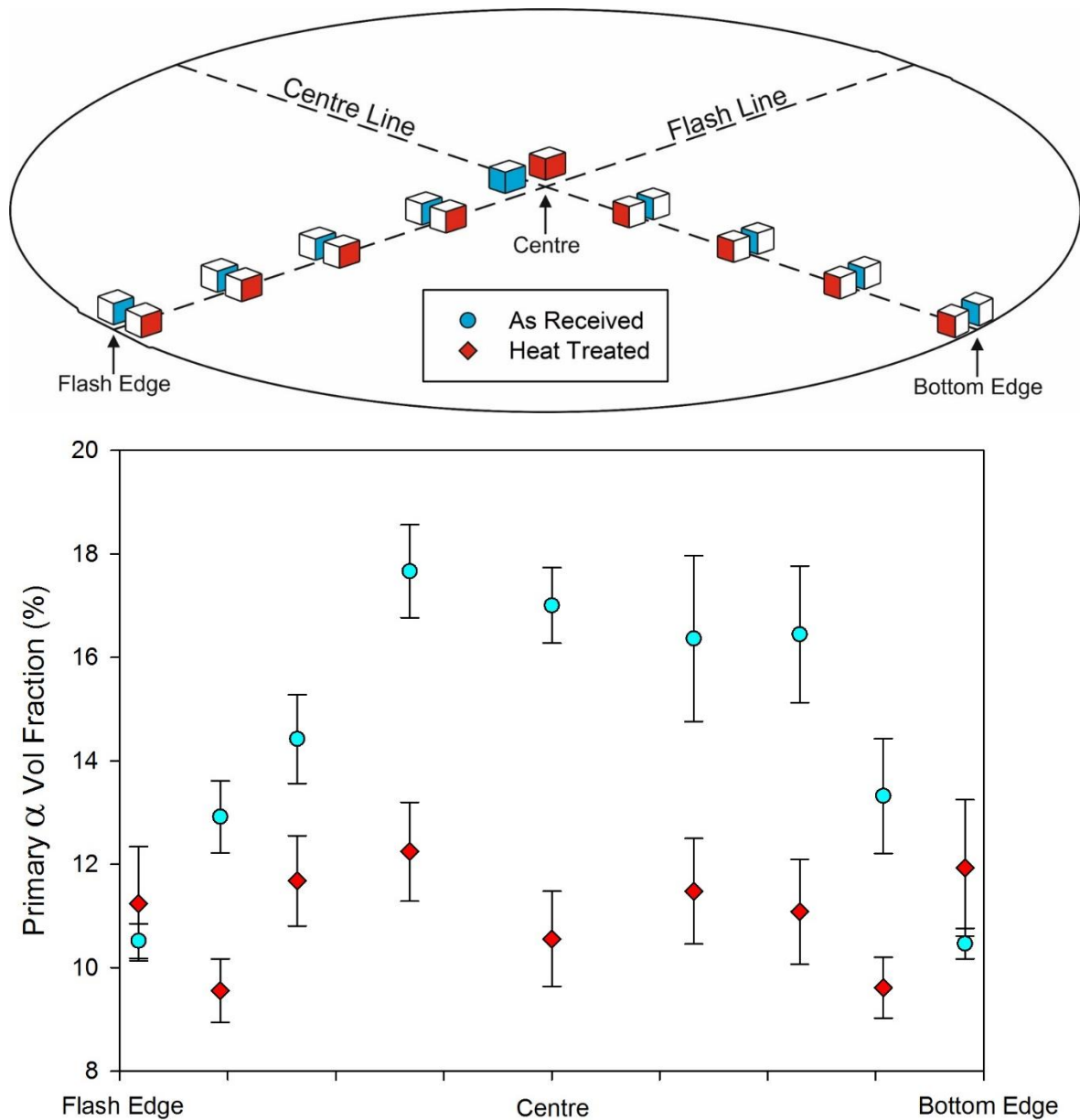
Figure 4.32: Primary α volume fraction across forging 2 in the as-received and heat treated condition. Error bars illustrate the 95% confidence limit.

Figure 4.33 and 4.34 compare the as-received and heat treated microstructures of forging 2 at high magnification. As with the low magnification micrographs, similar trends to those in forging 1 are observed. The higher resolution provides a more detailed view of the primary α, which appears to be of similar size to that in forging 1 (2-3 µm in diameter/thickness). The increasing globularisation of primary α particles towards the forging edge is also readily apparent. In the opposite direction, it can be seen that the PFZ increases in size towards the forging centre, presumably as a result of slower cooling. Across the flash line, the secondary α displays similar behaviour to that of forging 1. At the flash edge, the α precipitates are extremely fine, increasing in size and aspect ratio towards the forging centre. As with forging 1, the change in particle size and shape appears more significant between the forging edge and

mid-radius than the mid-radius and centre. However, this trend also seems to exist along the centre line, unlike forging 1, which exhibits a more consistent distribution of secondary α along the centre line (Figure 4.19). Whether this difference between the two forgings actually exists is uncertain, as subsequent investigation revealed significant variation of the secondary α within the edge specimens (see Section 4.6). This raised the possibility that the micrographs taken near the forging edge may not be representative of the microstructure there. Initial attempts to quantify the scale of secondary α are presented in Figure 4.35 and 4.36. These measurements were carried out in accordance with the procedures outlined in Chapter 3. The axial faces of microscopy specimens were selected for analysis (unlike the volume fraction measurements) since this orientation is shared by both the flash line and centre line without the need for rotation. This was intended to avoid complications that may arise from viewing a 3D object (α platelet) from different angles.

Figure 4.35 illustrates the mean interparticle spacing (d) of secondary α across forging 2 in the as-received and heat treated condition. It can be seen that there exists some variation across the forging in the as-received condition, although the magnitude of this appears less significant than the variation in primary α volume fraction (however, the Y-axis scale may suppress this in order to incorporate the heat treated values and error bars). The anticipated effect of this variation in secondary α on yield strength may be better visualised in Figure 4.36 as this shows the reciprocal interparticle spacing (1/d). This is linearly proportional to the number of particles per unit length (i.e. the density of obstacles to dislocation movement). Both the flash line and centre line of these figures broadly agree with the qualitative observations of the micrographs. That is to say they both show a trend towards finer secondary α nearer the forging edge.

However, it is the quantitative measurements of the centre line that more closely resemble the micrographs in Figure 4.33 and 4.34. The latter suggest less variation between the centre and mid-radius than the mid-radius and edge. In Figure 4.35 and 4.36 this appears to be the case along the centre line, with a marked reduction in the interparticle spacing between the outer two specimens. Indeed, the extra specimen (data point) between the mid radius and edge would suggest the most significant change occurs within the outer quarter of the radius. Along the flash line the magnitude of the variation appears smaller and more gradual. This appears to be inconsistent with the details of Figure 4.33, and with hindsight, may have provided an early indication of the unexpected variation in secondary α across the edge specimens.

Quantitative measurements were taken from sixteen micrographs per specimen arranged in a 4×4 grid with a 1.5-2 mm spacing (depending upon specimen dimensions). This grid was positioned approximately centrally since the microstructure was assumed to be nearly uniform within each specimen. However, given the variation subsequently discovered, a displacement of only a few millimetres in the grid may have significantly altered the mean value for that specimen. It is possible that the wider particle spacing and error bars of the flash edge specimen
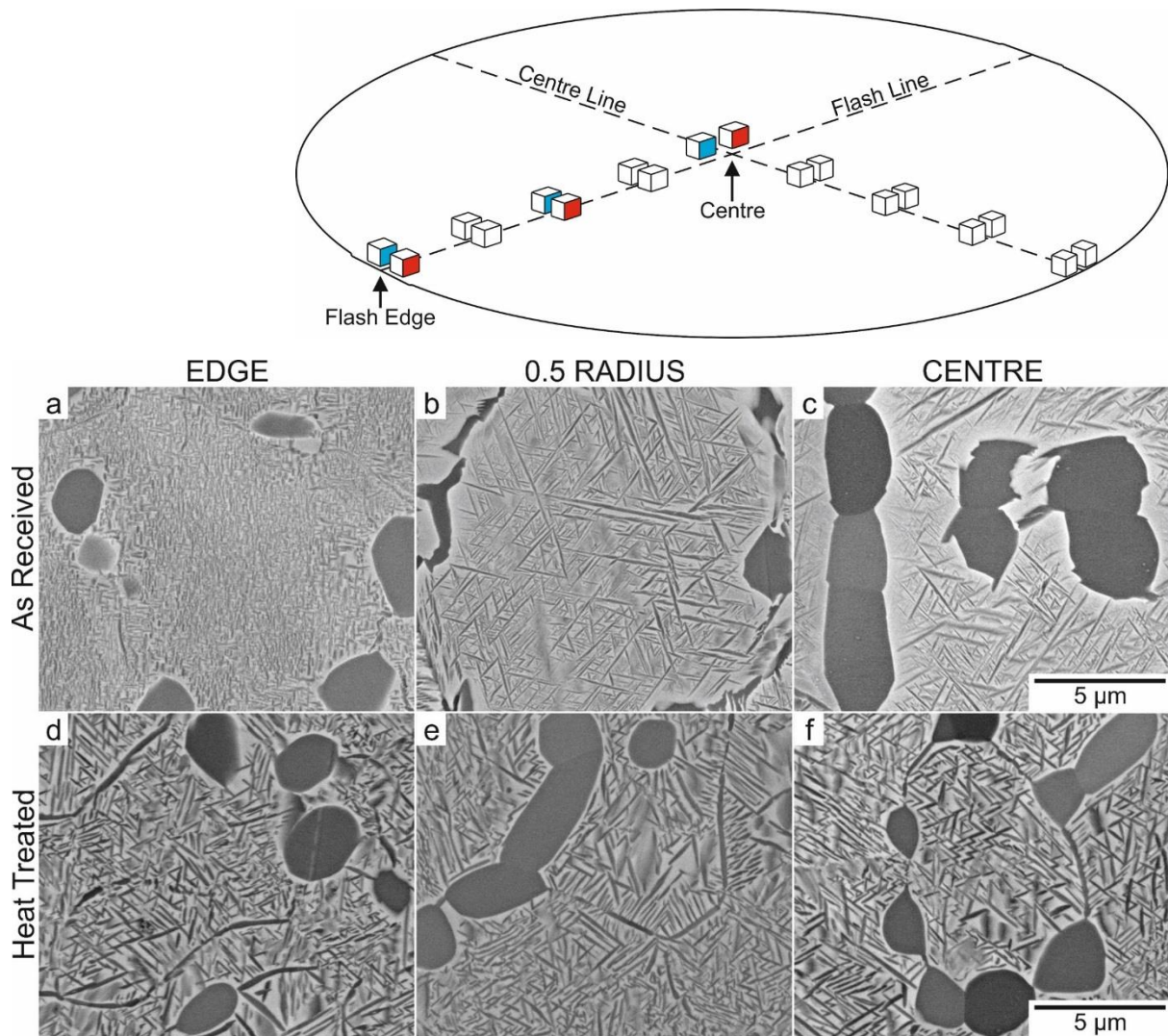
Figure 4.33: Forging 2, high magnification BSEI micrographs taken across the flash line in the as-received condition (blue faces) (a), (b), (c), and in the heat treated condition (red faces) (d), (e), (f). When comparing with forging 1, note that flash line samples are now on the left.

(relative to the bottom edge specimen) are an indication of this variability (by overlapping a coarser region of secondary α). Despite this unexpected variation within the edge specimens, the mean values of interparticle spacing still demonstrate an unmistakable trend towards finer secondary α at the forging edges. During the solution treatment the original secondary α will have dissolved, after which the ageing treatment produces a new distribution of α precipitates. Referring to the micrographs of heat treated specimens in Figure 4.33 and 4.34, it can be seen that the new distribution of secondary α is more consistent and has removed the previous variation. This consistency is reflected in the values of mean interparticle spacing presented in Figure 4.35 and 4.36. They also show a general increase in the interparticle spacing relative to the as-received material. This would be expected to provide less strength than the original, finer distribution of secondary α, although the net effect will also depend on the volume fraction. An unfortunate side effect of the heat treatment appears to be an increase in the presence of α phase along the subgrain boundaries near the forging edge. In addition, although the PFZ appears to
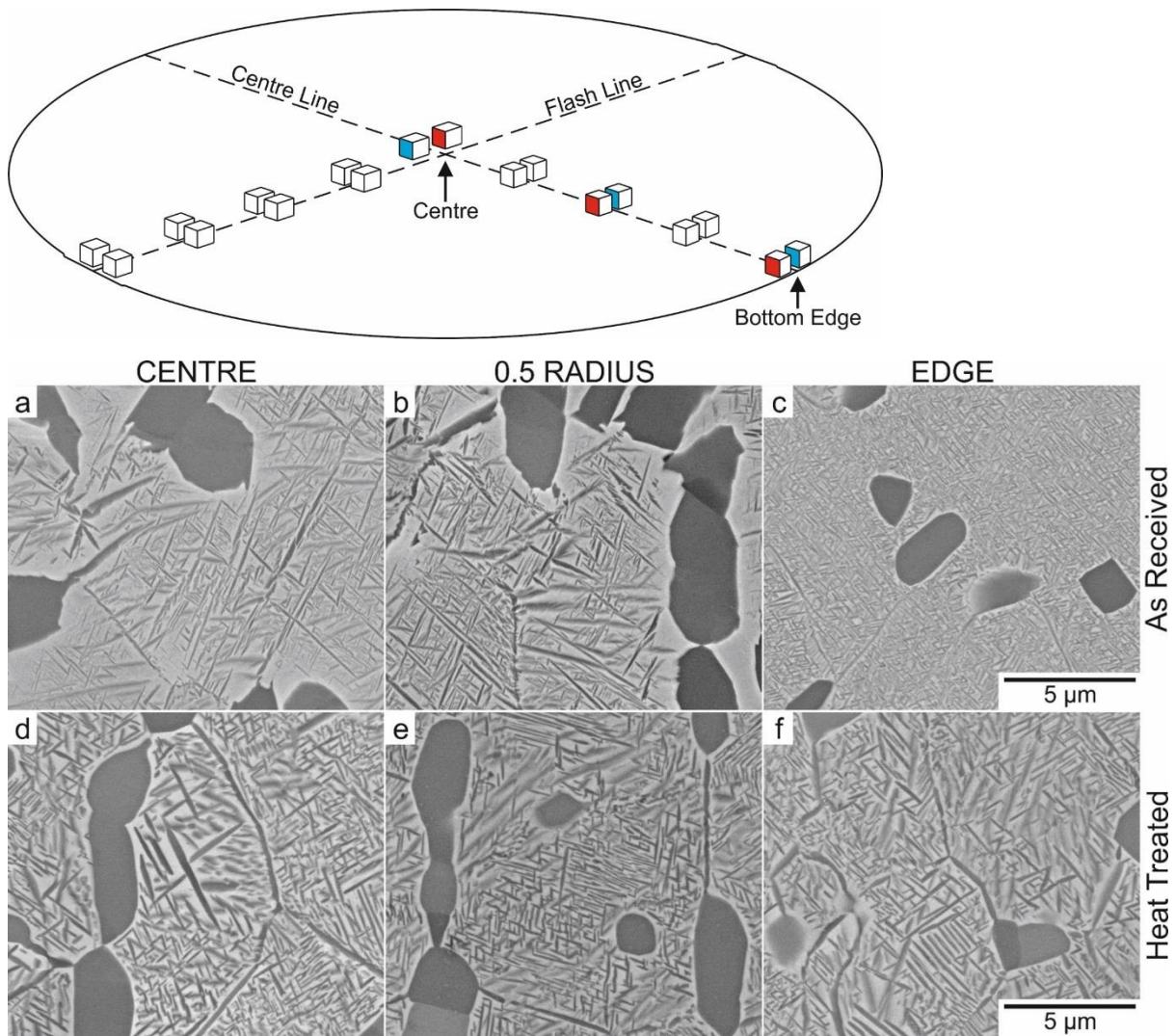
Figure 4.34: Forging 2, high magnification BSEI micrographs taken across the centre line in the as-received condition (blue faces) (a), (b), (c), and in the heat treated condition (red faces) (d), (e), (f). When comparing with forging 1, note that centre line samples are now on the right. Micrograph (d) provided courtesy of A. Cox.

have shrunk in the centre and mid-radius specimens, it may have increased in size at the forging edge. Given that the component wall is situated closest to this region, it would appear that the heat treatment is not without its drawbacks.
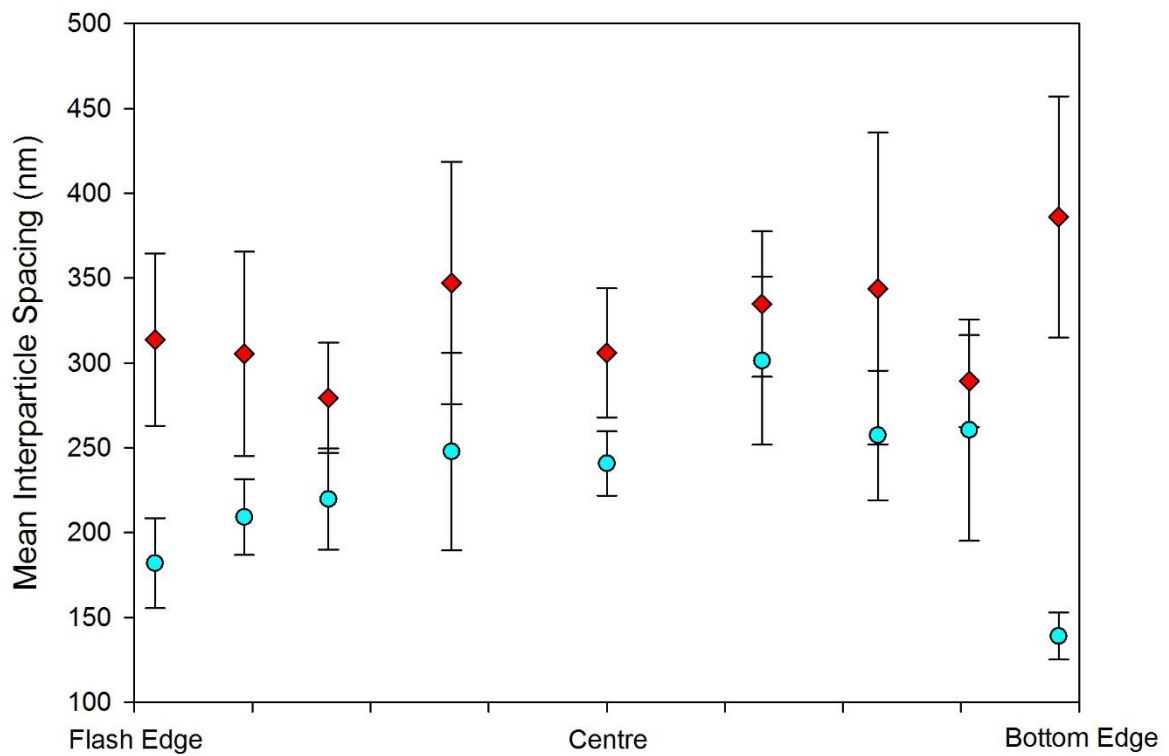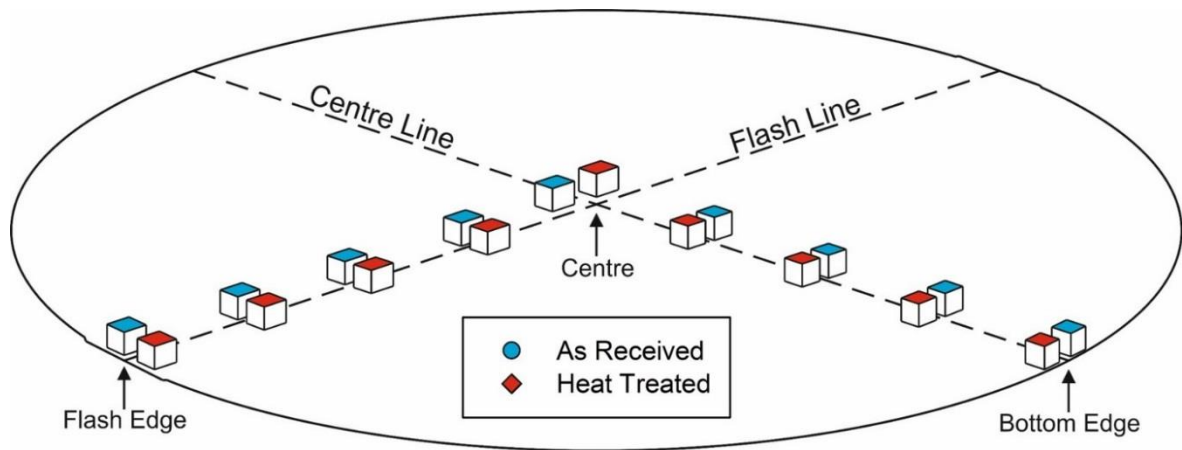
Figure 4.35: Mean interparticle spacing across forging 2 in the as-received and heat treated condition. Error bars illustrate the 95% confidence limit.
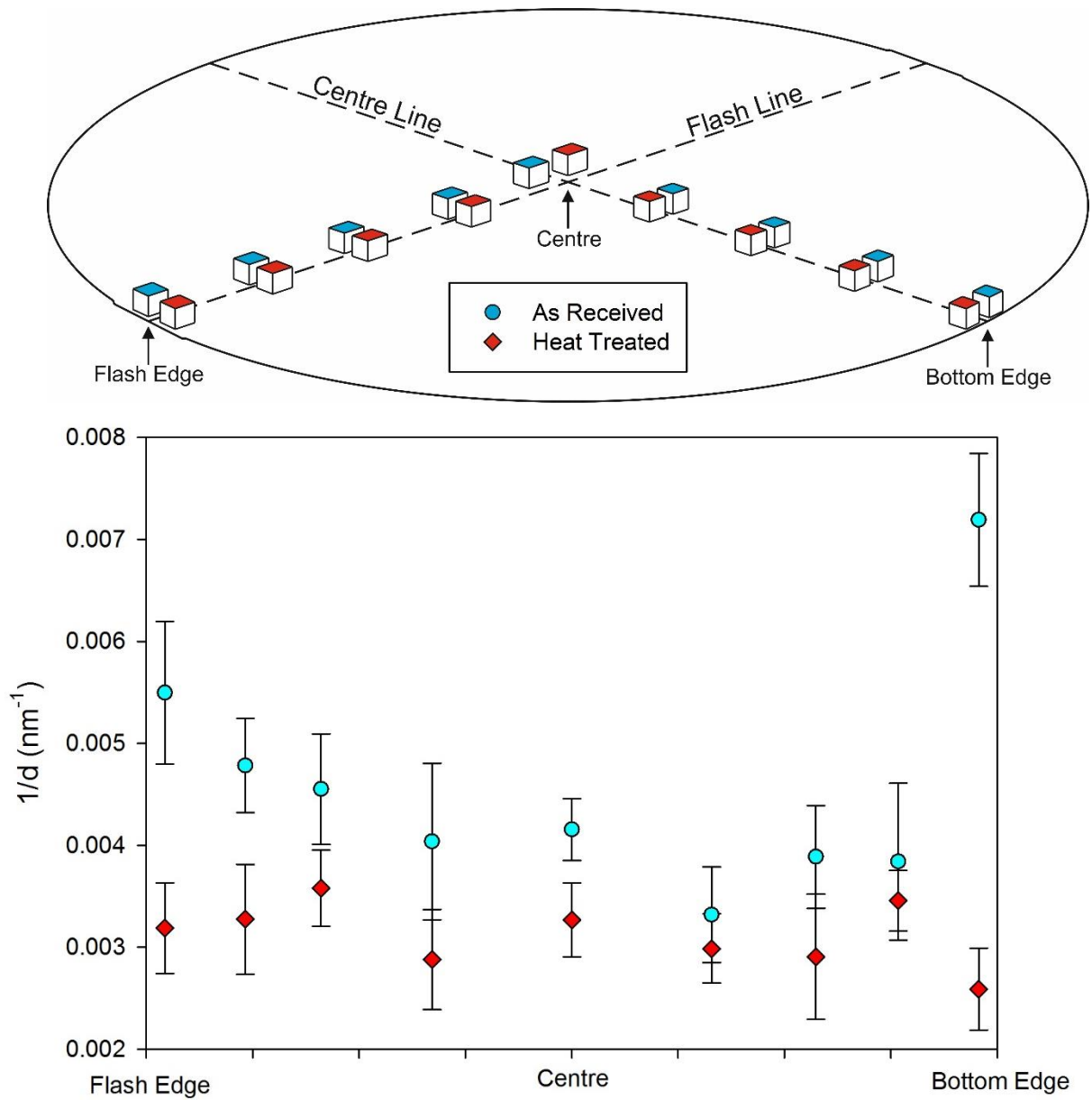
Figure 4.36: Reciprocal of the mean interparticle spacing across forging 2 in the as-received and heat treated condition. Error bars illustrate the 95% confidence limit.

4.5 Mechanical Property Assessment:

4.5.1 Tensile Testing

As explained earlier, the mechanical properties of forging 2 were investigated by means of tensile testing. This study focused on two key properties: strength and ductility. The stress-strain curve of a tensile test contains a large amount of information on both of these properties, making it necessary to restrict the analysis to a few dependent variables. In this case, the Ultimate Tensile Strength (UTS) and 0.2% proof stress were chosen as the criteria for assessing strength. For the evaluation of ductility, elongation to failure was selected for analysis. A limitation of this method is the influence of gauge length on the calculated value. During a tensile test, the occurrence of 'necking' results in localised deformation (elongation) within a short region of the gauge length. In determining the total elongation to failure, the gauge length at fracture is divided by the original length. If the initial gauge length is changed, the influence of the 'extra' deformation in the neck will vary, making comparison between tests unreliable.

An alternative measure of ductility is 'Reduction in Area', defined as the percentage reduction in cross sectional area of the gauge length at the point of fracture. This is unaffected by changes in gauge length, but requires putting the fracture surfaces back together for measurement. This would have compromised fractography, so elongation to failure was chosen instead. However, the strain gauge had to be removed before failure, so specimen elongation is based upon crosshead displacement. The elongation will therefore include machine compliance, making comparison with other data difficult. However, since all testing was carried out on the same machine, consistency between these tests should be preserved. To address any slack in the load train, a line was fitted to the linear (elastic) portion of the stress-strain curve and used to offset the curve to meet the true origin. This line was fitted to the region between 10% and 50% of the recorded UTS. The lower limit of 10% was selected in order to avoid any non-linear section of the stress-strain curve during initial loading. The upper limit of 50% was selected after inspection of the stress-strain curves revealed this to be well within the elastic region (the proof stress was never less than 90% of the UTS).

Figure 4.37-4.40 present the UTS data across forging 2. As with the metallographic analysis it is important to bear in mind that the two 'halves' of the X-axis, representing the flash line and centre line, are perpendicular to each other. Figure 4.37 and 4.38 compare the effect of orientation in the as-received and heat treated condition, respectively. Figure 4.39 and 4.40 compare the effect of heat treatment in each orientation (axial and tangential, respectively). In the as-received condition (Figure 4.37), a pronounced variation in the axial UTS is observed. The strength reaches a maximum at the forging edges, and drops nearer the centre. This would agree qualitatively with the microstructural observations of Figure 4.32 and 4.36. These showed that the volume fraction of retained β increases towards the forging edge, together with an increase in the secondary α particle density. Both of these factors would be expected to

increase strength [17][82]. The tangential UTS also shows some variation, although not as significant or as symmetrical as the axial tests. While the tangential specimens do exhibit a gradual increase in strength from the forging centre to the flash edge, the magnitude of this change is smaller than in the axial orientation. This may be due in part to the positioning of the tangential specimens. Since the trend in both cases is towards greater strength at the forging edge, and given that the outermost tangential specimen is further from the edge than the adjacent axial specimen, one would expect a lower value in the tangential orientation. However, given that the UTS in the tangential orientation is consistently higher than the axial UTS at all non-edge locations, this is unlikely to account for all of the difference. Furthermore, along the centre line the tangential UTS exhibits very little change at all. As discussed later in Section 4.6, a band of coarse secondary α was subsequently discovered approximately 15 mm from the forging edge. Within this region, it was found that the Vickers hardness could vary dramatically. There then exists the possibility that a small displacement between two adjacent tensile tests could lead to markedly different strengths. This might have explained the relatively low tangential UTS values in the as-received condition near the forging edge (Figure 4.37).

However, this conclusion seems questionable after considering the heat treated results. As can be seen in Figure 4.38, the axial UTS was significantly affected by heat treatment, reducing the variation across the forging. This would be consistent with the quantitative metallographic analysis, which identified greater microstructural homogeneity in the heat treated condition (see Figure 4.32 and 4.36). However, the tangential UTS seems relatively unaffected by heat treatment, and as a result would now appear to be the stronger orientation (see Figure 4.38). The lack of response to heat treatment in the tangential orientation is more clearly illustrated in Figure 4.40. This behaviour implies that the microstructural features modified by heat treatment (i.e. retained β volume fraction and secondary α particle density) have little effect on the tangential strength.

This seems surprising, given such high UTS values and the theory that metastable β alloys owe their high strength to precipitation of secondary α [17][6][82]. A more plausible explanation might be that above a certain strength level, the tensile properties become limited by another microstructural variable. Above this 'critical strength' then, the UTS may become independent of the retained β volume fraction and secondary α particle size. The identity of the unknown microstructural parameter (or parameters) is unclear at this stage. However, likely candidates could be the β grain morphology and/or the influence of α layers along these grain boundaries, since these appeared relatively unaffected by heat treatment. Texture effects may also play a role, but the exact cause remains unclear at this time.
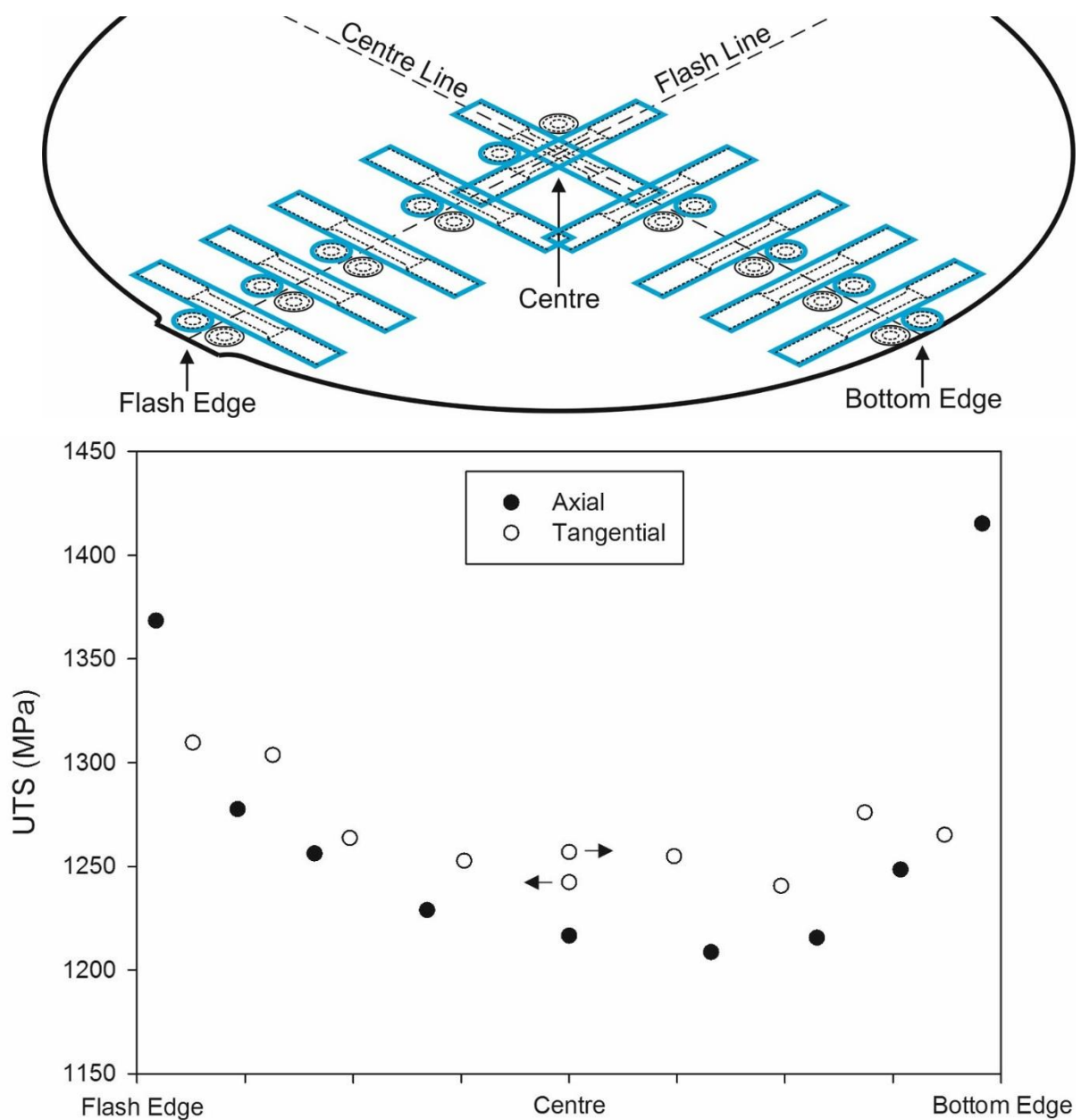
Figure 4.37: Forging 2, as-received condition. Comparison of UTS in the axial and tangential orientation (represented in the upper diagram by circles and rectangles, respectively). Horizontal arrows indicate whether a centre tangential value belongs to the flash line or centre line.

It could be argued that the relative insensitivity of tangential specimens to heat treatment is being overstated. As Figure 4.39 shows, the most significant change (reduction) in axial UTS was seen in the edge specimens. There is a sharp increase in strength observed in this region. Given that the tangential 'edge' specimens could not be as close to the edge, their initial strength is likely to be lower, and therefore the heat treatment would appear to have less effect. If the outermost axial tests are ignored, the influence of heat treatment in the axial orientation appears much less significant, and more akin to the tangential results.

Figure 4.38: Forging 2, heat treated condition. Comparison of UTS in the axial and tangential orientation (represented in the upper diagram by circles and rectangles, respectively). Horizontal arrows indicate whether a centre tangential value belongs to the flash line or centre line.

However, Figure 4.41 and 4.42 compare the heat treated UTS against the as-received material. If the heat treatment has little effect, these values should correlate well, since there will be relatively little difference between the two. As Figure 4.41 demonstrates, the axial values do exhibit a positive correlation, but not a very strong one, yielding an r^2 value of 0.392 when a trendline is fitted. Excluding the edge specimens narrows the range of as received strength to a level similar to that of the tangential specimens, but fails to improve the correlation (leaving a very similar r^2 value of 0.387).

Figure 4.39: Forging 2, axial orientation. Comparison of UTS in the as-received and heat treated condition.

On the other hand, the tangential data exhibits a very strong correlation ($r^2 = 0.900$), suggesting the heat treatment had very little effect. And for the purposes of comparison, exclusion of the edge specimens from the tangential analysis hardly alters the fitted line at all (see Figure 4.42). However, while it seems clear that unspecified microstructural variables are limiting the tangential UTS, closer examination of Figure 4.38 and 4.39 suggest that the axial UTS may also be influenced in some way. In these figures, the heat treated axial UTS still exhibits a gradual variation across the forging, which presents itself as the weak correlation observed in Figure 4.41.
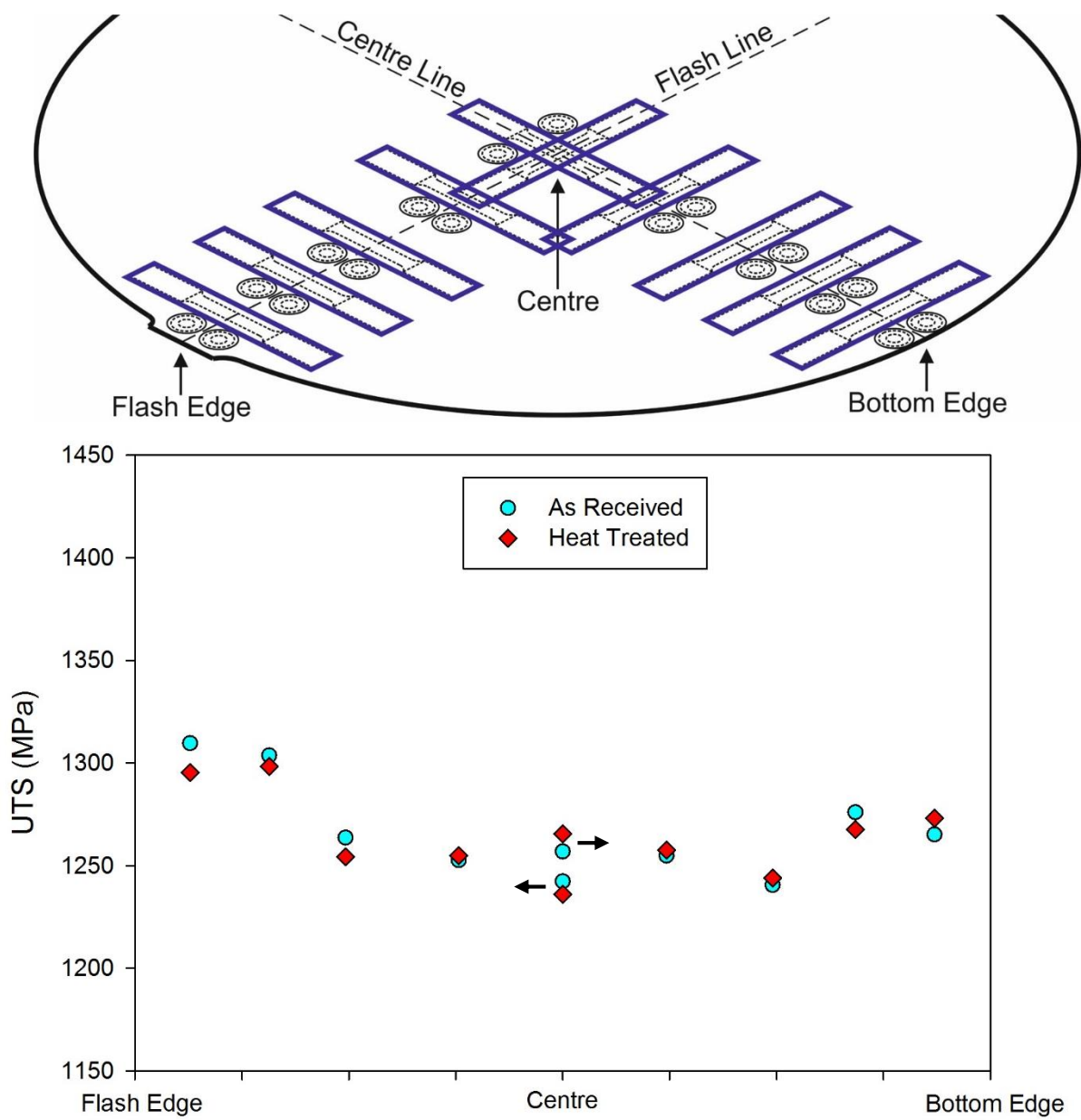
Figure 4.40: Forging 2, tangential orientation. Comparison of UTS in the as-received and heat treated condition. Horizontal arrows indicate whether a value belongs to the flash line or centre line.
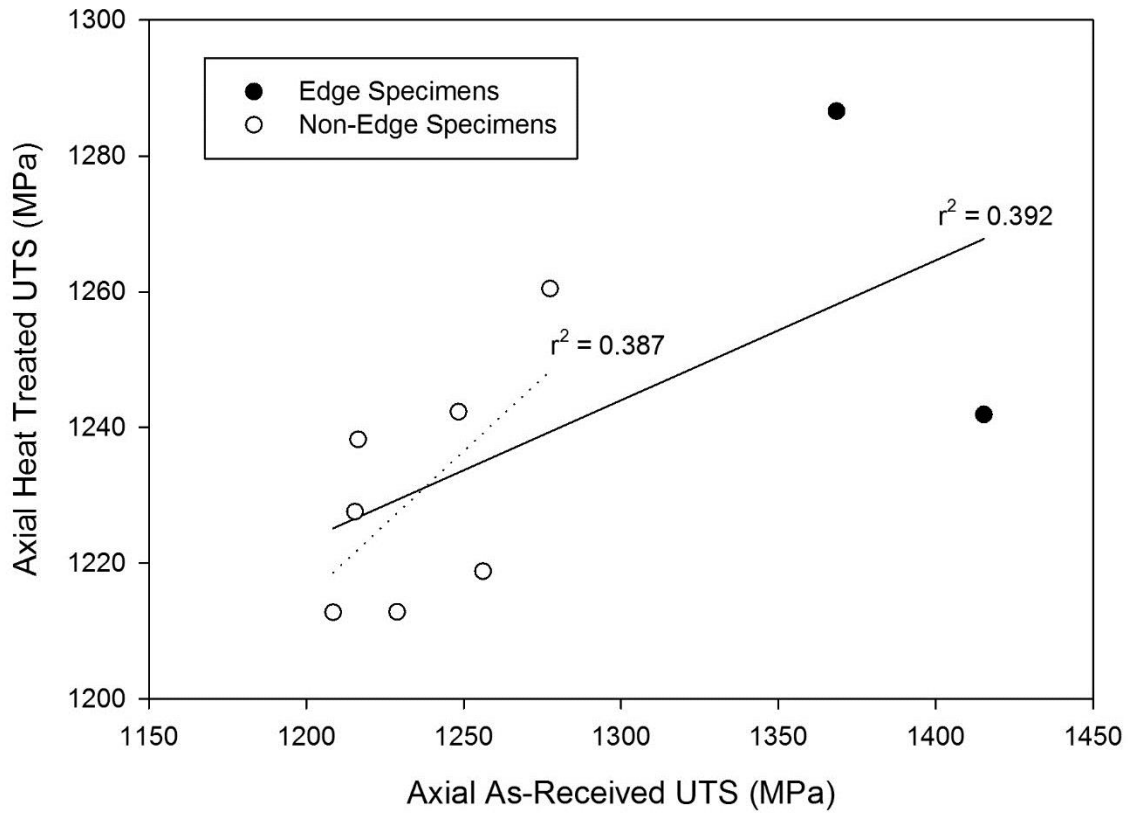
Figure 4.41: Correlation between heat treated and as-received UTS in the axial orientation. Solid line is fitted to all data points, whereas dotted line ignores edge specimens.
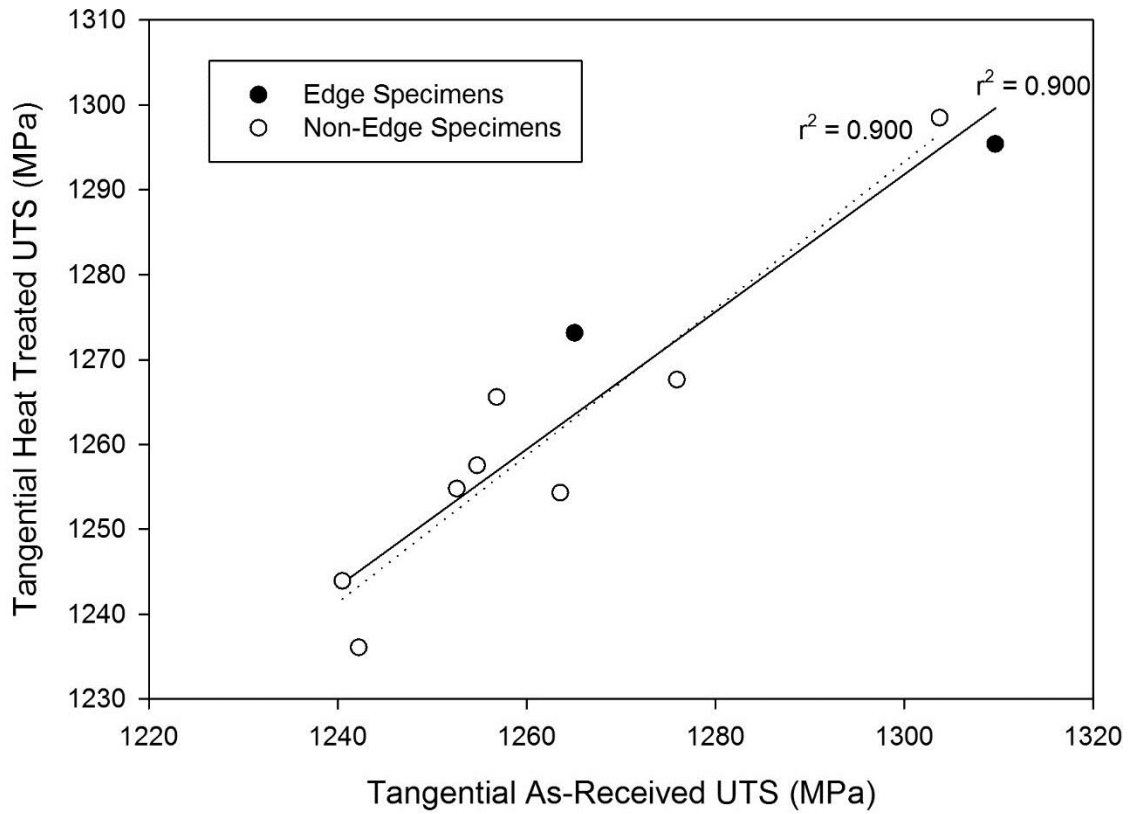
Figure 4.42: Correlation between heat treated and as-received UTS in the tangential orientation. Solid line is fitted to all data points, whereas dotted line ignores edge specimens.
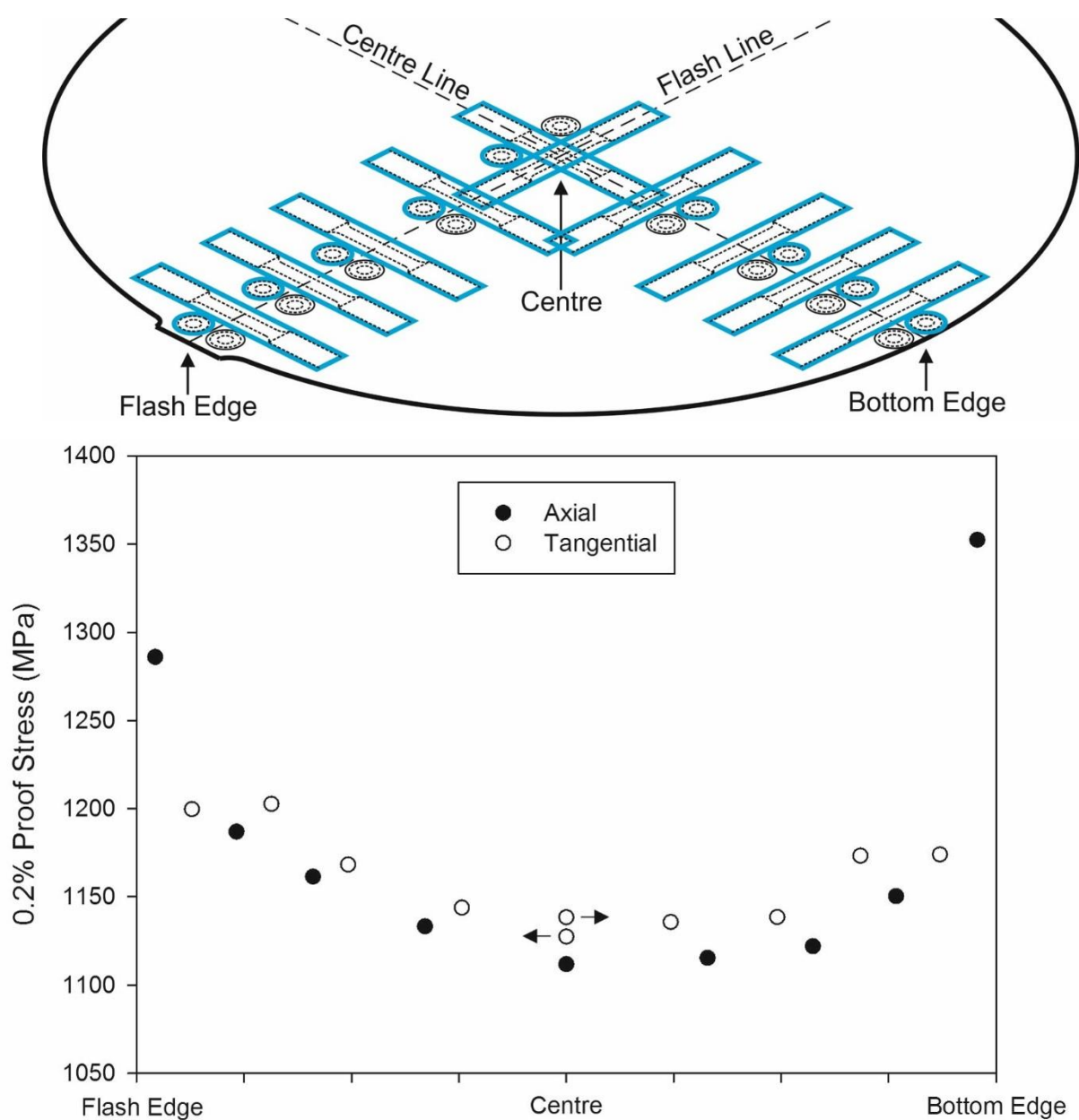
Figure 4.43: Forging 2, as-received condition. Comparison of proof stress in the axial and tangential orientation (represented in the upper diagram by circles and rectangles, respectively). Horizontal arrows indicate whether a centre tangential value belongs to the flash line or centre line.

Figure 4.43-4.47 illustrate the variation in proof stress across forging 2 in both orientations and material conditions. Figure 4.43 and 4.44 display very similar behaviour to that of the UTS (see Figure 4.37-4.38). The only obvious difference is that the values of proof stress are lower (as would be expected). However, another difference emerges in the axial orientation when comparing the effect of heat treatment. Ignoring the centre and edge specimens, it can be seen that the UTS was more heavily influenced by heat treatment on the flash line than the centre line (Figure 4.39). However, the reverse appears to be true with the axial proof stress (Figure 4.45). In either case, this is likely to be caused by changes in the work hardening behaviour. A

116
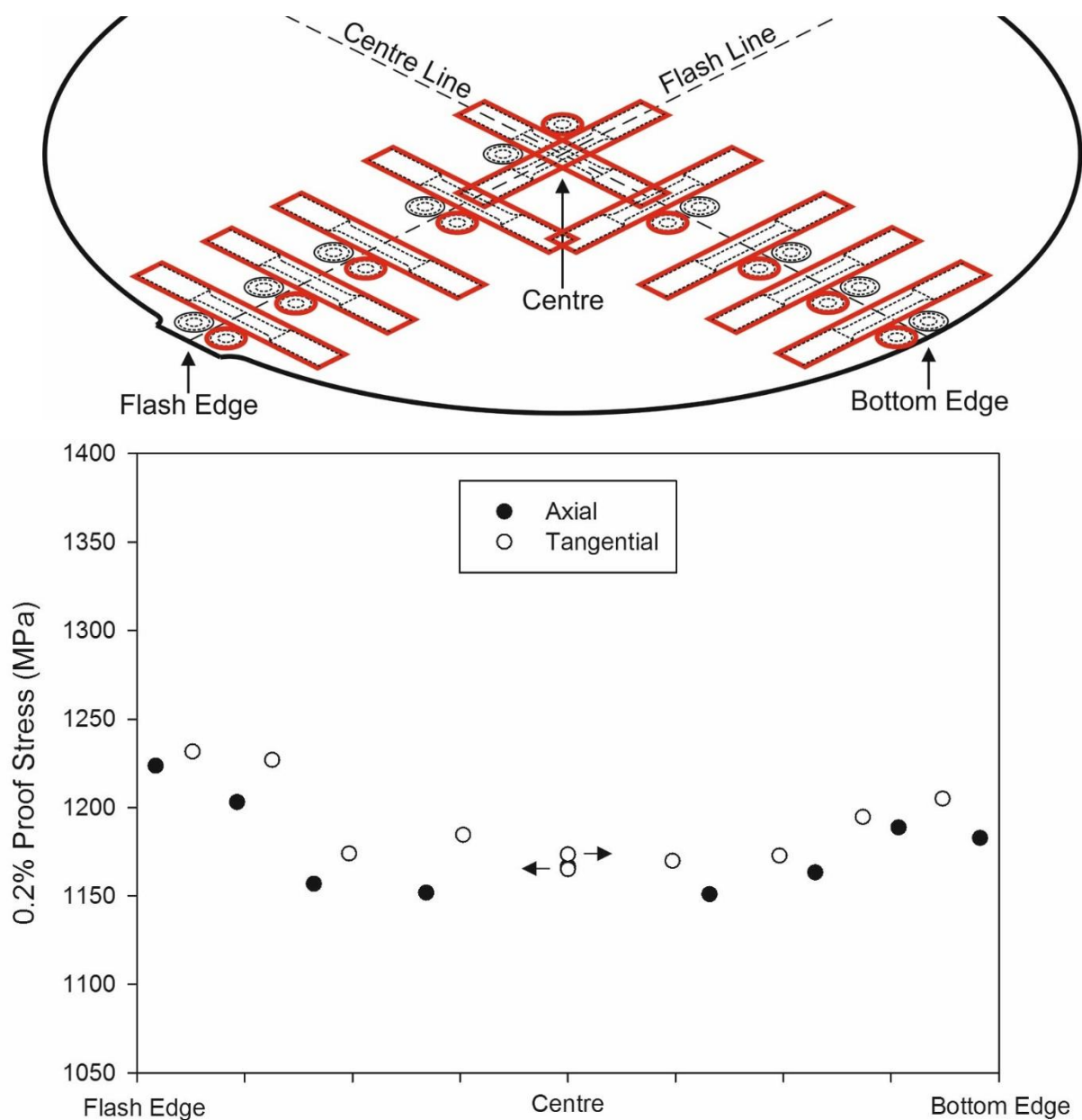
Figure 4.44: Forging 2, heat treated condition. Comparison of proof stress in the axial and tangential orientation (represented in the upper diagram by circles and rectangles, respectively). Horizontal arrows indicate whether a centre tangential value belongs to the flash line or centre line.

similar effect appears to exist in most of the tangential results. After observing little influence of heat treatment in the tangential UTS data (Figure 4.40), the tangential proof stress exhibits a very consistent increase in response to heat treatment (the exception being the mid-radius flash line specimen). Figure 4.47 presents part of the stress-strain curves for the quarter radius flash line tests in the tangential orientation. It can be seen that the maximum tensile stress is very similar, although the transition from elastic to plastic deformation becomes sharper in the heat treated condition. This will alter the point of intersection with the 0.2% offset line that defines the proof stress, while leaving the UTS relatively unaffected.
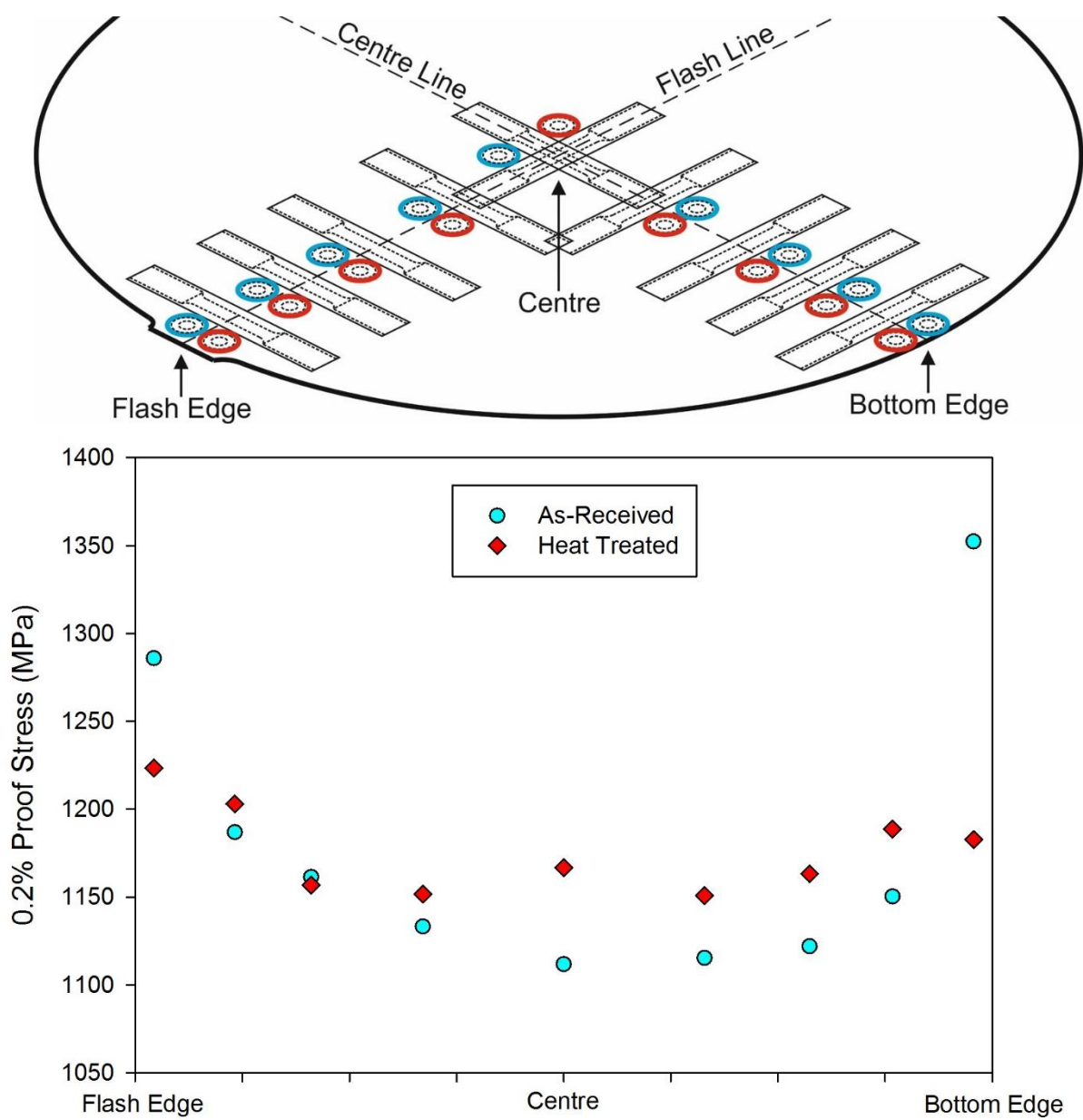
Figure 4.45: Forging 2, axial orientation. Comparison of proof stress in the as-received and heat treated condition.
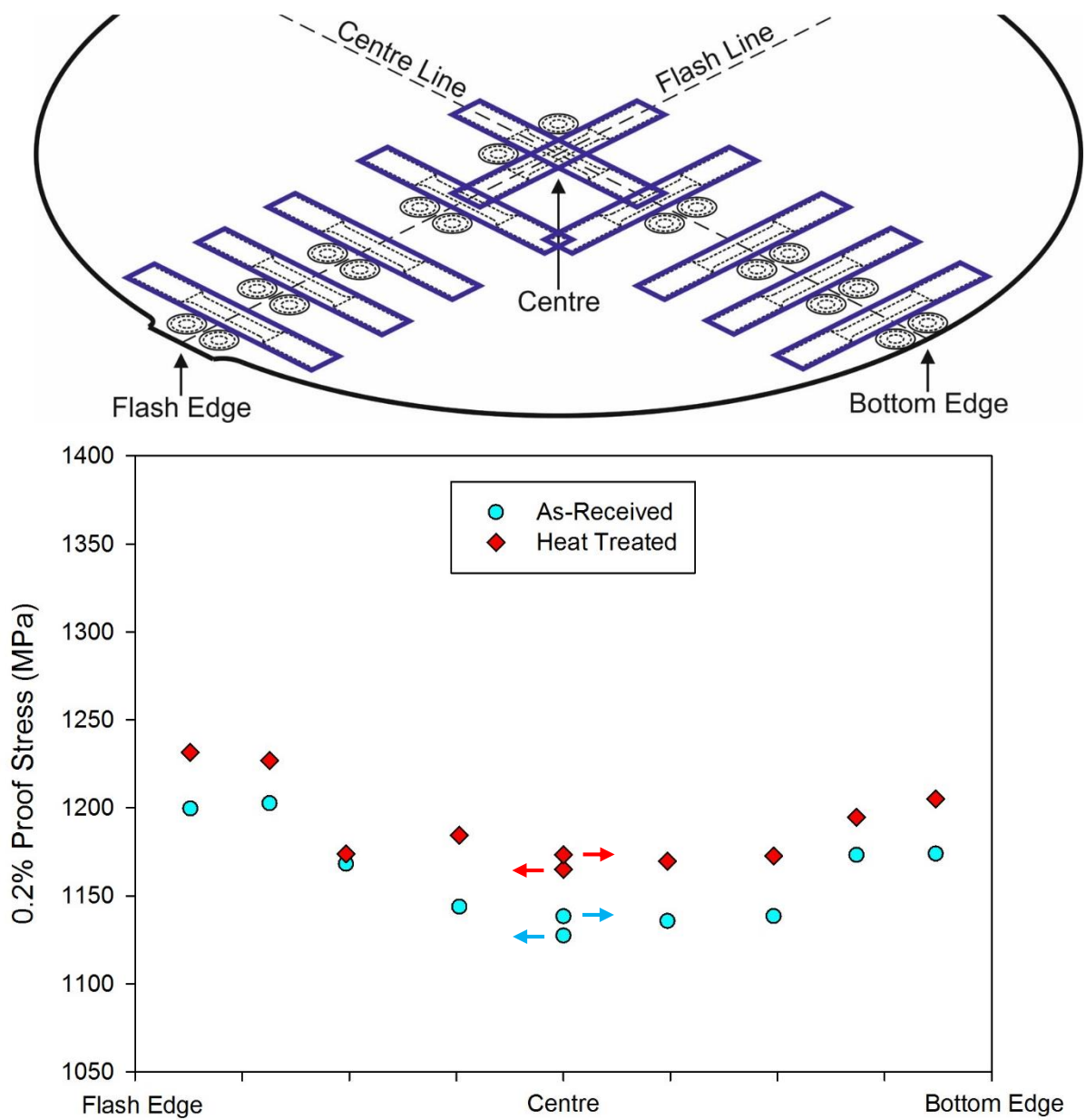
Figure 4.46: Forging 2, tangential orientation. Comparison of proof stress in the as-received and heat treated condition. Horizontal arrows indicate whether a value belongs to the flash line or centre line.
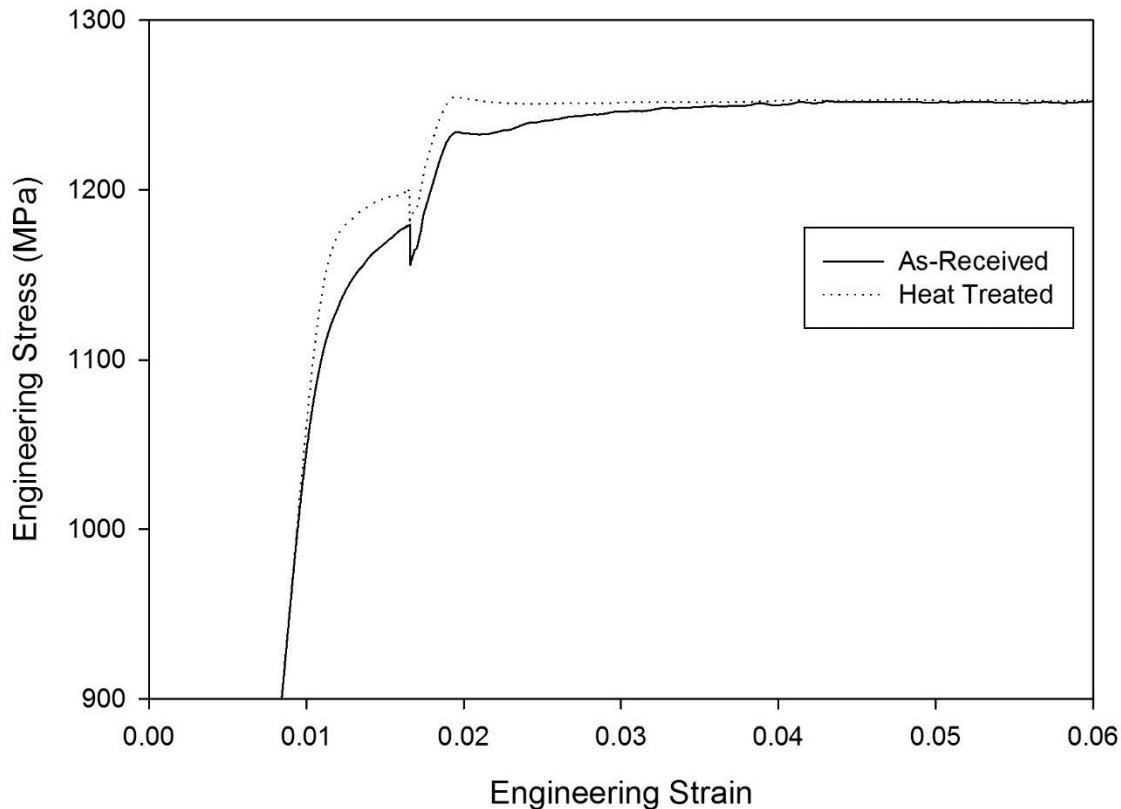
Figure 4.47: Section of the stress-strain curves for the quarter radius flash line specimens.

As mentioned earlier, the tangential UTS is probably limited by microstructural variables that prevent further increases in strength via heat treatment. However, since the proof stress is a measure of a materials resistance to plastic deformation it is likely to be less influenced by such limiting variables. Despite these differences though, the general trends in proof stress are still very similar to those of the UTS.

The elongation to failure data is presented in Figure 4.48-4.51. As with the UTS data, the as-received material exhibits a pronounced variation across the forging. However, unlike the UTS results, both the axial and tangential tests display this to a similar degree. It can be seen that the least ductile material is found at the forging edges, while the most ductile is located towards the forging centre. This is in broad agreement with the widely observed phenomenon whereby an alloy's ductility and strength are inversely related (see UTS values in Figure 4.37 and proof stress in Figure 4.43) [17]. It can also be seen that the axial orientation is consistently more ductile than the tangential orientation (see Figure 4.48). This would also agree with the microstructural observations of the β grain morphology and orientation. The longitudinal/working direction is widely reported to provide the best ductility, and would likely correspond to the axial direction in this forging [17][6]. Despite similar trends in both orientations, the response to heat treatment appears rather different, much like the UTS data. As might be expected from the reduction in UTS, the axial elongation to failure generally improves in the heat treated condition. However, the consistency is still relatively low, resulting

120

in considerable fluctuation (see Figure 4.49 and 4.50). It has been noted by others that the ductility of β alloys tends to exhibit greater scatter than α and α+β alloys, which may help explain the observed variation between heat treated specimens [17]. As with the UTS results, the % elongation in the tangential orientation appeared less responsive to heat treatment (see Figure 4.49 and 4.51). It is likely that the tangential ductility is relatively unaffected by the heat treatment because fracture properties of high strength β alloys are heavily influenced by the extent of grain boundary α and shape/orientation of the β grains [6].

Since these microstructural variables were less affected by heat treatment, they may have proved to be a limiting factor in the tangential orientation. Given that the axial ductility was already superior to the tangential ductility in the as-received condition, the improvement conferred to the axial specimens by heat treatment only exacerbated the disparity between the two orientations at the forging edge (see Figure 4.49). This is unfortunate considering the component wall is situated very close to this location (see Figure 4.3). Unlike the UTS data, the axial ductility in the heat treated condition does not appear to retain any noticeable trend. However, this could be due to the degree of scatter in the data, requiring a more comprehensive study to ascertain how the β grain morphology might exert influence.
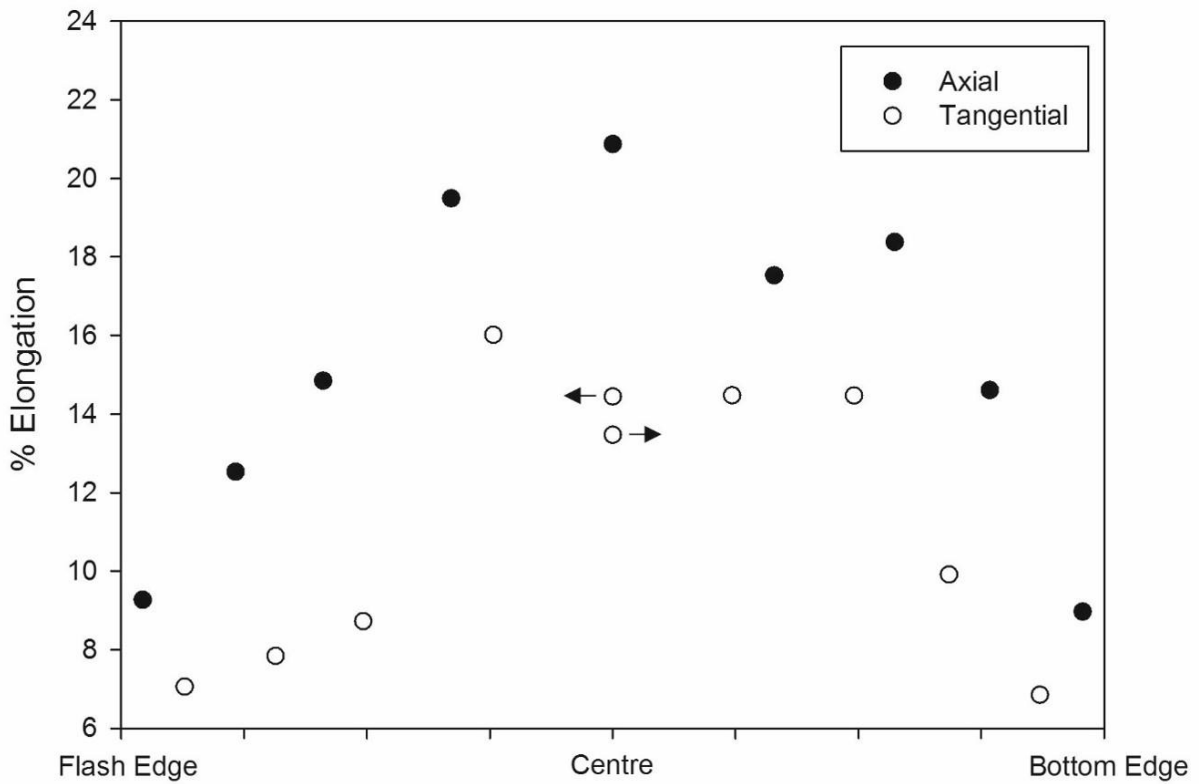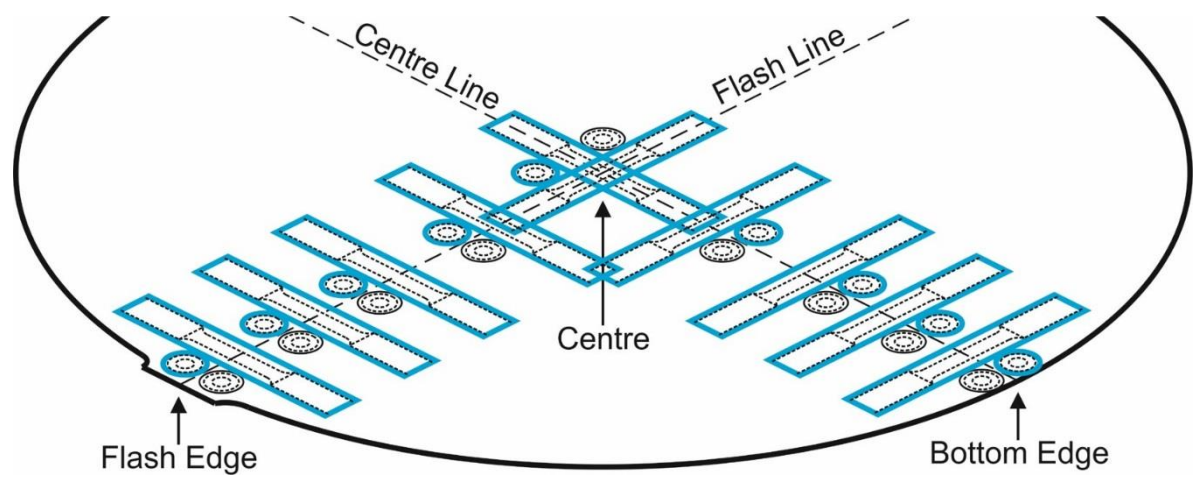
Figure 4.48: Forging 2, as-received condition. Comparison of % elongation in the axial and tangential orientation (represented in the upper diagram by circles and rectangles, respectively). Horizontal arrows indicate whether a centre tangential value belongs to the flash line or centre line.
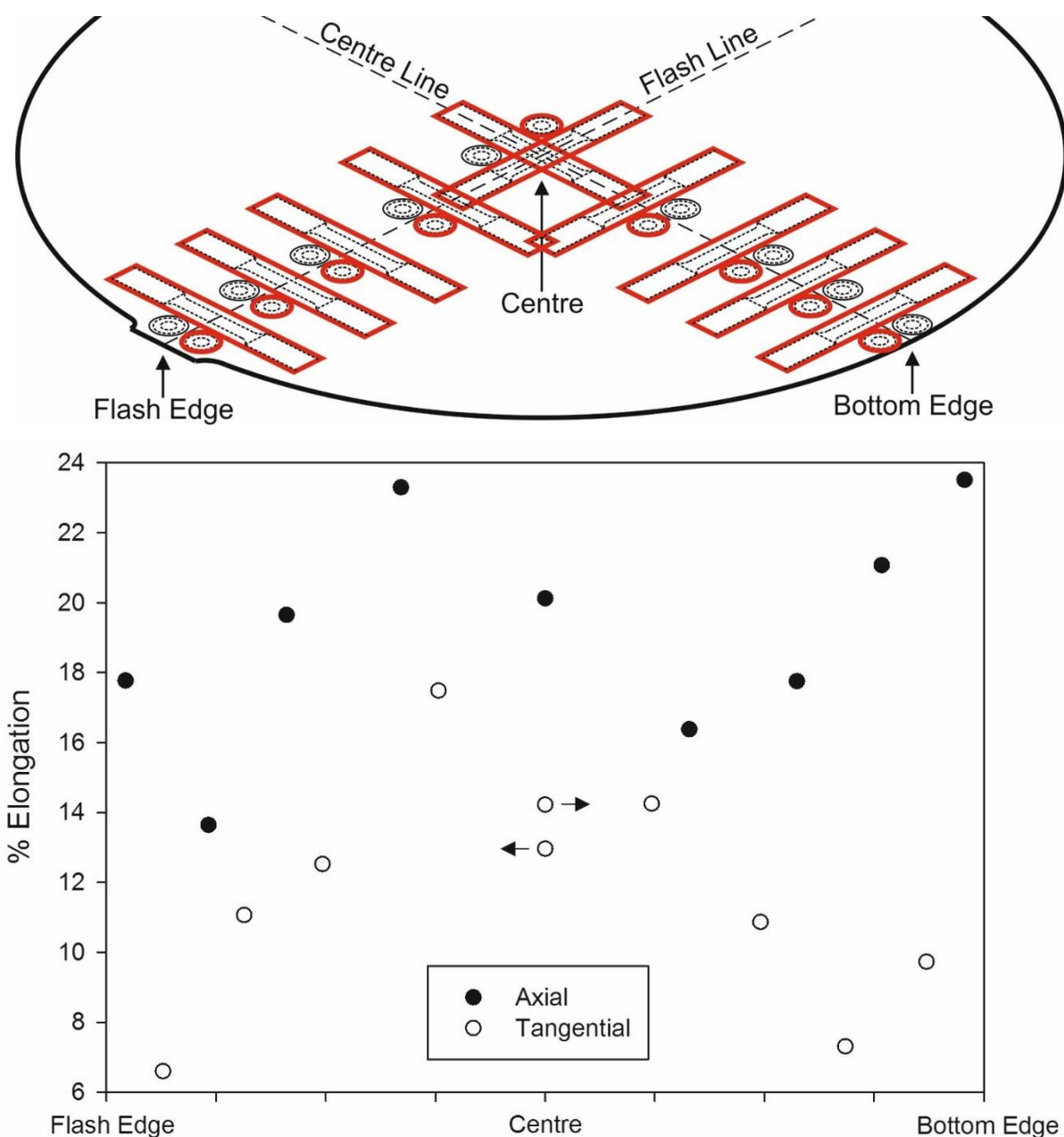
Figure 4.49: Forging 2, heat treated condition. Comparison of % elongation in the axial and tangential orientation (represented in the upper diagram by circles and rectangles, respectively). Horizontal arrows indicate whether a centre tangential value belongs to the flash line or centre line.
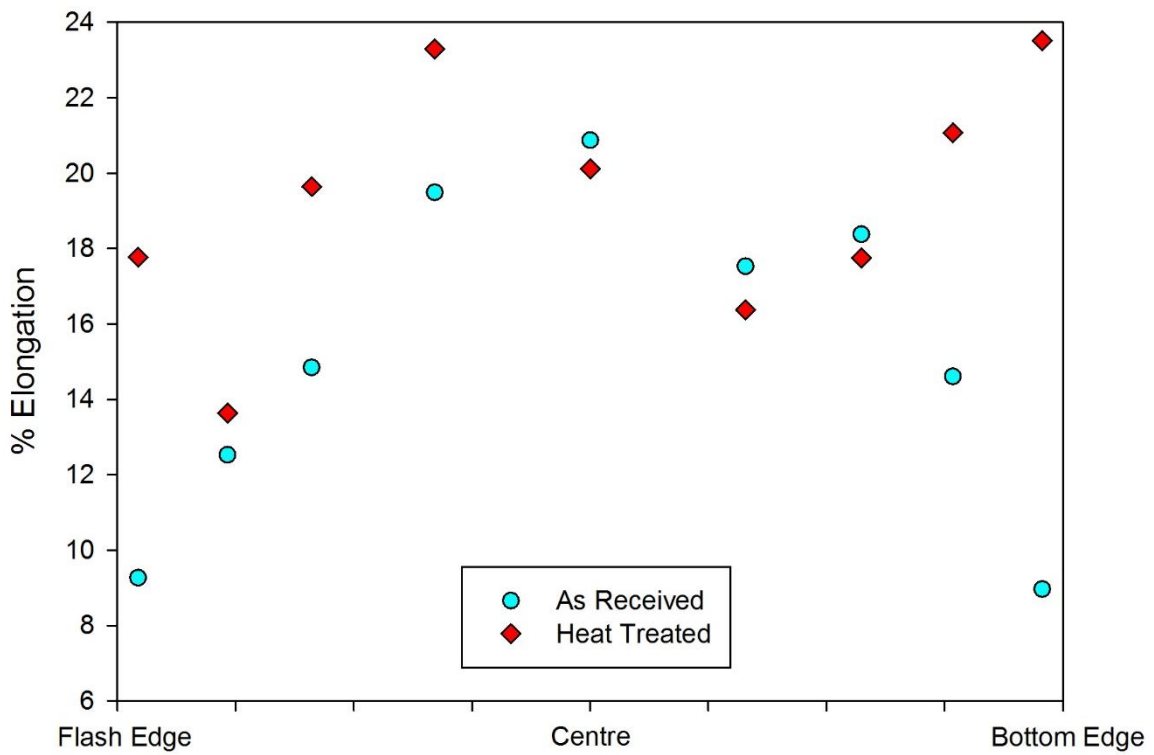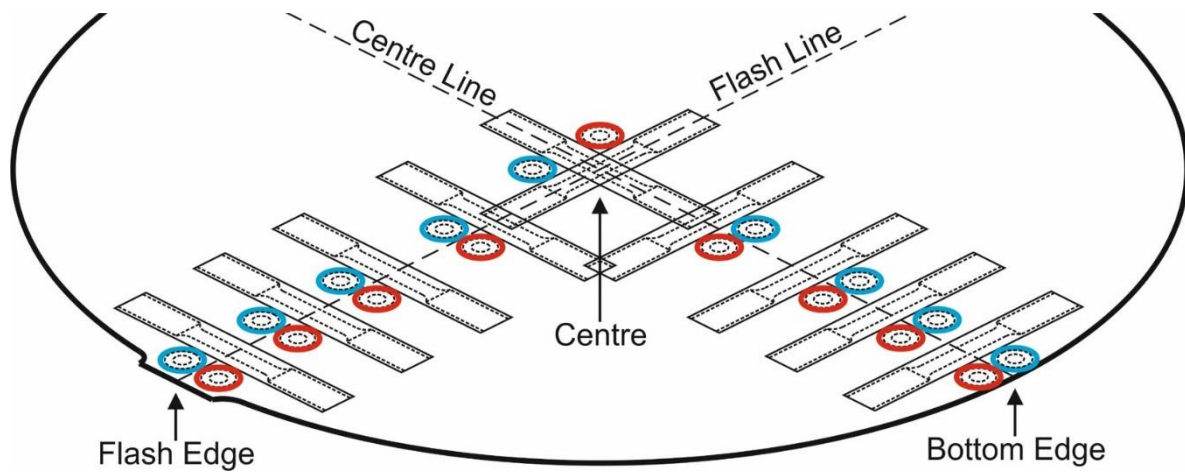
Figure 4.50: Forging 2, axial orientation. Comparison of % elongation in the as-received and heat treated condition.
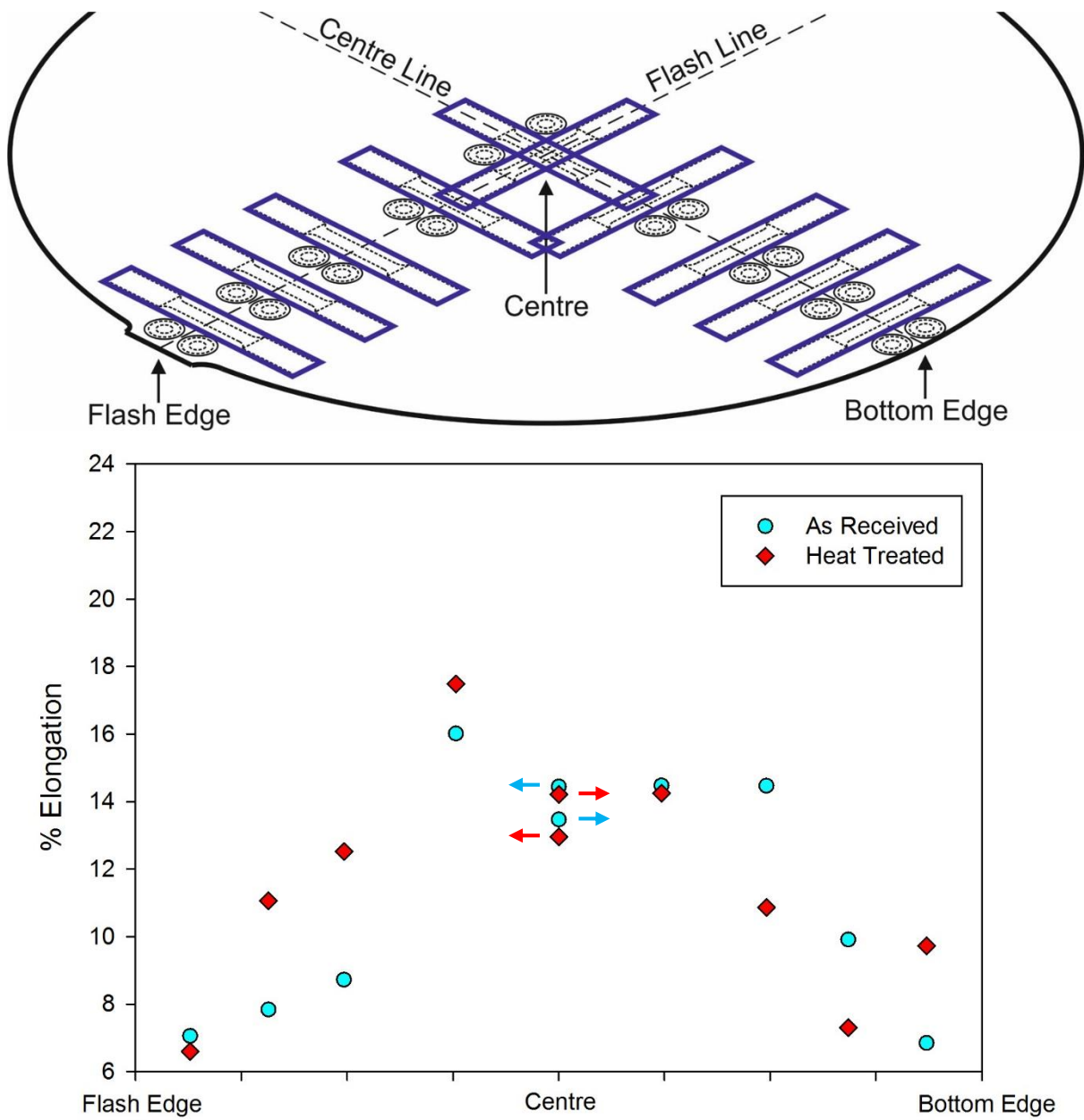
Figure 4.51: Forging 2, tangential orientation. Comparison of % elongation in the as-received and heat treated condition. Horizontal arrows indicate whether a value belongs to the flash line or centre line.

4.5.2 Hardness Testing

In addition to tensile testing, the mechanical properties of forging 2 were also assessed through the acquisition of hardness data. The specimen faces that were measured are illustrated in Figure 4.52. The axial hardness is taken as that recorded on the faces perpendicular to the forging/cylinder axis (i.e. 'top' faces shaded grey in the diagram). The tangential faces are those oriented perpendicular to the tangential directions of the forging/cylinder (i.e. the 'vertical' faces shaded grey in the diagram). The Vickers hardness of each specimen surface was computed from the mean of 25 indents. For details on settings see Section 3.4.

As the plot in Figure 4.52 illustrates, the correlation between tangential and axial hardness is relatively strong (r^2 = 0.922). The similarity between the two orientations may be due to the three dimensional nature of the deformation under the indenter tip. Furthermore, hardness testing itself is a measure of a materials resistance to plastic deformation, rather than complete fracture. Therefore, the influence of β grain shape/orientation and grain boundary α may be less significant under hardness testing, producing more consistent results between the two orientations. In order to simplify matters, it was decided to focus analysis upon the tangential orientation since this is shared by the macro-slices of forging 1, allowing comparison between the two.

Figure 4.53 presents the tangential hardness data of forging 2 in the as-received and heat treated condition. It can be seen that trends similar to those observed in the UTS data are present. In the as-received condition, the hardest material is located at the forging edge, with lower values recorded near the forging centre. There is also some degree of asymmetry in the as-received condition. The hardness is greater at the bottom edge than the flash edge, not unlike the axial UTS results. However, this disparity appears more significant in the hardness data. There is also a more consistent trend in the hardness data across the flash line when compared to the centre line. The latter exhibits a much larger 'jump' between the outer two specimens. The heat treatment appears to remove much of this variation, producing a more uniform set of values across the forging. It is difficult to tell whether any residual trends remain given the narrower data range of the heat treated results. Nevertheless, by comparing both conditions, it seems clear that the retained β volume fraction and secondary α particle density significantly influenced the Vickers hardness.

Given the empirical relationship between strength and hardness, it is possible to carry out a more detailed examination of the variation in mechanical properties of forging 1 by creating 'hardness maps' of the macro-slices (see Figure 4.54-4.57) [103]. The creation of such large, high resolution maps was made possible with the use of a Durascan-70 automated hardness tester. This facilitated the (relatively) rapid measurement of many thousands of indents for each plot. However, as explained in Section 3.4 this equipment only became available towards the

end of the project, and consequently the hardness maps were produced after other mechanical testing was complete. This is why the unexpected findings of the hardness maps (see below) were not taken into account during experimental planning of the tensile tests. Neither had the limited manual testing of microscopy specimens indicated such localised variation in strength. Later, to ensure consistency, all manual measurements of the microscopy specimens were disregarded and testing was repeated with the Durascan. Only this data is presented in this thesis. For further details on settings see Section 3.4. The layout of indents on the centre line and flash line slices took the form of a rectilinear grid, with a 2 mm spacing in the radial direction, and a 4 mm spacing in the axial direction. This represented a compromise between speed and accuracy. Since the most significant variation had been observed in the radial direction, the resolution in this direction took priority. Given that the centre line and flash line represent the two radial axes of the quarter cross-section, the indents here were placed in a 2 mm square grid. Due to the inherent scatter in hardness data, the results were smoothed using a pseudo-four point moving average. Each point on a colour contour plot was positioned equidistant between its four nearest indents and calculated from the mean of these values.

Figure 4.54 and 4.55 present the hardness maps for the centre line and flash line. As expected from earlier testing, there is a general increase in hardness towards the forging edge, and a strong directionality to the observed variation. Perhaps most striking though, is the presence of a narrow band of soft material situated approximately 15-20 mm from the edge of both slices. The magnitude of this abrupt drop in hardness is more clearly illustrated by the profile plots beneath the maps. These not only show the general trend, but also that the magnitude of the fluctuation within the soft band is on the order of the total variation seen across the forging. The quarter cross-section (Figure 4.56) confirms that this band extends around the forging between the two slices, maintaining a constant displacement from the edge. This is more clearly illustrated by the 3D stitch of Figure 4.54-4.56 (see Figure 4.57).

Comparison of the hardness maps with the macro-etches (Figure 4.8-4.11) now reveals the significance of some of the observations made previously. The light band near the edge of the macro-etches would appear to coincide with the soft band observed in the hardness maps. In the centre line macro-etch (Figure 4.8) the diagonal boundary between light and dark regions seems to correlate with an increase in the hardness (see Figure 4.54). It appears to be a similar case for the light/dark boundary in the quarter cross-section (compare Figure 4.10-4.11 with Figure 4.56-4.57). Although such changes in colour/shade of the macrostructure provide the naked eye with an indication of microstructural variation, it does not directly explain the mechanism by which the mechanical properties have been altered. However, it does provide guidance on where to focus the attention of microstructural characterisation techniques in order to identify the underlying cause. The light/dark boundary observed in the centre line and quarter cross-section is also present in the flash line (Figure 4.9) but the hardness map does not appear

to show a corresponding transition (Figure 4.55). However, it should be noted that the hardness of the flash line slice was generally higher than that of the centre line and quarter cross-section. It is possible that other, less visible microstructural changes masked such a boundary.
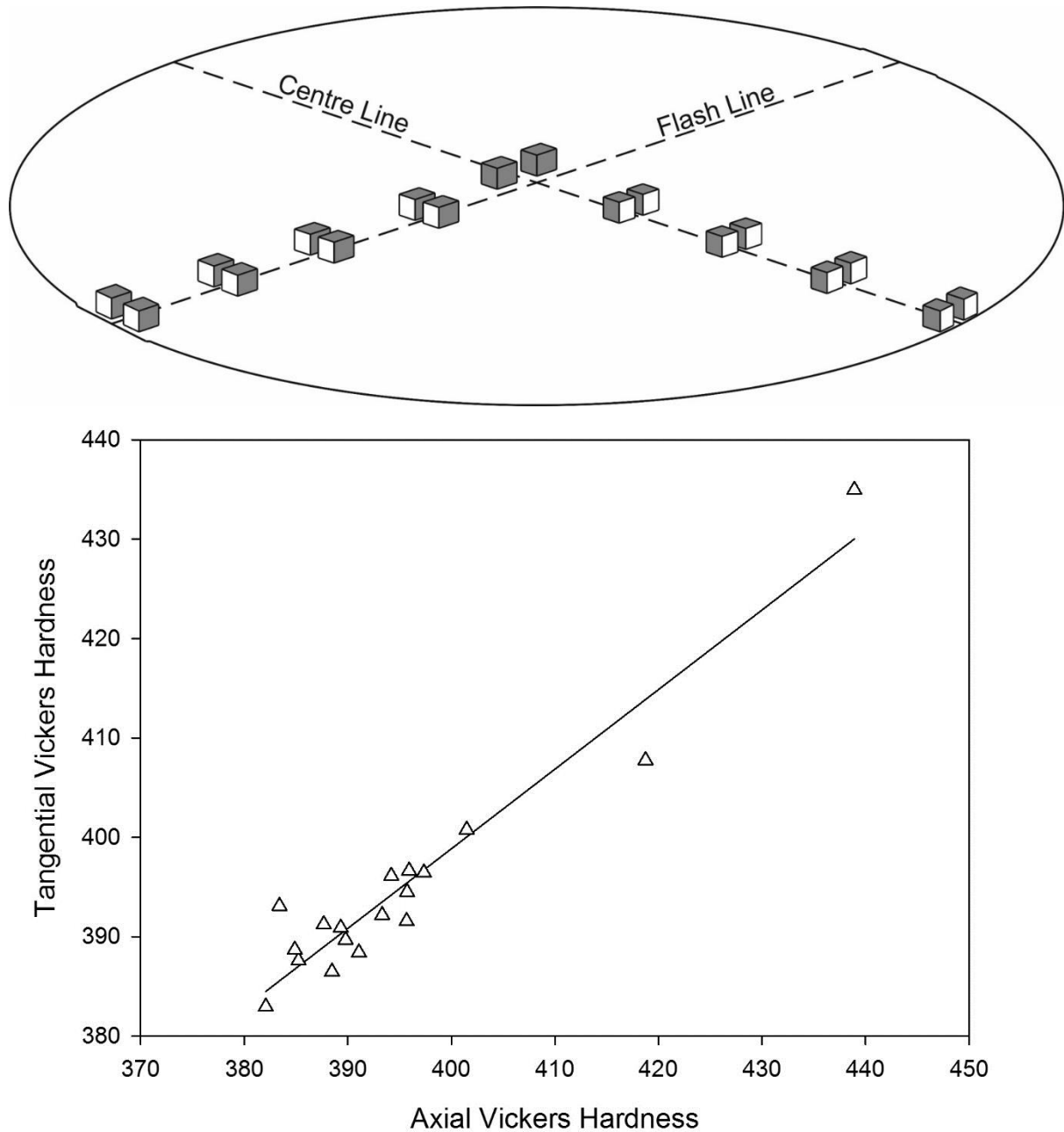
Figure 4.52: Correlation between tangential and axial Vickers hardness ($r^2 = 0.922$). The specimen faces measured (grey in the upper diagram) are defined by the direction they are perpendicular to.
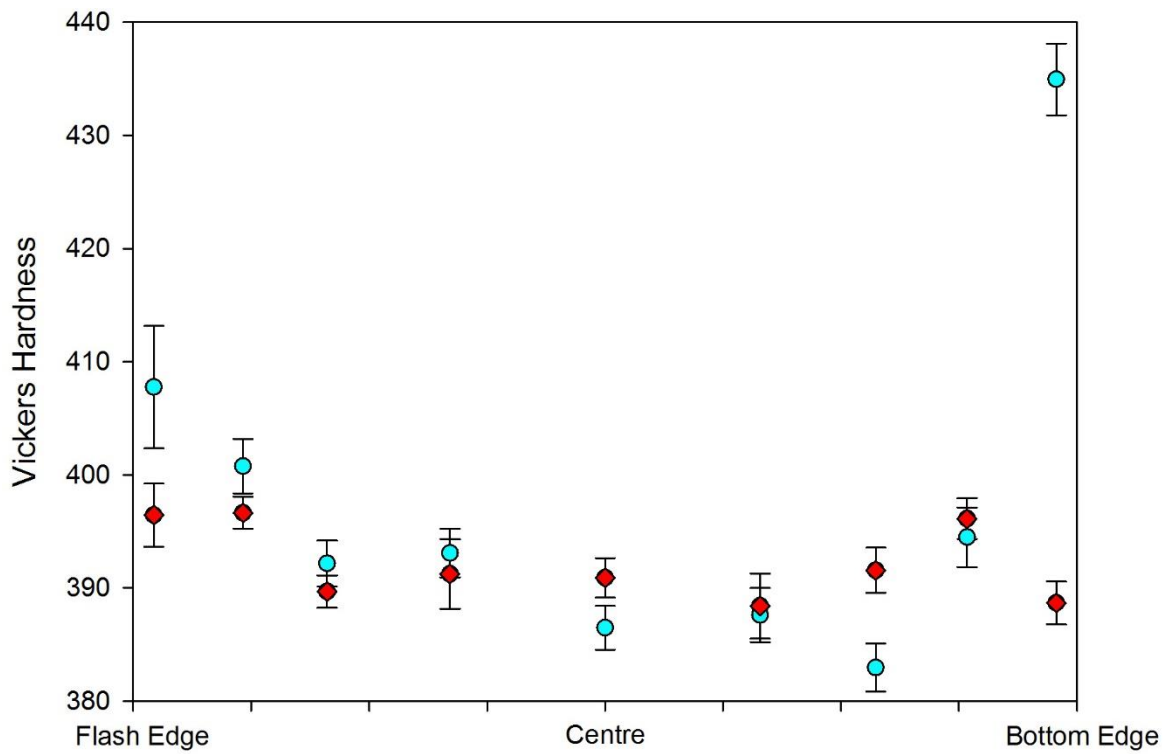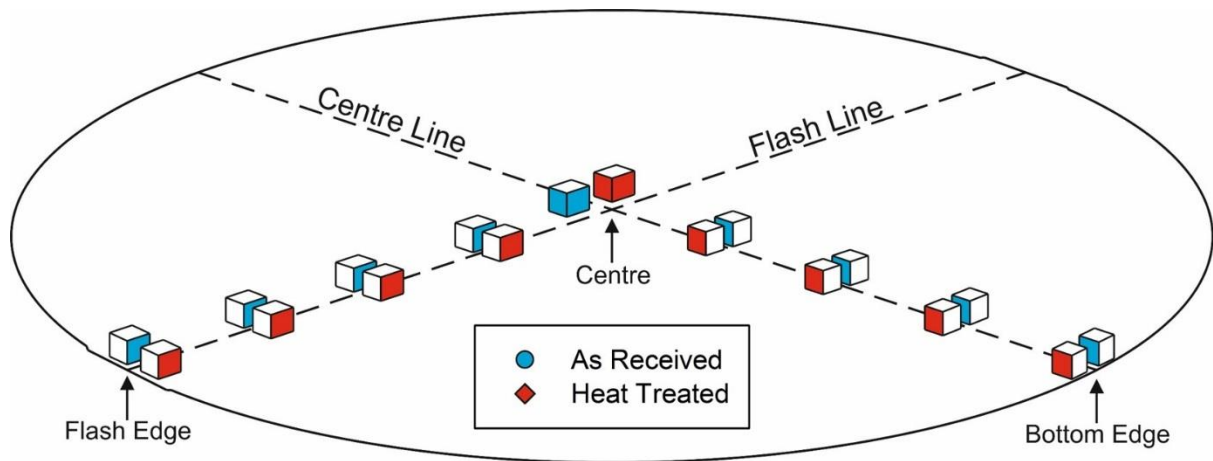
Figure 4.53: Tangential Vickers hardness across forging 2 in the as-received (blue) and heat treated (red) condition. Centre values are the mean of both central orthogonal faces. Error bars illustrate the 95% confidence limit.
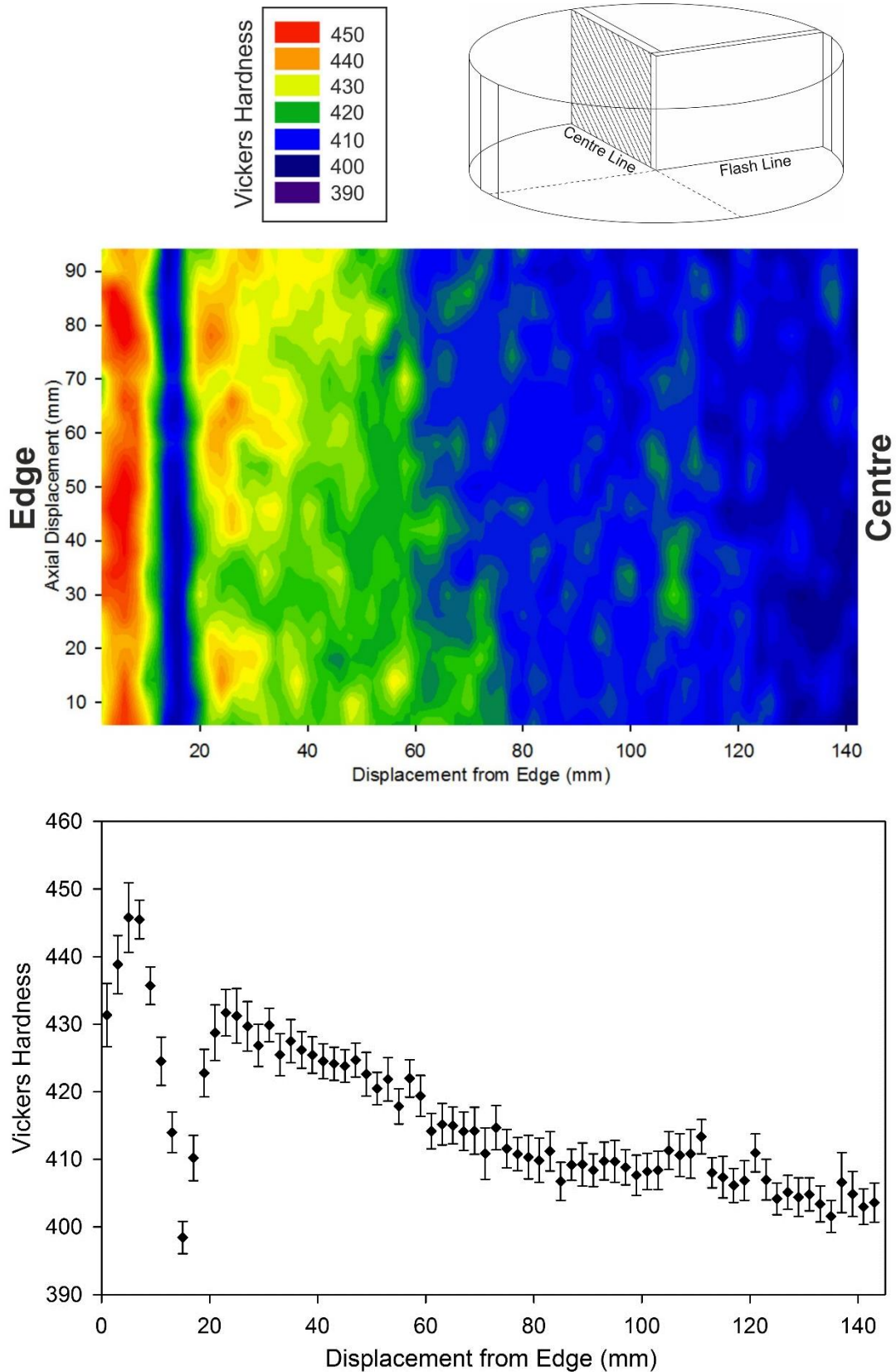
Figure 4.54: Forging 1, hardness map of the centre line above a profile plot of the same area. Note, the hardness scale is not equivalent to Figure 4.55 (opposite page). Error bars illustrate the 95% confidence limit.
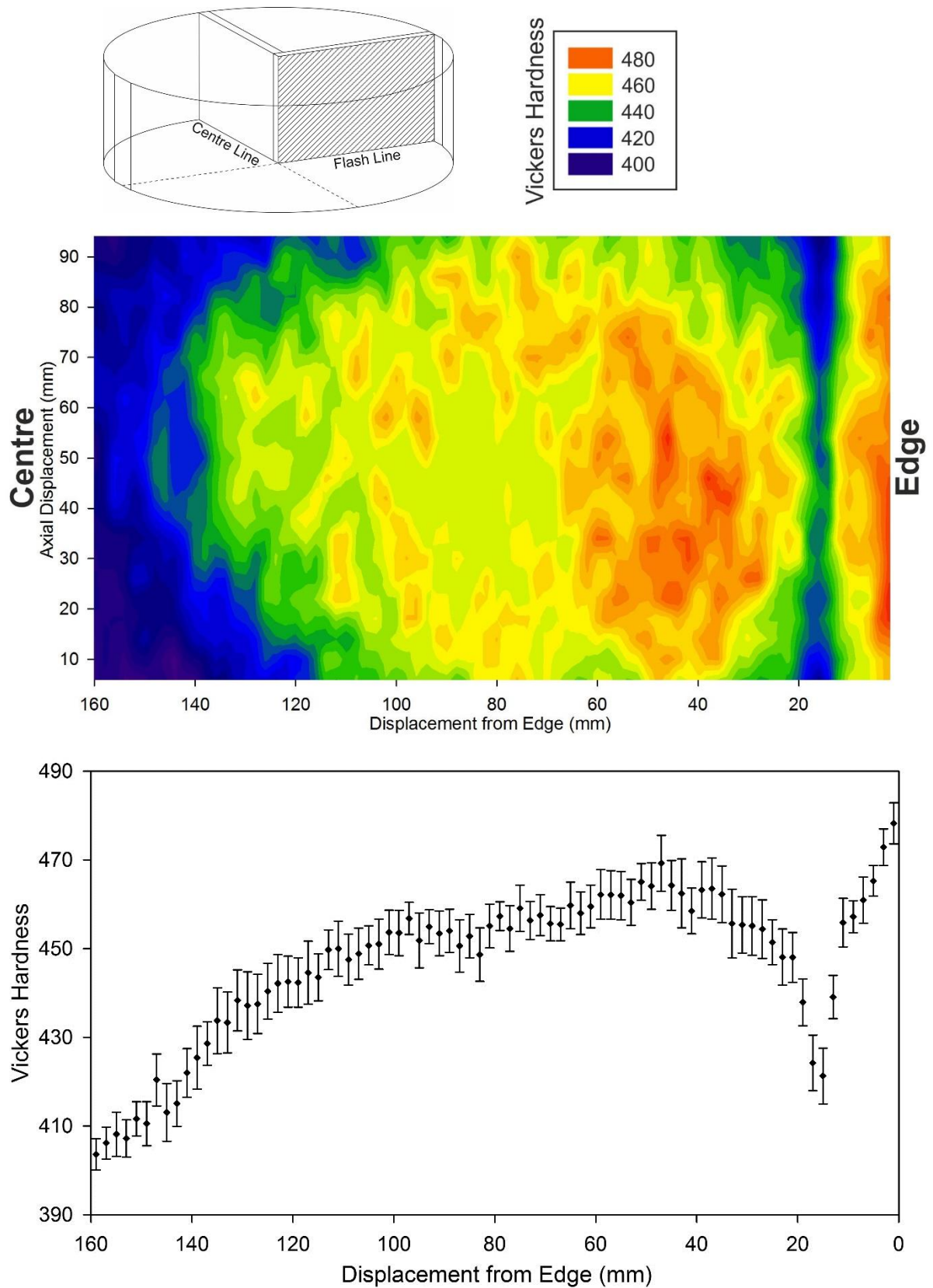
Figure 4.55: Forging 1, hardness map of the flash line above a profile plot of the same area. Note the hardness scale is not equivalent to Figure 4.54 (previous page). Error bars illustrate the 95% confidence limit.
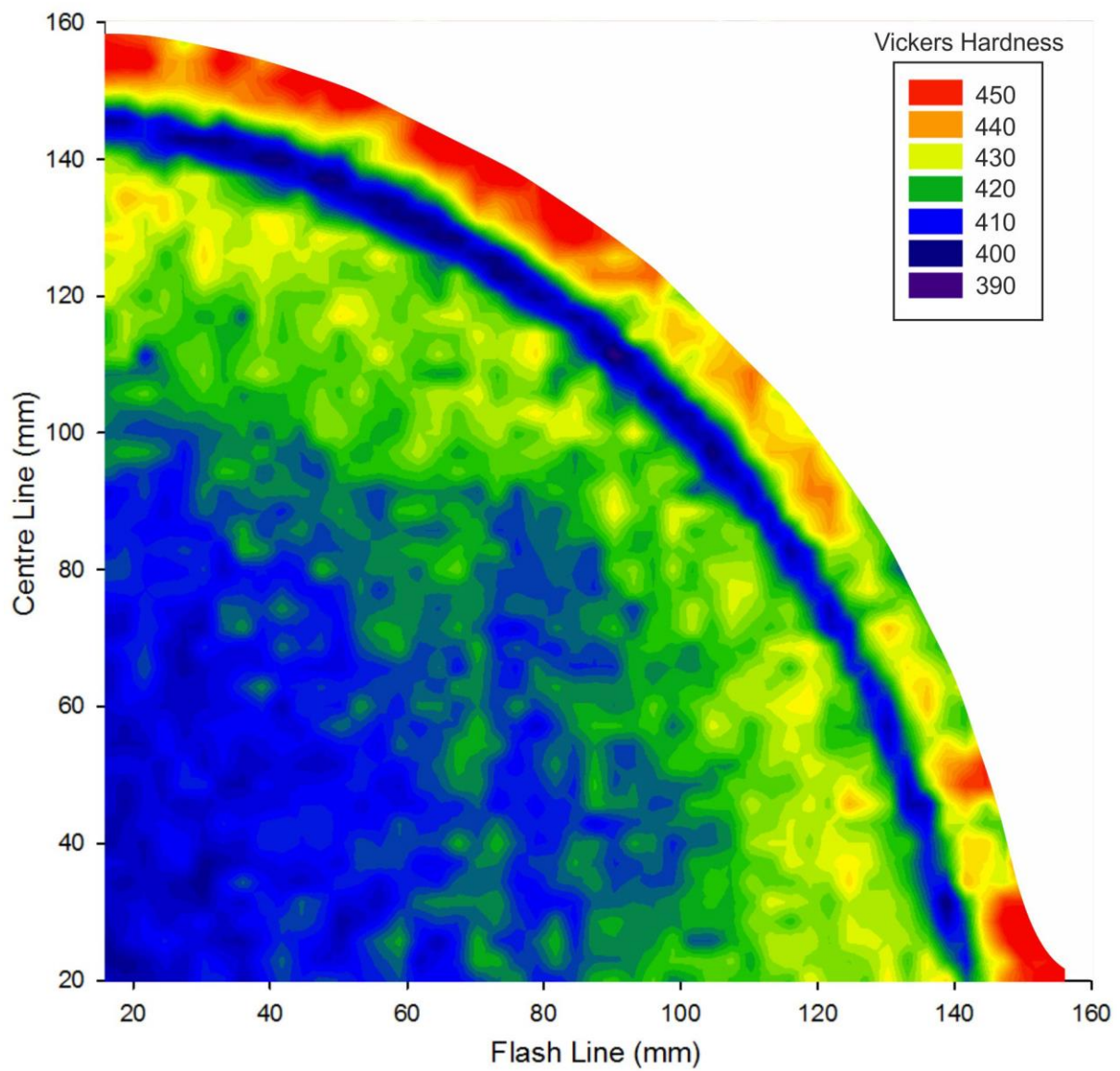
Figure 4.56: Hardness map of the quarter cross-section. Note that the hardness scale is equivalent to Figure 4.54, but not Figure 4.55.
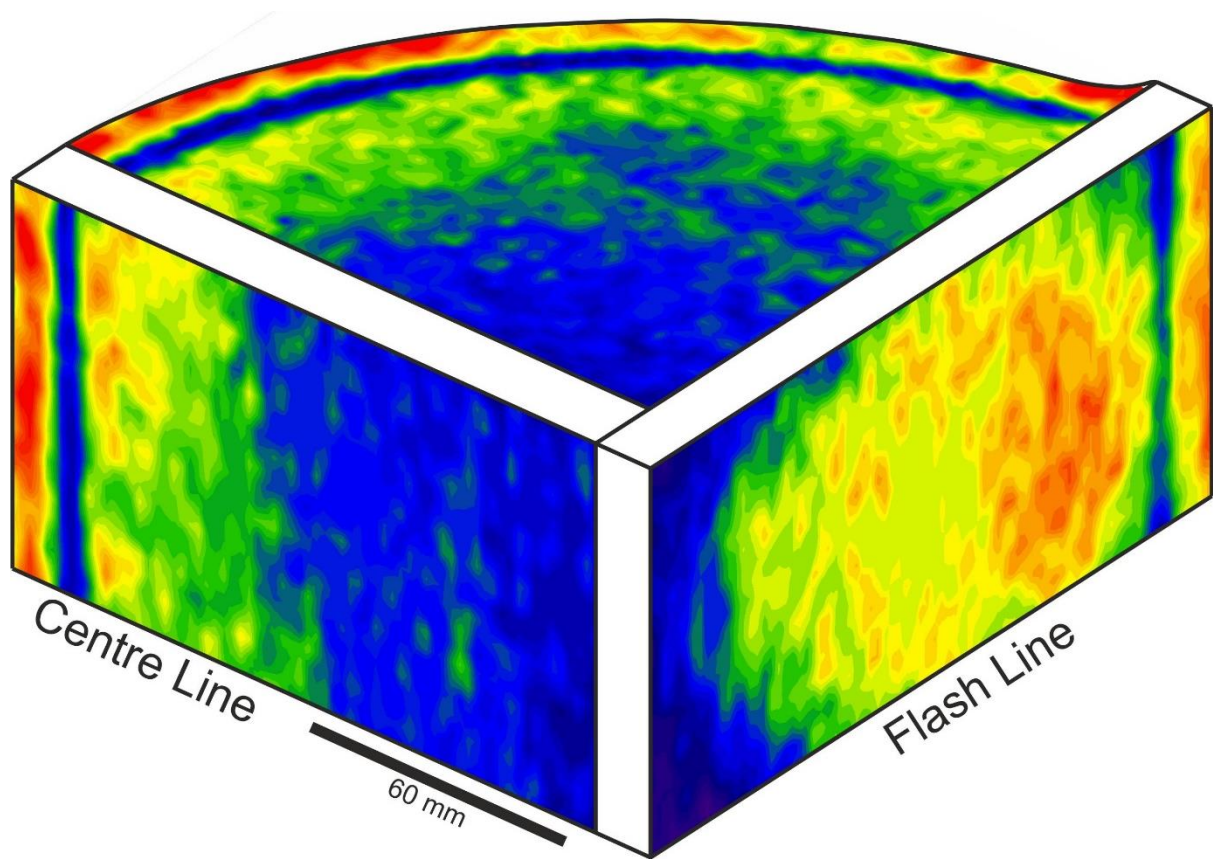
Figure 4.57: Three dimensional representation of the 2D hardness maps in Figures 4.54-4.56. For the colour scale of each map, refer to the respective 2D figure. Note that while these are equivalent for the centre line and top surface, the flash line covers a wider range.

As with forging 2, the hardness values taken from the microscopy specimens of forging 1 were based upon a 5×5 grid of indents placed on each specimen. As Figure 4.58 demonstrates, the 'columns' of this data could be averaged in order to look for radial variation across them. Figure 4.59 and 4.60 compare this data (referred to as 'sample breakdown') with that of the macro-slices. The mean of each specimen displays the same general trend of increasing hardness towards the forging edge, although the mid-radius flash line specimen deviates from the macro-slice considerably. The edge specimens also exhibit significant variability relative to the others. Although the centre line edge specimen may have just missed the 'soft band' it appears to have overlapped another decline in hardness next to the forging edge. However, the flash line edge specimen does appear to have covered some of the soft band. Elsewhere, the 'column data' is more tightly clustered around the sample mean, albeit there still appear to be some trends of smaller magnitude across the flash line specimens.

The large discrepancy between the mid-radius flash line specimen and the macro-slice may be partially explained when considering the raw data of the hardness map (Figure 4.61). Without the four point averaging, it can be seen that the central region exhibits a slight reduction in hardness. This may account for some of the discrepancy, although there is still some difference between the map values and the microscopy specimen. Another factor could be the displacement between the surface of the macro-slice and microscopy specimen. As Figure 4.62 illustrates, the strain distribution within the flash line may be higher than elsewhere in the forging, and possibly less uniform [104]. If this is the case, it may have exacerbated the deviation between the macro-slice and microscopy specimens. It might also account for the generally higher hardness of the flash line relative to the centre line and quarter cross-section.
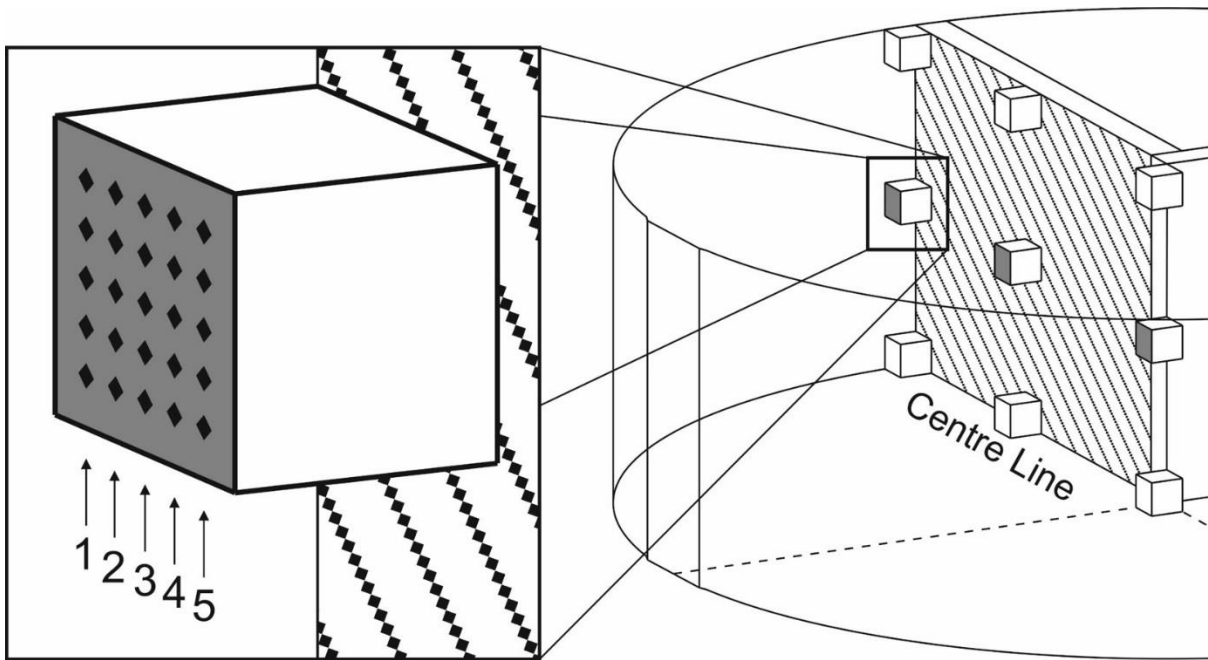
Figure 4.58: Layout of Vickers hardness indents (not to scale). Each grid can be divided into columns and averaged to examine radial variation. A similar procedure can be applied to the primary and secondary α measurements.
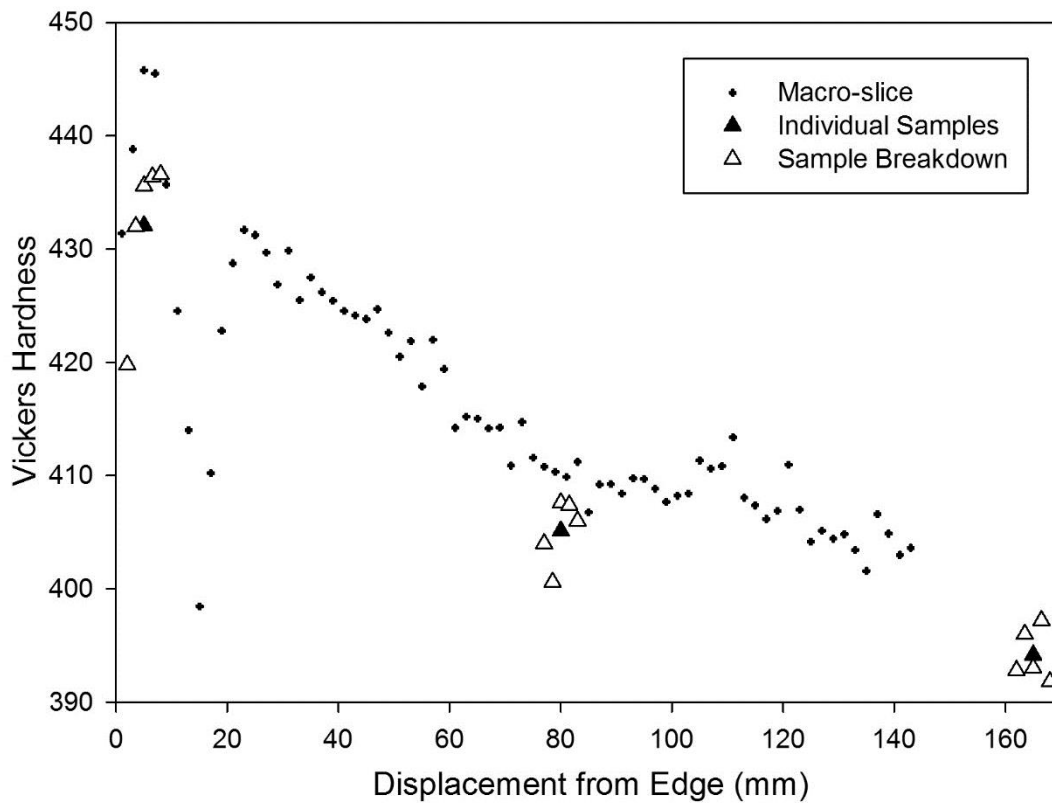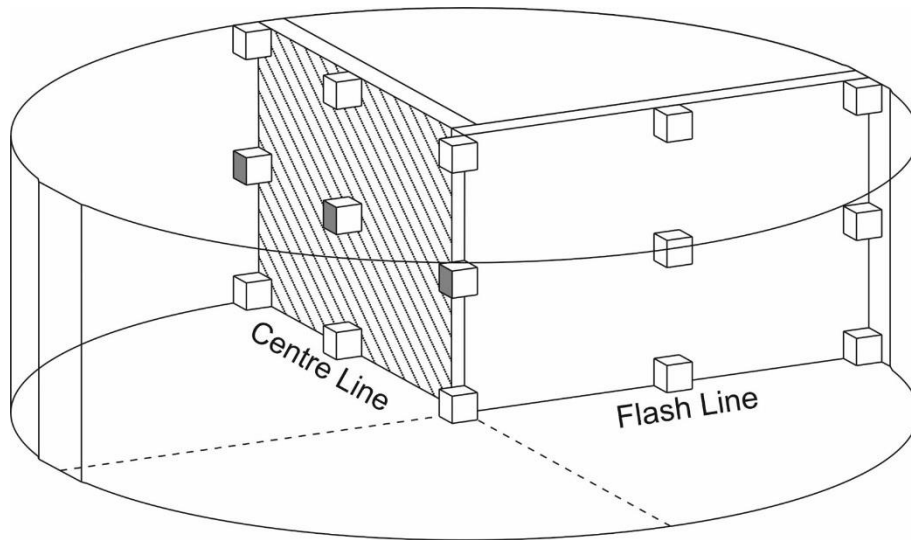
Figure 4.59: Hardness profile across the centre line of forging 1, showing the macro slice, individual samples (grey faces) and partial subdivision of the latter (sample breakdown). Note that the Y-axis scale differs from Figure 4.60 (opposite page). Error bars have been omitted for clarity.
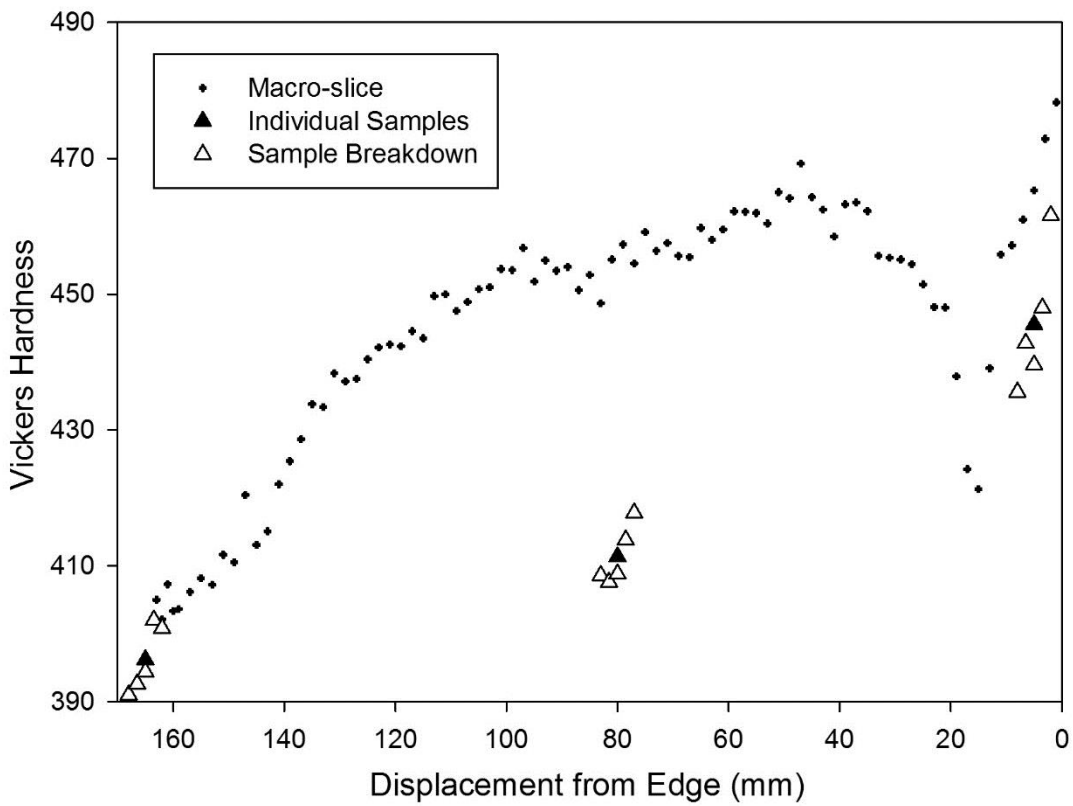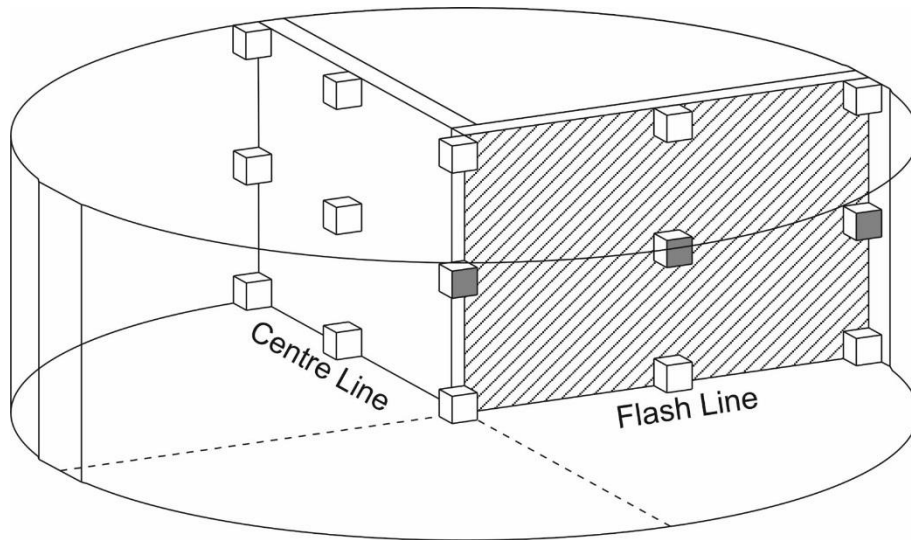
Figure 4.60: Hardness profile across the flash line of forging 1, showing the macro slice, individual samples (grey faces) and partial subdivision of the latter (sample breakdown). Note that the Y-axis scale differs from Figure 4.59 (previous page). Error bars have been omitted for clarity.
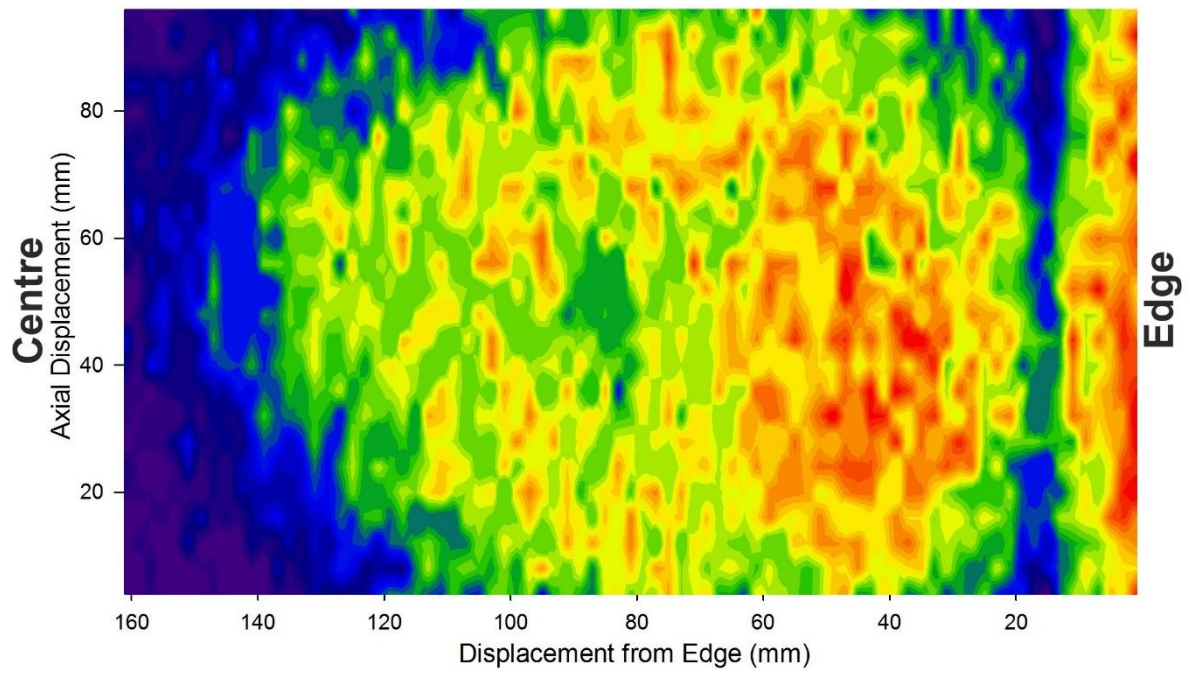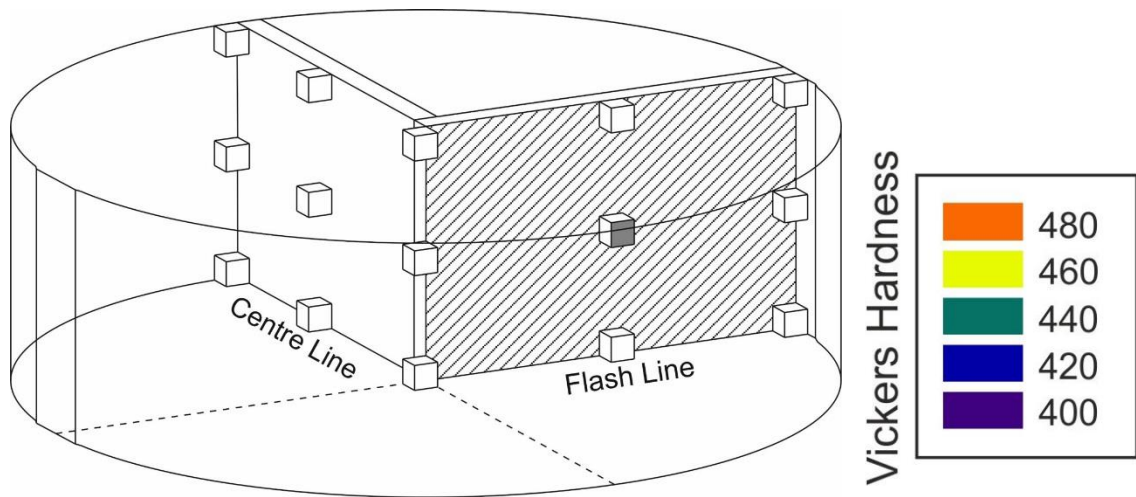
Figure 4.61: Unsmoothed hardness map of forging 1 flash line.
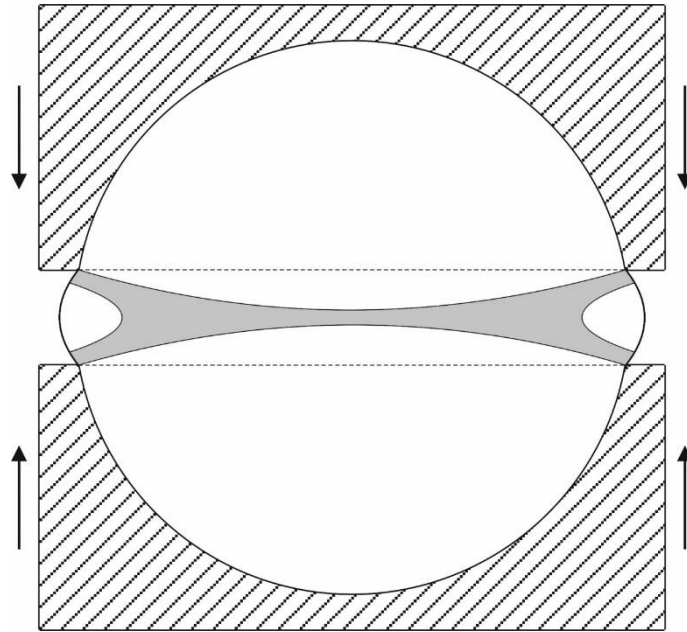
Figure 4.62: Cross section of a closed die forging operation. Once die fill has been achieved, it is postulated that the strain distribution within the flash line may be analogous to that of an axisymmetric compression test [104].

4.6 Microstructure-Property Analysis

If the soft band discovered in forging 1 is also present in forging 2, this may explain some of the asymmetry in mechanical properties. Slight deviations in the exact positioning of test specimens may have altered the mechanical properties if they were situated on or near such a band. Without macro-slices to examine, the hardness data of forging 2 was analysed in a similar manner to Figure 4.58. Figure 4.63 and 4.64 present these results in the as-received condition. Although they do not definitively confirm the presence of a soft band, it can be seen that there exists much greater variation across the edge specimens than elsewhere in the forging. The flash edge specimen in particular shows a significant drop, which then appears to 'bottom out'. This might be the minima if a soft band does exist.

The bottom edge specimen does not present quite as significant a range. However, if there is a soft region, it could be that the positioning of the bottom edge specimen differed slightly from the flash edge, although without intermediate data points it is difficult to say with certainty. Comparison with the heat treated condition (Figure 4.65 and 4.66) reveals that much of this variation is removed, leaving the data more tightly clustered around the sample mean. In an attempt to identify the cause of the original variability, the primary α volume fraction and interparticle spacing of the secondary α was re-examined. Figure 4.67 and 4.68 present partial subdivision (sample breakdown) of the reciprocal interparticle spacing of the as-received condition in a manner analogous to that used for the hardness data (see Figure 4.58). The reciprocal interparticle spacing is presented since the yield strength should be proportional to this [82].

It can be seen that there is significant variation in this parameter across the edge specimens, consistent with the variation in hardness. Although there also appears to be some scatter in the interparticle spacing of the quarter radius specimen along the flash line, this seems to be an exception, and is inconsistent with the corresponding hardness data. Further, the heat treatment appears to remove the as-received trends in secondary α size (Figure 4.69 and 4.70). This would suggest that the secondary α was at least partially responsible for the observed fluctuations in hardness.

Although the primary α does not directly influence yield strength (and by extension, hardness), it does dictate the volume fraction of retained β that is available for hardening during ageing. The yield strength (and hardness) should therefore be proportional to the volume fraction of aged matrix (i.e. retained β plus α_s, where α_s is secondary α). Figures 4.71-4.74 therefore present a breakdown of the aged matrix ($\beta+\alpha_s$) volume fraction in the as-received and heat treated condition to show whether there was any fluctuation across the specimens that might have contributed to the observed variation in hardness. It can be seen that although there was some scatter in the data around the sample means, there were no trends consistent with the

short range variation in hardness, and the heat treatment only appears to reduce the long range variation. This would suggest that changes in secondary α are largely responsible for the short range fluctuations in hardness. Figure 4.75 qualitatively illustrates this variation in secondary α size/morphology across the flash edge specimen in the as-received condition, and compares it with the homogeneity of the heat treated specimen.
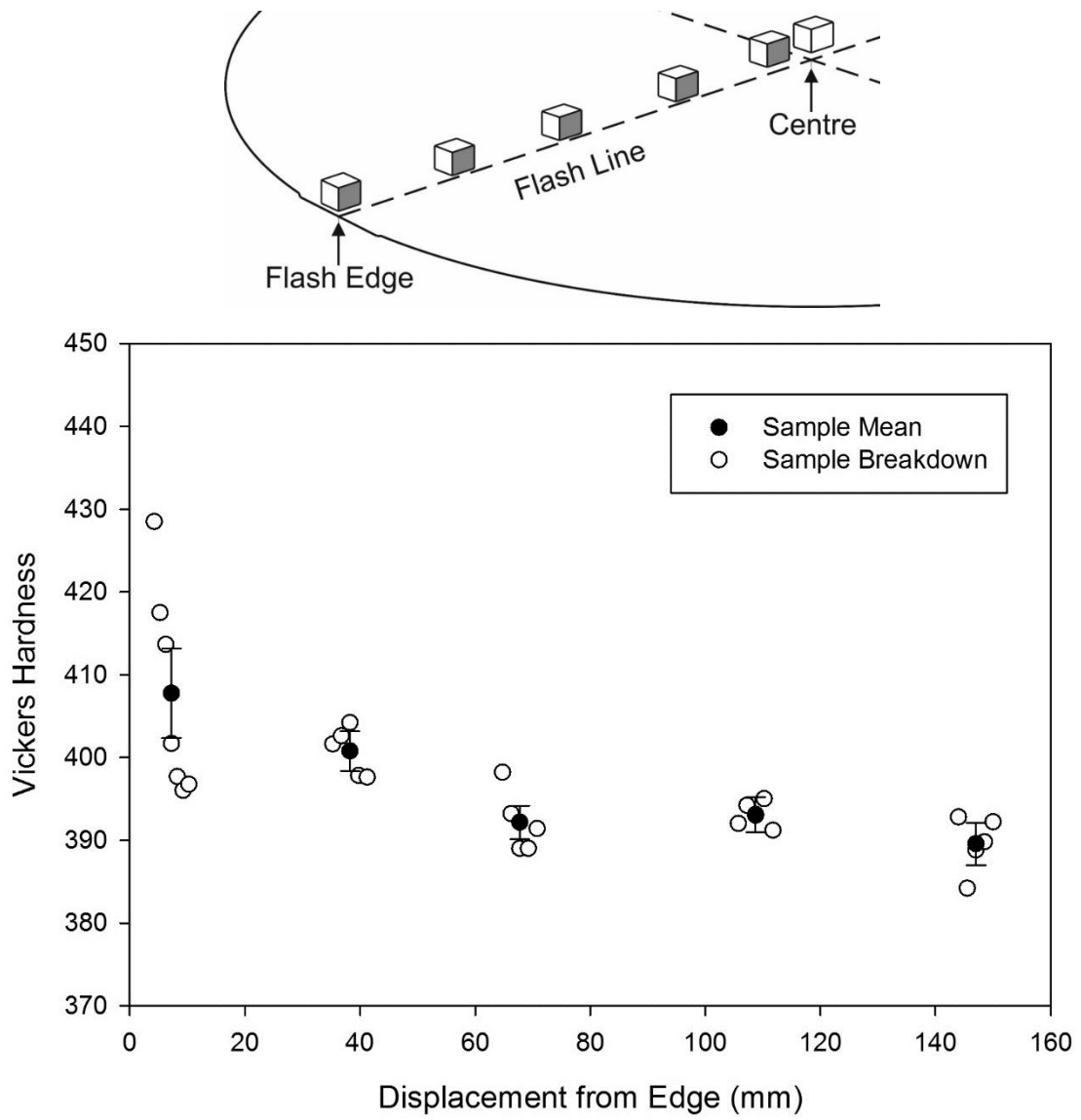
Figure 4.63: Vickers hardness across forging 2 flash line in the as-received condition, showing the mean sample data, and partial subdivision across each specimen (Sample Breakdown).
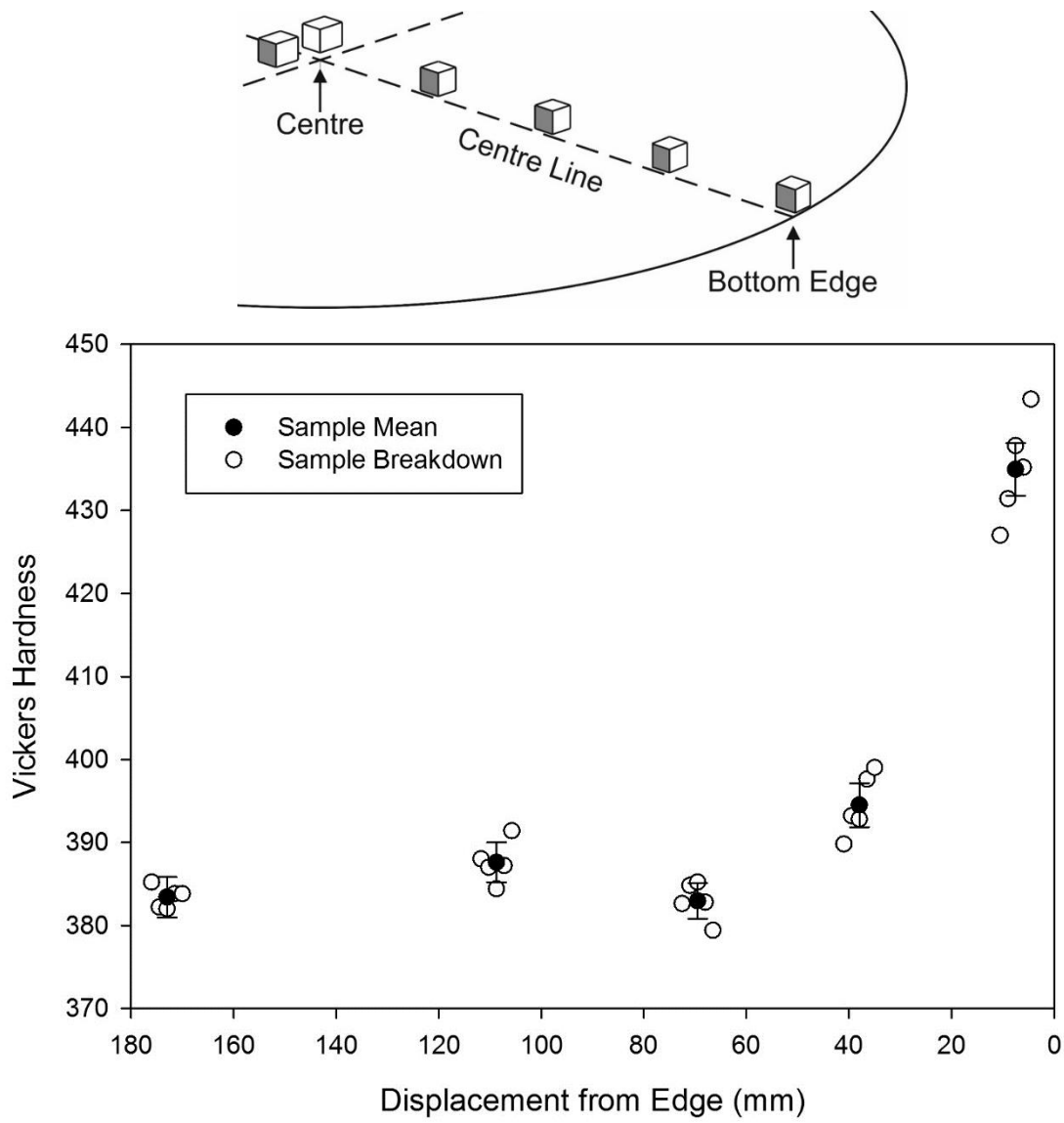
Figure 4.64: Vickers hardness across forging 2 centre line in the as-received condition, showing the mean sample data, and partial subdivision across each specimen (Sample Breakdown).
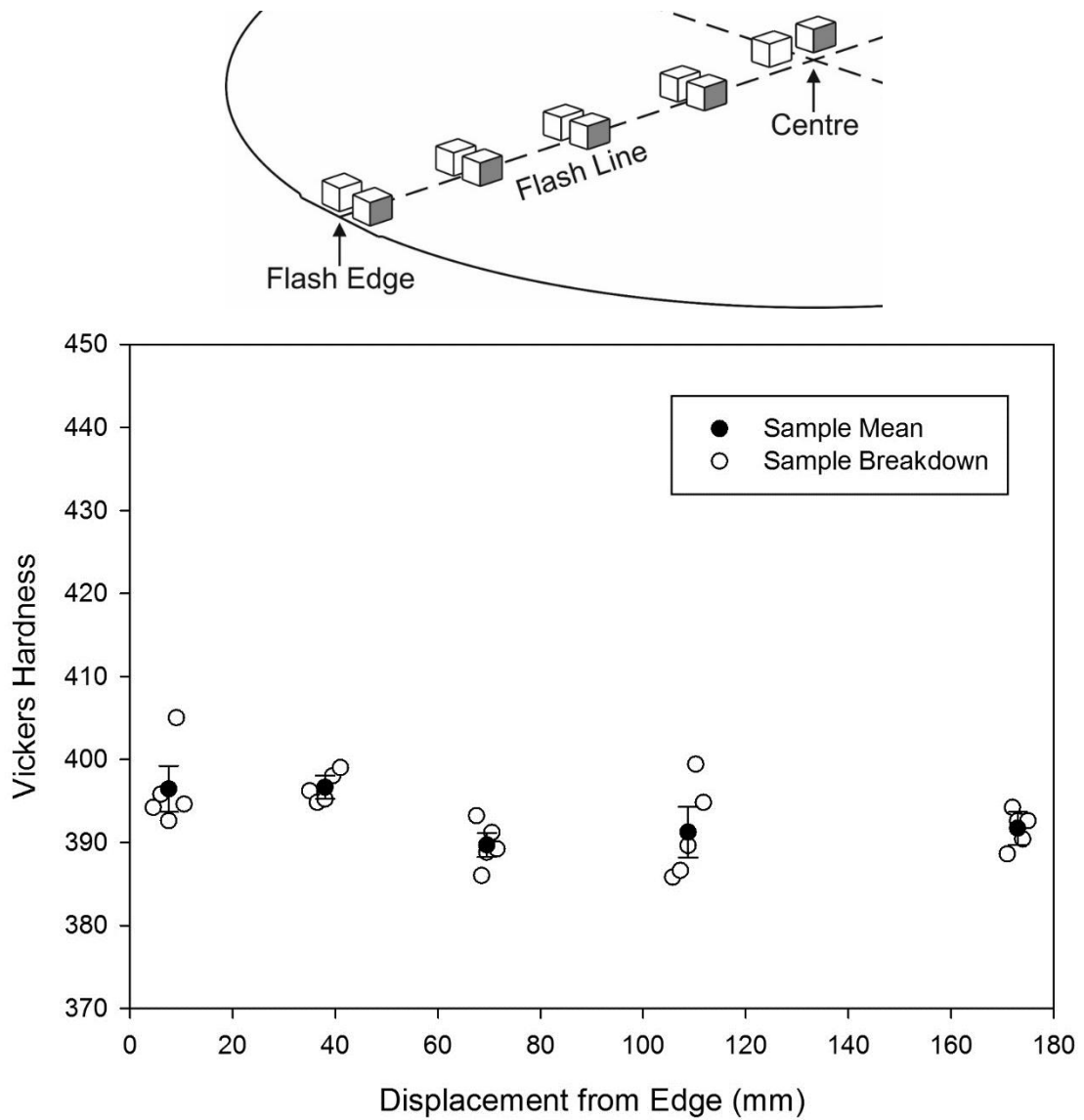
Figure 4.65: Vickers hardness across forging 2 flash line in the heat treated condition, showing the mean sample data, and partial subdivision across each specimen (Sample Breakdown).

144
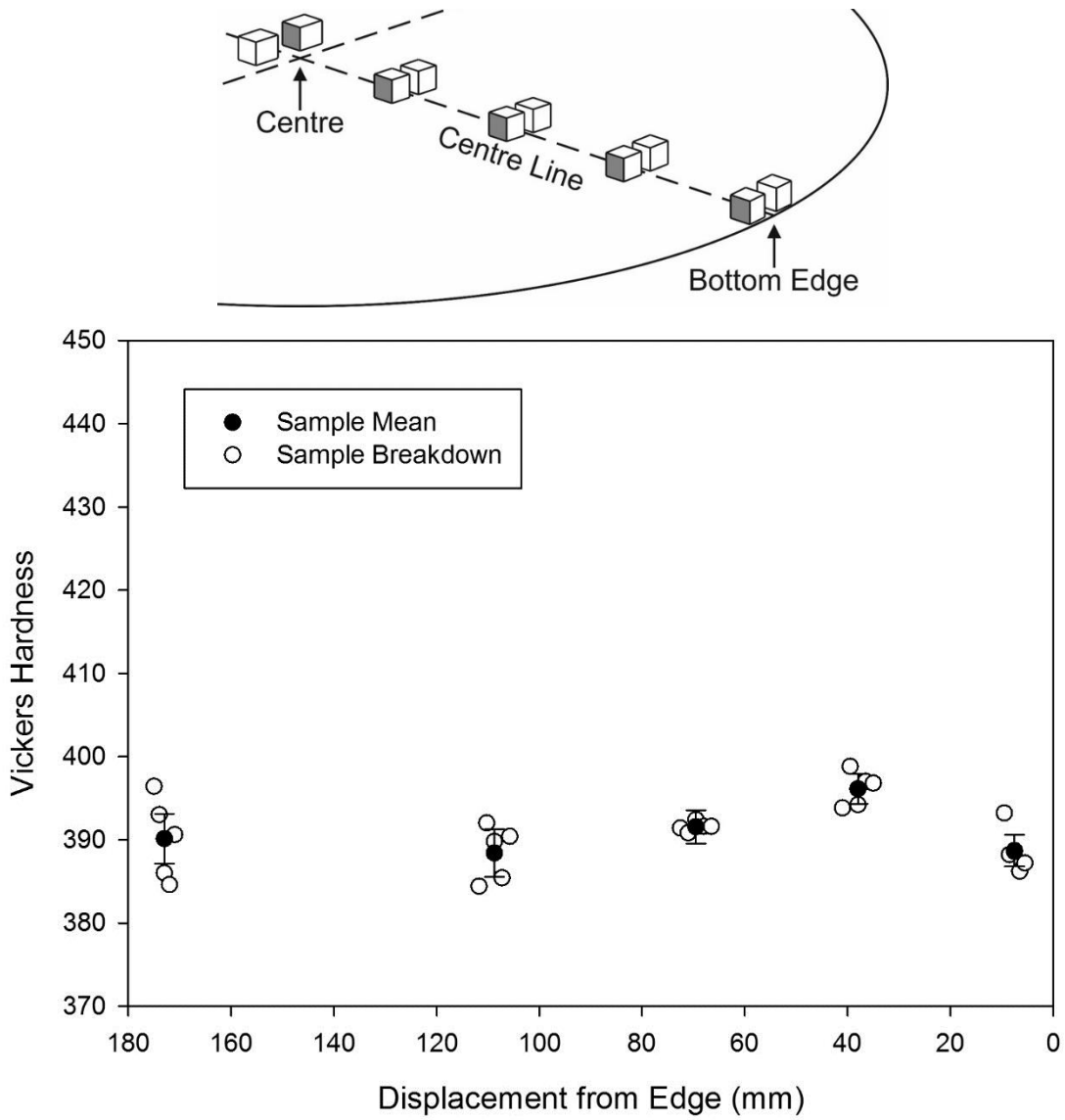
Figure 4.66: Vickers hardness across forging 2 centre line in the heat treated condition, showing the mean sample data, and partial subdivision across each specimen (Sample Breakdown).
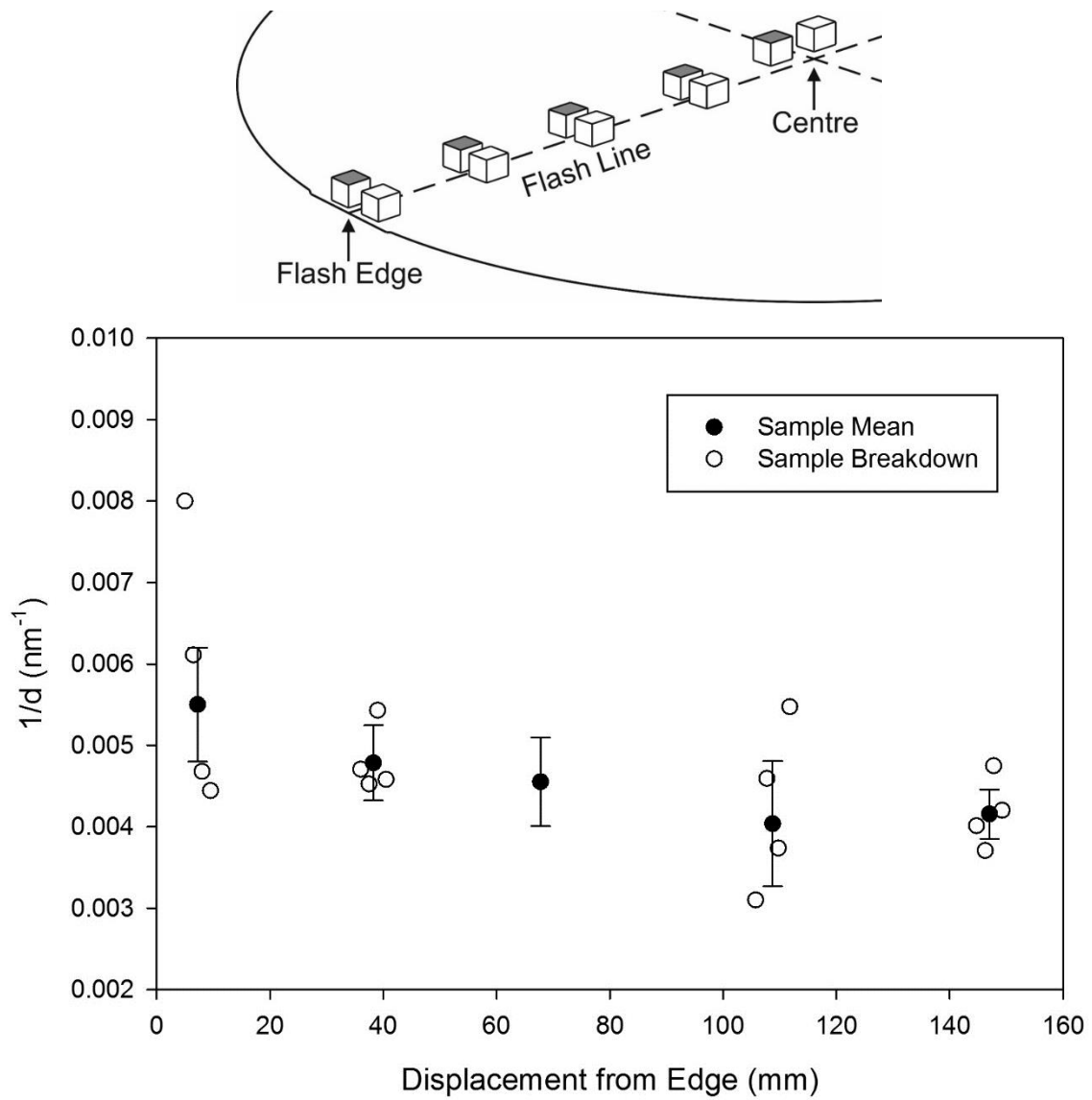
Figure 4.67: As-received condition. Reciprocal of the interparticle spacing across the flash line of forging 2, showing the mean sample data, and partial subdivision across each specimen (Sample Breakdown). The mid-radius specimen is not subdivided as the local displacement information was unreliable.
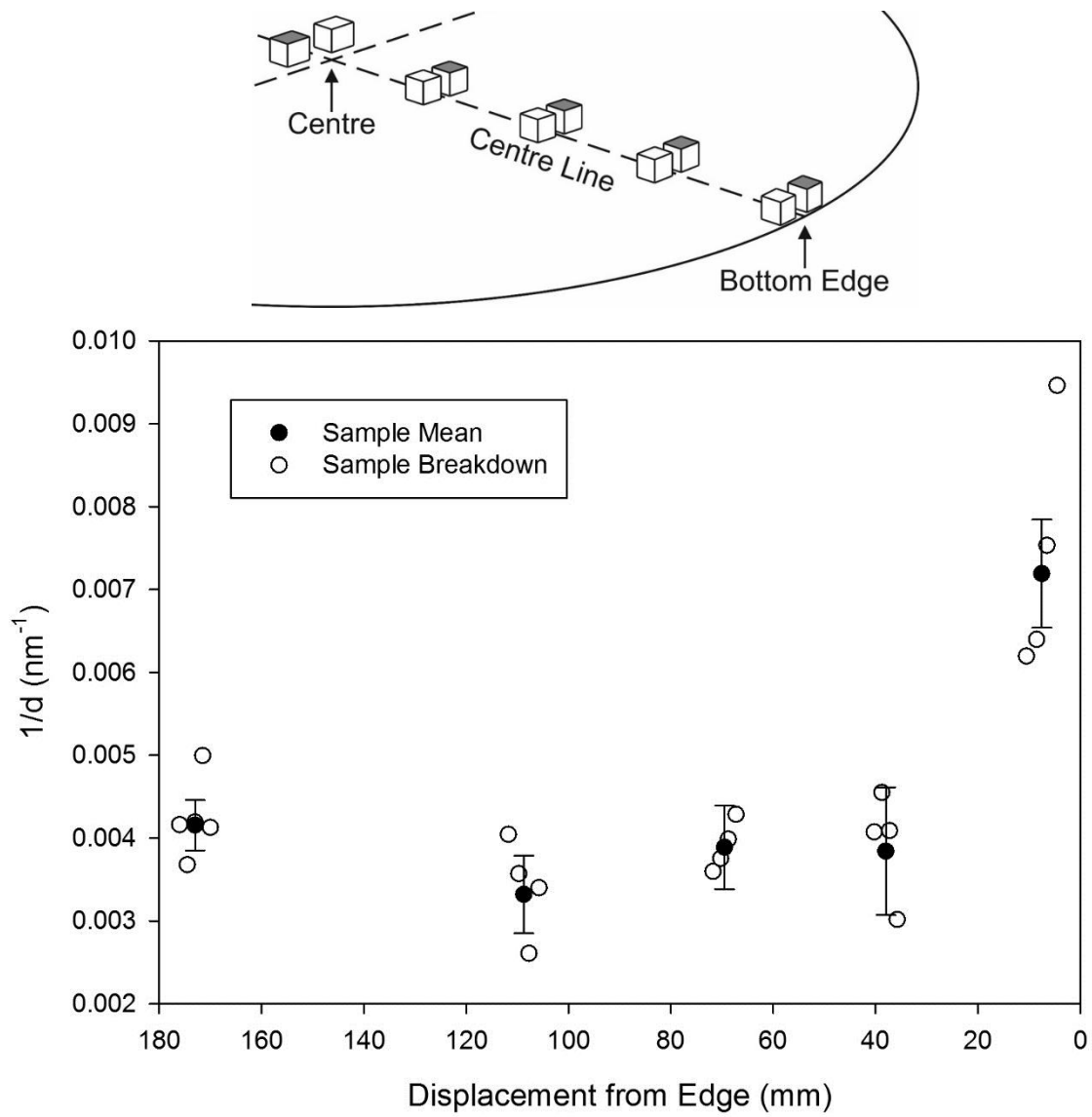
Figure 4.68: As-received condition. Reciprocal of the interparticle spacing across the centre line of forging 2, showing the mean sample data, and partial subdivision across each specimen (Sample Breakdown).
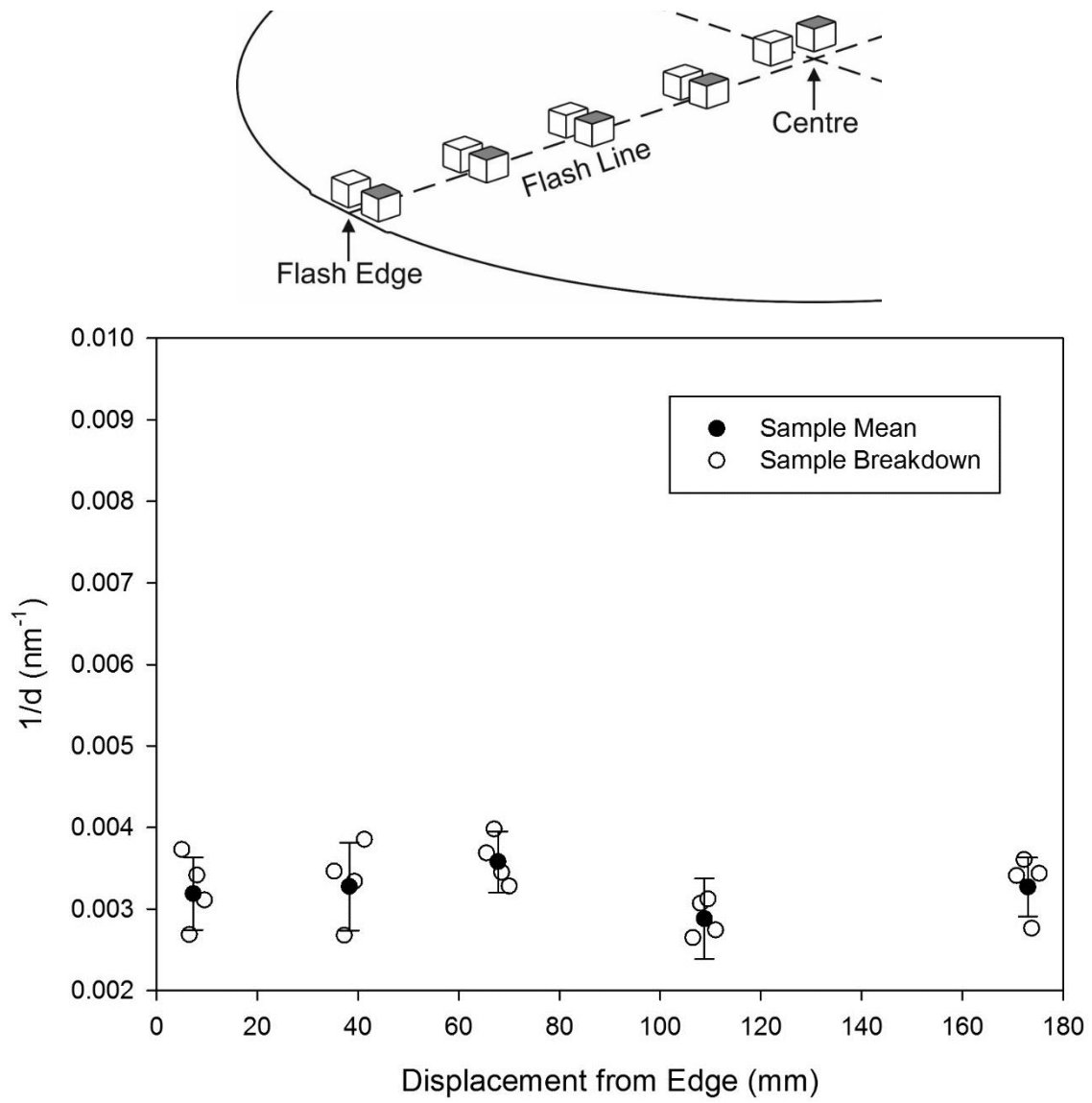
Figure 4.69: Heat treated condition. Reciprocal of the interparticle spacing across the flash line of forging 2, showing the mean sample data, and partial subdivision across each specimen (Sample Breakdown).
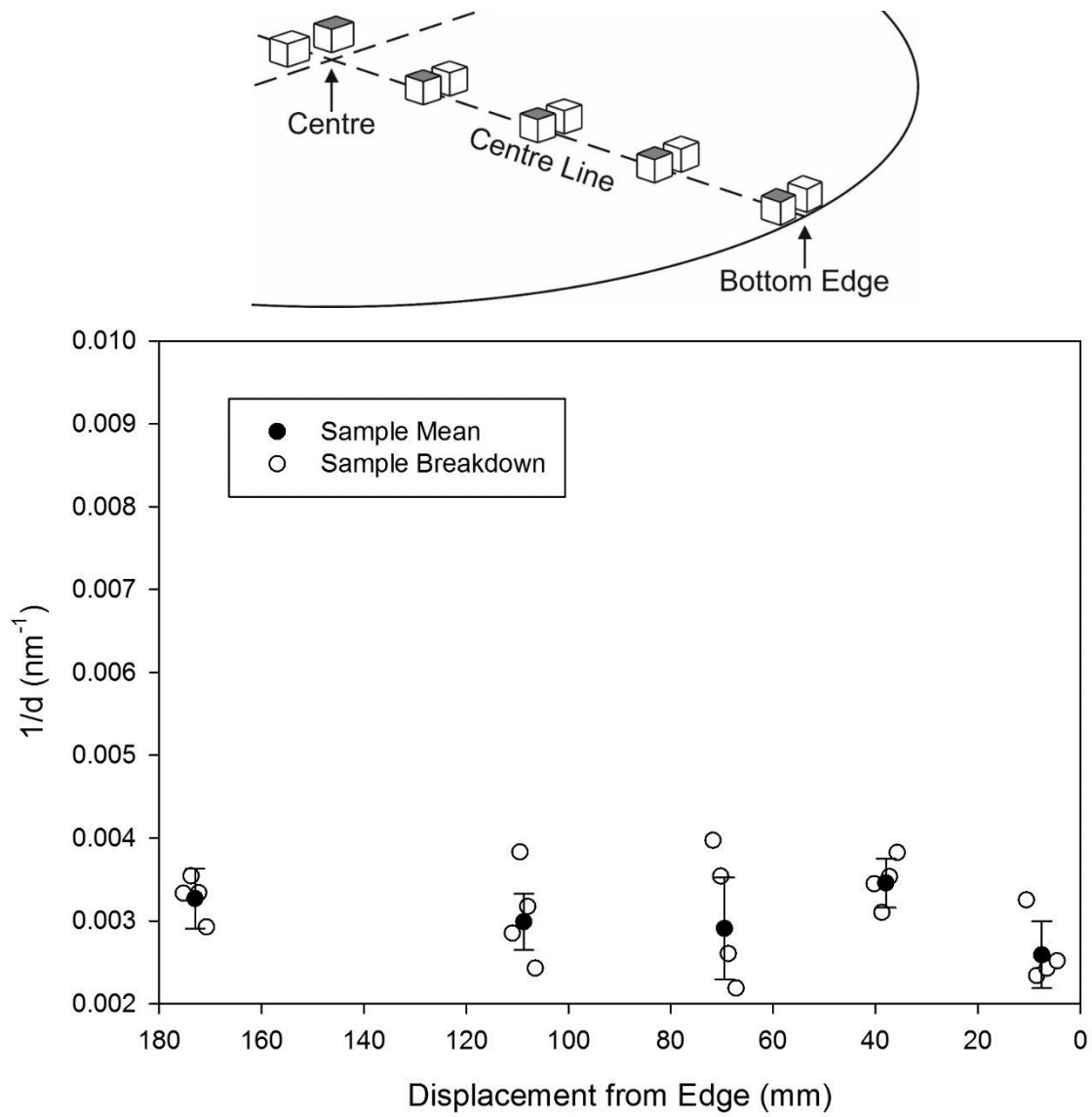
Figure 4.70: Heat treated condition. Reciprocal of the interparticle spacing across the centre line of forging 2, showing the mean sample data, and partial subdivision across each specimen (Sample Breakdown).
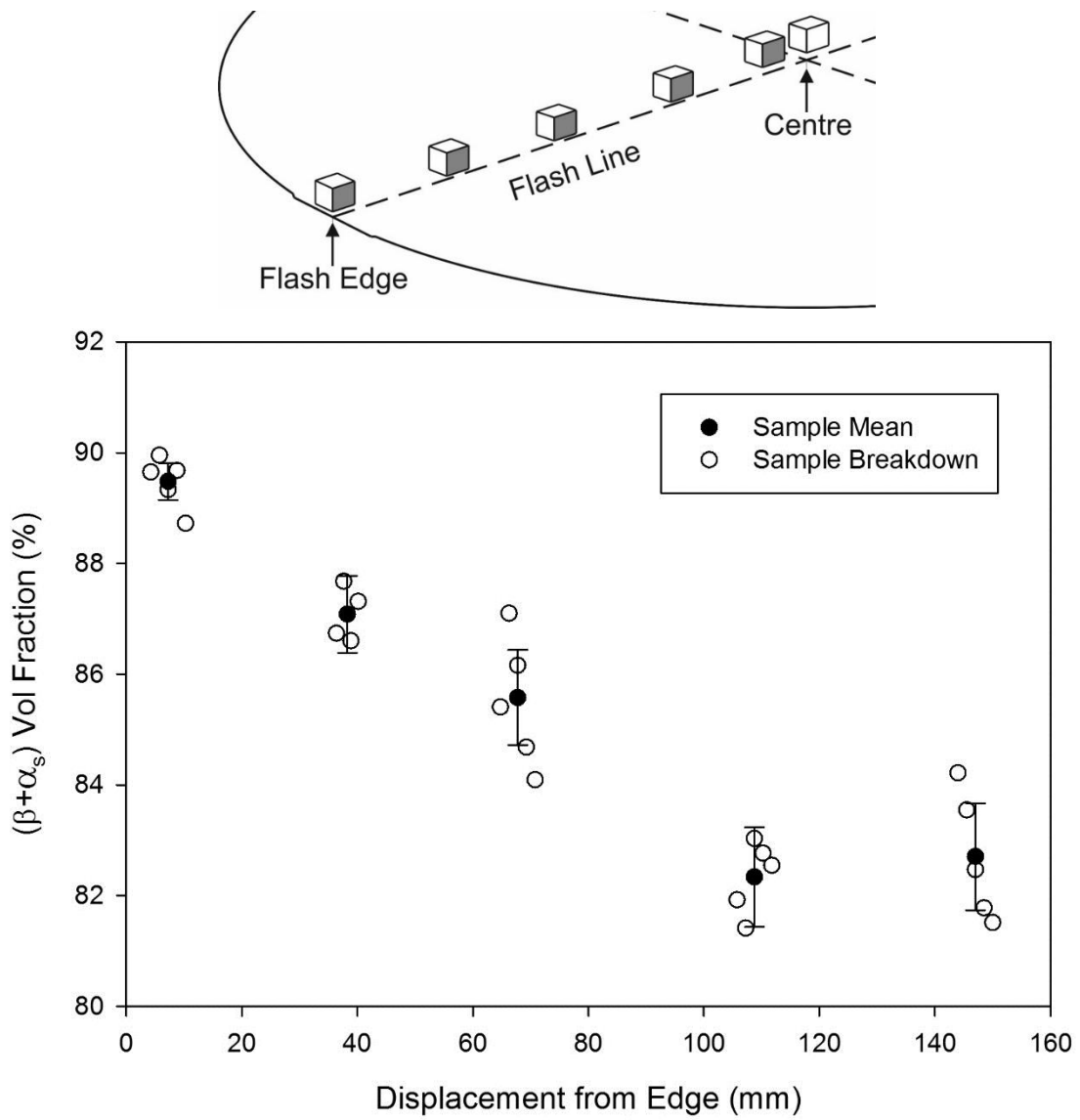
Figure 4.71: As-received condition. $(\beta+\alpha_s)$ volume fraction across the flash line of forging 2, showing the mean sample data and partial subdivision across each specimen (Sample Breakdown).
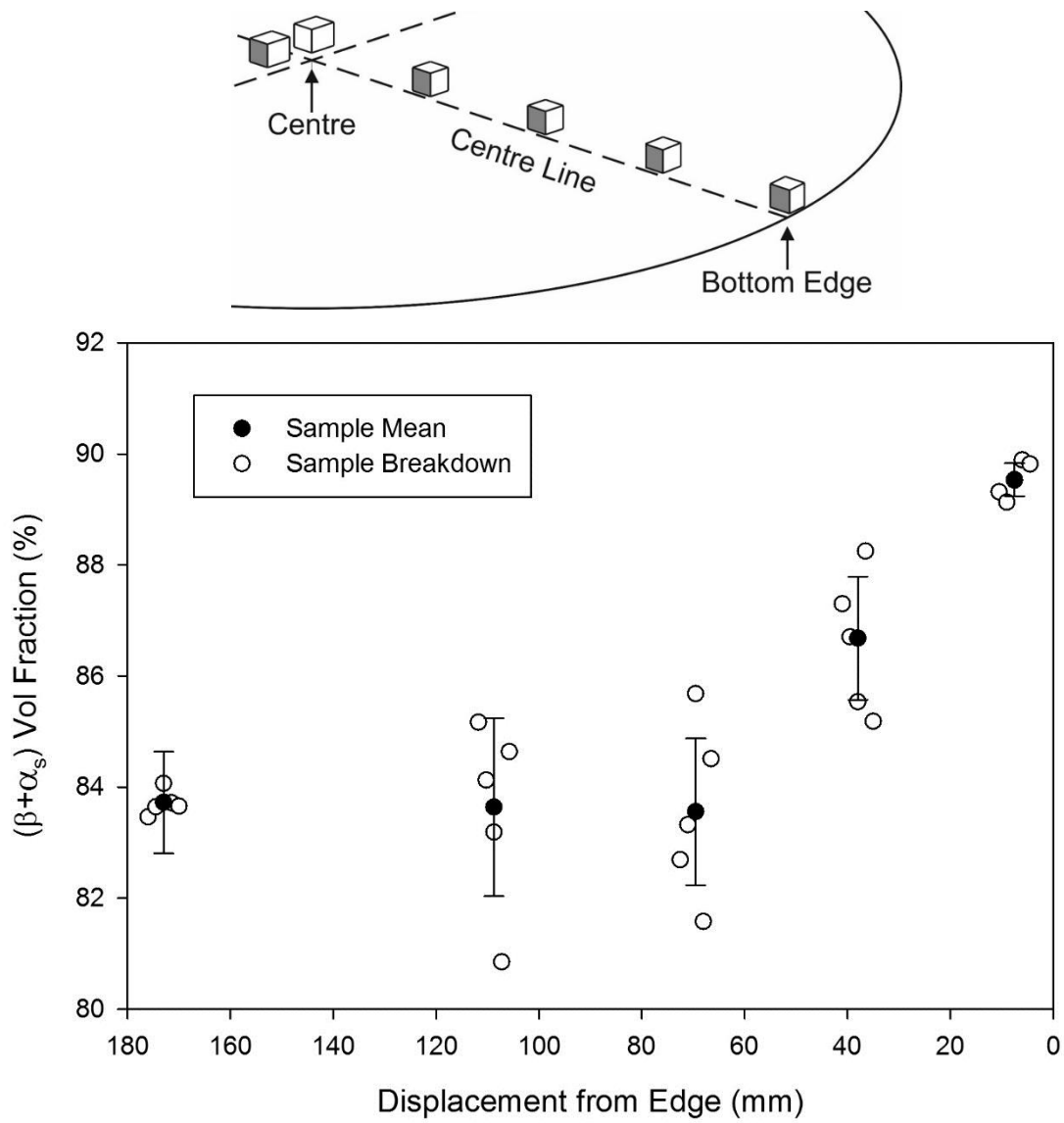
Figure 4.72: As-received condition. $(\beta+\alpha_s)$ volume fraction across the centre line of forging 2, showing the mean sample data and partial subdivision across each specimen (Sample Breakdown).
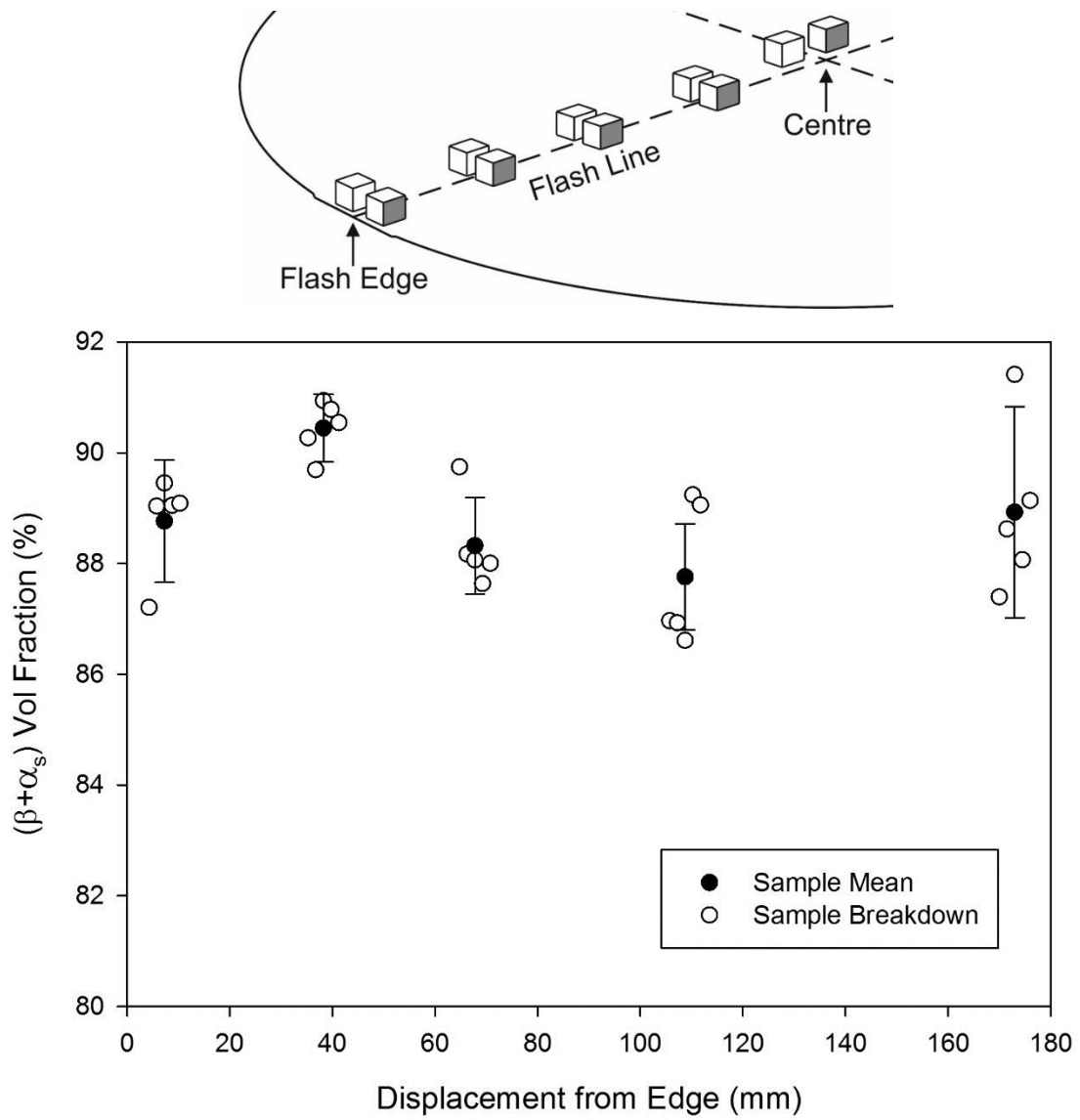
Figure 4.73: Heat treated condition. ($\beta+\alpha_s$) volume fraction across the flash line of forging 2, showing the mean sample data and partial subdivision across each specimen (Sample Breakdown).
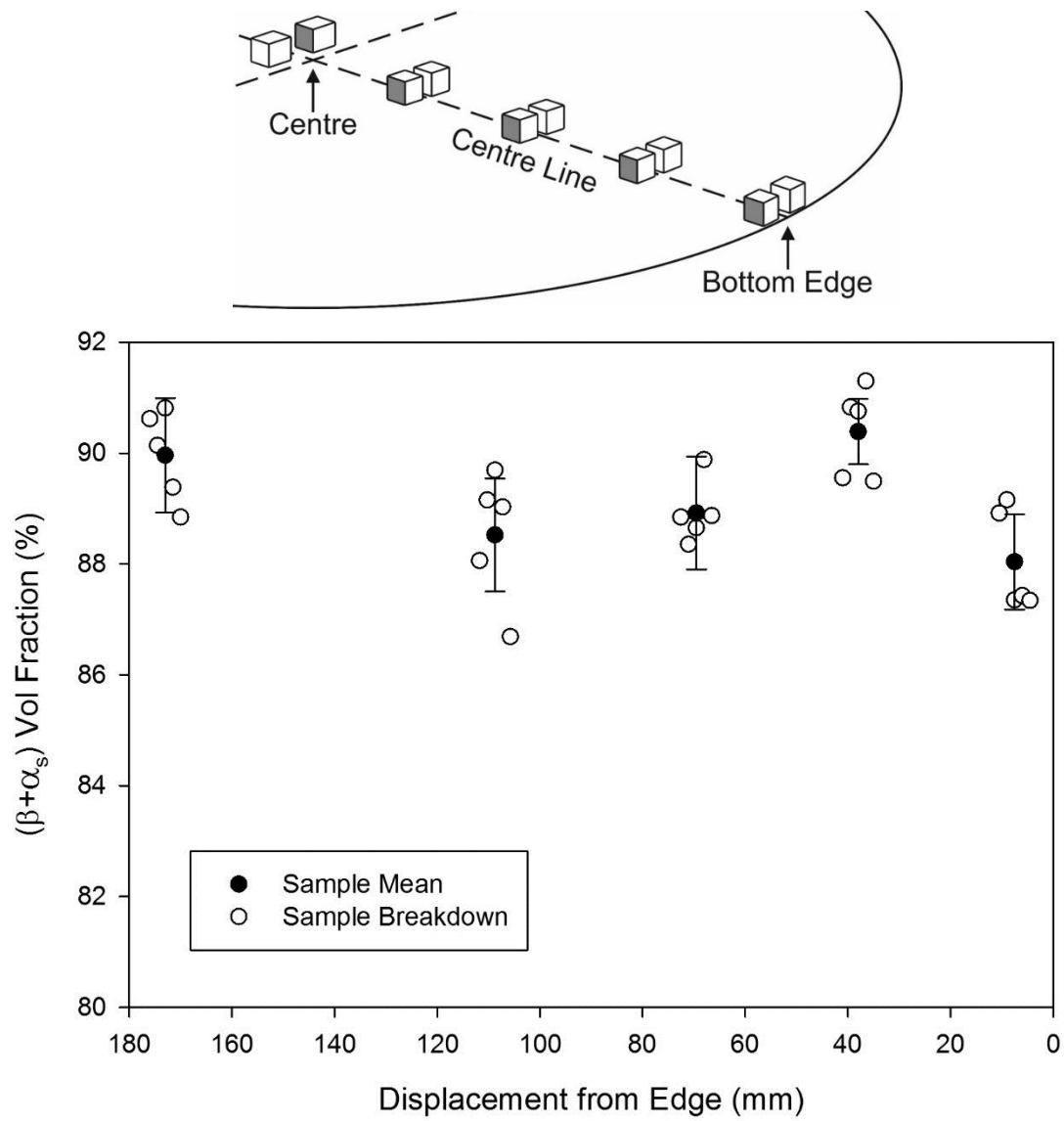
Figure 4.74: Heat treated condition. $(\beta+\alpha_s)$ volume fraction across the centre line of forging 2, showing the mean sample data and partial subdivision across each specimen (Sample Breakdown).
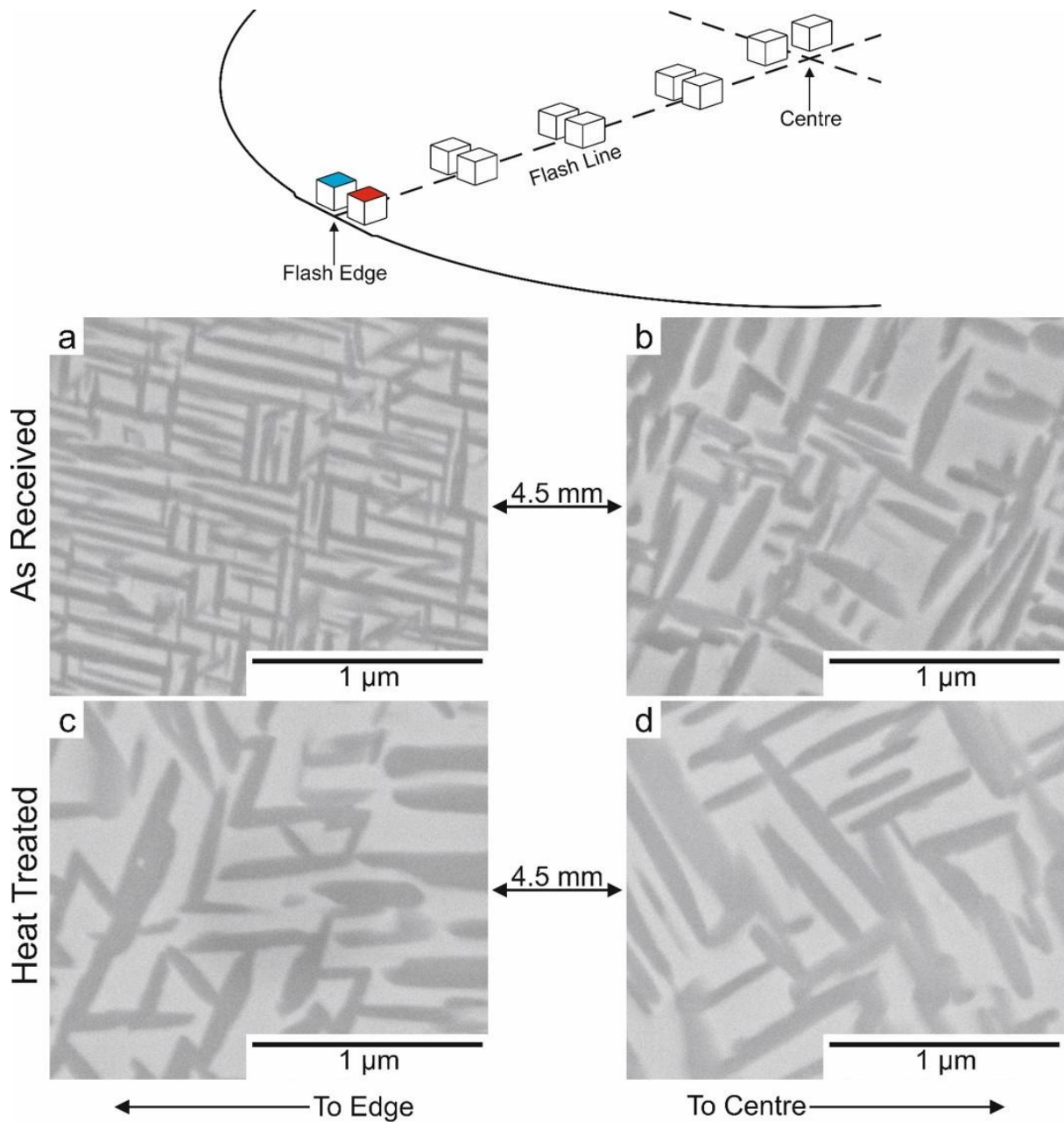
Figure 4.75: High magnification BSEI micrographs of the flash edge specimens, (a) and (b) comparing the secondary α across the as-received specimen (blue face), (c) and (d) comparing the secondary α across the heat treated specimen (red face). The 4.5 mm displacement between each pair of micrographs is in the radial direction (flash line).

Having ascertained the highly influential role that secondary α played in controlling the hardness, Figure 4.76-4.88 illustrate other correlations observed between microstructural variables and their dependent properties. However, given what is now known about the microstructural variability near the forging edge, caution must be exercised when interpreting these results. The properties and microstructural parameters quoted for the edge specimens may not be truly representative. In addition, while the displacement between microscopy samples and tangential specimens was always going to introduce some error, this may now be exacerbated by such localised microstructural variation. With this in mind, Figure 4.76 illustrates the correlation between the retained β volume fraction and axial proof stress. The term 'retained β', or simply 'β', is used here to describe the combined volume fraction of retained β and secondary α as these together constitute the 'aged matrix'. The yield stress should be a function of this parameter, as it is the aged matrix which provides the high strength of β alloys. Since the proof stress is the best available indicator of yield stress, it is this property that is plotted as a function of retained β in Figure 4.76-4.79.

As can be seen in Figure 4.76, the proof stress shows a general increase as the β volume (β_{vf}) fraction rises. Since the aged matrix is responsible for much of the strength of a metastable β alloy, it stands to reason that the strength would increase as the volume fraction of this constituent increases. The non-linearity of the correlation is likely to be the result of other microstructural parameters changing simultaneously. It can be seen that the edge specimens (numbered) are the major outliers. Since the secondary α spacing was at its lowest in these regions, it is unsurprising that these exhibit strengths well above the expected trend. If these data points are ignored, the correlation improves significantly. This is most likely because the interparticle spacing of the secondary α was more consistent between the non-edge as-received and heat treated specimens.

A weak correlation is also observed between the axial proof stress and d^{-1} (Figure 4.77, where d is the secondary α interparticle spacing). As with Figure 4.76 the simultaneous variation of other microstructural features (in this case β volume fraction) confuses the relationship. Figure 4.78 attempts to compensate for this by dividing the proof stress by β_{vf}. This is an approximation at best, since it implies the strength would go to zero as β_{vf} goes to zero. However, it does improve the fit of the data, and over the range in question it provides a better fit than a multi-linear regression approach. The edge specimens (both as-received and heat treated) are still all situated above the fitted line. This might suggest that there are other unknown microstructural parameters providing additional strength. However, assuming these effects are minor, and taking the equation of the line, the axial proof stress σ0.2 is then given by:

$$\sigma_{0.2} = \beta_{vf}(4.15 \times 10^{-5}d^{-1} + 1.19 \times 10^{3}) \qquad (2.1)$$
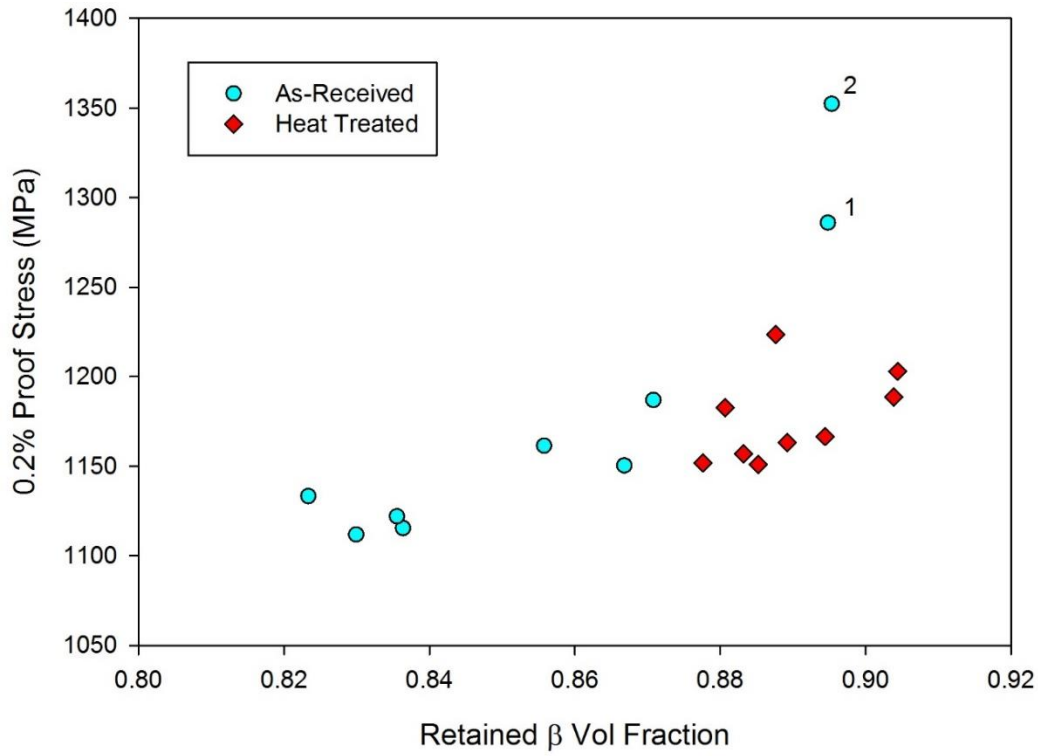
Figure 4.76: Axial proof stress vs retained β volume fraction. 1 and 2 denote the flash edge and bottom edge specimens, respectively.
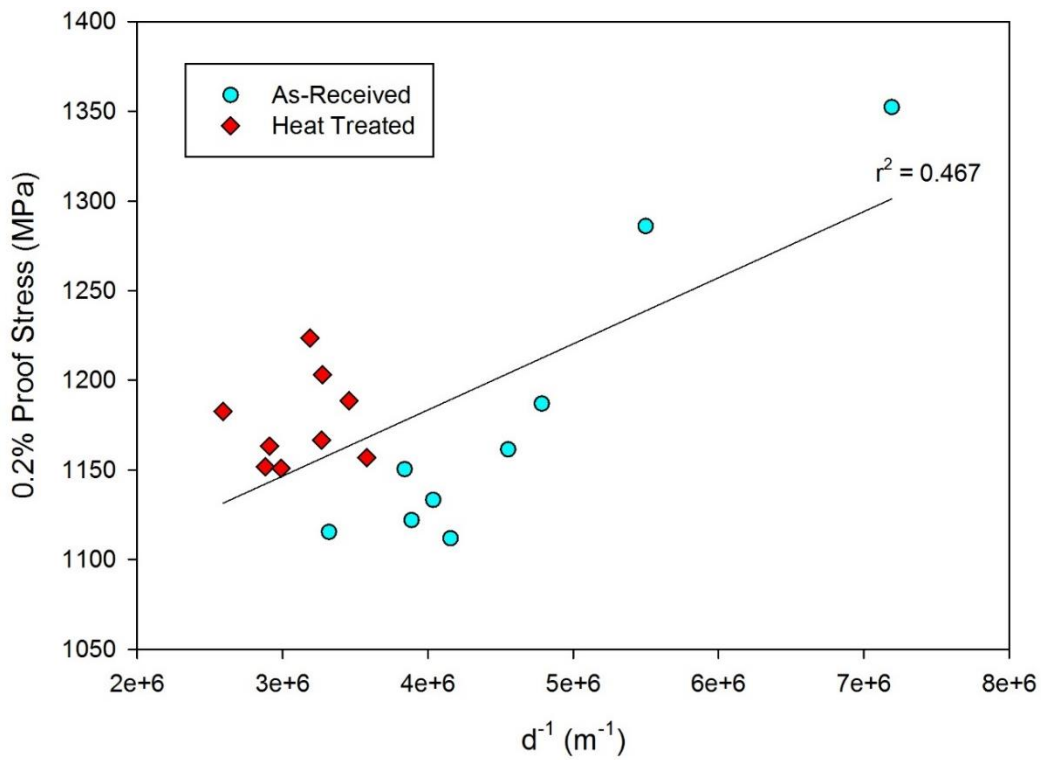
Figure 4.77: Axial proof stress vs reciprocal interparticle spacing of secondary α.
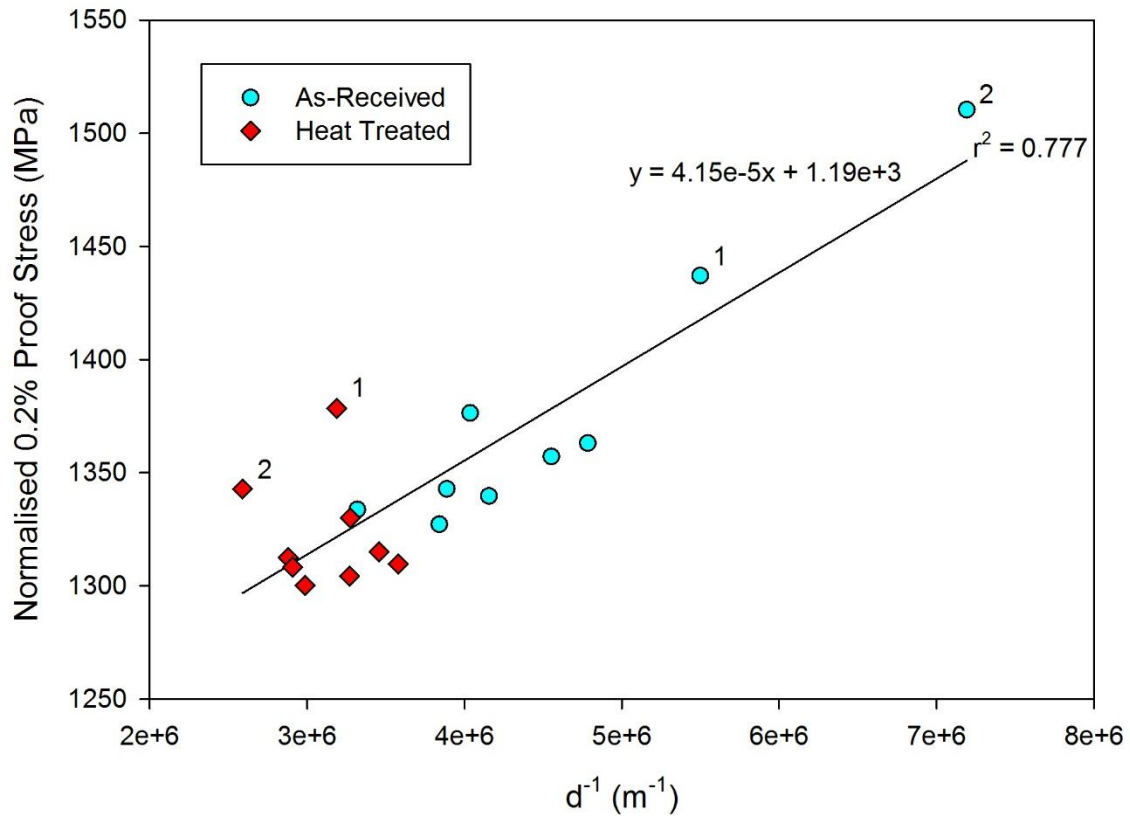
Figure 4.78: Normalised axial proof stress vs reciprocal interparticle spacing of secondary α (normalised to 100% β_{vf}). 1 and 2 denote the flash edge and bottom edge specimens, respectively.

The tangential proof stress appeared less sensitive to d^{-1} and a positive correlation could only be found with β_{vf} (Figure 4.79, $r^2 = 0.592$). As noted earlier (see Section 4.5.1), this orientation was less responsive to heat treatment, suggesting that tensile properties were being limited by other microstructural variables (e.g. β grain morphology, texture, grain boundary α etc). This would limit the predictive capability of the microstructural features that were measured (β_{vf} and d^{-1}).
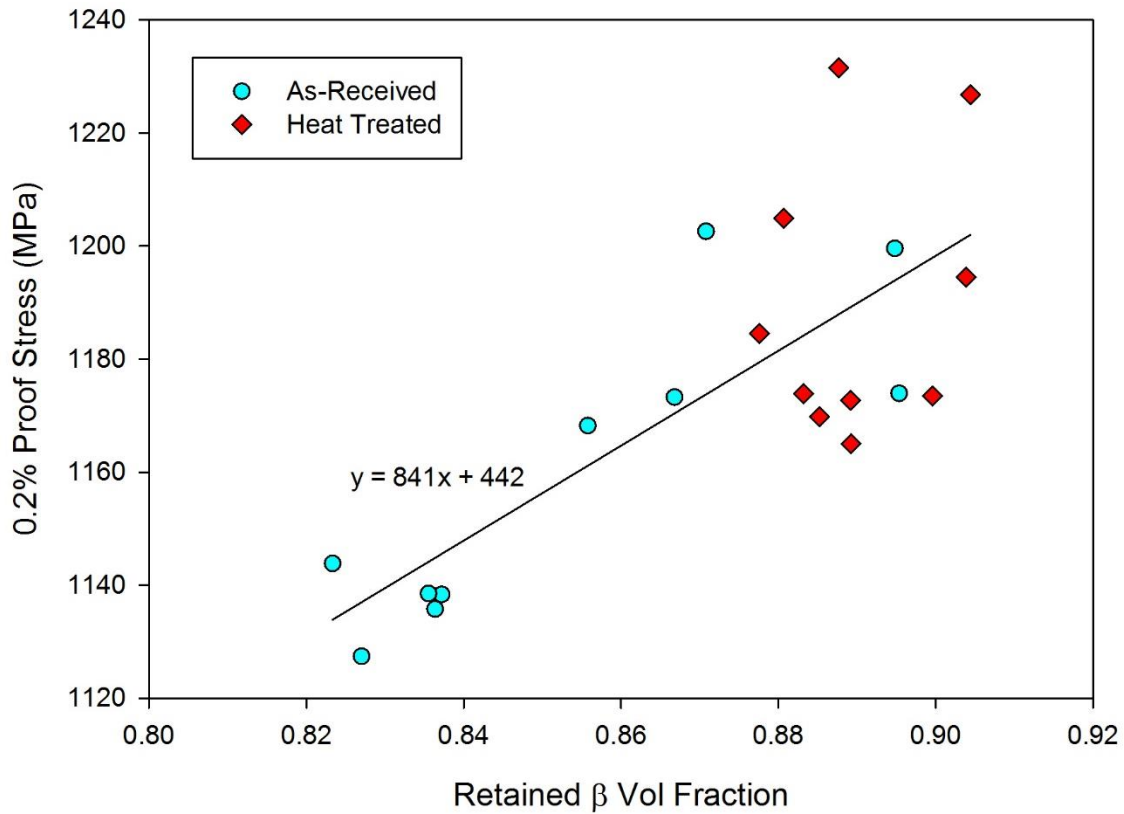
Figure 4.79: Tangential proof stress vs retained β volume fraction.

Figure 4.80 illustrates the correlation between the axial hardness and β_{vf}. The trend appears very similar to the proof stress data (Figure 4.76) although there is less consistency between the as-received and heat treated condition. However, when plotted as a function of d^{-1} (Figure 4.81) a better fit is achieved than with the proof stress data. As with the proof stress though, the correlation is weakened by other variables changing simultaneously. If the macroscopic hardness is assumed to be a linear function of β_{vf}, it can be expressed as:

$$HV = \beta_{vf} \cdot h + c \qquad (2.2)$$

Where *HV* is the Vickers hardness, *h* is the hardness of the aged β_{vf} and *c* is a constant representing the intrinsic hardness of the alloy without any ageing. If the aged hardness of the retained β, *h* is linearly proportional to d^{-1}, Equation 2.2 can be rewritten as:

$$HV = m\beta_{vf}d^{-1} + c \qquad (2.3)$$

158

Where *m* is a constant. If the axial hardness is then plotted against the term $\beta_{vf}d^{-1}$, as in Figure 4.82, a better fit is achieved, giving:

$$HV = 1.21 \times 10^{-7} \cdot \beta_{vf}d^{-1} + 3.54 \times 10^2 \tag{2.4}$$

This approach was tried with the proof stress data, but did not correlate with d^{-1} as well as $\sigma_{0.2}\beta_{vf}^{-1}$ (Figure 4.78). This may have been due to the inherent difficulty of defining the yield point (in this case, as a deviation from the linear elastic region by 0.2% strain). However, the hardness may have been a more reliable measure of the materials resistance to plastic deformation, and therefore correlated better with these two parameters (β_{vf} and d^{-1}).
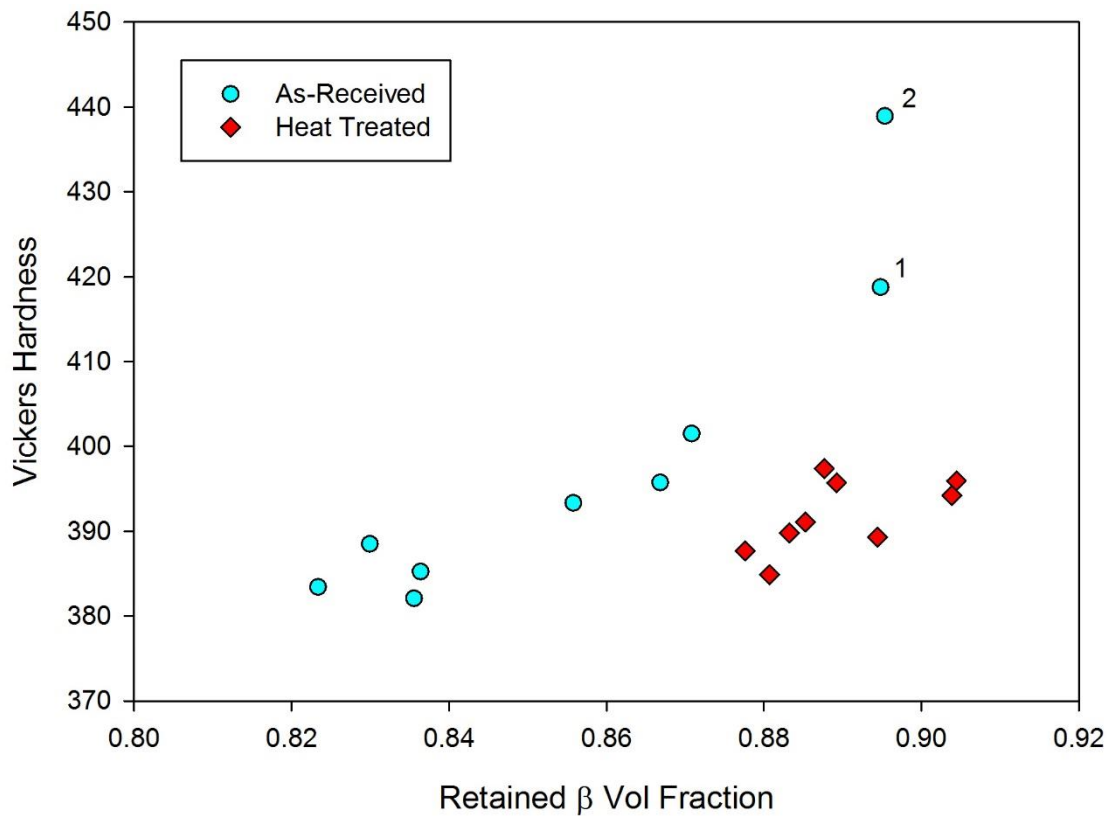
Figure 4.80: Axial hardness vs retained β volume fraction. 1 and 2 denote the flash edge and bottom edge specimens, respectively.
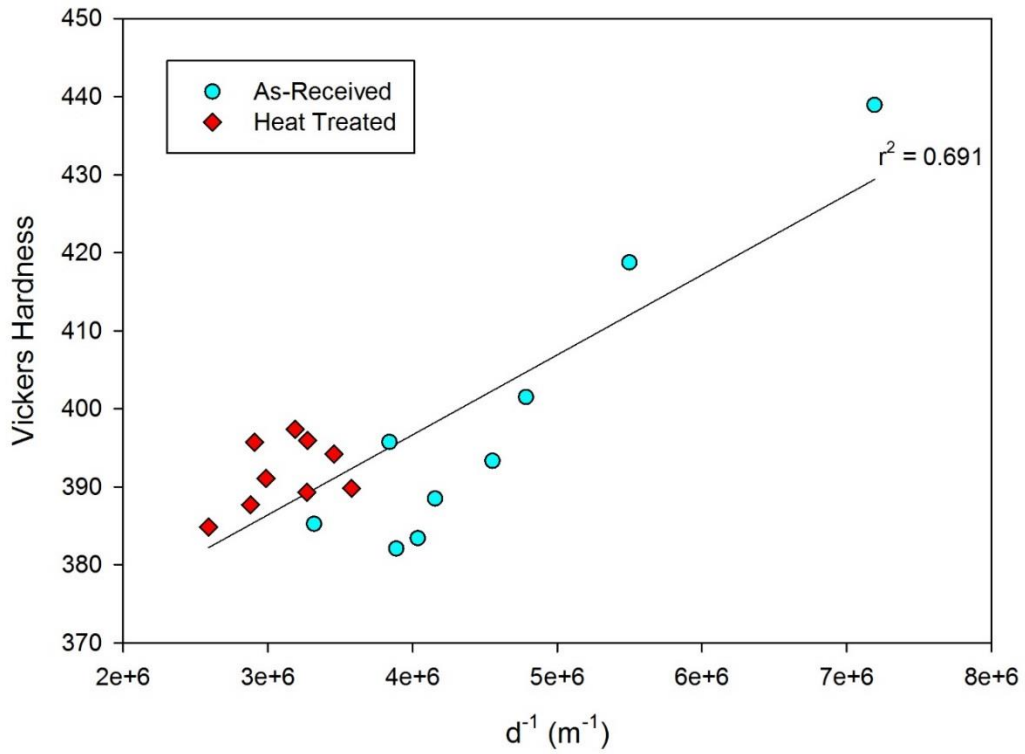
Figure 4.81: Axial hardness vs reciprocal interparticle spacing of secondary α.
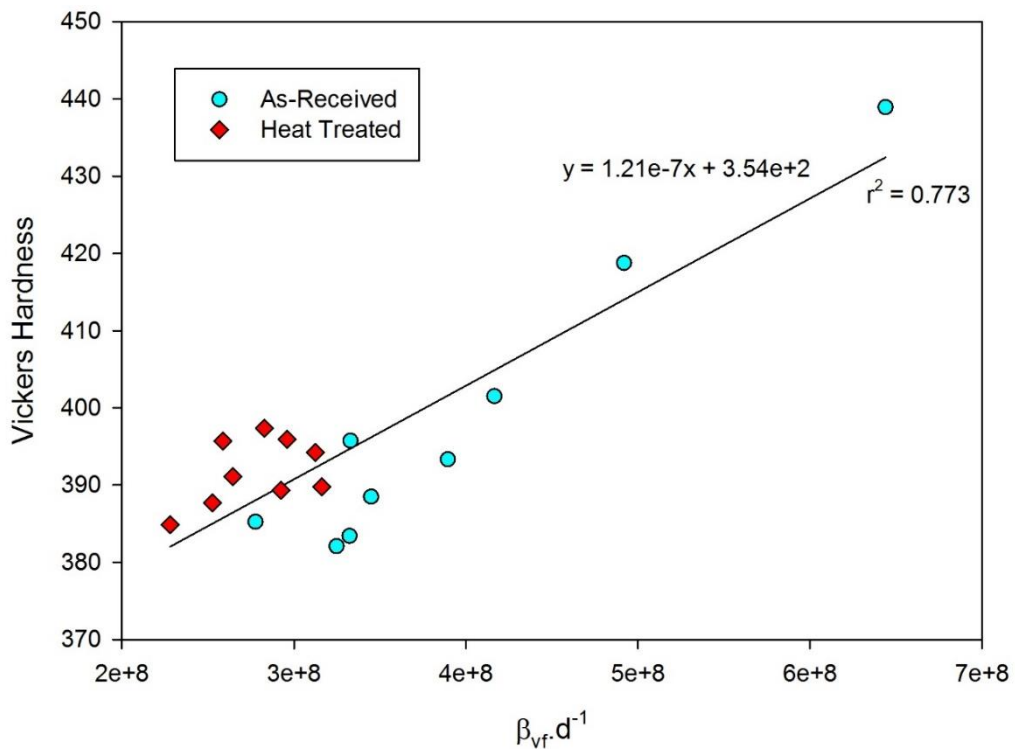
Figure 4.82: Axial hardness vs $\beta_{vf}d^{-1}$.

The much higher strength of the aged matrix relative to the primary α phase concentrates deformation in the latter [17]. In the aged condition, a higher volume fraction of primary α (α_p)

would therefore be expected to improve ductility. Figure 4.83 presents the % elongation to failure (E_f) as a function of α_p volume fraction for the axial orientation in the as-received and heat treated condition. It can be seen that the as-received material exhibits a very strong correlation ($r^2 = 0.964$), although the heat treated condition does not. If the heat treatment achieved the objective of homogenising the microstructure, the only variation in E_f would be random statistical fluctuations that would yield no trend. This appears to be the case, but the cluster of heat treated points also fails to coincide with the as-received material of similar α_p volume fraction. Again, this is likely due to the effect of other variables, such as d^{-1}. As the strength of the matrix increases (as d^{-1} rises), the strain localisation within the primary α intensifies, reducing ductility. Plotting E_f as a function of d illustrates this in Figure 4.84 (since strength is proportional to d^{-1}, the elongation should be proportional to d). Although the fitted line indicates a weaker correlation than that between α_p and E_f in the as-received condition, this is still far better than a fit of all the data in Figure 4.83 ($r^2 = 0.055$). If the elongation to failure is assumed to be the sum of elongation in the aged matrix E_β and primary α E_α, plus a constant b, it can be expressed as:

$$E_f = E_\beta + E_\alpha + b \tag{2.5}$$

If the contribution from the aged matrix is proportional to d, weighted by β_{vf}, and the contribution from the primary α is proportional to its volume fraction α_{pf}, Equation 2.5 can be written as:

$$E_f = kd\beta_{vf} + p\alpha_{pf} + b \tag{2.6}$$

Where k and p are constants. Performing multi-linear regression on the terms $d\beta_{vf}$ and α_{pf} then produces:

$$E_{fa} = 6.05 \times 10^7 d\beta_{vf} + 73.6\alpha_{vf} - 6.71 \tag{2.7}$$

Where E_{fa} is the % elongation to failure in the axial orientation. In order to assess the accuracy of Equation 2.7 it was used to normalise all the axial elongation data to the mean α/β ratio and plot this as a function of d (Figure 4.85). Comparing this with Figure 4.84, it can be seen that the trendline fits slightly better. The difficulty with obtaining a good fit could be for a number

of reasons. As mentioned earlier, the use of % elongation as a measure of ductility is not ideal as the calculated value is influenced by the gauge length. In addition, this elongation was based upon crosshead displacement. This will have incorporated machine compliance and distorted the true values considerably. There is also greater scatter in ductility data, further reducing the consistency of a correlation, and on top of this it is likely that other microstructural variables are unaccounted for by Equation 2.7. The issue with compliance is particularly unfortunate, as it prevents the application of Equation 2.7 to other data. The determination of RA (Reduction in Area) would be a useful addition, as it would circumvent both the problem with compliance and the complication of specimen geometry.

Figure 4.86 illustrates the tangential E_f as a function of α_{pf}. As with the axial orientation, the as-received condition correlates better than the heat treated. However, the correlation with d is much weaker than in the axial orientation (Figure 4.87). Carrying out multi-linear regression as explained above produces Equation 2.8, but normalising by this provides only marginal improvement in the correlation (Figure 4.88).

$$E_{ft} = 3.10 \times 10^7 d\beta_{vf} + 83.6\alpha_{pf} - 6.64 \qquad (2.8)$$

Where E_{ft} is the % elongation to failure in the tangential orientation. The poorer fit of the data in the tangential orientation is probably due to an unspecified variable. The effect of β grain morphology and relative orientation is one factor that may be more significant in the tangential testing direction. Given the pancaked or elongated equiaxed β grains present in the forging, the tangential specimens may experience greater variation in the relative morphology/orientation of the β grains between the flash line and centre line. This might represent a 'confounding variable', which distorts or masks the correlation between other variables.
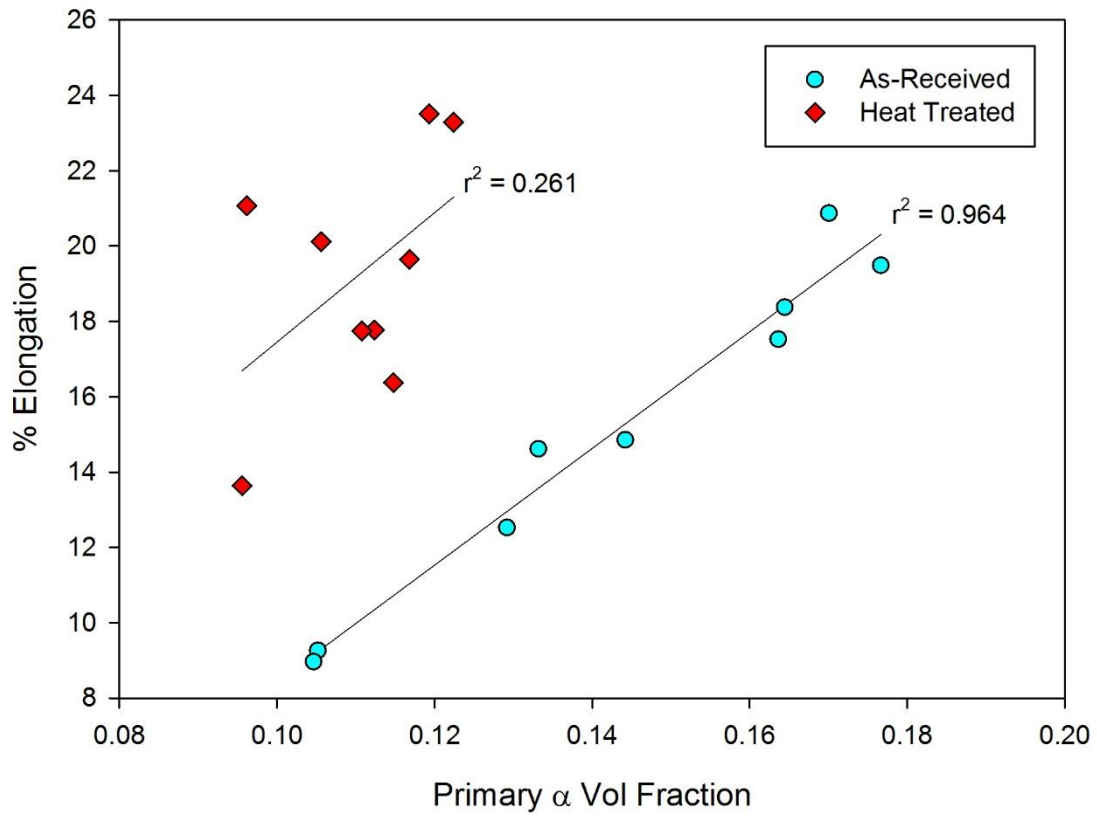
Figure 4.83: Axial % elongation vs primary α volume fraction.
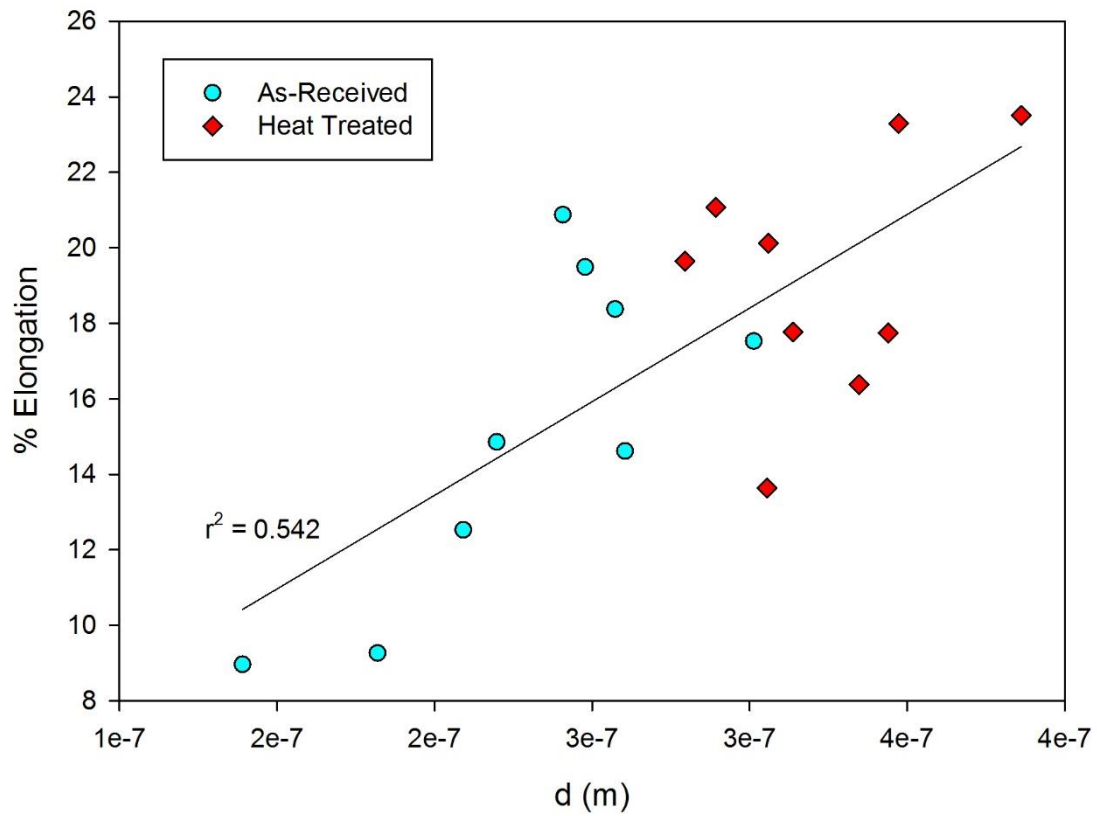
Figure 4.84: Axial % elongation vs secondary α interparticle spacing.

163
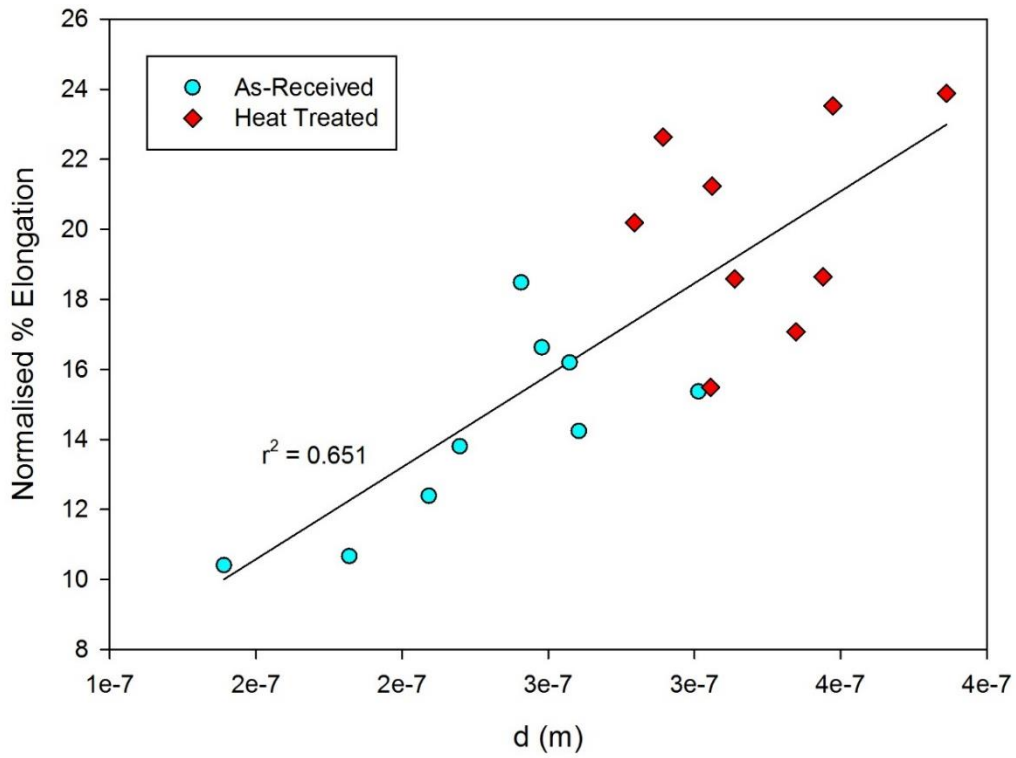
Figure 4.85: Normalised axial % elongation vs secondary α interparticle spacing (normalised to mean α/β ratio).
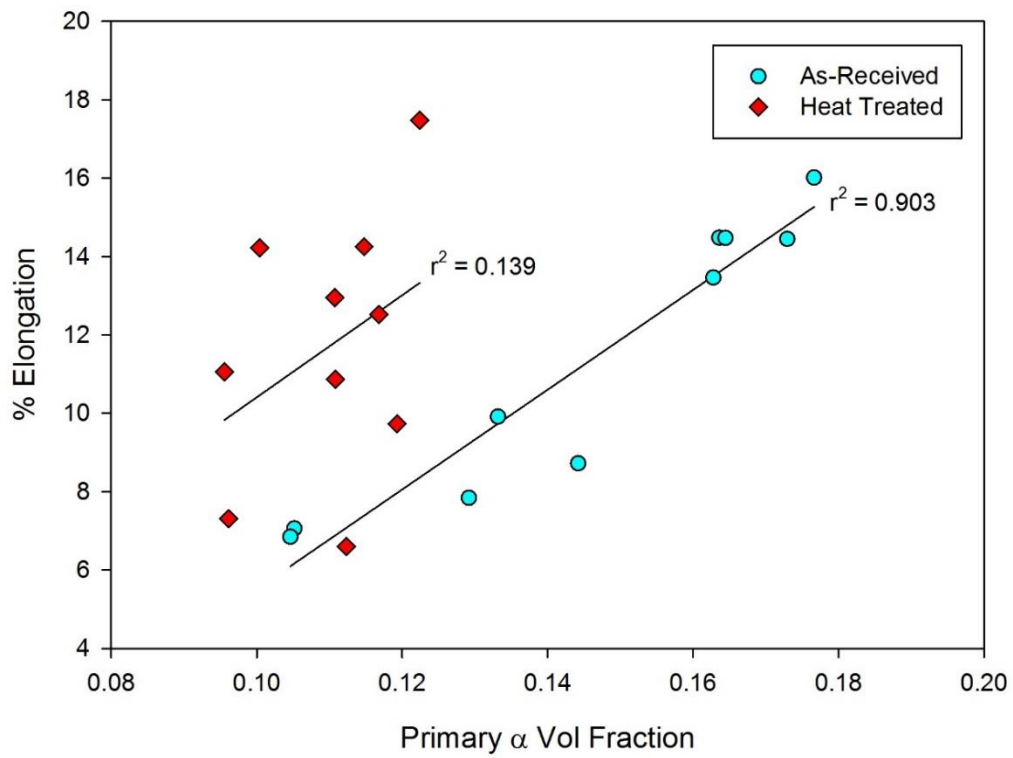
Figure 4.86 Tangential % elongation vs primary α volume fraction.
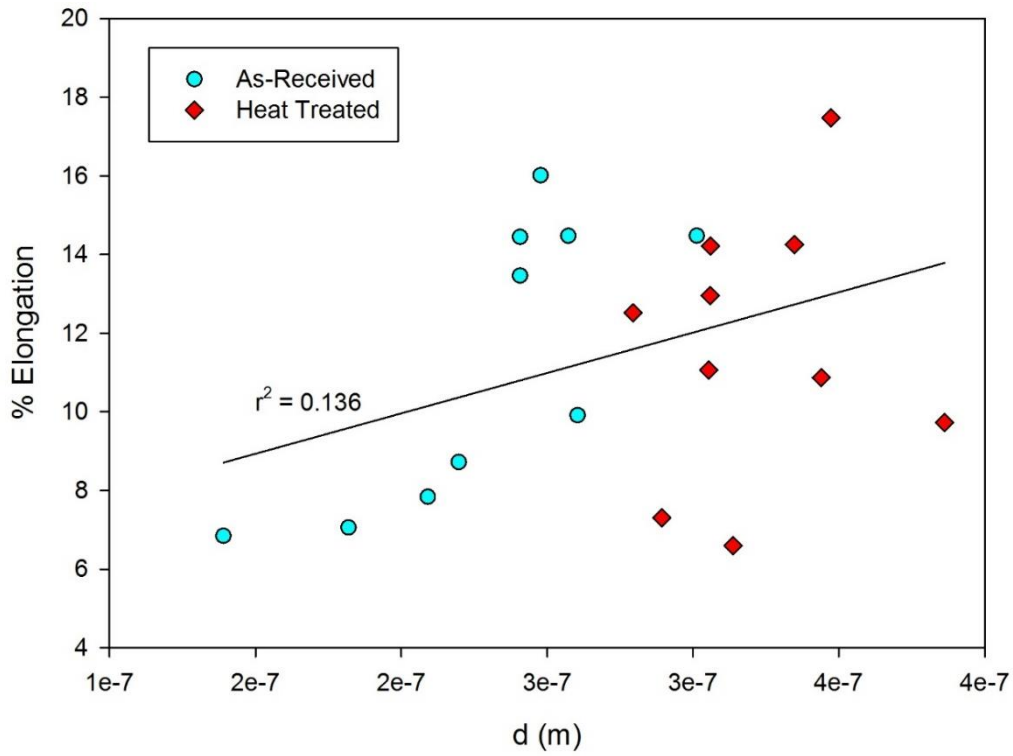
Figure 4.87: Tangential % elongation vs secondary α interparticle spacing.
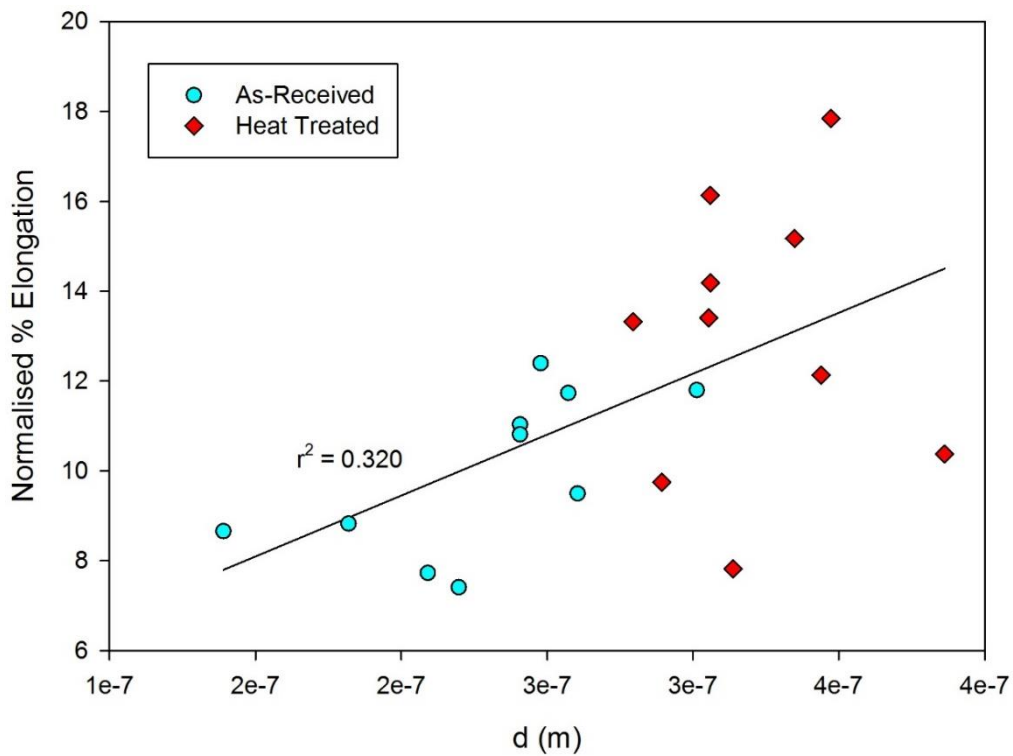
Figure 4.88: Normalised tangential % elongation vs interparticle spacing of secondary α (normalised to the mean α/β ratio).

4.7 Summary

The work presented in this chapter has illustrated the microstructural and mechanical property variation within a Ti-5553 forging. The primary α morphology varies from equiaxed, globular particles near the forging edge to more elongated plates at the forging centre. This is likely due to a lack of strain penetration during forging. However, most of the central region is removed during subsequent machining so the final component properties should be unaffected. The prevalence of grain boundary α also increases towards the centre, probably as a result of slower cooling. The β grain structure consists of deformed, unrecrystallised grains, oriented parallel to the longitudinal axis of the forging. The axial cross-section of these grains varies from an equiaxed morphology at the 'top' edge of the forging to a more 'pancaked' structure along the flash line. At the flash edge, these grains become highly deformed, extending further in the direction of material flow.

It was found that the strength generally increased towards the forging edge, while the ductility showed the opposite trend. The cause of this variation was due in part to changes in the secondary α interparticle spacing (d) and volume fraction of retained β (β_{vf}). This allowed the fitting of equations to provide predictive capabilities, with varying degrees of success. The limitations in the accuracy of this approach are likely due to unspecified variables that distorted the observed correlations. Other microstructural features, such as β grain morphology, orientation and grain boundary α are possible causes of such deviation. It was also noted that the heat treatment response varied with orientation. The axial specimens exhibited the most significant change in mechanical properties post-heat treatment.

The unresponsiveness of the tangential specimens is believed to be the result of other microstructural features that limited the properties in this orientation. The β grain structure is a likely candidate for this role, since the fracture properties of high strength β alloys are heavily influenced by the relative orientation of these grain boundaries [6]. Despite the lack of response in the UTS and % elongation, the tangential proof stress was modified by heat treatment. This appeared to be the result of changes in work hardening behaviour, leaving the UTS essentially unchanged. EBSD analysis confirmed adherence to the Burger's Orientation Relationship (BOR) throughout the forging. Hardness mapping also revealed that changes in the secondary α could cause localised variation in mechanical properties. This variation was significant enough that it could completely reverse the long range trends across the forging. Fortunately, it appears that heat treatment can remove such fluctuations, although it follows that great care is needed to avoid inducing others.

Chapter 5 Microstructural Evolution of Ti-10-2-3

The previous chapter highlighted the importance of microstructural control in order to achieve the required mechanical properties in a metastable β alloy. This chapter examines the relationship between processing and microstructure of the metastable β alloy Ti-10-2-3. While it would have been preferable to continue this investigation on Ti-5553 for consistency, logistical issues in the acquisition of billet material prevented this. However, both Ti-10-2-3 and Ti-5553 are metastable β alloys used in aero structural applications (particularly landing gear), so there is a common goal in optimising both. Initial work began with characterisation of the as-received material and a study of thermal effects on microstructure. Investigation of isothermal forging was carried out through axisymmetric compression testing and torsion tests. The latter permitted application of much larger strains and non-linear strain paths. This is particularly relevant to industrial forging processes which cannot be adequately modelled by monotonic deformation tests. Microstructural development was investigated through microscopy and EBSD. The deformed specimens were then subjected to hardness testing before and after heat treatment in order to infer any changes in mechanical properties. Further microstructural characterisation was then employed to investigate these effects.

5.1 Experimental Method

Figure 5.1 illustrates the as-received Ti-10-2-3 after sectioning. This took the form of a slice of material removed from a cogged billet, provided by TIMET UK. The nominal composition is 10 wt% vanadium, 2 wt% iron and 3 wt% aluminium. The composition specification is included in Table 5.1 [23]. Referring to Figure 5.1, torsion test specimens were removed from the ten oblong blocks, while the excess material at the right-hand end was utilised for initial characterisation and axisymmetric compression tests. Most microstructural observations were made on the plane perpendicular to the Y-axis in Figure 5.1. The exceptions to this were the compression test specimens. Since these were axisymmetric and sectioned along the cylinder axis for analysis, the viewing plane may have been at any angle around the Z-axis (since the cylindrical specimens were removed parallel to the Z-axis).

Small, cube shaped samples, approximately 10 x 10 x 10 mm in size were removed to investigate the effects of time at temperature. These were placed in a furnace pre-heated to 760 °C for intervals of 5, 30, 60 and 600 minutes, before water quenching to room temperature. They were sectioned, mounted and prepared for electron microscopy (SEM) in accordance with the procedures set out in Chapter 3. Quantitative measurements were also made following these methods. A β transus approach curve was constructed using samples solutionised at various temperatures for 60 minutes and then water quenched to room temperature. The solution time of 60 minutes was selected after earlier results confirmed that the equilibrium volume fraction of β phase is reached well within this time period. The quenched specimens were then sectioned, mounted and examined via SEM in the same manner as the time at temperature study.

Hot isothermal compression testing was carried out with the University of Sheffield servo-hydraulic thermomechanical compression (TMC) testing machine. Figure 5.2 illustrates the key dimensions of the test specimen and the experimental setup. The flow stress during testing is calculated from Equation 5.1, where σ_i is the instantaneous stress, and F_i and A_i are the instantaneous load and area at that point in the test. A_i is found by dividing the original volume of the cylindrical specimen by the instantaneous height h (since constant volume is assumed). The strain, ε is given by Equation 5.2, where h_0 is the specimen's original height. Strain rate, $\dot{\varepsilon}$ is determined from Equation 5.3 based on the instantaneous tool velocity, v and the corresponding sample height. In order to minimise the effects of friction, a boron nitride lubricant was applied to all specimens.

The fast thermal treatment unit (FTTU) employs induction heating to rapidly bring a specimen to the required temperature. The tools (platens) are situated within an electric furnace in order to maintain the specimen temperature during deformation. Temperature feedback was provided by a K-type thermocouple inserted into a 1.1 mm diameter hole drilled horizontally into the

specimen at mid height. Once deformation is complete, samples were immediately water quenched. Test specimens had an initial height of 15 mm and diameter of 10 mm. This gives an aspect ratio of 1.5, one of the recommended values from the NPL good practice guidelines [105]. Deformation was carried out at a temperature of 750 °C and at three separate strain rates (1 s^{-1}, 0.1 s^{-1} and 0.01 s^{-1}). The temperature of 750 °C was chosen, rather than the industrial forging temperature of 760 °C due to the proximity of the β transus (about 800 °C). Specimens were deformed to a final height of 6.75 mm (a strain of 0.8). After testing, specimens were sectioned, mounted and prepared for light and electron microscopy as described in Chapter 3.

$$\sigma_i = \frac{F_i}{A_i} \qquad (5.1)$$

$$\varepsilon = \ln\frac{h}{h_0} \qquad (5.2)$$

$$\dot{\varepsilon} = \frac{v}{h} \qquad (5.3)$$

Axisymmetric compression tests are now widely used to provide flow data for forging simulations. However, there are limitations to such tests. The maximum achievable strain is restricted by friction effects that lead to inaccurate flow stresses at high strains. Deformation is also monotonic, meaning the strain path is linear, whereas in real forging operations it can be far more complex. The arbitrary strain path (ASP) testing machine at the University of Sheffield was developed to address these shortcomings. It is capable of applying tension, compression and torsion in sequence or concurrently. The incorporation of induction heating and accelerated cooling equipment also permits the implementation of various thermal treatments during deformation. In this study, it was employed to carry out hot torsion tests in order to investigate the effect of process variables on microstructural development.

Figure 5.3 illustrates the testpiece used in these tests. It is oriented vertically in the machine and clamped at either end. The reduced length (gauge length) is heated by an induction coil encircling it and torque is applied by an upper actuator. Figure 5.4 shows a DEFORM simulation of the strain distribution within the gauge length of a Ti-10-2-3 specimen. Because the specimen is twisted during torsion, a thermocouple cannot be placed directly in the reduced length. Instead, a hole is drilled diagonally into the specimen shoulder as close as possible to the deformation region (see Figure 5.3). This leads to a temperature difference between the thermocouple reading and the actual temperature in the gauge length. As such, the first test

carried out was a static one in order to determine the temperature difference between the shoulder thermocouple and one positioned in the gauge length. At 760 °C, this difference was found to be approximately 12 °C. Consequently, the target temperature for the software was set 12 °C below the intended temperature in the gauge length.

Figure 5.1: Ti-10-2-3 as-received material after sectioning (305 mm ruler)

Table 5.1: TIMET specification for Ti-10-2-3 [88].

	V	Fe	Al	O	C	N	H	Residuals (each)	Residuals (total)
Max (wt%)	11.0	2.2	3.4	0.13	0.05	0.05	0.015	0.10	0.13
Min (wt%)	9.0	1.6	2.6	-	-	-	-	-	-
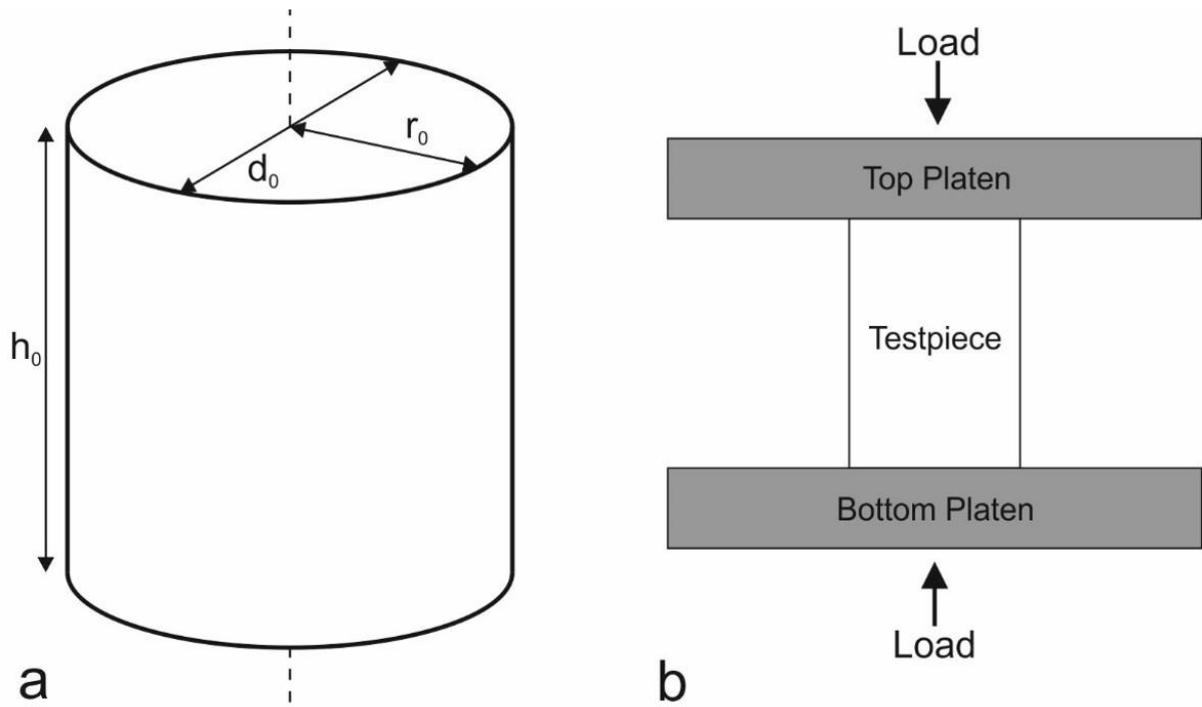
Figure 5.2: (a) Axisymmetric TMC specimen and (b) test setup
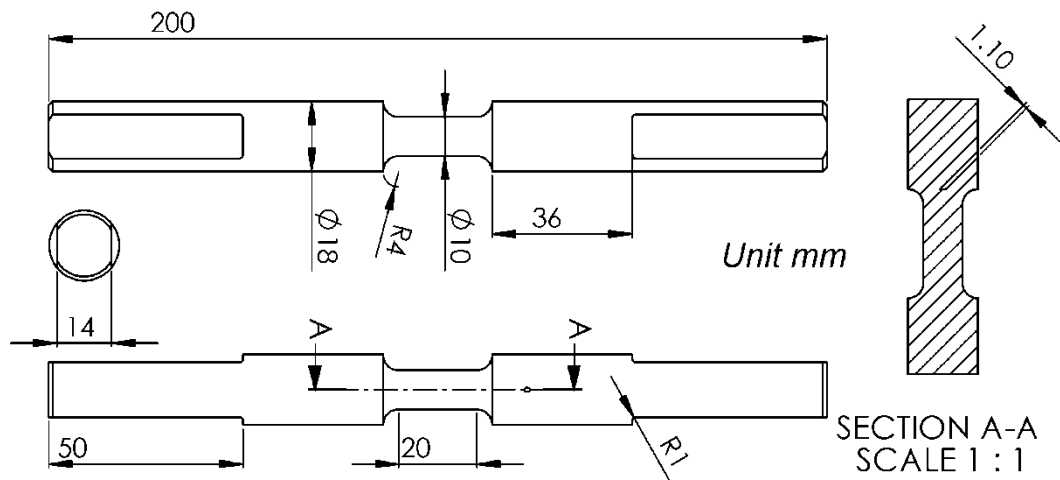
Figure 5.3: Solid torsion test specimen for use with the ASP. Image provided courtesy of L. Sun.
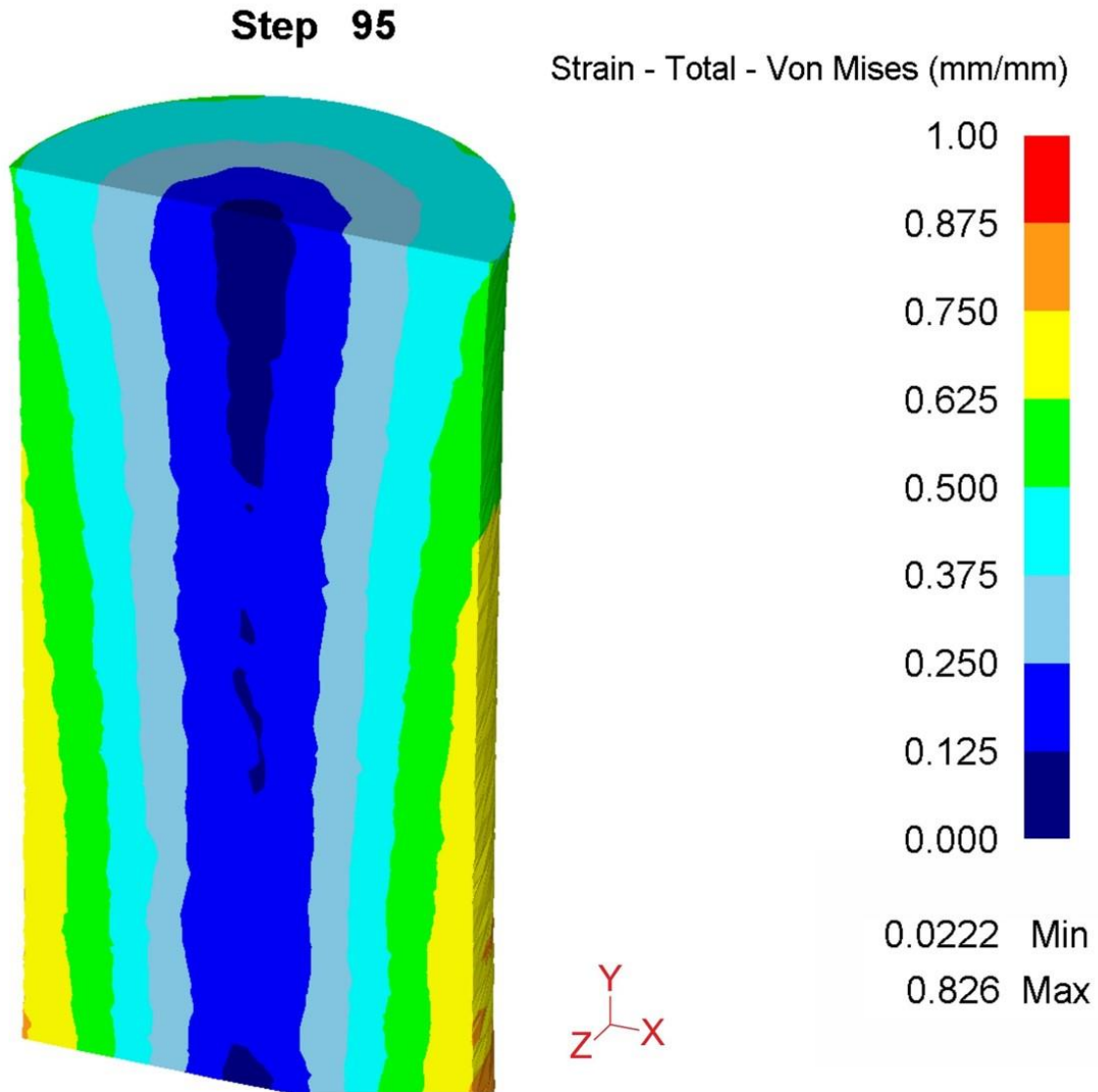
Figure 5.4: DEFORM simulation of the strain distribution within the gauge length of a solid torsion test specimen. Courtesy of B. Thomas.

In order to compare a hot torsion test with other thermomechanical tests (e.g. axisymmetric compression), the torque-angle data must be converted into equivalent stress-strain. As illustrated in Figure 5.5, deformation of a cylinder through torsion can be related to shear by considering it as the rotation of many thin 'slices'. The shear strain (γ) and shear strain rate ($\dot{\gamma}$) during a torsion test can thus be calculated with use of the following equations:

$$\gamma = \tan \alpha = \frac{r\theta}{l} \qquad (5.4)$$

$$\dot{\gamma} = \frac{r\dot{\theta}}{l} \qquad (5.5)$$

172

Where r is the radius of interest, θ is the twist angle (in radians), $\dot{\theta}$ is the angular velocity (in radians per second) and l is the gauge length. The shear strain and shear strain rate can then be used to determine the von Mises equivalent strain (ε_{vm}) and strain rate ($\dot{\varepsilon}_{vm}$) with Equations 5.6 and 5.7.

$$\varepsilon_{vm} = \frac{\gamma}{\sqrt{3}} \tag{5.6}$$

$$\dot{\varepsilon}_{vm} = \frac{\dot{\gamma}}{\sqrt{3}} \tag{5.7}$$
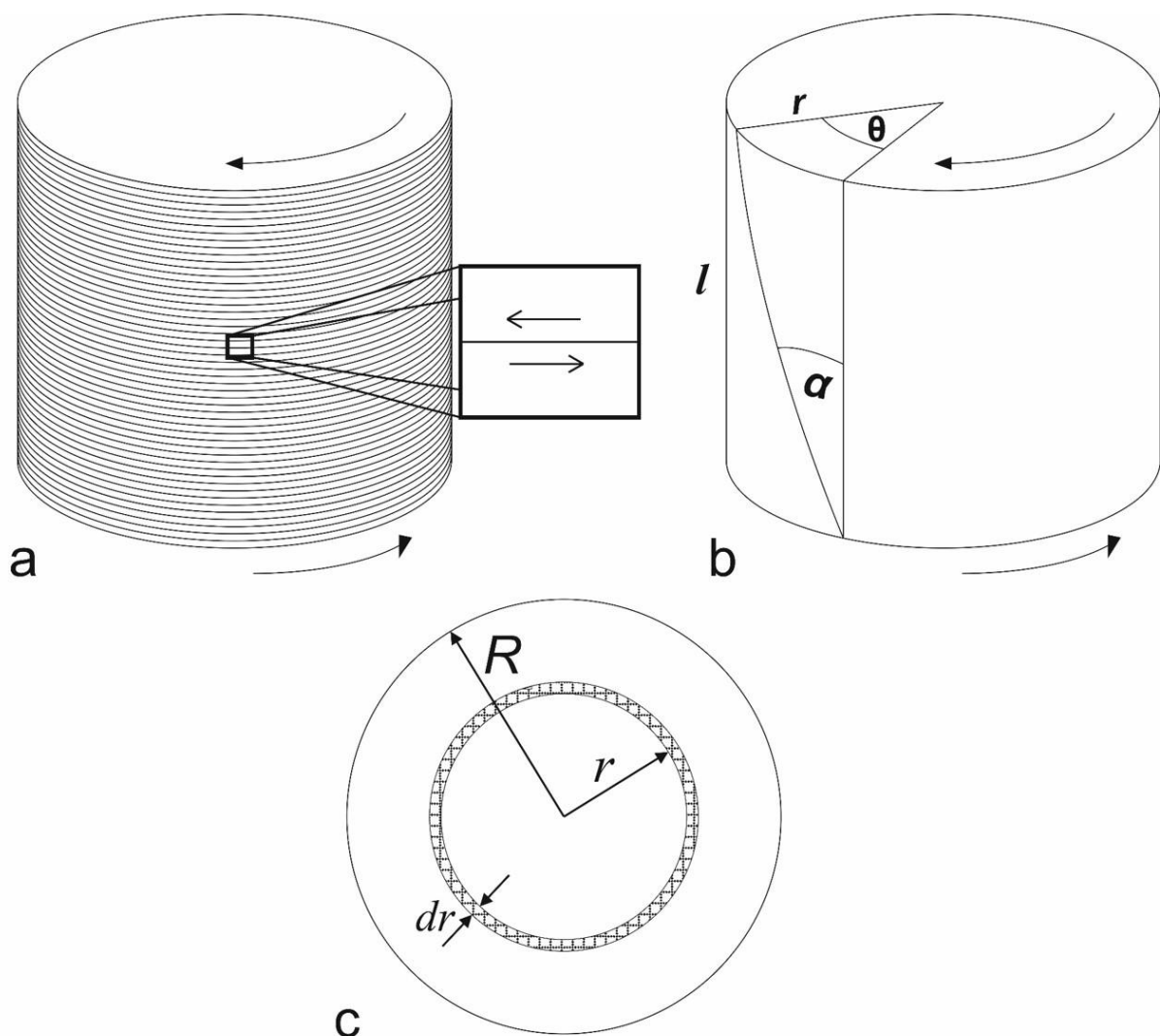
Figure 5.5: (a) Illustrates the relationship between torsion and shear by considering a cylinder subdivided into many 'thin slices', (b) the geometrical quantities required for calculation of shear strain and (c) cross section through a solid test specimen, oriented perpendicular to the specimen axis. Redrawn from [106].

It should be noted that the strain and strain rate will vary linearly from zero at the cylinder centre to a maximum at the cylinder surface. If the surface strain/strain rate is calculated first, the value at any fraction of the radius can be found simply by multiplying by that fraction. However, calculation of the von Mises equivalent stress in a solid bar torsion test is somewhat more complex than determining the strain. During torsion of a solid specimen, the component of torque $d\Gamma$ at radius r is given by:

$$d\Gamma = r \times dF \tag{5.8}$$

Where dF is the component of force at radius r. This force can be determined from the shear stress at r and the cross sectional area on which it acts dA:

$$dF = \tau_r \cdot dA \tag{5.9}$$

In principle, the cross sectional area is zero, since r traces a circular line. However, by considering the specimen cross-section as a series of concentric rings of infinitesimal width dr (see Figure 5.5(c)) the area dA can be found from:

$$dA = 2\pi r \cdot dr \tag{5.10}$$

Combining Equations 5.8, 5.9 and 5.10:

$$d\Gamma = 2\pi r^2 \tau_r \cdot dr \tag{5.11}$$

The total torque for a solid specimen can then be found by integrating across the radius from centre to edge:

$$\Gamma = 2\pi \int_0^R r^2 \tau_r \cdot dr \tag{5.12}$$

Given that the shear stress is a function of shear strain and shear strain rate, the following relationship is assumed [107]:

$$\tau_r = K\gamma^n \dot{\gamma}^m \tag{5.13}$$

Where n is the strain hardening exponent, m is the strain rate sensitivity and K is a constant.

Combining Equations 5.4, 5.5 and 5.13:

$$\tau_r = K \left(\frac{r\theta}{l}\right)^n \left(\frac{r\dot{\theta}}{l}\right)^m \tag{5.14}$$

And substituting Equation 5.14 into 5.12:

$$\Gamma = 2\pi \int\limits_0^R r^2 K \left(\frac{r\theta}{l}\right)^n \left(\frac{r\dot{\theta}}{l}\right)^m \cdot dr$$

$$= 2\pi K \left(\frac{\theta}{l}\right)^n \left(\frac{\dot{\theta}}{l}\right)^m \int\limits_0^R r^{m+n+2} \cdot dr$$

$$= \frac{2\pi K \left(\frac{\theta}{l}\right)^n \left(\frac{\dot{\theta}}{l}\right)^m R^{m+n+3}}{m+n+3}$$

$$= \frac{2\pi K \left(\frac{R\theta}{l}\right)^n \left(\frac{R\dot{\theta}}{l}\right)^m R^3}{m+n+3}$$

$$= \frac{2\pi \tau_R R^3}{m+n+3} \tag{5.15}$$

Rearranging Equation 5.15 to give shear stress τ_R at the specimen surface ($r = R$) as a function of total torque Γ:

$$\tau_R = \frac{(m+n+3)\Gamma}{2\pi R^3} \tag{5.16}$$

Equation 5.16 represents the method developed by *Fields* and *Backofen* [108]. However, the values of n and m must be determined experimentally, and their own dependence on strain and strain rate (respectively) makes conversion arduous. Barraclough et al. devised a method involving an '*effective radius*', where the influence of m and n can be assumed to cancel [107]. Rewriting Equation 5.15 as a function of shear stress at a given radius, r:

$$\Gamma = \frac{2\pi \tau_r R^{m+n+3}}{(m+n+3)r^{m+n}} \tag{5.17}$$

And rearranging for shear stress:

$$\tau_r = \frac{(m + n + 3)r^{m+n}\Gamma}{2\pi R^{m+n+3}} \tag{5.18}$$

From Equation 5.15, now consider the case where (m+n) = 0, giving a constant value of shear stress τ^*:

$$\Gamma = \frac{2\pi \tau^* R^3}{3} \tag{5.19}$$

And rearranging for shear stress:

$$\tau^* = \frac{3\Gamma}{2\pi R^3} \tag{5.20}$$

Therefore, from Equations 5.18 and 5.20, at a constant torque, the ratio of τ^* to τ_r is given by:

$$\frac{\tau^*}{\tau_r} = \frac{3}{(m + n + 3)} \cdot \left(\frac{R}{r}\right)^{m+n} \tag{5.21}$$

Figure 5.6 presents τ^*/τ_r as a function of the fractional radius (r/R) for a range of (m+n) values. It can be seen that there is an 'effective radius' r_e where the influence of (m+n) is zero. Furthermore, the position of this radius is almost independent of (m+n).
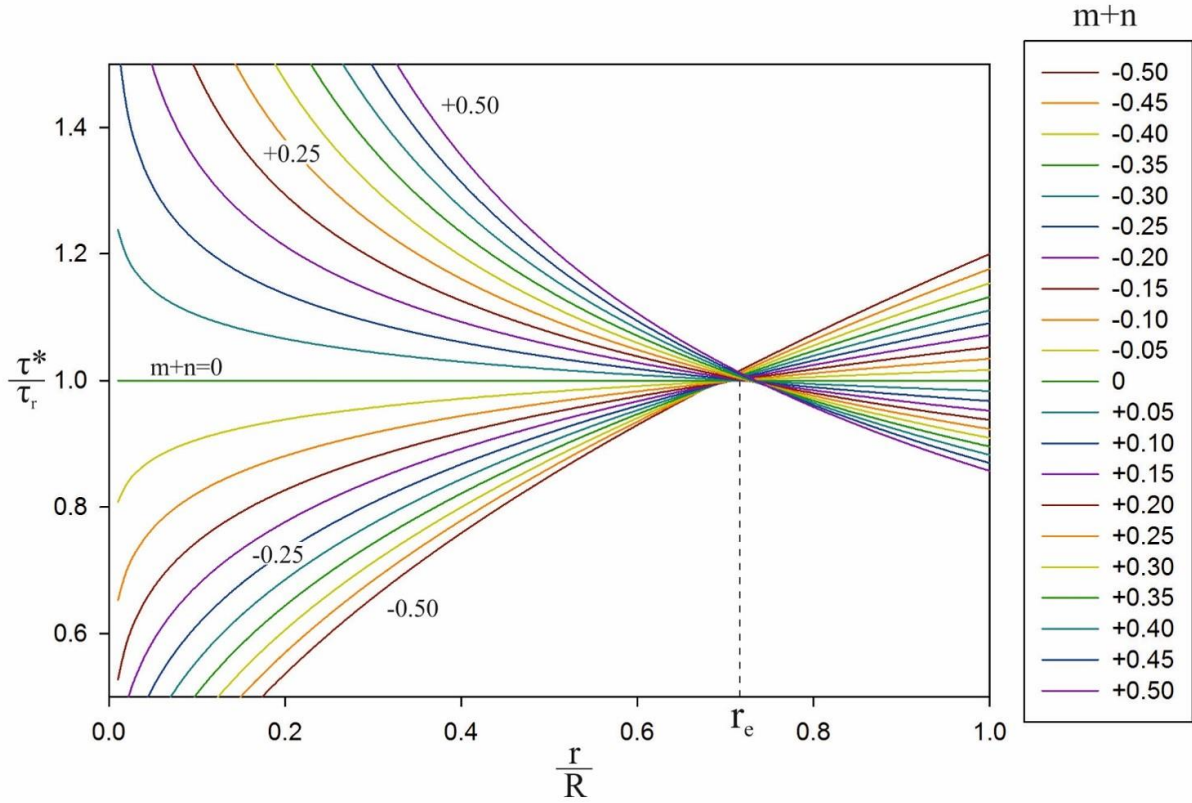
Figure 5.6: τ^*/τ_r as a function of the fractional radius (r/R) for a range of (m+n) values. Based upon [106][107].

At the effective radius, $\tau^*/\tau_r = 1$. Substituting this and r_e into Equation 5.21:

$$1 = \frac{3}{(m+n+3)} \cdot \left(\frac{R}{r_e}\right)^{m+n} \tag{5.22}$$

Setting R = 1 and rearranging for r_e:

$$r_e = \left(\frac{3}{m+n+3}\right)^{\frac{1}{m+n}} \tag{5.23}$$

For an (m+n) value of +0.2, this gives an effective radius of 72.4% of the surface radius. As Figure 5.7 shows, the value of τ^*/τ_r at this radius varies by less than 0.5% between (m+n) values of -0.2 and +0.4. Therefore, the method proposed by Barraclough et al. allows a reasonable comparison between tests, and simplifies the calculation of flow stress by avoiding the need for m and n. This technique has been utilised by a number of researchers on various materials, including titanium [106][109][110].
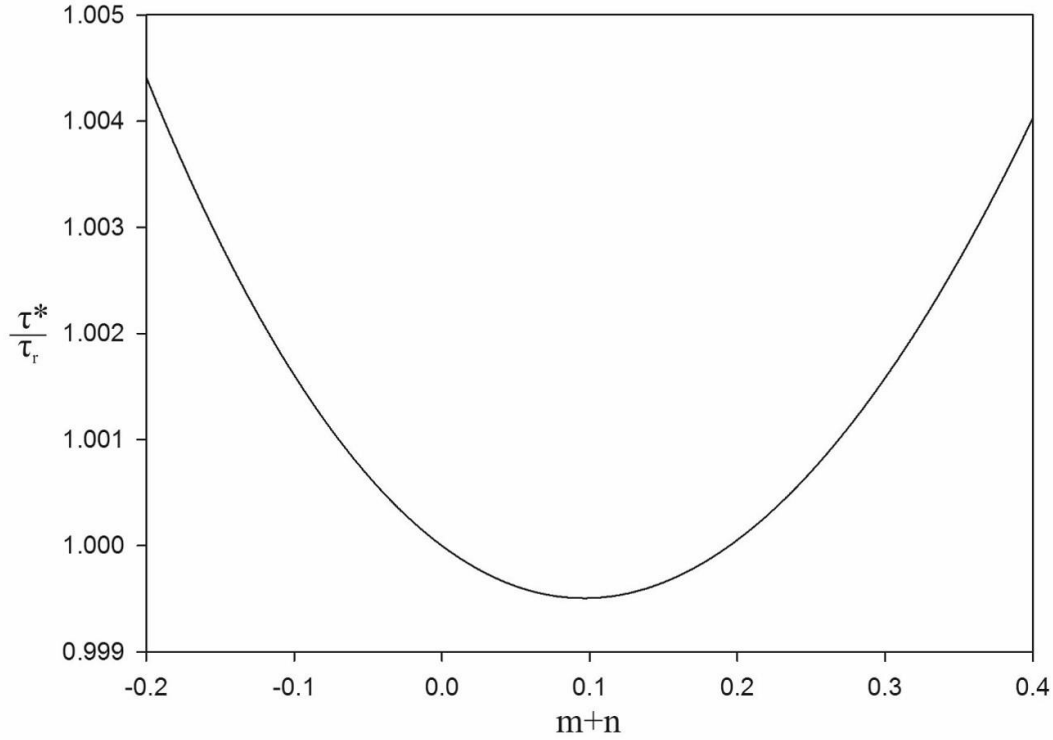
Figure 5.7: Variation of τ^*/τ_r with a range of (m+n) values at a radius of 0.724R. Based upon [107].

Conversion of the shear stress to von Mises equivalent stress is then achieved through:

$$\sigma_{vm} = \sqrt{3}\tau \tag{5.24}$$

Where σ_{vm} is von Mises equivalent stress. Substituting Equation 5.20 into Equation 5.24 then gives the equivalent flow stress at the effective radius:

$$\sigma_{vm} = \frac{3\sqrt{3}\Gamma}{2\pi R^3} \tag{5.25}$$

The test series is set out in Table 5.2. The first test was static in order to determine the temperature difference between the gauge length and thermocouple. Test 2-4 share the same strain path (0.724 'forward' at the critical radius) but cover three separate temperatures. These include the industrial forging temperature (760 °C) and two temperatures either side of this to examine the effect of temperature. The term 'forward' (or FWD) describes the fact that these specimens were twisted in only one direction, whereas tests 5 and 7 incorporated 'strain reversal'. In this investigation, all reversed tests were 'fully reversed' back to their starting positions, making the total strain of such tests exactly double their FWD strain. However, for brevity 'fully reversed' tests will be referred to simply as 'reversed' tests. For consistency with

178

the TMC results, tests (5-7) were carried out at 750 °C. Test 6 shares the same total strain as test 5, and the same FWD strain as test 7, in order to study the effect of strain reversal. The strain rate for all tests was 0.01 s^{-1} at 72.4% of the specimen radius (0.724R). This was chosen to minimise adiabatic heating in an attempt to maintain isothermal conditions. After deformation, all samples were water quenched to preserve the high temperature microstructure for characterisation. SEM and EBSD were employed to examine the as-deformed microstructures, and hardness testing was utilised to try and elucidate any mechanical property variation.

Tests 1 and 5-7 were also heat treated to investigate indirect effects upon microstructure and mechanical properties. The treatment was carried out in accordance with the TIMET specification for the high strength condition. This consisted of a solution treatment at 42 °C below the β transus (±21 °C) for 30 minutes, followed by ageing at 496 °C (±14 °C) for 8 hours. The solution treatment temperature was common to all strength levels, but the ageing temperature varied, with the high strength condition having the lowest ageing temperature. Samples were water quenched from the solution temperature, although air cooling had been an option due to their small size. Air cooling to room temperature was employed after ageing [88].

Table 5.2: Test conditions for Ti-10-2-3 hot torsion tests (strain rate = 0.01 s^{-1} at 0.724R, excluding test 1).

Test No.	Strain Path	Target Temp (°C)
1	None	760
2	0.724 FWD	750
3	0.724 FWD	760
4	0.724 FWD	775
5	0.6 FWD 0.6 REV	750
6	1.2 FWD	750
7	1.2 FWD 1.2 REV	750

5.2 Time at Temperature

Figure 5.8 shows the microstructure of the as-received material. It can be seen that the primary α takes the form of high aspect ratio plates of about 1 µm in thickness. There are also semi-continuous layers of α along the β grain boundaries. At higher magnification, a fine distribution of secondary α platelets is visible within the retained β matrix. The lack of globular α and its 'angular' shape would suggest that the primary α has not been subjected to deformation. This would imply that the billet was β forged, and both the coarse and fine α distributions formed during subsequent thermal treatments and/or cooling [84]. The coarse α plates may not therefore fit the technical definition of 'primary α' since they might not have been present at the forging temperature. However, since they were present during the subtransus forging carried out in this study, the term 'primary α' will continue to be used. Figure 5.9 illustrates the effect of time at temperature on this microstructure. At 760 °C the secondary α dissolves relatively quickly, aided by its small size.
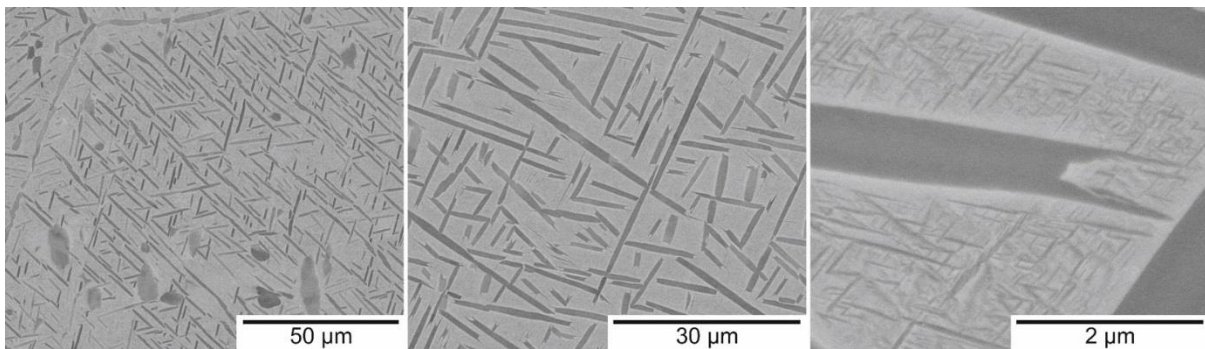
Figure 5.8: BSEI micrographs of as-received material (plane perpendicular to Y-axis).

While the primary α does not respond quite as rapidly, it does show a large drop in volume fraction in the first 5 minutes at temperature (see Figure 5.10). There is a much smaller reduction in the following 25 minutes, at which point the equilibrium volume fraction appears to have been reached as there is very little variation over the following 550 minutes. The initial drop in volume fraction is noticeable in Figure 5.9 as a reduction in the size and density of the primary α particles. Figure 5.11 illustrates the change (or lack thereof) in particle morphology by showing the variation in median feret diameter (see Section 3.2). Since the data was not normally distributed, the median was taken to be a more reliable measure of central tendency than the mean. It can be seen that the feret min and feret max exhibit very little variation over the entire heat treatment, with only a slight increase after 600 minutes. However, it is difficult to say whether such a small change is significant or merely a random fluctuation. Either way, the process of spheroidisation is clearly very slow. However, it does still lead to a noticeable rounding of the ends of the α particles.
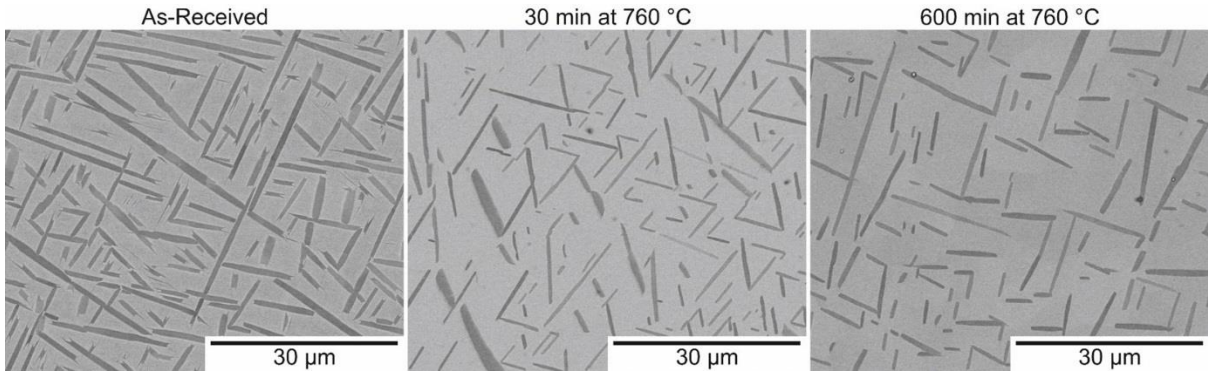
Figure 5.9: BSEI micrographs of the effect of time at temperature on the as-received microstructure.
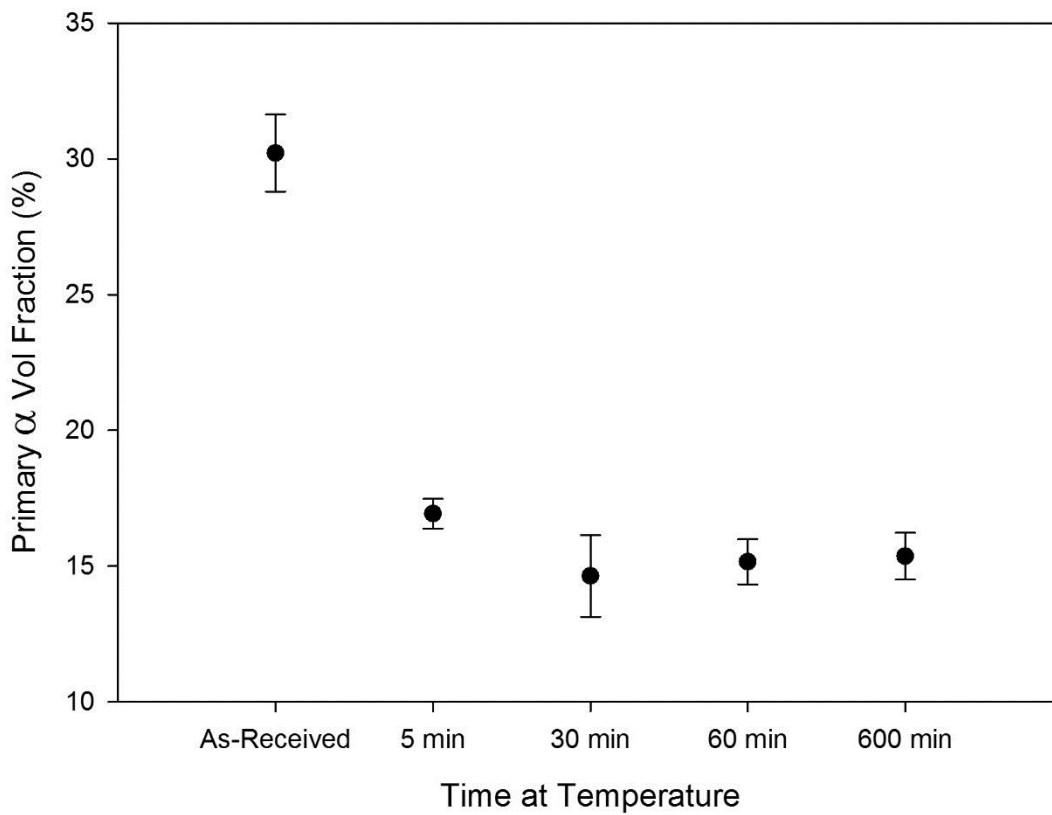
Figure 5.10: Effect of time at temperature (760 °C) on the primary α volume fraction. Error bars illustrate the 95% confidence limit.
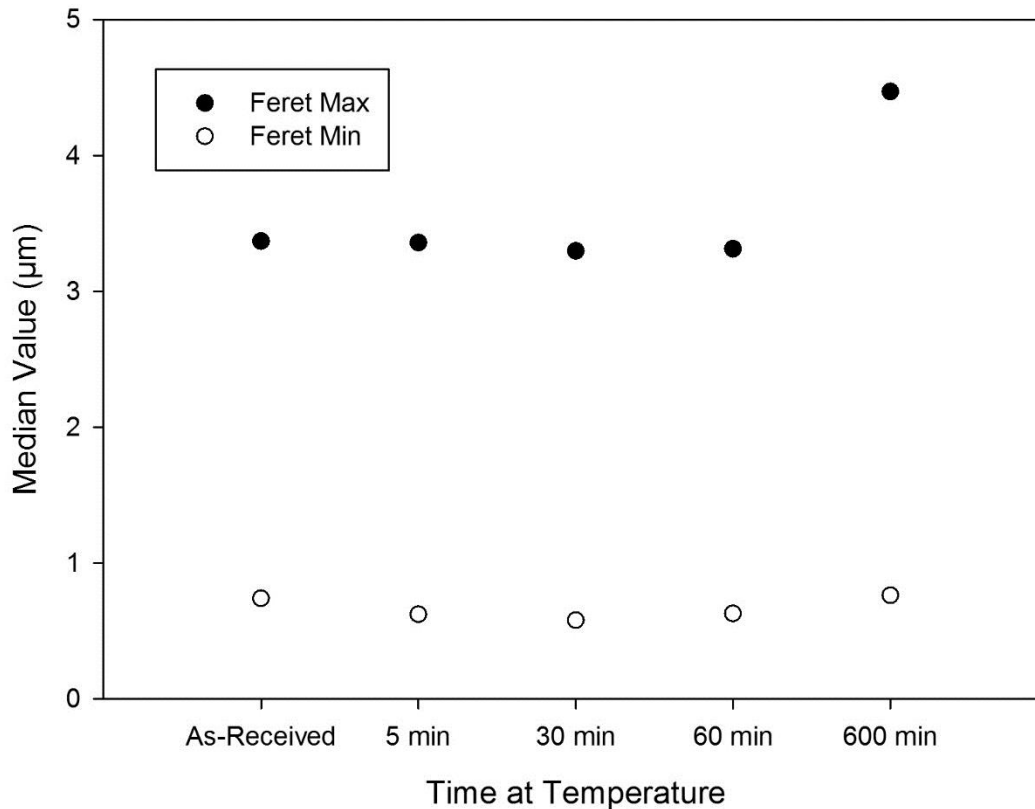
Figure 5.11: Effect of time at temperature (760 °C) on the feret min and feret max of the primary α particles (median values).

5.3 Beta Approach Curve

The β transus approach curve of the as-received material is shown in Figure 5.12. Each data point represents the mean area fraction of β phase computed from 10 micrographs per sample. Over the temperature range in question, the trend appears reasonably linear. A straight line was then fitted and extrapolated to 100% β in order to estimate the transus. This gave a value of approximately 805 °C, not far from the TIMET specification (800 °C). It should also be noted that long range segregation could lead to variation in the exact value of the transus throughout the billet. The slope of the approach curve can also be used to estimate the actual temperature of thermomechanical tests based on the retained β volume fraction (referred to in Table 5.3 as the 'metallographic' temperature).

One of the advantages that the newer, Ti-5553 is reported to offer over Ti-10-2-3 is a shallower approach curve. This provides more forgiving processing characteristics as the volume fraction of primary α is less sensitive to minor temperature fluctuations. The approach curve for Ti-5553 determined by Jones gave a β volume fraction of 92% at T_β-45°C, compared to 85% for the Ti-10-2-3 at the same relative temperature in Figure 5.12 [93]. This would concur with the reports of others about the shallower approach curve in Ti-5553 [8].

182
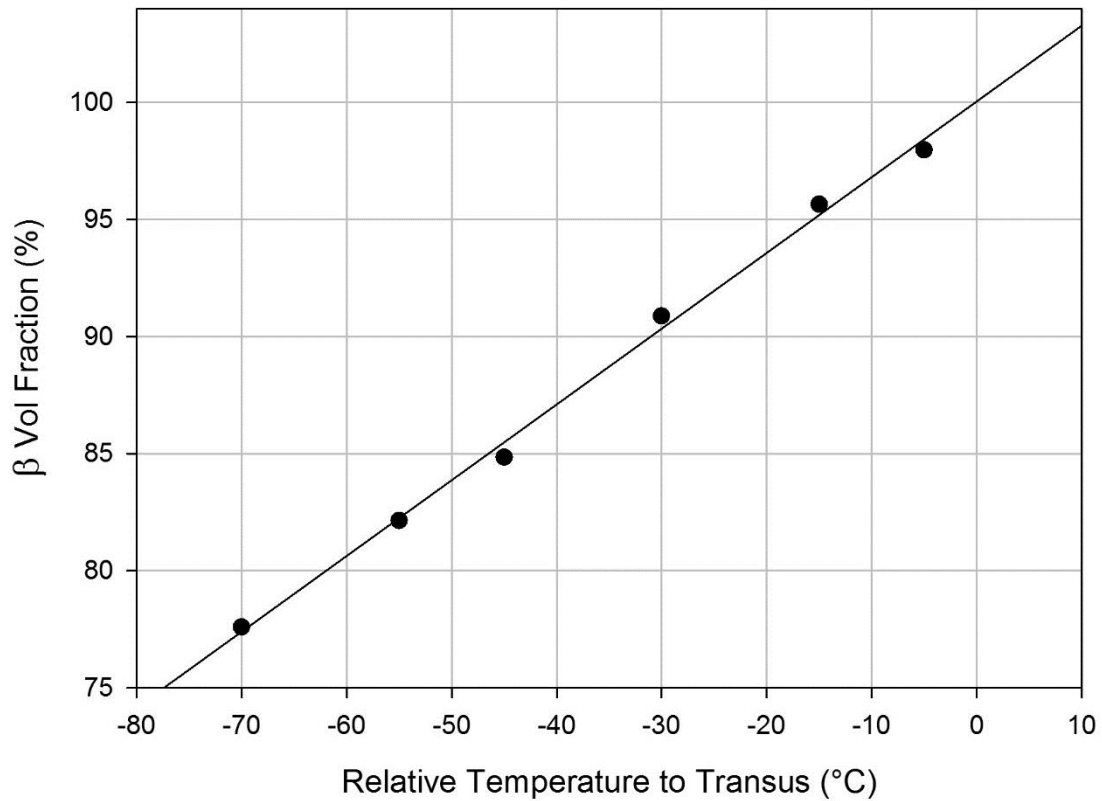
Figure 5.12: Ti-10-2-3 β approach curve (transus approximately 805 °C).

5.4 Thermomechanical Compression Testing

Flow curves of the axisymmetric compression tests at 750 °C are presented in Figure 5.13. It can be seen that the flow stress rises as the strain rate is increased. A significant degree of flow softening is also observed at all three strain rates, the magnitude of which is greatest at the highest strain rate (1 s^{-1}). The cause of such softening has been ascribed to several factors, including the break-up of primary α particles and adiabatic heating effects [66][111]. As Figure 5.14 illustrates, isothermal conditions were not maintained during testing, with significant temperature fluctuations recorded throughout deformation. All specimens began deformation below the target temperature (750 °C) and then exhibited some degree of temperature fluctuation. The greatest variation is seen in the highest strain rate test (1 s^{-1}), with a temperature rise of approximately 50 °C. At such a strain rate, the strain is imparted too quickly to allow adequate heat dissipation during deformation. However, the smallest variation is not seen at the slowest strain rate (0.01 s^{-1}), but at the intermediate strain rate (0.01 s^{-1}). The slowest strain rate specimen actually saw a drop in temperature of about 10 °C, before a gradual recovery to its initial temperature. This was likely due to the tools being heated slightly below the test temperature in order to help dissipate heat generated during deformation. This may have overcompensated for the low strain rate test, and under compensated for the high strain rate test, leading to the observed fluctuations. These factors

may have better balanced each other in the intermediate strain rate test, which exhibited the most consistent temperature profile. However, despite the temperature rise at high strain rates (which should lower the flow stress) and temperature drop at the lowest strain rate (which should increase the flow stress), the shape of the flow curves all appear qualitatively similar. This would suggest that the temperature fluctuations cannot account for all of the observed flow softening. However, the magnitude of flow softening does increase with increasing strain rate, indicating that the contribution from adiabatic heating plays a greater role at higher strain rates. Another factor to consider is the strain rate. Fortunately, as can be seen in Figure 5.15, the strain rate control of the TMC machine was quite good. At low and intermediate strain rates, the equipment was able to maintain a relatively consistent rate of deformation. At the highest strain rate there was an initial fluctuation as the machine responded to the sudden increase in load, after which the strain rate settled around its intended value (1 s^{-1}). This fluctuation consisted of a brief drop in strain rate, followed by a minor increase, which seems inconsistent with the observed flow softening, and therefore seems unlikely to be the cause.
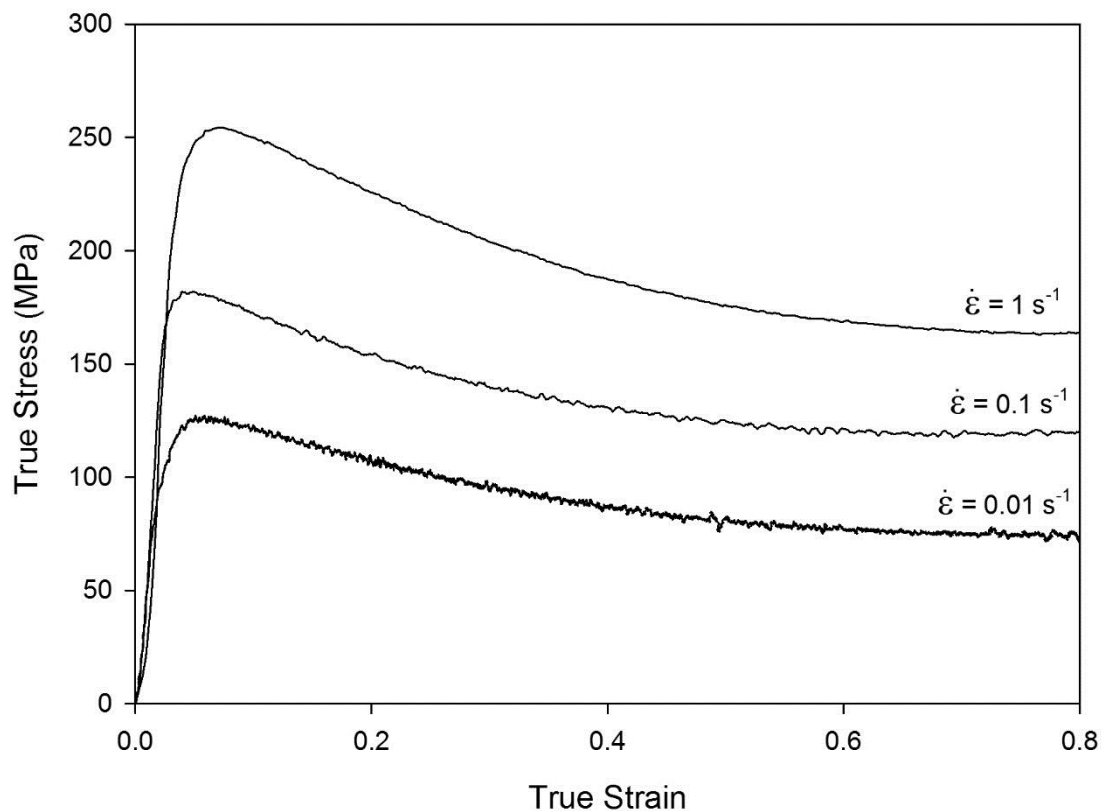
Figure 5.13: Flow curves for axisymmetric compression of Ti-10-2-3 at 750 °C.
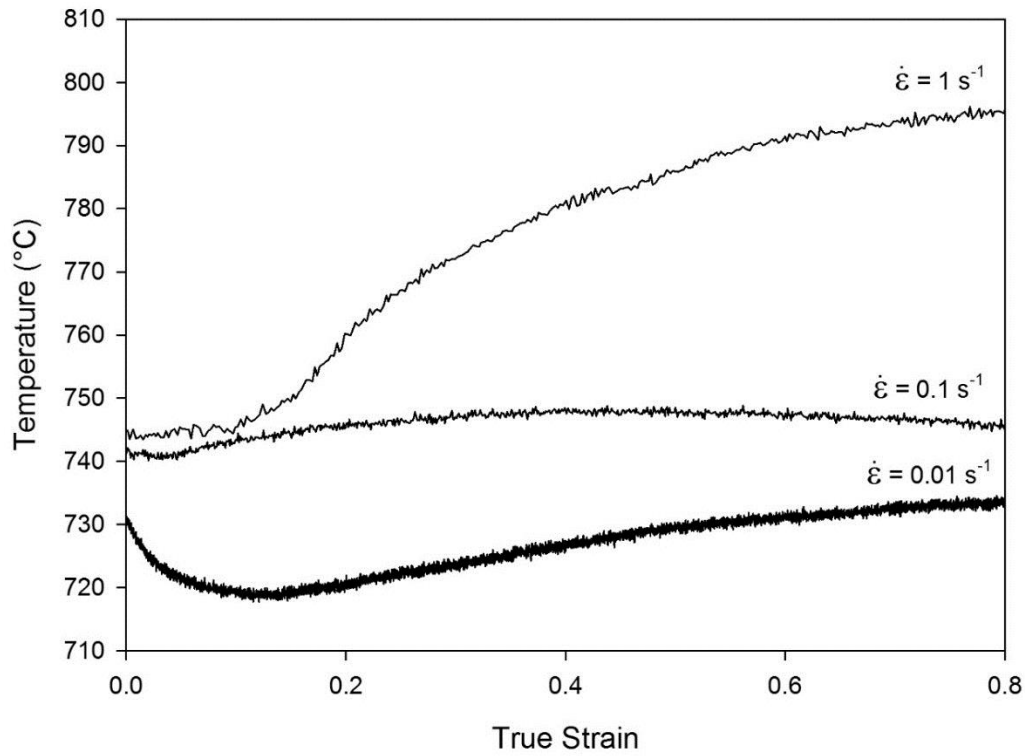
Figure 5.14: Temperature-strain plot of axisymmetric compression tests of Ti-10-2-3 (target temperature: 750 °C).
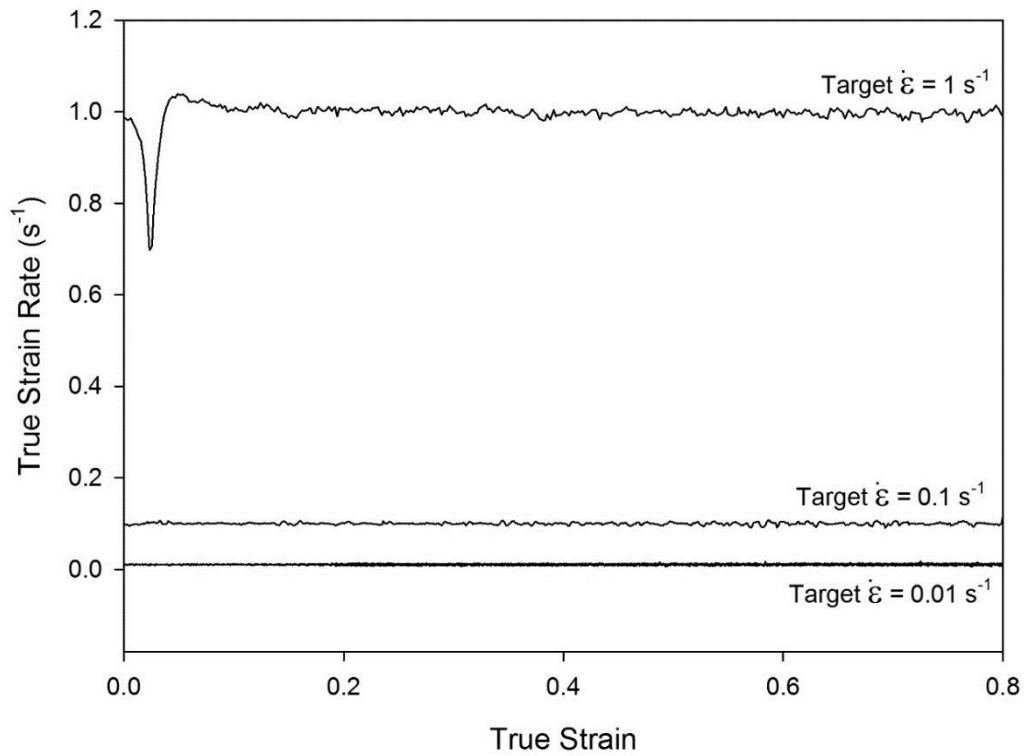
Figure 5.15: Strain rate-strain plot of axisymmetric compression tests of Ti-10-2-3 (target temperature: 750 °C).

Figure 5.16 illustrates the macrostructure of the specimens after sectioning along the cylinder axis. The distortion of the β grains is more apparent as the strain rate increases. In the highest strain rate test (Figure 5.16(c)), a characteristic X of intense deformation is just visible. However, even in the lower strain rate tests, there is still evidence of localised deformation at the specimen mid height. Here the β grains appear more pancaked relative to the 'dead zones', near the tool interface. This strain inhomogeneity is caused by friction constraining material at the specimen-tool interface, giving rise to the 'barrelled' shape of the specimen.
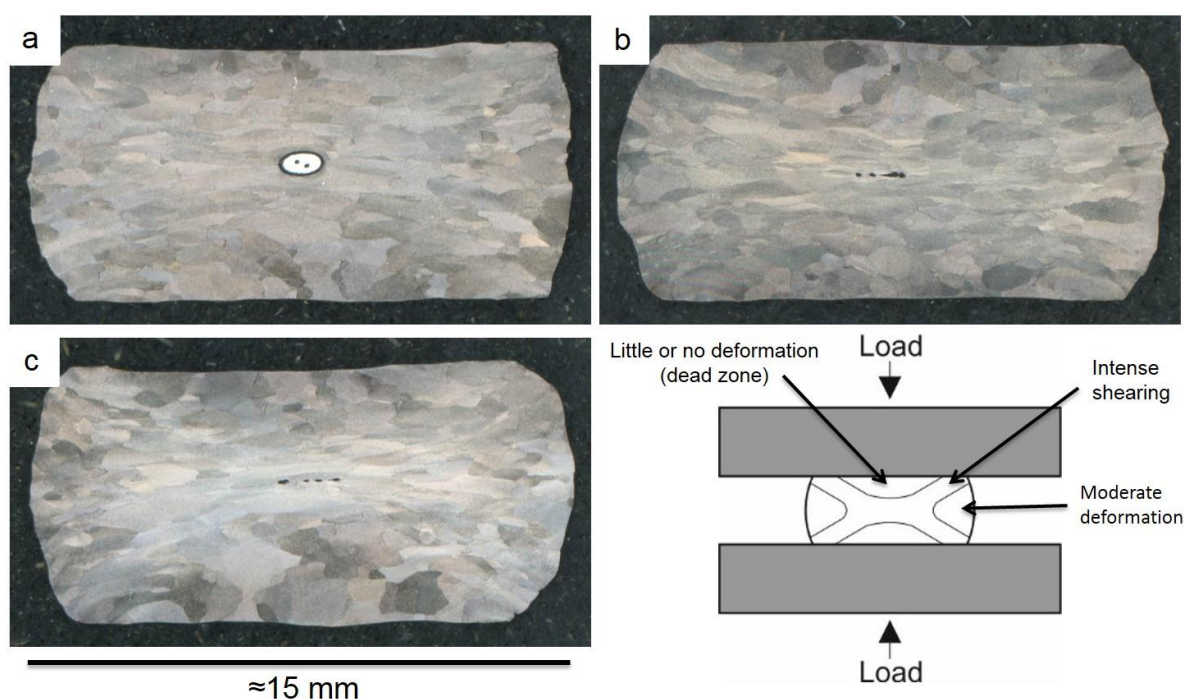
Figure 5.16: Etched macrostructural cross-sections of Ti-10-2-3 axisymmetric TMC specimens at strain rates of (a) 0.01 s^{-1}, (b) 0.1 s^{-1}, (c) 1 s^{-1} and (d) illustration of non-uniform strain distribution due to friction. Ellipse at (a) centre is the thermocouple.

Light microscopy of the high strain regions reveal rotation of the α plates parallel to the shear direction (see Figure 5.17). Electron microscopy also shows the microstructural variation brought about by the non-uniform strain distribution throughout the specimen (see Figure 5.18). Near the sample centre (Figure 5.18(b)), the high level of strain has led to fragmentation/globularisation of the primary α plates, although some elongated particles persist even in this area. Towards the sample edge (Figure 5.18(c)), where the level of strain was lower, there is some distortion of the primary α but considerably less globularisation. Meanwhile, at the top of the sample, in one of the 'dead zones', the microstructure appears essentially undeformed (Figure 5.18(a)). Such microstructural inhomogeneity is difficult to avoid in compression tests, although finite element modelling (FEM) has shown in many alloys that the average stress/strain data produced is still quite reliable in spite of such variation

[111][112]. However, as mentioned earlier, the maximum achievable strain and complexity of the strain path are limited by the testing methodology. To address this, the ASP machine was employed to investigate further.
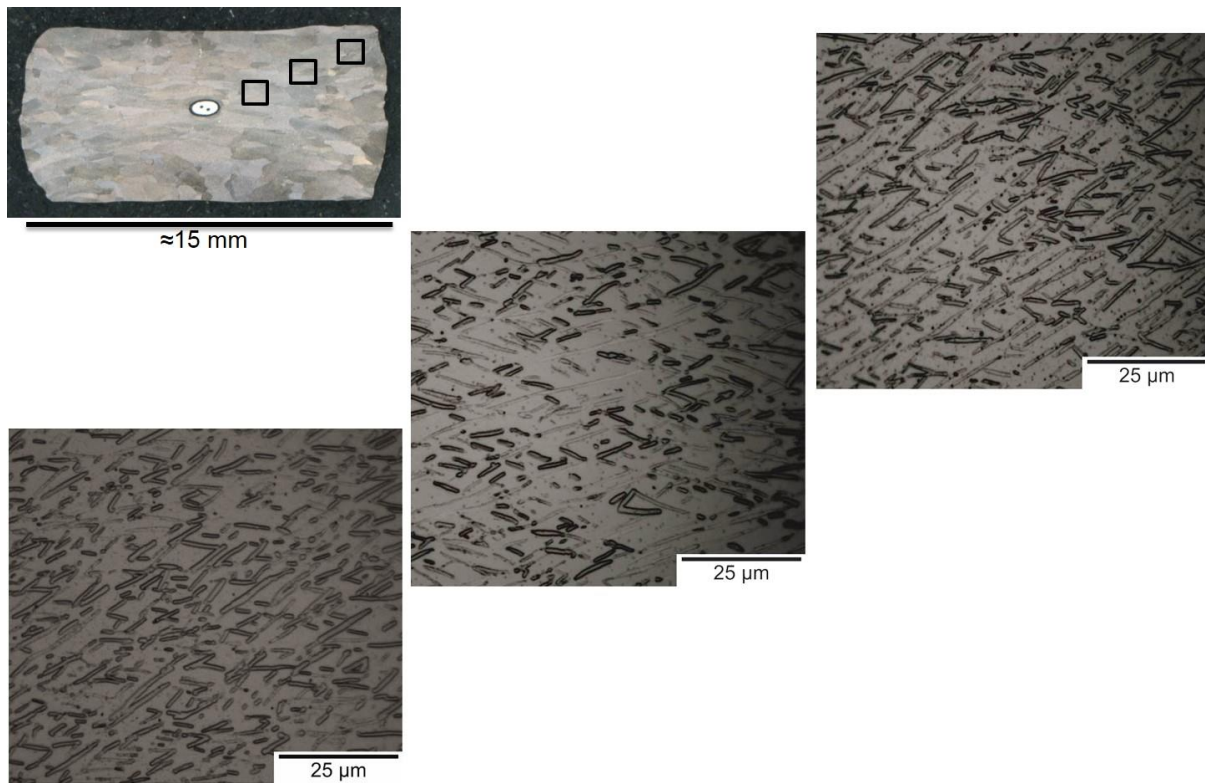
Figure 5.17: Etched light micrographs from across TMC Ti-10-2-3 specimens (deformed at strain rate of 0.01 s^{-1} and target temperature of 750 °C).
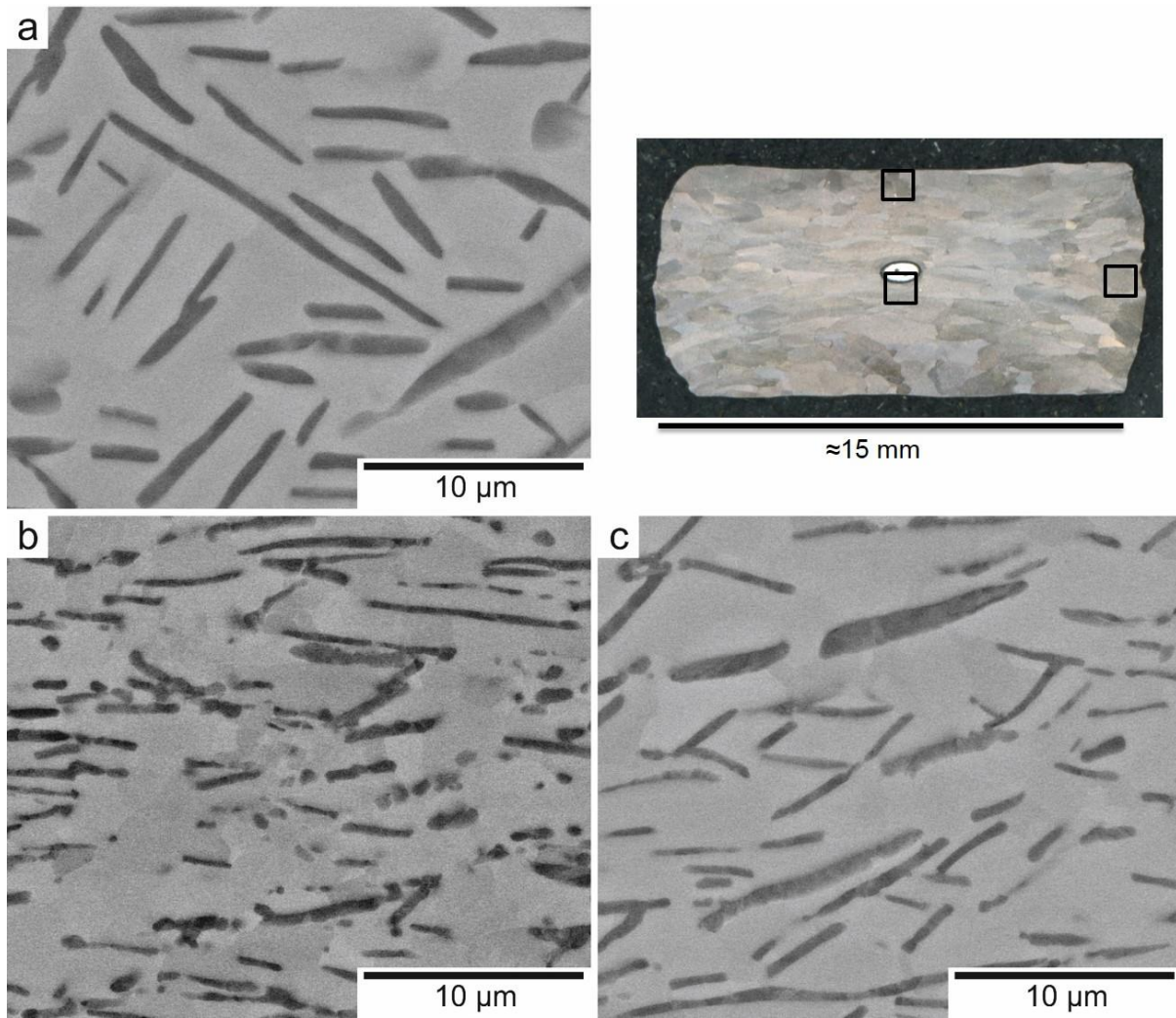
Figure 5.18: BSEI micrographs illustrating microstructural variation within a Ti-10-2-3 axisymmetric compression specimen (strain rate of 0.01 s^{-1} and target temperature of 750 °C). (b) was positioned just off-centre to avoid thermocouple.

5.5 Arbitrary Strain Path Testing

5.5.1 Flow Behaviour

An initial comparison of the temperature control between the TMC and ASP torsion tests is presented in Figure 5.19. The ASP tests in question were tests 2-4, as these incorporated the full range of intended test temperatures. Note that the target thermocouple temperature was set 12 °C below the intended gauge length temperature to account for the temperature difference between the shoulder and gauge length. It can be seen that the ASP tests display a more consistent temperature profile than the TMC results. This may be partly due to the lower strain rate employed in the ASP tests (0.01 s^{-1} at 0.724R) relative to the intermediate and high strain rate TMC tests (0.1 s^{-1} and 1 s^{-1} respectively). However, the ASP temperature profiles are also more consistent than the TMC test of comparable strain rate (0.01 s^{-1}). This may be due to the direct temperature control offered by the induction loop surrounding the deforming gauge length during a torsion test. However, it should also be noted that there is probably a 'time lag' between a temperature fluctuation in the gauge length and that recorded by the thermocouple in the specimen shoulder. This might help smooth any variation and avoid overcompensation by the feedback loop in the software.

As mentioned earlier, a relatively low strain rate of 0.01 s^{-1} at 72.4% of the specimen radius was selected in order to minimise adiabatic heating. This required an angular velocity of 5.48 °.s^{-1} for the specimens in question (10 mm diameter). Unfortunately this was near the lower limit of the ASP machine's capabilities and led to a significant fluctuation in the strain rate. The periodic nature of this fluctuation and its effect on flow stress are demonstrated in Figure 5.20. Recalling Equation 5.13, a correction for this oscillation requires a value for the strain rate sensitivity, m. This can be determined from the gradient of a plot of log σ vs log $\dot{\varepsilon}$ at a constant strain. However, only one nominal strain rate was employed in these tests, preventing calculation by such a method. Nevertheless, in the flow curve presented in Figure 5.20, it can be seen that a steady state regime appears to exist from about 0.4 strain onwards. In this region, the flow stress can be assumed to be independent of strain, and a plot of log σ vs log $\dot{\varepsilon}$ produces a fairly linear relationship (see Figure 5.21). The slope of a fitted line then yields a value for m of 0.277. This could then be used to correct the original flow curve by use of the following equation:

$$\sigma_c = \sigma \left(\frac{\dot{\varepsilon}^m}{\dot{\varepsilon}_i^m} \right) \tag{5.26}$$

Where σ_c is the corrected stress, σ is the original stress, $\dot{\varepsilon}$ is the target strain rate (0.01 s⁻¹ in this case) and $\dot{\varepsilon}_i$ is the instantaneous strain rate. A comparison between the original and corrected flow curves is made in Figure 5.22. However, while this did significantly reduce the 'noise' in the flow curve, it was found that the exact value of *m* varied between tests, and therefore required a separate determination in each case. This presented a problem for the tests which did not appear to reach a true steady state, since the stress must be independent of strain when plotting log σ against log $\dot{\varepsilon}$ to obtain *m*. It was therefore decided to adopt an empirical approach by examining the deviation of the stress from a straight line fitted to a short section of each flow curve. When plotted against the strain rate, a reasonable correlation was found (see Figure 5.23) and a second order polynomial was fitted to the data. This equation could then be used to correct the original flow stress, and a comparison between the *m* based strain rate correction and the empirically based strain rate correction is made in Figure 5.24. The deviation was considered minimal, and therefore the empirical approach was adopted for consistency across all tests.
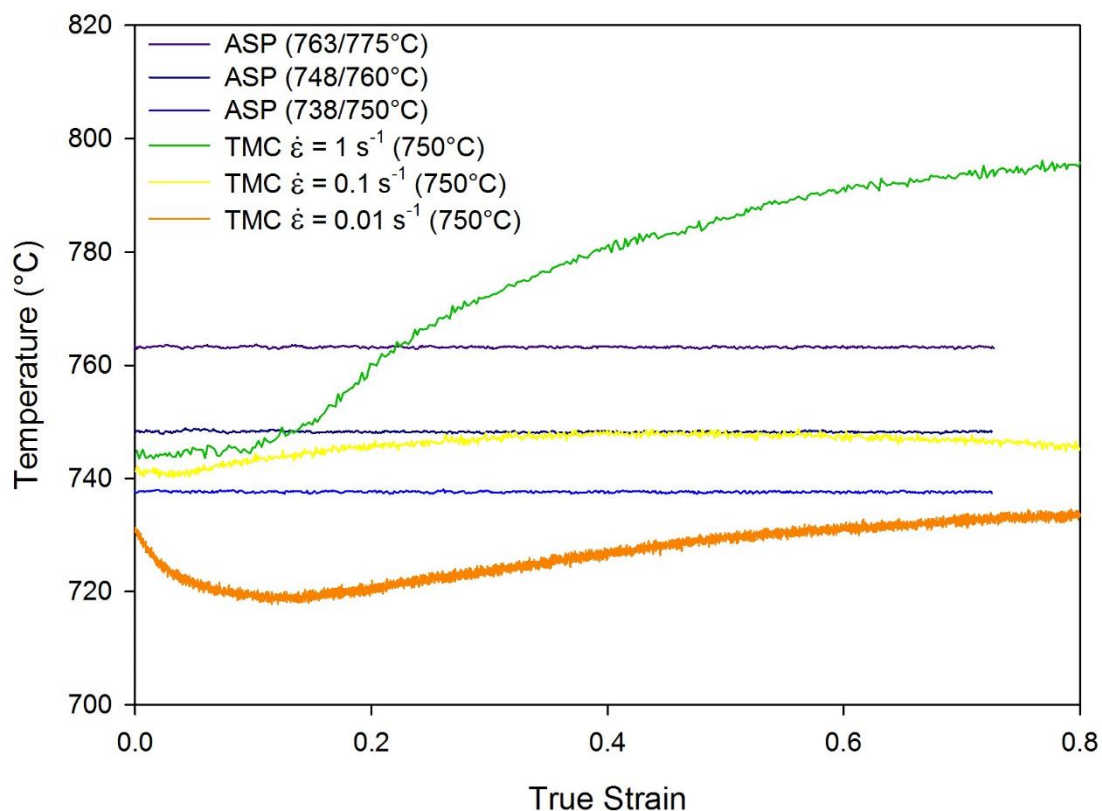
Figure 5.19: Thermocouple derived temperature-strain plot comparing ASP and TMC tests (all ASP tests conducted at a strain rate of 0.01 s⁻¹ at 0.724R). For ASP tests, left and right temperatures are thermocouple target temperatures and gauge length target temperatures, respectively (12 °C difference). Target temperatures of TMC tests in brackets.
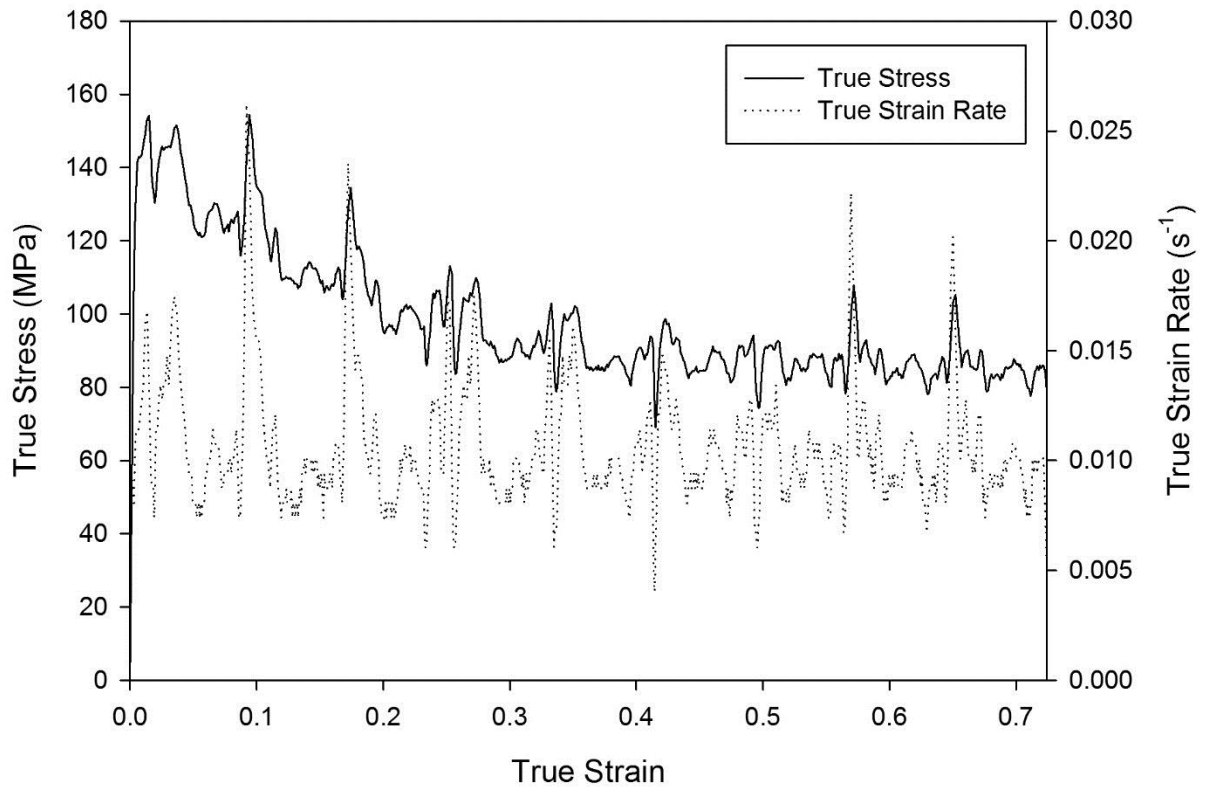
Figure 5.20: Comparison of stress and strain rate ASP test 2 (0.724 FWD strain at 0.724R and 750 °C).
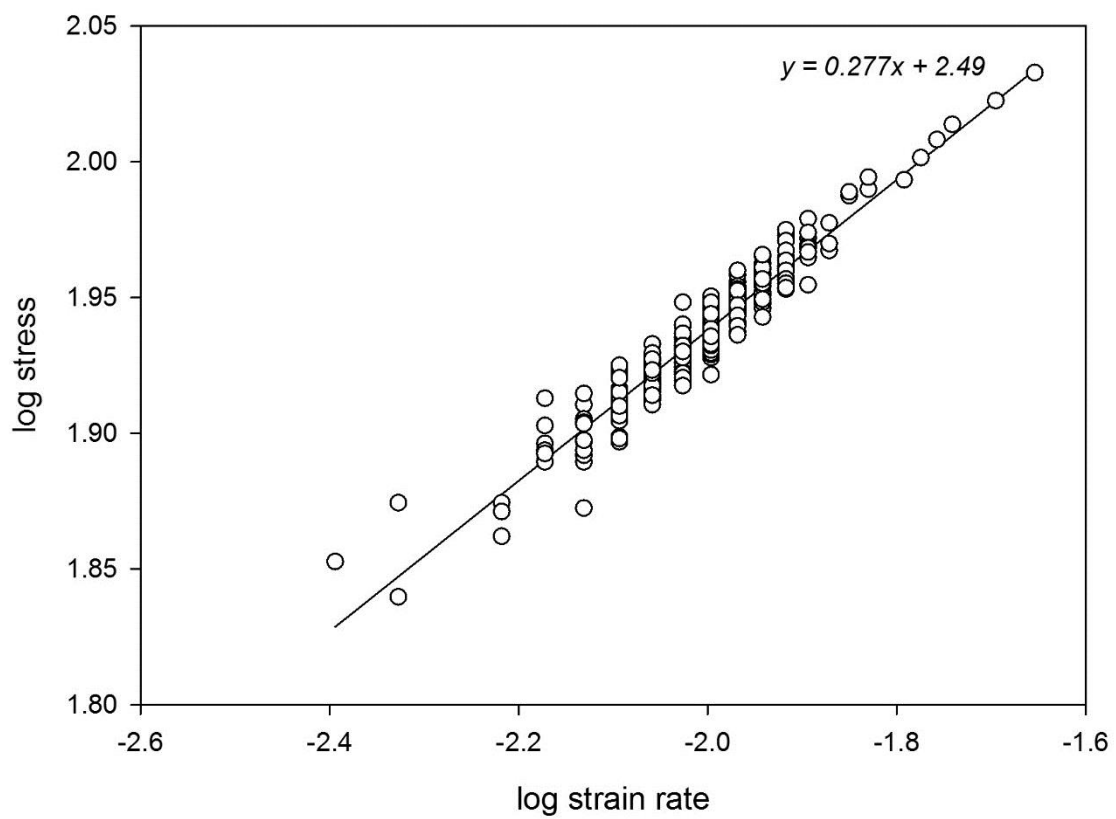
Figure 5.21: Log stress vs log strain rate of ASP test 2 in steady state region.

191
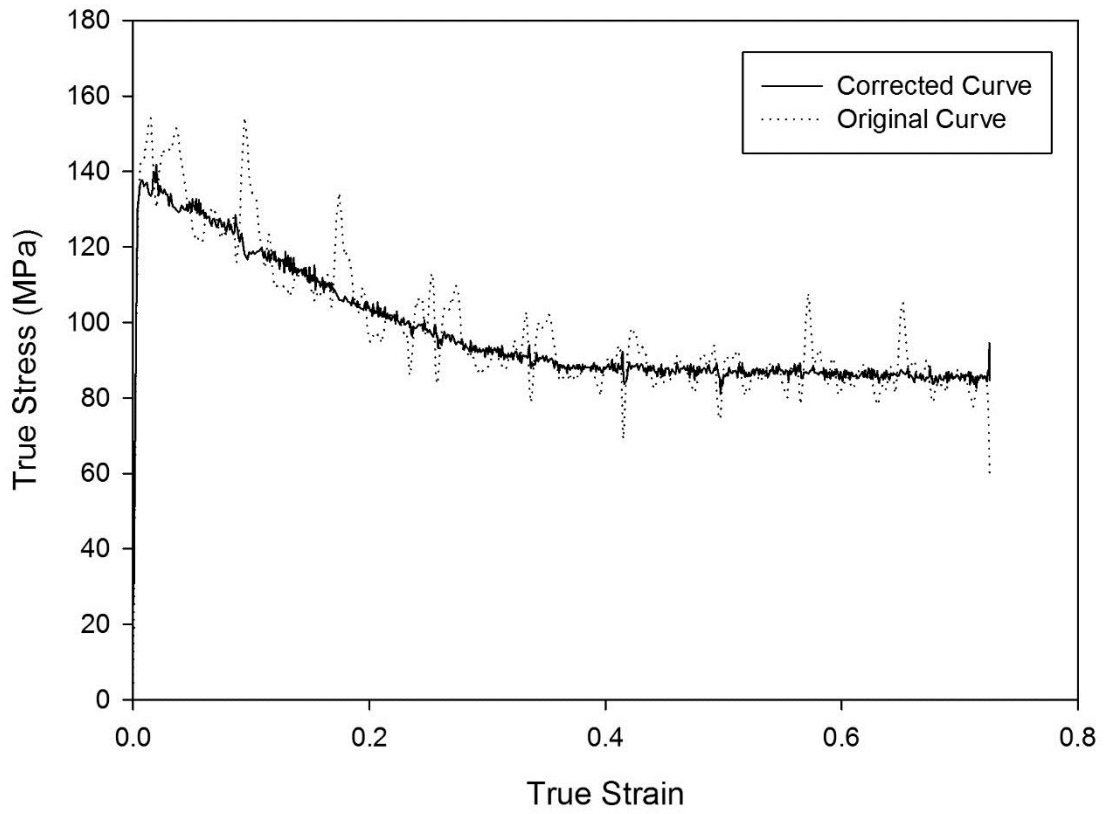
Figure 5.22: Comparison of original and strain rate corrected flow curve (ASP test 2).
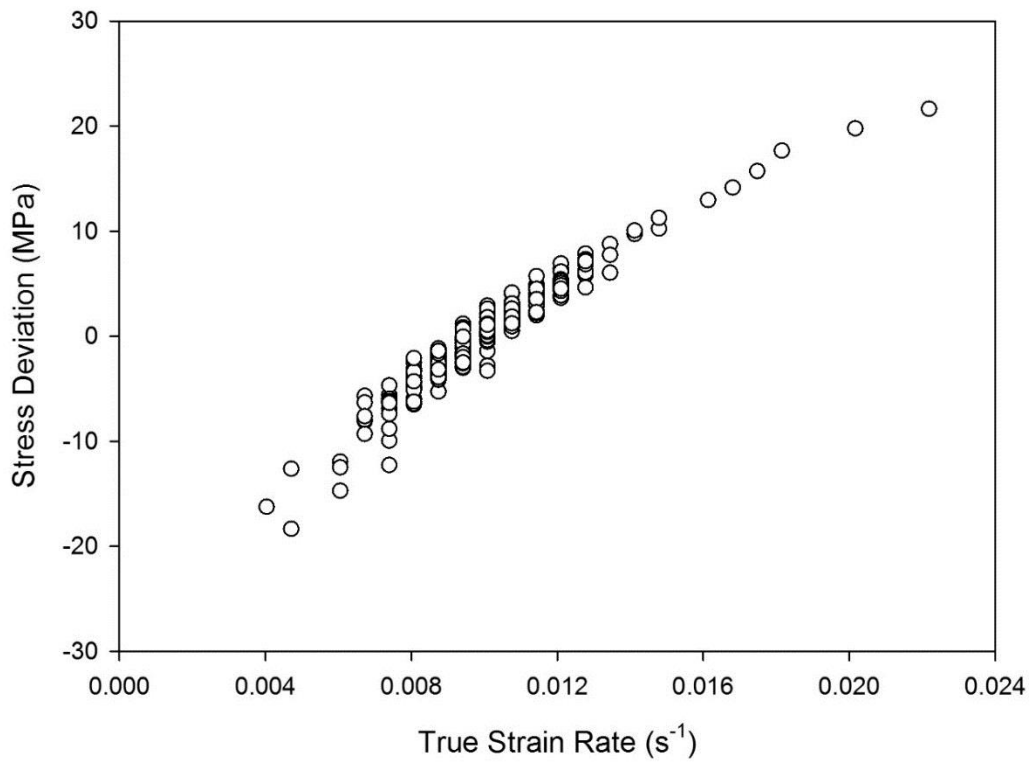
Figure 5.23: Deviation of flow stress in the steady state region (from fitted line) as a function of strain rate.
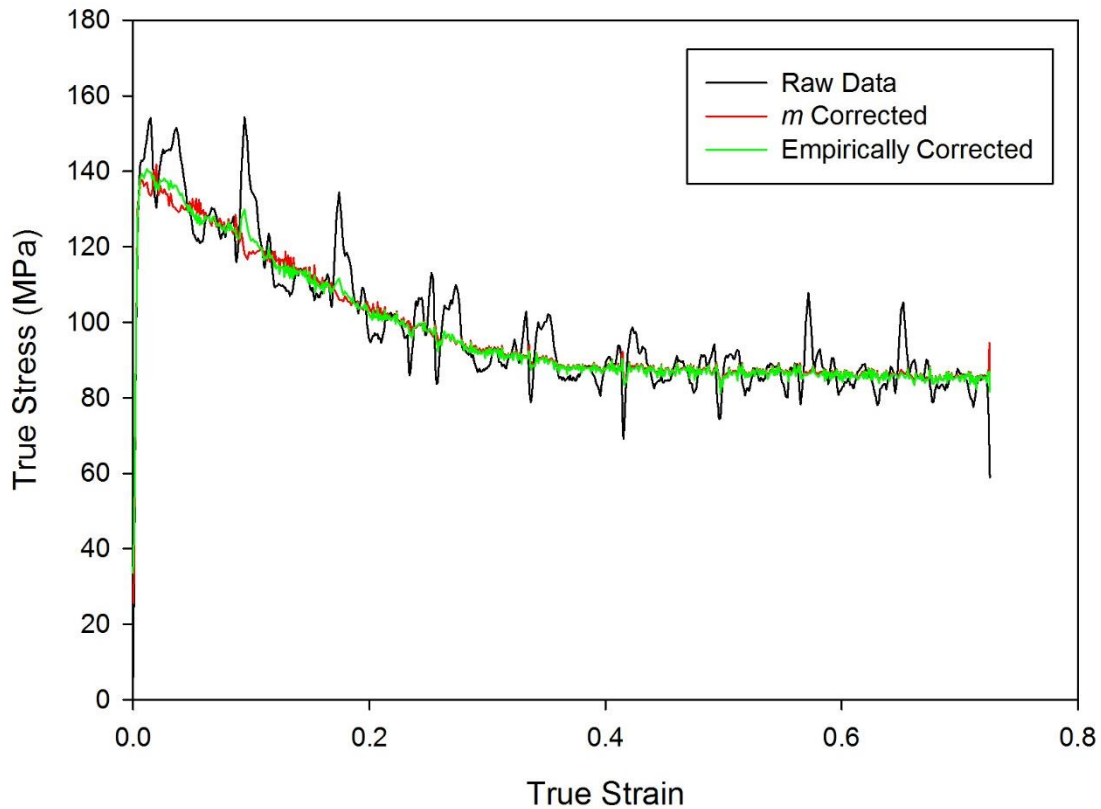
Figure 5.24: Comparison of the original flow curve (raw data) with the strain rate corrected and empirically corrected flow curves (ASP test 2).

Figure 5.25 presents a comparison between the TMC and torsion flow curves at a strain rate of 0.01 s^{-1} (representing the macroscopic and 0.724R strain rate respectively). It can be seen that both exhibit significant flow softening, although the peak flow stress is slightly higher in the torsion test. This initial peak is also sharper in the torsion test, with a very steep rise to a maximum at around 0.01 strain, whereas the TMC flow curve peaks at about 0.05 strain. The flow softening in the TMC curve also appears more gradual, making a smoother transition to steady state at a higher strain (approximately 0.7-0.8). On the other hand, the torsion flow curve softens more rapidly before flattening out at around 0.3-0.4 strain. The cause of these differences is unclear.

Although the target temperature for both tests was 750 °C, as Figure 5.19 demonstrated, this was not reached and maintained throughout the TMC test. In order to better gauge the temperature profile within the torsion specimens, the variation in retained β volume fraction was analysed. Specimens were sectioned perpendicular to the longitudinal axis and a series of micrographs were taken in radial traverses from centre to edge. The volume fraction of retained β was measured in accordance with the procedures set out in Chapter 3 and plotted against the radial location (defined as a fraction of the specimen radius). The results for torsion tests 2-4, which cover the full range of intended test temperatures are presented in Figure 5.26. Although there is some fluctuation, it can be seen that there was no consistent trend, implying that the

temperature distribution was reasonably uniform throughout the specimens. Given this finding, the data within each specimen could be combined to produce a mean β volume fraction for each respective test (see Table 5.3). It was then possible to estimate the actual temperature using the β approach curve in Figure 5.12. Table 5.3 compares these 'metallographic temperatures' with the intended test temperatures and reveals some significant deviation. The cause of such discrepancies is uncertain. If thermocouples were not in good contact with the testpiece, the temperature feedback may have been affected, leading to inadequate control. Another possibility is the positioning of the gauge length within the induction coil. Variation in the position relative to the coil could have altered the temperature distribution in the specimen, and consequently affected the accuracy of temperature measurements. Regardless of the cause, the new temperature data is still unable to account for the difference in peak stress between the TMC and torsion tests, since the TMC temperature was lower and this should have raised the flow stress. However, it is possible that the conversion of load-displacement and torque-angle data into stress-strain curves could introduce unknown errors unique to each methodology. Alternatively, this could simply be random fluctuation that a more comprehensive study may remove.
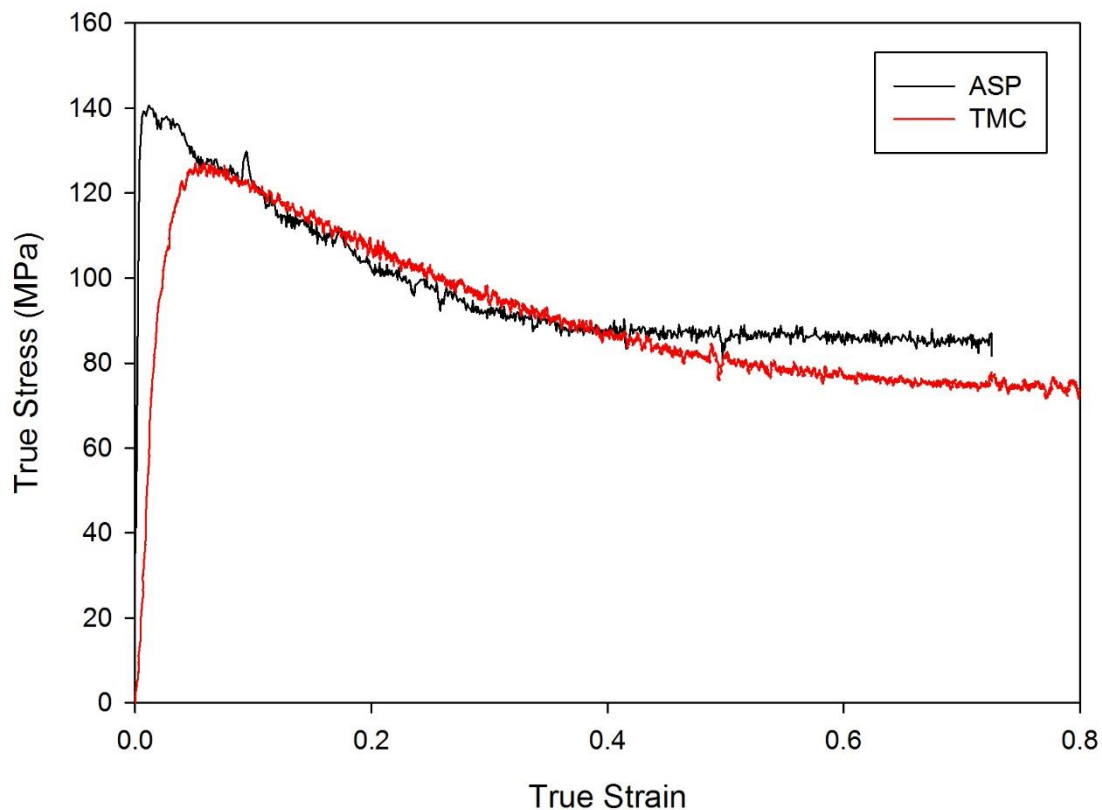
Figure 5.25: ASP-TMC comparison at a target temperature of 750 °C and strain rate of 0.01 s^{-1} (at 0.724R for the ASP test).
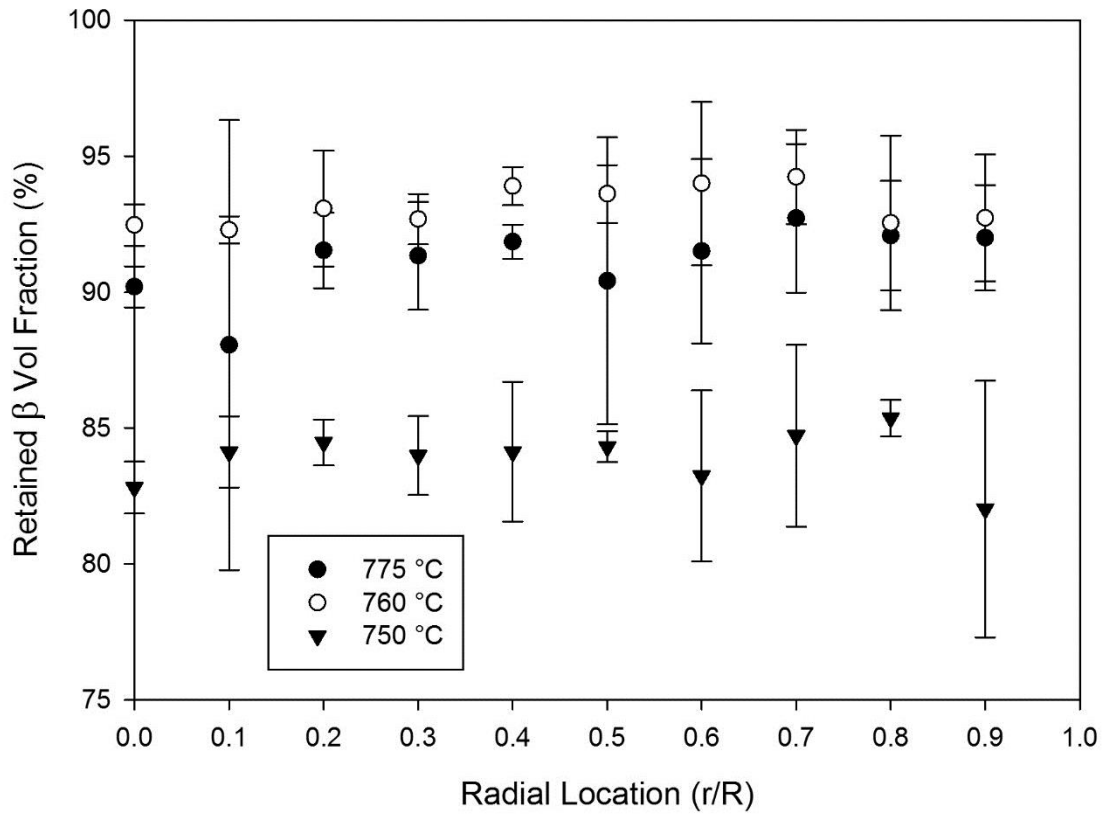
Figure 5.26: Retained β volume fraction across torsion specimens. Note that the legend specifies the target temperature, which may differ from actual temperature (see relative positions of tests at 775 °C and 760 °C).

Table 5.3: Comparison of target temperature and that determined from metallographic observation.

Test No.	Strain Path	Target Temp (°C)	Retained β Vol. Fraction (%)	Metallographic Temp (°C)
1	None	760	86.6 ± 0.4	764
2	0.724 FWD	750	83.9 ± 0.5	755
3	0.724 FWD	760	93.1 ± 0.4	784
4	0.724 FWD	775	91.1 ± 0.7	777
5	0.6 FWD 0.6 REV	750	86.4 ± 0.3	763
6	1.2 FWD	750	82.2 ± 0.4	750
7	1.2 FWD 1.2 REV	750	87.4 ± 0.5	766

The metallographic temperatures also help explain the torsion flow curves in Figure 5.27. These curves represent tests 2-4, and were intended to demonstrate the effect of temperature. As would be expected there is some variation between both the peak flow stress and the steady state flow stress (although the latter is smaller). However, the original target temperatures do not explain this variation well. While they concur with the observation that the lowest temperature test has the highest flow stress, they do not adequately explain the positioning of the other two. On the other hand, the metallographic temperatures are consistent with the relative positions of all the flow curves. In addition, the difference between the peak flow stress of tests 2 and 4 is greater than that between tests 4 and 3. This is consistent with the smaller temperature variation between the latter two. It is also more apparent now that the degree of flow softening appears to reduce as the test temperature is increased.
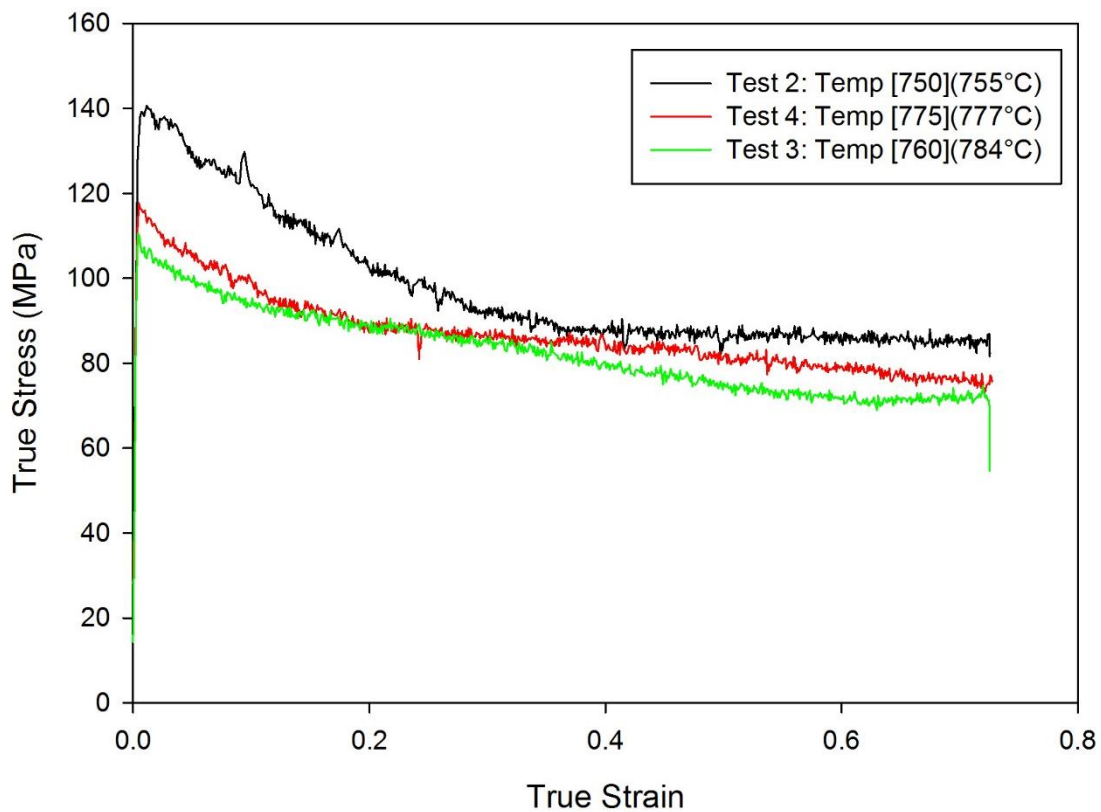
Figure 5.27: Comparison of ASP tests conducted at different temperatures (target temperature in square brackets, metallographic temperature in round brackets).

Figure 5.28 compares the flow curve of a reversed torsion test with that of a specimen deformed forwards only to the same total strain. There is a significant difference between the peak flow stresses, which only widens throughout the first half of the tests. In this case, the discrepancy cannot be explained by temperature variation, since the higher flow stress belongs to the higher temperature test. The response of this test to strain reversal also differs to that of test 7 (see Figure 5.29). Here it can be seen that the flow stress rapidly returns to its pre-reversed level, and then rises slightly further. However, in test 5 (Figure 5.28) the flow stress quickly rises to about 60-70MPa, before climbing more gradually to its pre-reversed level over the next 0.4 strain. Referring to Figure 5.29 again, it can also be seen that there is greater consistency between test 6 and the forward section of test 7. However, it should also be noted that test 7 does exhibit an unusual 'wave-like' flow curve, which may be an indication of alignment issues. This might suggest that at least one of the two reversed flow curves is anomalous, although it is difficult to say which at this point. There is evidently a need for repeatability.
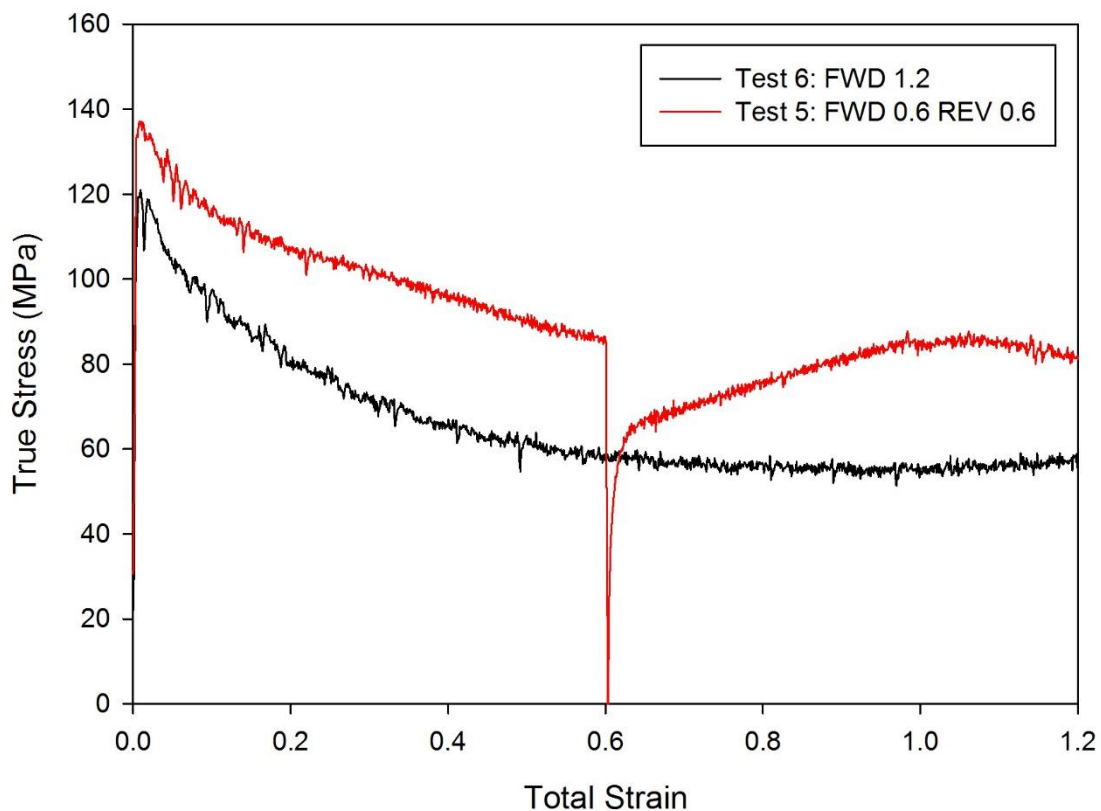
Figure 5.28: Comparison of forward and forward-reverse torsion tests (target temperature 750 °C, and strain rate of 0.01 s^{-1}).
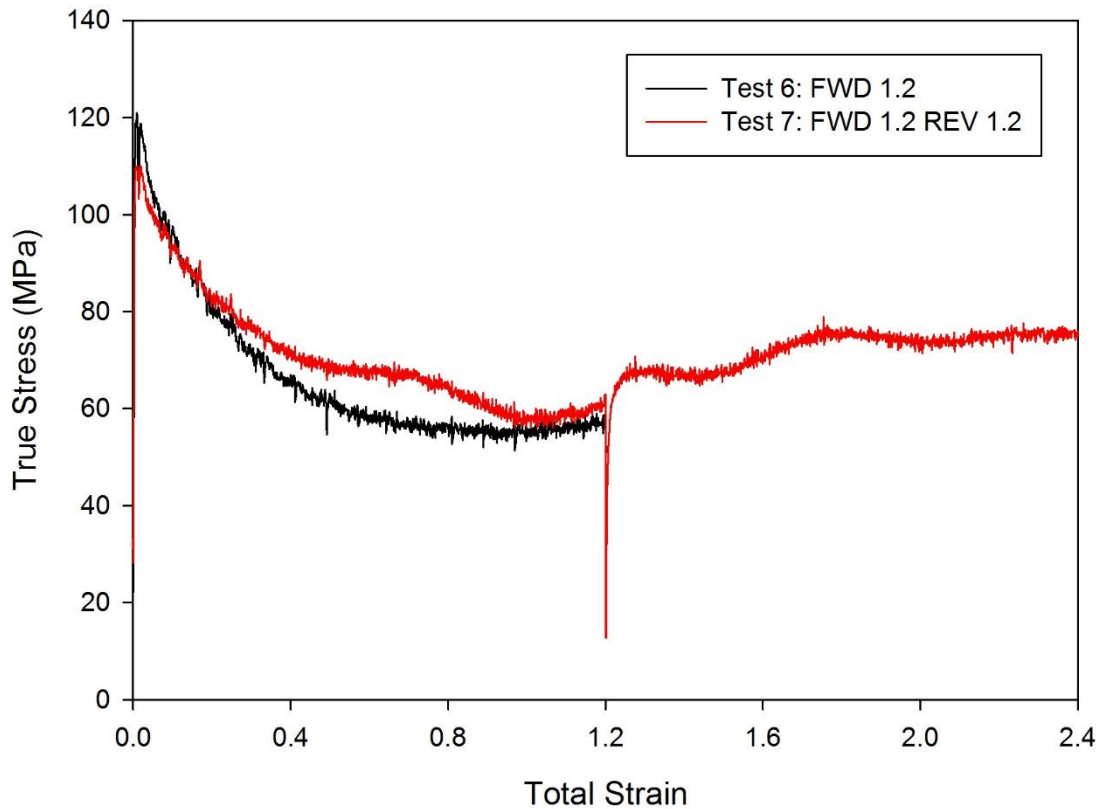
Figure 5.29: Comparison of forward and forward-reverse torsion tests (target temperature 750 °C, and strain rate of 0.01 s^{-1}).

5.5.2 Microstructural Analysis: Electron Microscopy

The microstructural evolution of tests 2-4 is presented in Figure 5.30. This illustrates the effect of strain and temperature on primary α and β substructure. With increasing strain, the elongated primary α plates begin to bend and kink, finally fragmenting to form small globular particles. The initially uniform β matrix develops subgrains which become more clearly defined as deformation proceeds. Channelling contrast within the primary α provides an indication of deformation prior to break-up of the plates themselves. At higher temperatures, the α particles are smaller to begin with as a result of the lower α volume fraction. These thinner plates would be expected to buckle and fragment more easily, accelerating the process of globularisation. However, it is difficult to discern this from the micrographs in Figure 5.30, so a quantitative approach is needed.
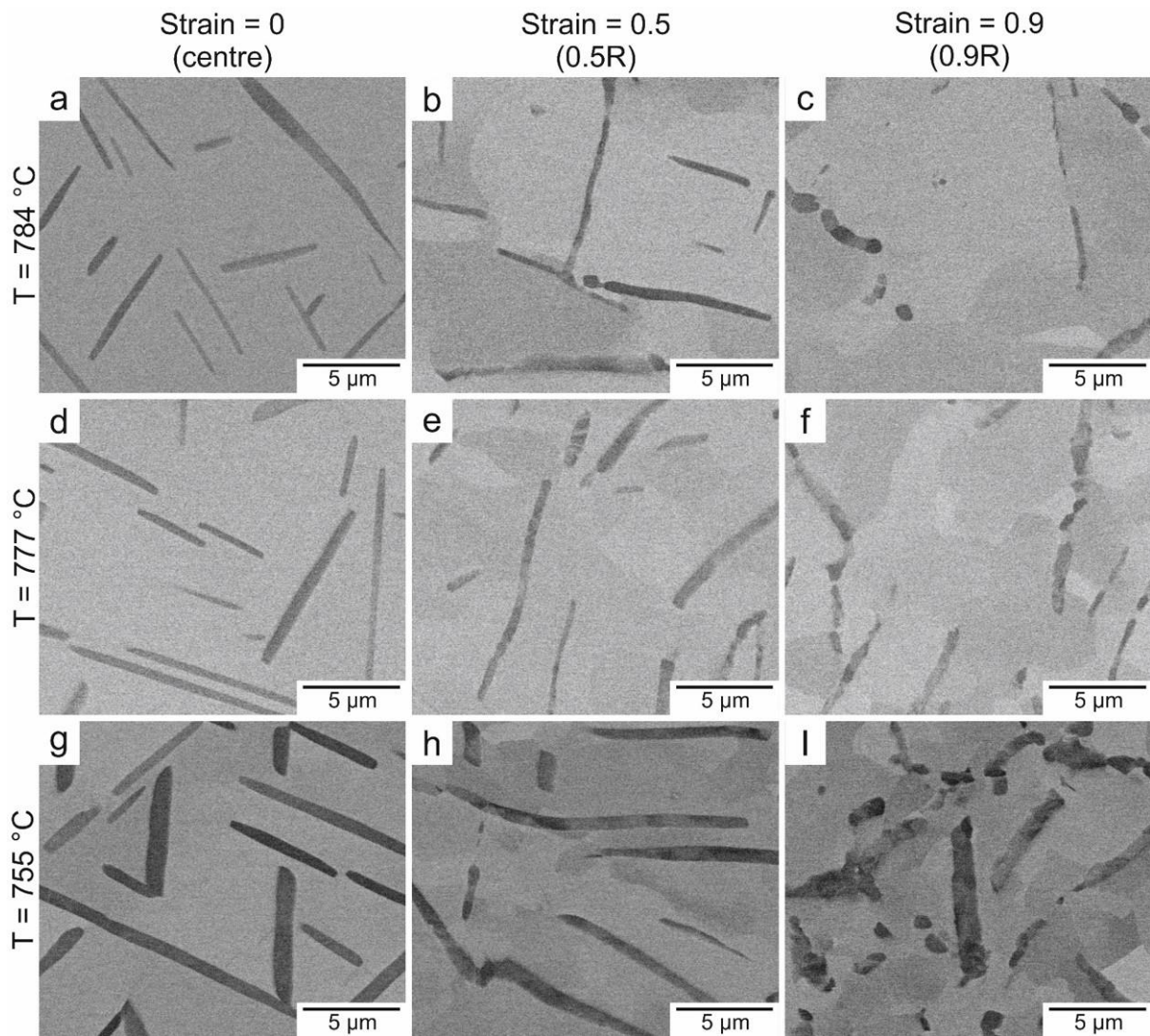
Figure 5.30: BSEI micrographs illustrating the effect of temperature on microstructural development of Ti-10-2-3 during torsion (note that tests have now been re-ordered in accordance with their metallographic temperature).

The micrograph traverses employed for β volume fraction measurements were also analysed to quantify morphological changes in the primary α. By calculating the equivalent strain at each radial location, the evolution of primary α particles could then be plotted as a function of strain. An important point to consider in this approach is the variation in strain rate over the specimen radius. This was an additional reason for selecting a low strain rate. While the linear variation of strain rate as a function of radius is unavoidable, the absolute magnitude of this variation can be reduced by lowering the maximum strain rate in the first instance. It is also worth noting that, in principle at least, the process of spheroidisation can be ignored within a specimen because the duration of the test is the same throughout the specimen, regardless of the local strain rate.

Figure 5.31 presents the median feret diameter vs true strain. As with the time at temperature results (see Figure 5.11), the median value of the feret min and feret max data was calculated rather than the mean since the data was not normally distributed. For information on how the feret min and feret max are defined see Section 3.2. At each temperature, it can be seen that the feret min remains essentially unchanged throughout deformation. Between each temperature, it can just be seen that there is a small but consistent difference between the α particle thickness (feret min). This would agree with the temperature data, as the higher temperature tests have the narrower plates, presumably due to the lower volume fraction. The feret max drops from about 3.5 µm at zero strain to about 1.5-2.5 µm at 0.9 strain, depending upon deformation temperature. At zero strain there is relatively little difference between the feret max over the temperature range in question. However, over the course of deformation, the feret max appears to reduce more rapidly at higher temperature, suggesting globularisation of thinner plates proceeded more quickly than thicker, lower temperature ones. On the scale presented in Figure 5.31, the reduction in feret max diameter does not appear to have any sharply defined transition at which fragmentation of the primary α occurs.
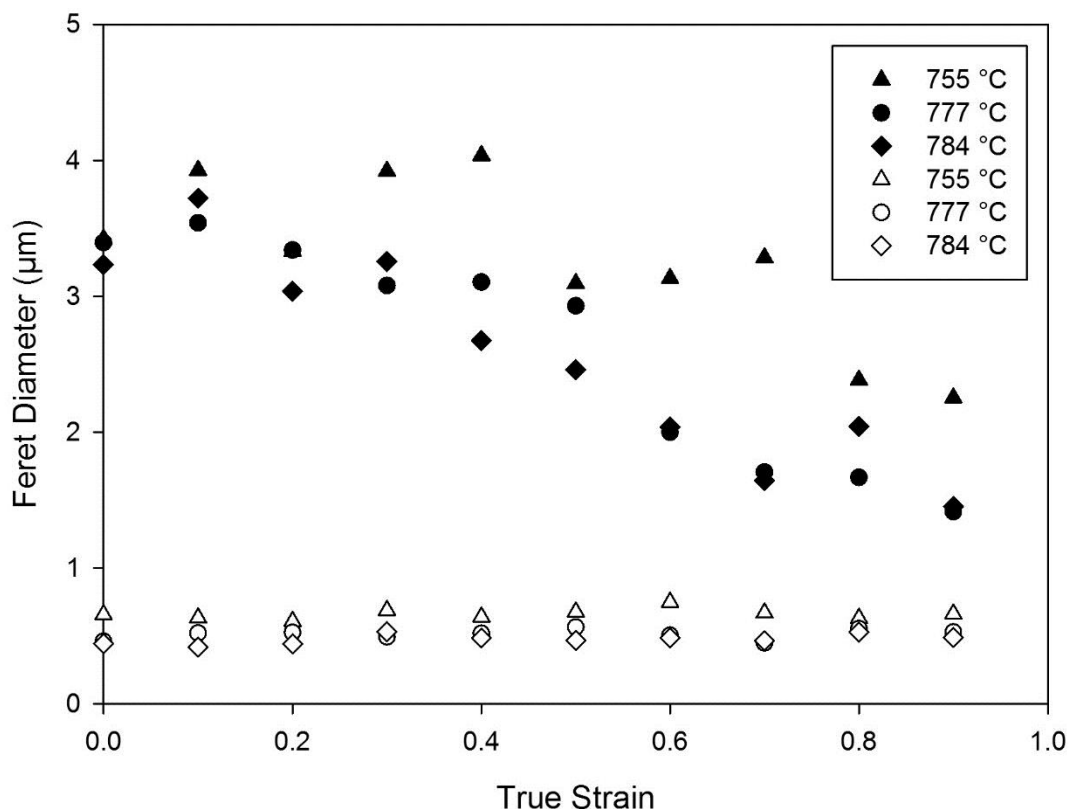
Figure 5.31: Effect of temperature and strain on the primary α morphology. Filled symbols are feret max, hollow symbols are feret min (median values).

However, extending the X-axis to a higher strain, as in Figure 5.32, it becomes more apparent that a rapid drop in feret max takes place between about 0.4-0.8 strain. This may represent a critical strain or strain range, at which point the primary α, after buckling, suddenly gives way and fragments into smaller particles. This behaviour is thought to be responsible for the observed flow softening in this alloy [66]. However, the flow curves do not exhibit a clearly defined drop at around the point where primary α break-up occurs. This could indicate other factors are at work. That said, it is important to bear in mind that the flow curve is based upon the torque required to deform the entire specimen. Since the strain varies linearly from centre to edge, for a given surface strain all points will be at some earlier stage in the process of globularisation. Thus, even if the true flow curve did experience a sharp drop, the 'aggregate' flow curve of the specimen might not show this as the flow stress will be a function of all components of strain across the radius. The same may be true of an axisymmetric compression test given the non-uniform strain distribution (see Figure 5.18). For a given macroscopic strain, some regions may have globularised, while others may not, producing a mean pressure based on multiple points in the true flow curve.

Figure 5.32 also illustrates the effect of strain reversal. The X-axis displays forward strain only, so the total strain for each data point from a reversed test is double that of its forward strain (whereas the forward strain and total strain are identical for the non-reversed tests). If the strain reversal were to have an effect on the feret diameter, this would lead to a deviation between the reversed and non-reversed data sets in Figure 5.32. However, this does not appear to be the case, suggesting that the strain reversal did little to further globularise the primary α. This is further illustrated by plotting the feret diameter as a function of total strain (see Figure 5.33). Since the total strain is double the forward strain of the reversed tests, this pushes the point of globularisation to a higher strain.

This has implications for industrial forging operations where non-linear strain paths may have included redundant work that achieved very little in further refining the microstructure. Figure 5.34 demonstrates similar behaviour when comparing tests 6 and 7. There was no forward only test to match the total strain of test 7, but the deviation between the reversed and non-reversed tests is readily apparent at 1.5 total strain. Figure 5.35 compares the microstructures at 0.724R of tests 5-7. It can be seen that Figure 5.34(a) and (b) exhibit markedly different microstructures despite having experienced the same total strain. On the other hand Figure 5.34(b) and (c) show much greater similarity in spite of the differing total strain.
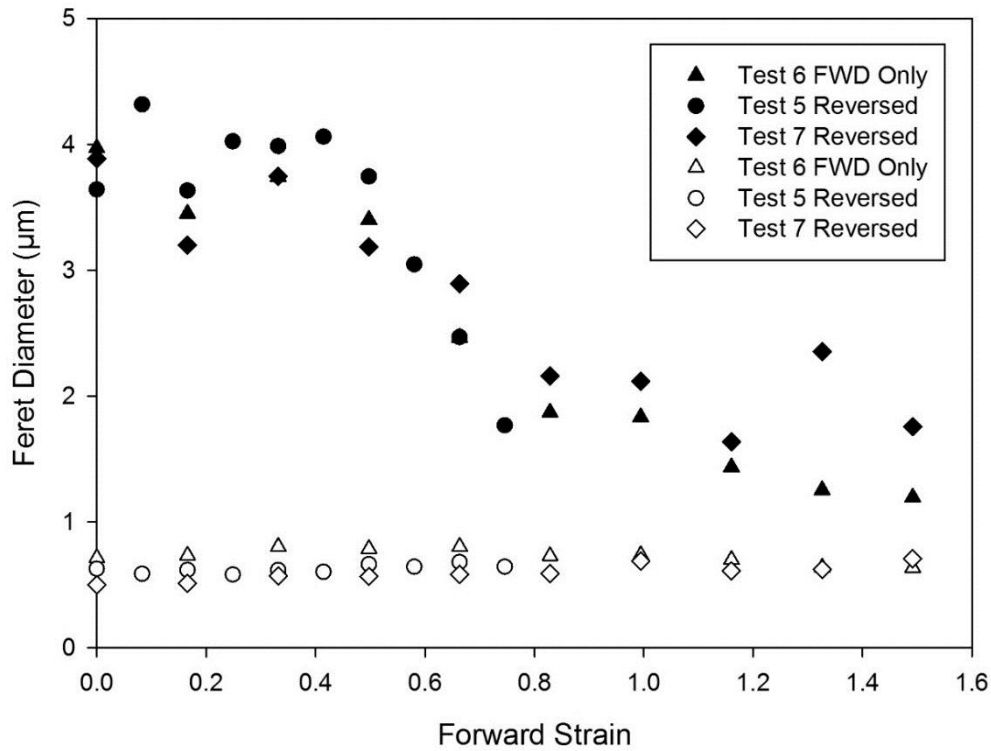
Figure 5.32: Evolution of primary α morphology in deformed Ti-10-2-3 as a function of forward strain. Filled symbols are feret max, hollow symbols are feret min (median values).
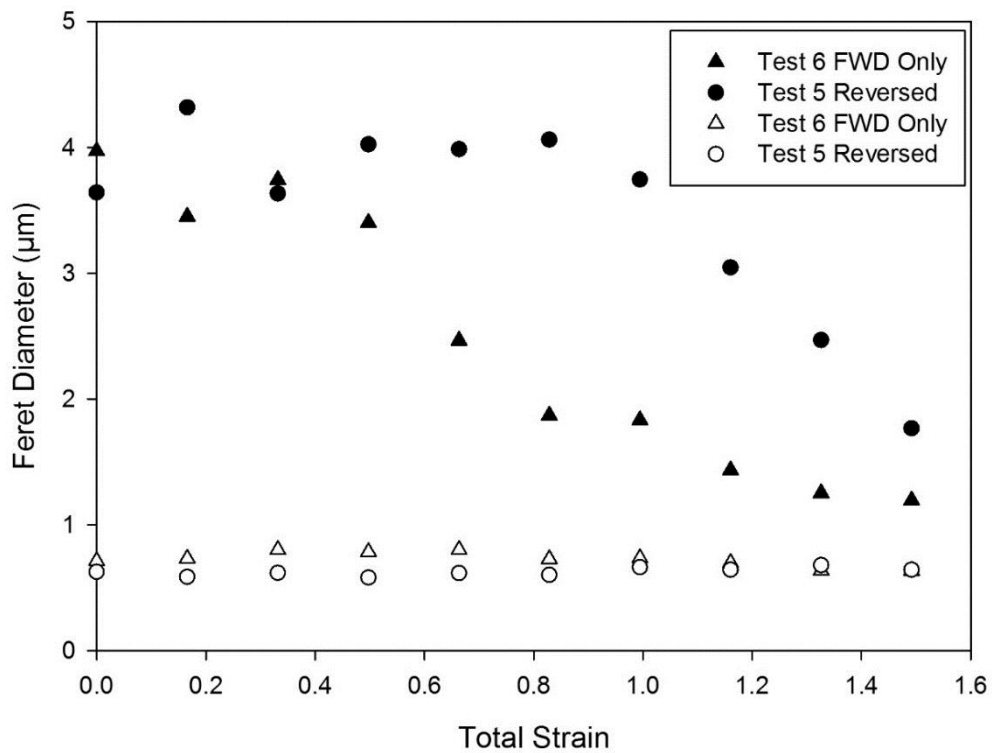
Figure 5.33: Evolution of primary α morphology in deformed Ti-10-2-3 as a function of total strain. Filled symbols are feret max, hollow symbols are feret min (median values).
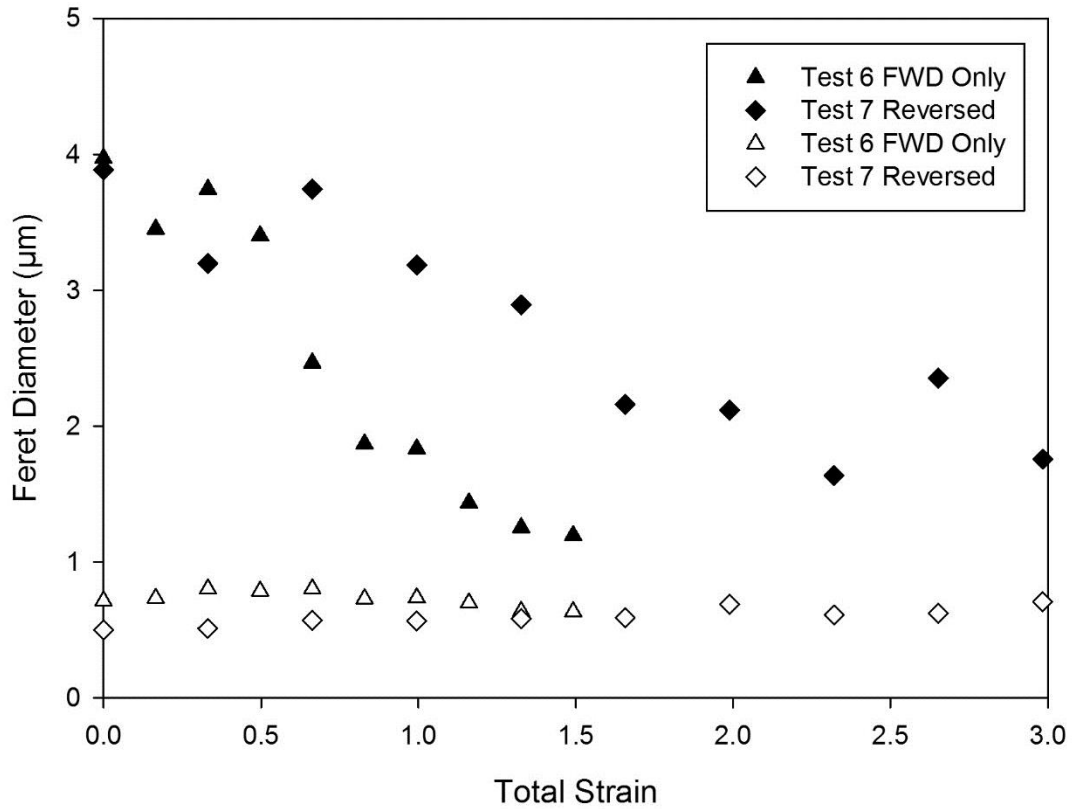
Figure 5.34: Evolution of primary α morphology in deformed Ti-10-2-3 as a function of total strain. Filled symbols are feret max, hollow symbols are feret min (median values).
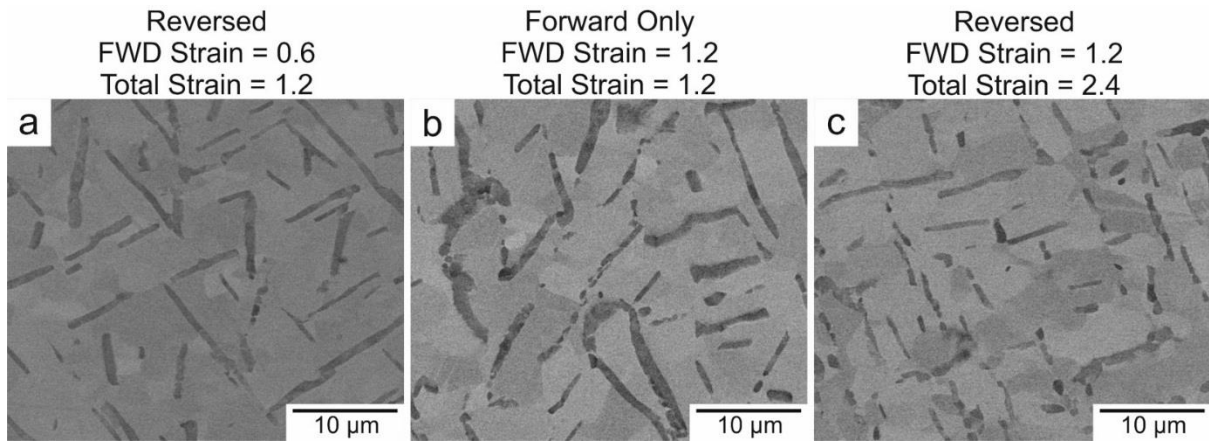
Figure 5.35: Effect of strain path on microstructural evolution of Ti-10-2-3 during hot deformation, (a) and (b) have the same total strain, (b) and (c) have the same forward strain.

5.5.3 Microstructural Analysis: EBSD

Figure 5.36 presents an EBSD map taken across specimen 2 (FWD strain = 0.724 at 0.724R) covering a band from the centre to about 78% of the radius (the sample holder prevented access to the very edge of the specimen). The size of this map relied on the use of Fast Acquisition Software (FAS) to make multiple maps which could be stitched together to provide an overview of a large area. Ignoring the thickness (height) of the band, the strain increases from zero at the left hand end to approximately 0.78 at the right hand end. It can be seen that the undeformed, 'parent' β grains are very large, on the order of 0.5-1 mm in diameter. Such large grains only permit the observation of a small number of grains, even in a map of this size. However, based on what can be observed, the shape of the parent β grains appears relatively unaffected by deformation, even as subgrains form within them.
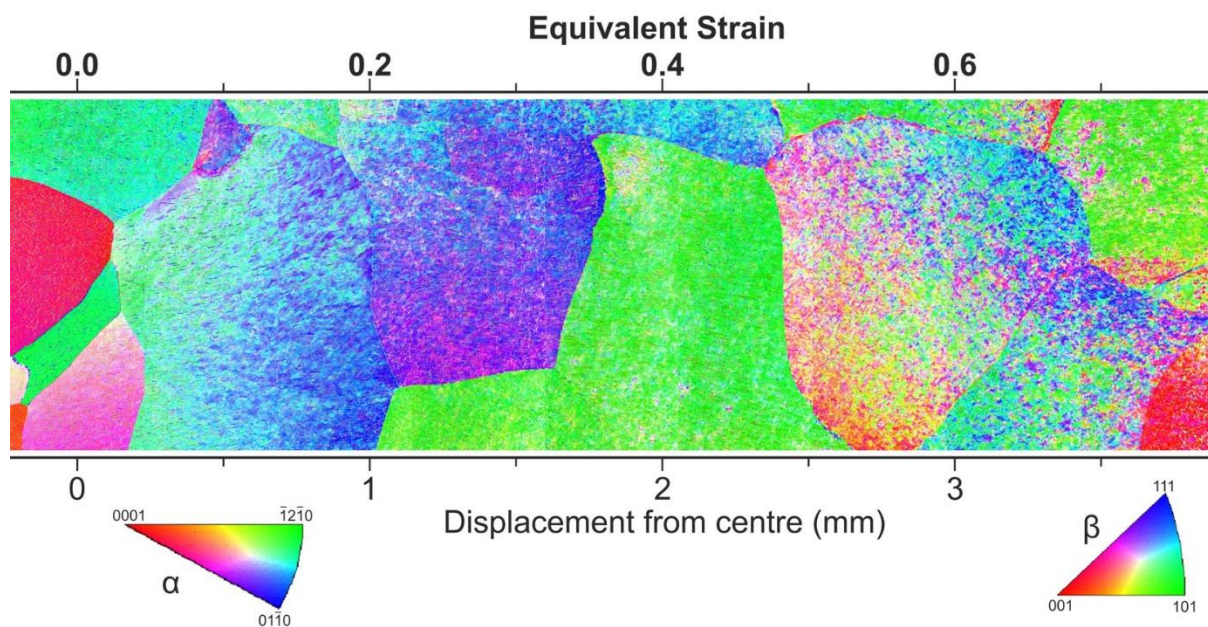
Figure 5.36: Low magnification EBSD map taken across specimen 2 (forward torsion only) (surface radius is 5mm). Plane of map is perpendicular to specimen axis. IPF colouring.

Higher resolution maps of tests 6 and 7 reveal the evolution of substructure in the β phase (see Figure 5.37). In the forward strained sample, the β phase dynamically recrystallizes to form small grains with high angle boundaries (>15°, indicated by thick black lines). The reversed specimen also exhibits high angle boundaries at 1.49 FWD strain, but the grains appear slightly larger. The reversed test will have taken twice as long as the FWD only test, perhaps allowing some limited grain growth in spite of the continuing deformation. At 0.5R, there appear to be significantly fewer high angle boundaries in the reversed test, with a well developed substructure of low angle grains instead (boundaries 2°>θ>15°). Beta titanium alloys have a tendency to undergo continuous dynamic recrystallization (CDRX) rather than discontinuous dynamic recrystallization (DDRX) on account of their high stacking fault energy (SFE). DDRX occurs through nucleation and growth of entirely new grains, whereas CDRX occurs by the

increasing misorientation of subgrains as dislocations accumulate at the subgrain boundaries [113][114]. It is possible that the process of strain reversal may have induced a greater proportion of dislocations of opposite sign. There would then be a greater tendency for dislocation annihilation through dynamic recovery, restoring a lower angle substructure in the reversed tests.
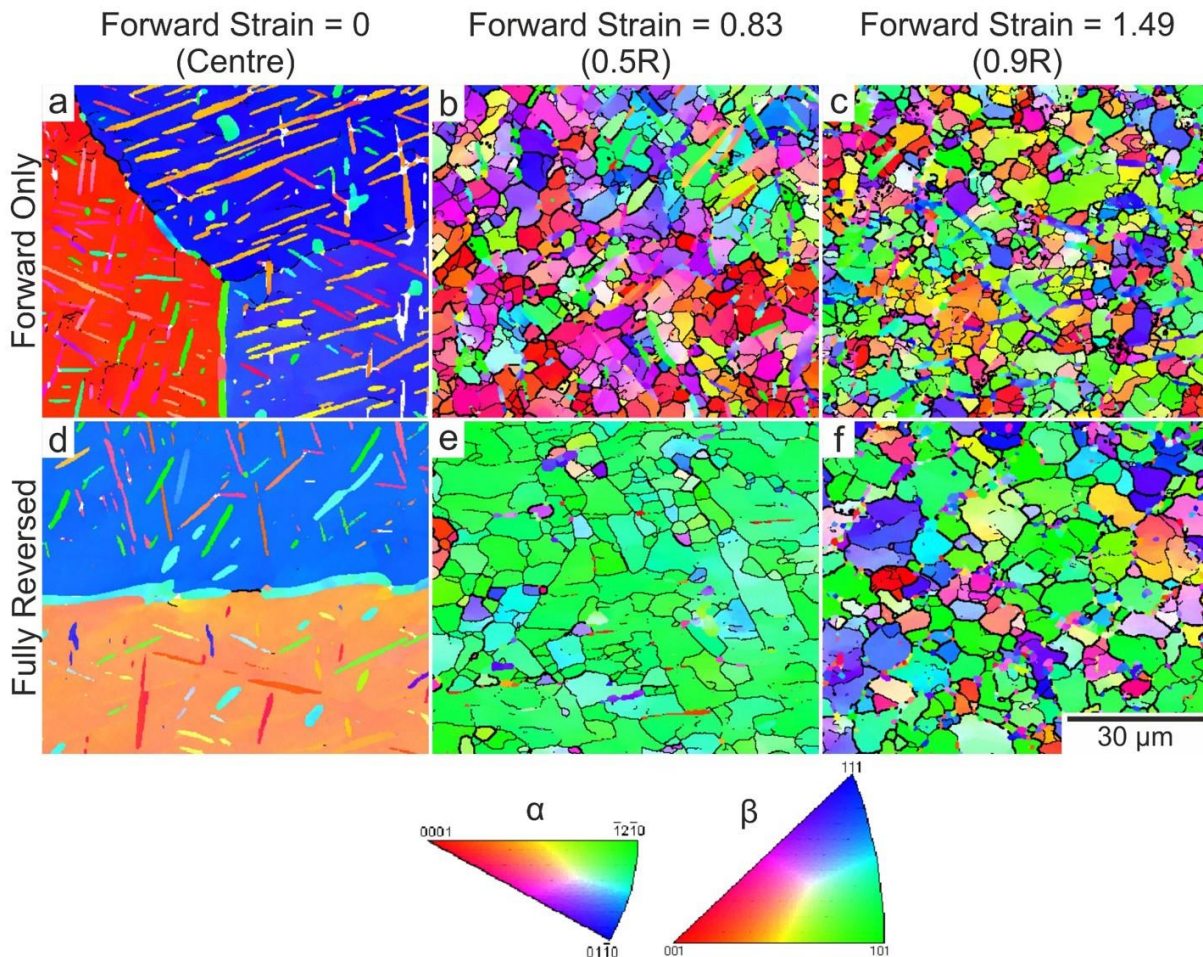
Figure 5.37: High magnification EBSD map illustrating the effect of strain path on microstructural evolution. Presented in IPF colouring with low and high angle boundaries marked ($2° > θ > 15°$ as thin black lines, and $>15°$ as thick black lines respectively).

Figure 5.38 presents pole figures of the basal plane {0001} for the α phase and {110} plane for the β phase from tests 6 and 7. The Burger's Orientation Relationship (BOR) states that the hexagonal {0001} plane and cubic {110} plane should be parallel, giving rise to coincidence of these plane normals on the pole figures. If the distribution of orientations were entirely random, this would not be noticeable in the figures. However, since individual β grains produce areas of greater pole density on a figure (as indicated by the colour scale), these regions should coincide with the pole density peaks of the {0001} plane of the α phase. At the centre of the samples, where the strain is negligible, there are sharply defined peaks that coincide with each

other very well, in both the FWD only and FWD-REV tests (see Figure 5.38(a) and (d)). As the FWD strain increases, the consistency of this agreement reduces and appears to be largely absent by a FWD strain of 1.49. However, the FWD only specimen may still have a coincident point at a strain of 1.49. If the pole density scale (in Multiples of Uniform Density, or MUD) is set to a uniform range across all the pole figures, the intensity of these peaks becomes much weaker in the deformed regions (see Figure 5.39). The global maximum was set at 25 based on the centre (zero strain) pole figures since these had exhibited the maximum MUD. This seems very high and is likely due to the size of the β grains, leaving the individual maps to cover only one or two grains (orientations). Nevertheless, at 0.5R (FWD strain = 0.83) the reversed specimen now shows a more clearly defined BOR relative to the FWD only specimen. Near the edge, both show a much weaker, more random distribution. However, it is still difficult to be certain about consistency of the BOR since a random distribution of orientations does not necessarily mean the BOR isn't maintained. It could in principle be that the β subgrains/grains have adopted a random orientation distribution, and the primary α particles have taken a pseudo-random distribution where each particle is still consistent with the β subgrain in which it resides.
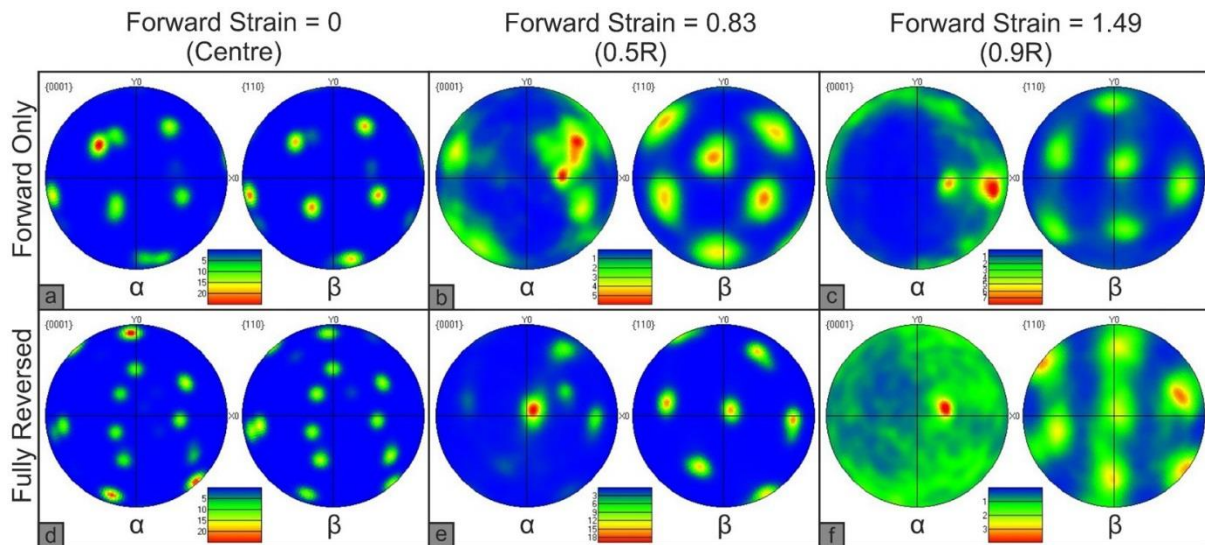
Figure 5.38: Pole figures illustrating the effect of strain path on the Burger's orientation relationship, showing the hexagonal {0001} plane, and cubic {110} plane. Colour contour scale is in multiples of uniform density (MUD).

| Forward Strain = 0 (Centre) | Forward Strain = 0.83 (0.5R) | Forward Strain = 1.49 (0.9R) |
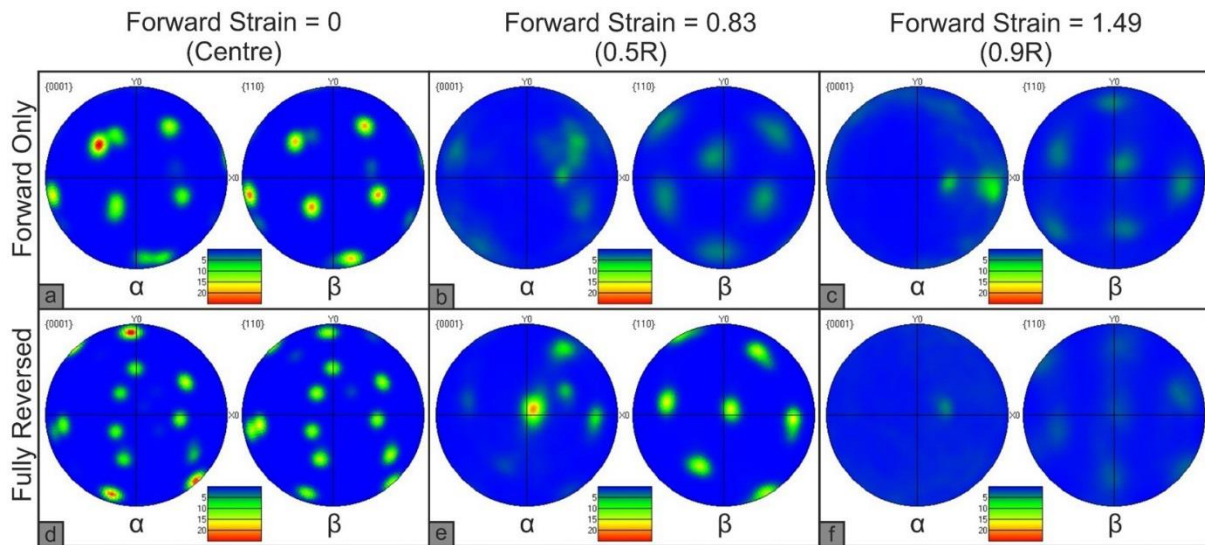
Figure 5.39: Data from Figure 5.38 presented across a uniform MUD scale (global maximum of 25).

In order to try and clarify whether the BOR is maintained, Figure 5.40-42 illustrate the misorientation angle distribution of the α phase in selected EBSD maps. An arrangement of α particles that precipitate from within a single parent β grain should adopt a specific set of misorientation angles. These angles take values of 10.529°, 60°, 60.832°, 63.262° and 90° while the precipitates are oriented in accordance with the BOR [115][116][117]. A normalised histogram of the correlated misorientation angle distribution at the centre of sample 2 is shown in Figure 5.40. A 'correlated' distribution represents the misorientation angles between adjacent points in the map, rather than randomly selected ones. Given the inherent noise in such data, all angles below 3° have been omitted (since a sharp peak is expected here due to slight misorientation between adjacent points within individual α particles).

Unlike α and α+β alloys, where the α phase is continuous or near-continuous, metastable β alloys pose a problem when determining the correlated misorientation angle distribution since the α precipitates are not in contact with one another. To overcome this issue, the β phase was removed, and the remaining α phase was extensively noise-reduced until each particle impinged on its neighbours. For the purposes of comparison, Figure 5.40 also includes the misorientation angle distribution of a randomly oriented array of crystallites in CP-Ti [118]. As Figure 5.40 demonstrates, the misorientation angle distribution in the centre (undeformed) region of specimen 2 exhibits significant data clustering around the critical BOR angles. This would indicate strict adherence to the BOR. Figure 5.41 presents the correlated misorientation angle distribution at 0.9R of specimen 6 (FWD strain of 1.49, no reversal). The BOR peaks have largely been removed, and replaced by a much more uniform spread of data, suggesting the Burger's Orientation Relationship has broken down. However, there now exist three distinct peaks at around 5°, 30° and 90°, the latter of which is a BOR peak, albeit much weaker than in the undeformed region. The peak at about 90° may be the result of some remnant BOR

consistent fraction, but the other two peaks are at non-BOR angles. The 'low-angle' peak (at around 5°) may be related to an increase in noise close to the 3° cut-off, whereas the 30° peak might be the result of some texture development during deformation. Ignoring these small peaks, the spread of data is much more uniform relative to the undeformed region of specimen 2, but still deviates from the theoretical random misorientation angle distribution. However, after strain reversal (test 7), the misorientation angle distribution at 0.9R (FWD strain = 1.49, total strain = 2.98) more closely matches the theoretical random distribution (see Figure 5.42). The low-angle peak also appears to have been removed, although the 30° and 90° peaks remain. Whether these changes are due to the nature of the strain path or simply the greater total strain is unclear.
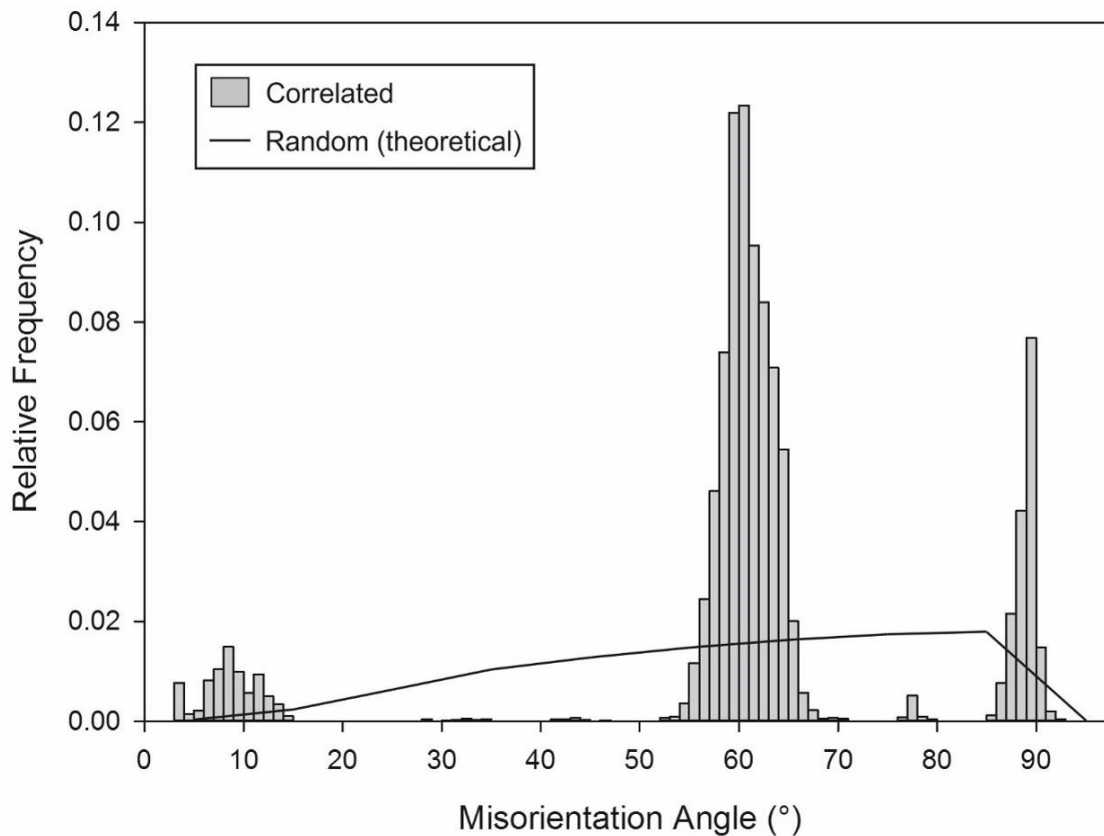
Figure 5.40: Misorientation angle distribution for the centre (zero strain) of specimen 2, and that of a randomly oriented array of crystallites in CP-Ti [118]. Misorientations below 3° are omitted.
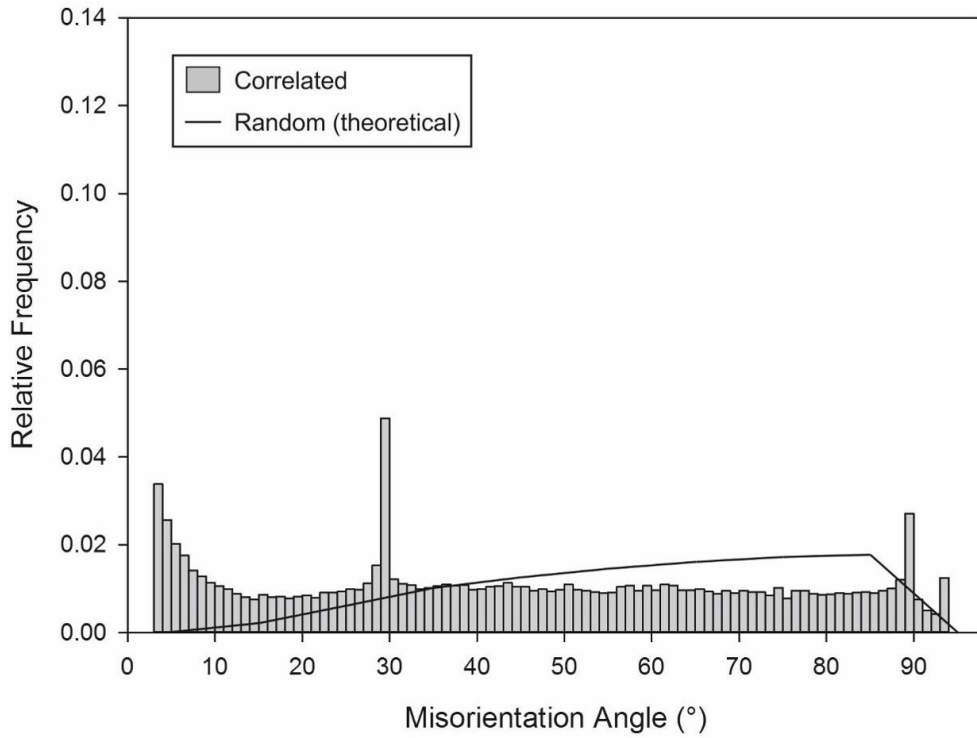
Figure 5.41: Misorientation angle distribution for the edge (1.49 FWD/Total strain) of
specimen 6, and that of a randomly oriented array of crystallites in CP-Ti [118].
Misorientations below 3° are omitted.
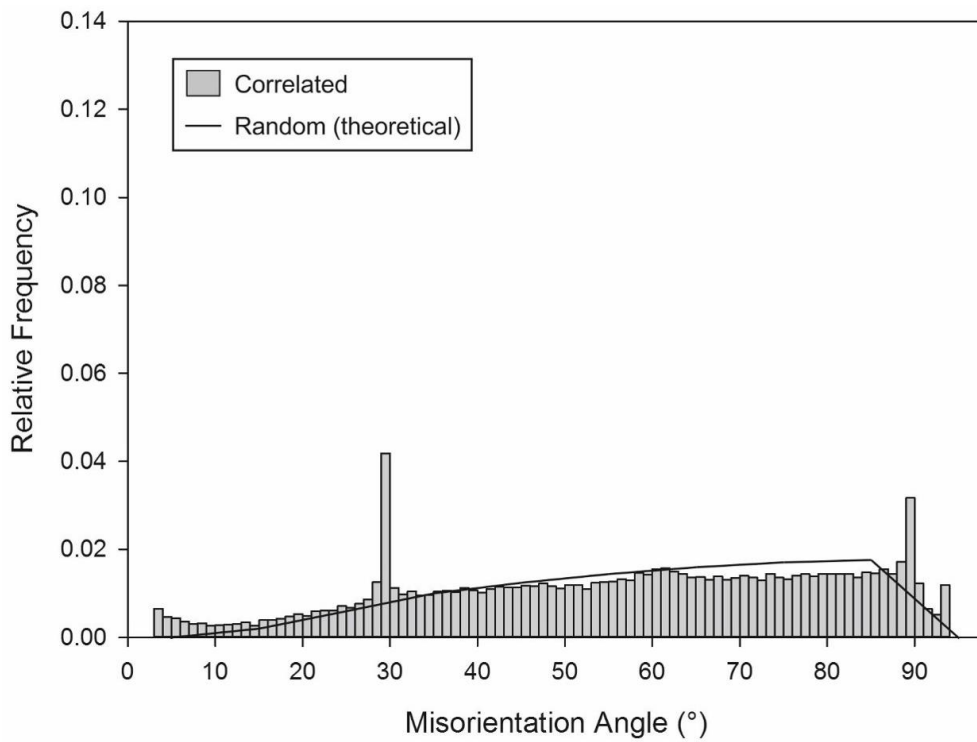
Figure 5.42: Misorientation angle distribution for the edge (1.49 FWD strain, 2.98 Total
strain) of specimen 7, and that of a randomly oriented array of crystallites in CP-Ti [118].
Misorientations below 3° are omitted.

In order to quantify the consistency of the BOR and how it evolved throughout deformation, the fraction of Burger's consistent misorientations is plotted as a function of FWD strain in Figure 5.43. However, as Figure 5.40 illustrated, there is usually a degree of scatter around the expected peaks, mostly due to the orientation accuracy of the data acquisition process. It is therefore necessary to define a tolerance to account for such 'noise'. In this case, a tolerance angle of 3° was chosen based on the literature [115][117]. Therefore, any misorientation which fell within 3° of a characteristic BOR angle was defined as Burger's consistent, while those falling outside this limit were excluded. It can be seen that specimen 6 (deformed only forwards) exhibits a decline in the Burger's consistent fraction until about 0.5 FWD strain, where it levels off at around 25%. Given the 3° tolerance on the Burger's consistent misorientations, the magnitude of the angular range they cover is 21.262°, which corresponds to approximately 23.6% of the full 90° range. This would suggest that in specimen 6, the BOR was no longer present from about 0.5 (FWD) strain onwards.

It should be noted that most EBSD maps were produced individually at each radial location on a given specimen. However, specimen 6 was mapped twice in an automated procedure, whereby all 10 maps (from 0R-0.9R) were acquired in one go. This provided two data sets for specimen 6, between which there was reasonable agreement at most radial locations (see Figure 5.43). However, there is a considerable discrepancy at 0.166 FWD strain. The cause of this is uncertain, but could relate to positioning errors in EBSD mapping, misalignment during deformation or grain (orientation) effects on BOR preservation.

Referring to the reversed specimens, it can be seen that the process of strain reversal appears to restore some of the Burger's consistent fraction up to a FWD strain of around 0.8. Beyond this limit, the BOR seems to be unrecoverable, and the consistent misorientation fraction settles at around the same level as the FWD only specimen (about 25%). Based on specimen 6 and the reversed tests, it appears as if the consistency of BOR was greater at the centre of the reversed specimens. In principle this should not have been the case, but it is possible that imperfect positioning of the centre EBSD map could have led to deviations from the true minimum strain. There is also the issue of alignment during deformation itself since torsion tests are very sensitive to this. The centre EBSD maps were positioned at the geometrical centre of the cylindrical specimens, but minor misalignment could have shifted the true axis of rotation, and consequently affected the actual strain values at each radial location. It is also possible that the discrepancy simply arises from the fact that the theoretical point of zero strain is an infinitesimal point at the specimen centre. Since the EBSD map covers a much larger area, the measured material will have been strained to some extent. In the reversed specimens, the effect of this may have been less since some restoration of the BOR would take place during strain reversal. Specimen 2, which was deformed forwards only (but to a lesser extent than specimen 6) displays a Burger's consistent fraction at its centre that is comparable to the

reversed specimens. The observation that the rest of this specimen also shows reasonable agreement with test 6 would support the latter explanation. Given that strain reversal has the effect of partially restoring Burger's consistency, the reversed specimens require a much larger total strain to break the orientation relationship between the two phases (see Figure 5.44).
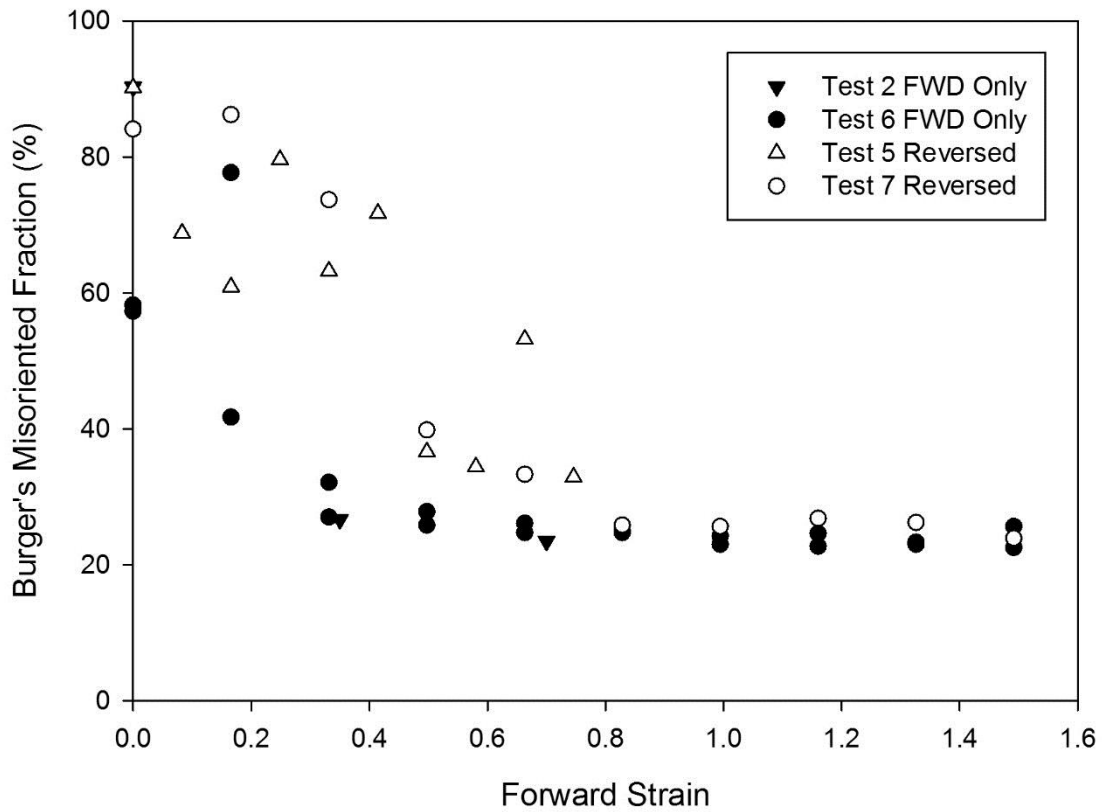
Figure 5.43: Fraction of Burger's consistent misorientations as a function of forward strain. Filled symbols are forward torsion only, hollow symbols are reversed torsion. Note overlapping triangular data points at zero strain, and test 6 was mapped twice.
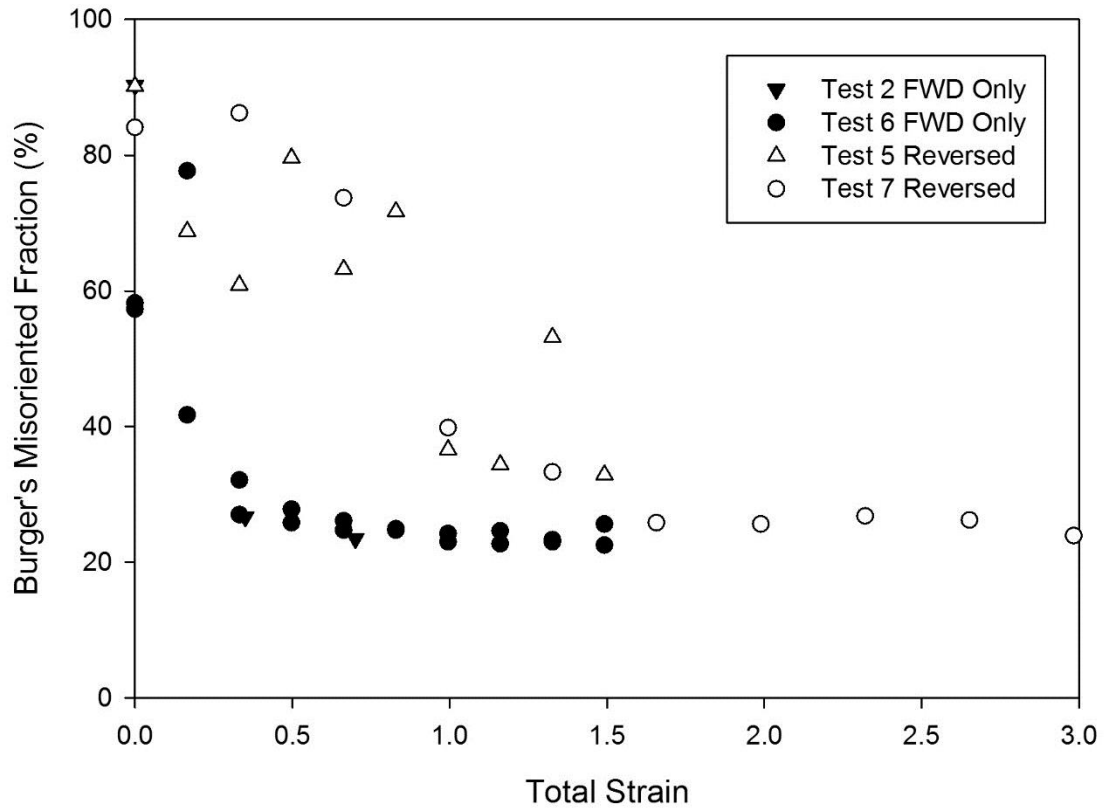
Figure 5.44: Fraction of Burger's consistent misorientations as a function of total strain. Filled symbols are forward torsion only, hollow symbols are reversed torsion. Note overlapping triangular data points at zero strain, and test 6 was mapped twice.

5.5.4 Effect of Heat Treatment

Figure 5.45 illustrates the effect of heat treatment upon the Vickers hardness of specimen 1. The data is plotted as a function of radius rather than strain since this sample was not deformed. The as-heated condition refers to the condition after heating in the ASP testing machine. This serves as a control for the deformation tests. It can be seen that there is very little difference between the as-heated and solution treated conditions. This is unsurprising given how similar the temperatures of the two treatments were (760 °C in the ASP test and 758±21 °C for the solution treatment). However, the ageing has a dramatic effect upon the hardness. The precipitation of secondary α increases the hardness by approximately 90-95 points. The minimal variation across the specimen would suggest that the temperature distribution was reasonably uniform (in agreement with volume fraction measurements of the deformed tests). Taking the mean value of all the data gives an average hardness in the as-heated condition of 304 HV ±4 (error is 95% confidence limit based on a t-distribution). In the solution treated condition the hardness is essentially unchanged, sitting at 301 HV ±1. Ageing then raises the mean hardness to 395 HV ±1. The wider confidence limit in the as heated condition may be an indication of slight microstructural variation within the specimen. The duration of the ASP test (10 minutes) was shorter than either of the subsequent heat treatments, allowing less time to establish equilibrium conditions within the specimen.
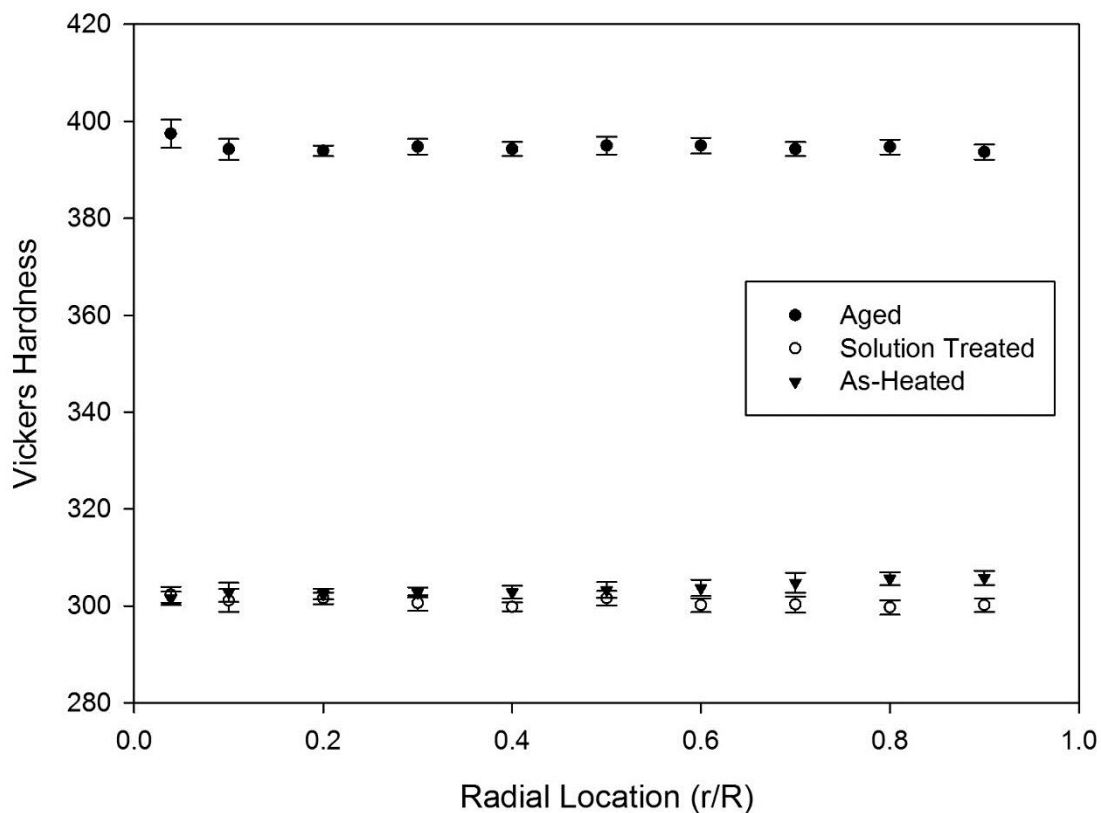
Figure 5.45: Effect of thermal treatments on the Vickers hardness of specimen 1 (no deformation). Error bars illustrate the 95% confidence limit.

213

A comparison of the as-heated hardness in specimen 1 with the as-deformed hardness of specimen 6 is made in Figure 5.46. Although specimen 6 was deformed (forwards only), the lack of deformation in specimen 1 necessitated a comparison based on radial displacement rather than strain. For an indication of the deformation level, the surface strain was 1.66. On this scale, the undeformed specimen (1), displays a slight hardening towards the edge. Ignoring the central two data points, the deformed specimen shows the opposite trend, although in both cases the variation is so small that it may well be insignificant. However, near the centre of the deformed specimen there is a pronounced drop in hardness.

This may be due to the larger β grain size in the low strain region (centre). However, it is also possible that it could be the result of an inherent limitation in the test methodology. The hardness values were based on a series of indents placed in concentric 'rings' around the specimen centre. The mean value for each 'ring' of indents was taken as the hardness for the radius of each respective ring. For the outer 8 radial locations, each ring consisted of 32 indents. However, in order to avoid placing indents too close together, this number had to be restricted to 16 indents at 0.1R and a 3×3 matrix of indents at the centre. This will have reduced the statistical reliability of the results since a much smaller area (or circumference) was analysed (and given the size of the β grains, this effect may be quite significant). If a β grain at the centre was in a 'soft' orientation, this could have brought the mean hardness down.

Another point to consider is the lower mean hardness in the deformed specimen. If the recrystallized grain size is responsible for the higher hardness away from the specimen centre, the undeformed specimen should have a lower hardness, but this is not the case. This discrepancy cannot be explained by the primary α volume fraction since this has minimal effect on yield strength [17]. In any case there was slightly more present in specimen 6 (see Table 5.3). However, the two specimens in question were situated at opposite ends of the as-received slice of material (see Figure 5.1). Since this slice is believed to be a quarter of the original billet cross section, that would put specimen 1 near the middle, and specimen 6 nearer the edge. Over this distance there could be other unexpected microstructural variation, particularly in such a segregation prone alloy.
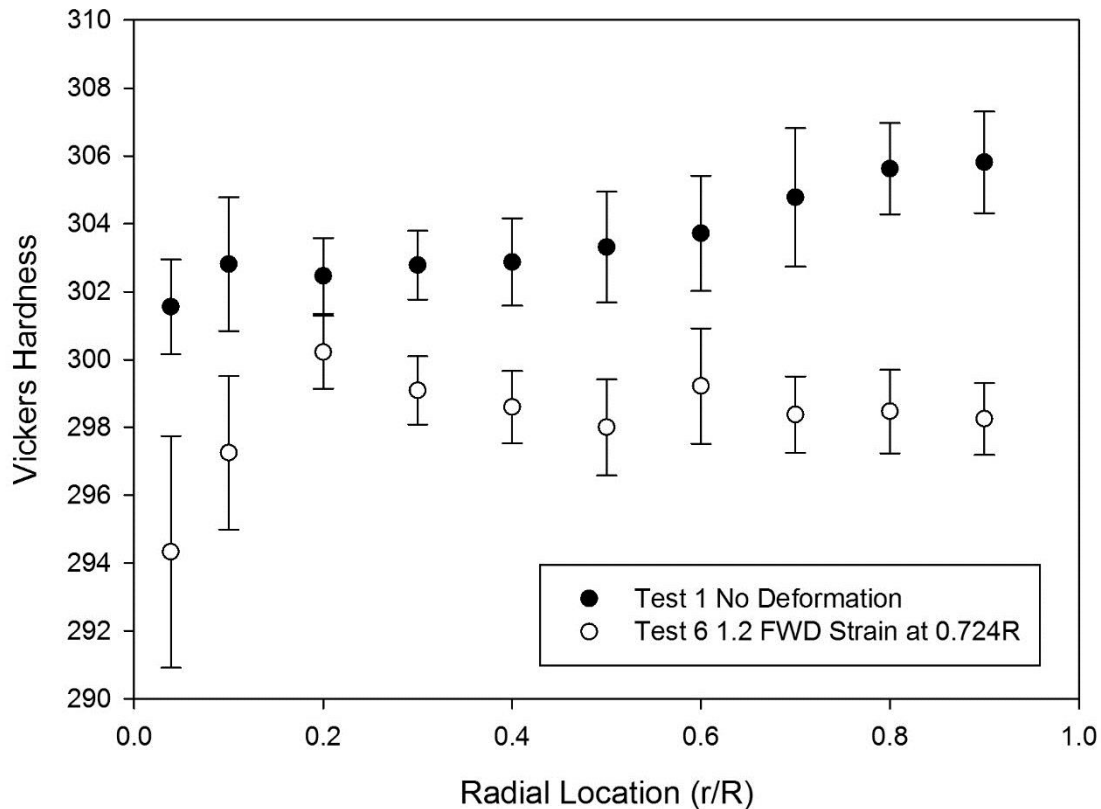
Figure 5.46: Vickers hardness across undeformed and deformed Ti-10-2-3 specimens. Error bars illustrate the 95% confidence limit.

When a comparison between test 1 and 6 is made in the aged condition, a significant difference emerges (see Figure 5.47). In the deformed specimen, there is a consistent decline in the hardness from 0.1R to the edge (of around 12 HV in total). However, the undeformed specimen exhibits negligible variation over the same radius. Both specimens do seem to display an anomalous value at their centre. The undeformed specimen is unexpectedly high, and the deformed specimen shows a slight drop. Figure 5.48 compares the aged hardness of other deformed specimens (error bars have been omitted for clarity, see appendix for these). Test 7 (a reversed test) also exhibits a decrease in hardness with increasing strain, although its peak hardness is lower than test 6. However, test 5 does not appear to exhibit such an obvious reduction in hardness, although it was not deformed as far as the other two tests. This may have cut off a decline in the hardness if it was occurring at slightly higher strain. The slight drop in hardness at the centre of specimen 6 now appears less likely to be an anomaly, as the other two deformed specimens also exhibit this reduction. It may be that a certain amount of strain improves the ageing response of Ti-10-2-3, but a further increase leads to a lower aged strength.

Although the morphology of the primary α exhibits similar trends to the ageing response (see Figure 5.32), it seems unlikely that it could be responsible for the hardness variation since the latter was not observed in the unaged condition (see Figure 5.46). Figure 5.49 illustrates the volume fraction of the aged matrix in the deformed specimens (where the aged matrix is the

combined volume fraction of retained β and secondary α). It can be seen that it remains fairly consistent across the specimen radii and therefore seems unlikely that this was responsible for the variation either. It can be seen though, that test 6 had a higher matrix volume fraction than the other two tests. This may explain the higher peak hardness in test 6 relative to test 7, although this is inconsistent at higher strains as the discrepancy between test 6 and 7 reduces. Neither does this account for the generally higher hardness in test 5 compared to test 7, since the volume fraction of the aged matrix was approximately equal in both. However, since the forward (and total) strain of test 5 was half that of test 7, the strain rate was effectively doubled (since the radial displacement will be double for a given strain, and the strain rate increases linearly with the radius). This increase in the strain rate may have reduced the recrystallized β grain size, leading to an increase in hardness. It may also explain the greater hardening exhibited in the first 0.25 strain of specimen 5. In addition it would also imply that the increasing strain rate across the radius of a torsion specimen is not responsible for the reduced ageing response.
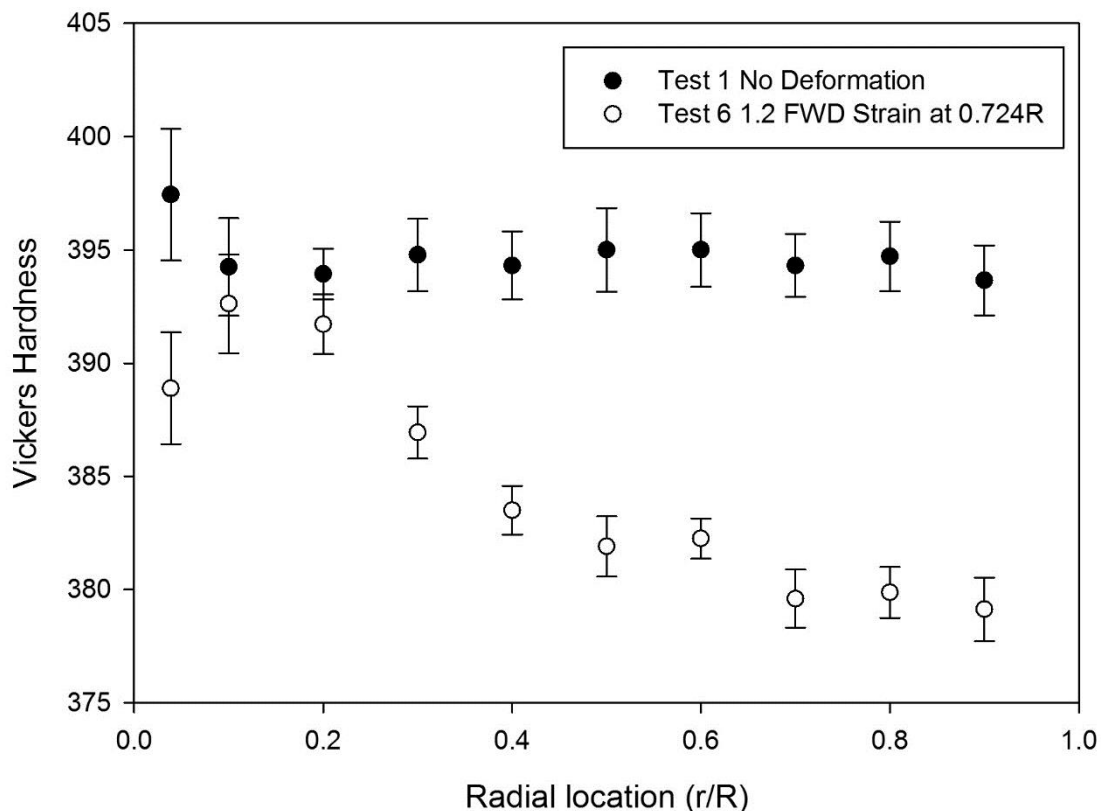
Figure 5.47: Effect of ageing on undeformed and deformed Ti-10-2-3 specimens. Error bars illustrate the 95% confidence limit.
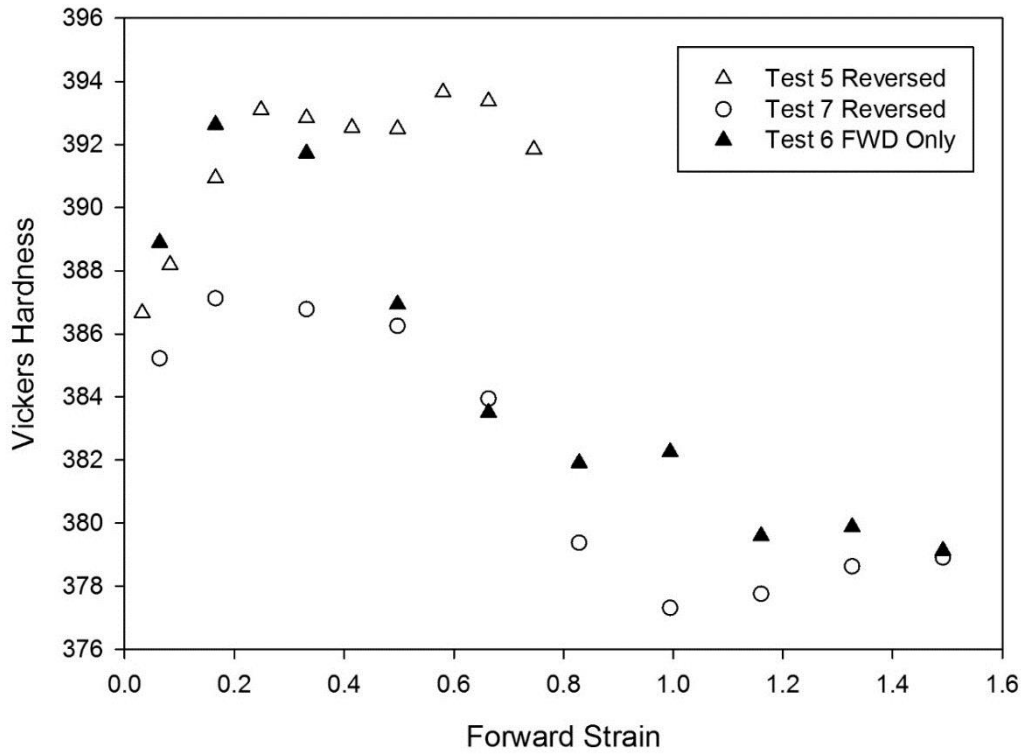
Figure 5.48: Effect of ageing on deformed Ti-10-2-3 specimens as a function of forward strain. Error bars omitted for clarity (see appendix for 95% confidence limits).
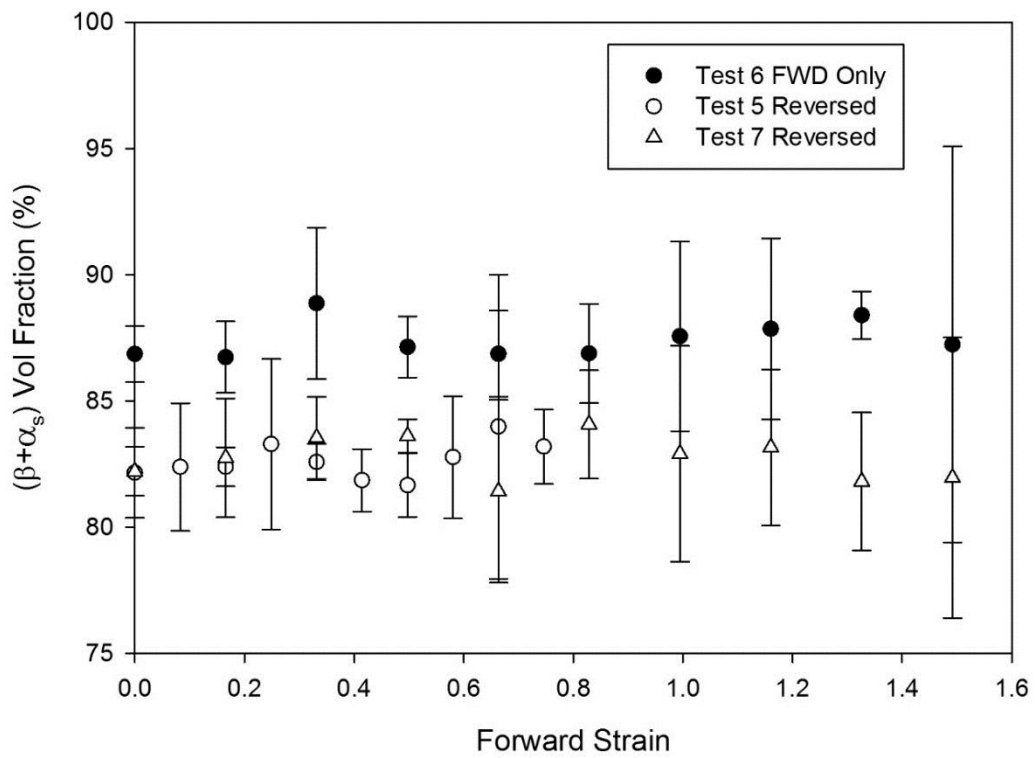
Figure 5.49: Volume fraction of aged matrix as a function of forward strain. Error bars illustrate the 95% confidence limit.

One possible explanation for this ageing behaviour could be the effect of hot work on precipitation of precursor phases such as ω (see Section 2.3). A study of β-III revealed that thermomechanical processing could suppress the formation of ω phase [119]. Other studies have shown that cold work can also suppress ω formation [17][120]. The increase in dislocation density and grain boundaries is believed to obstruct the atomic movements necessary for the phase transformation[120]. Since the ω phase assists with precipitation of secondary α, it is possible that increasing strain during hot work might actually lead to a coarser, less uniform distribution of secondary α particles[93]. Figure 5.50 compares high magnification micrographs taken at the centre and 0.9R of specimens 5-7. These appear to show coarser secondary α particles at 0.9R of specimen 6 (FWD strain = 1.49), but less of a disparity between the other two specimens.

It has also been shown that during deformation of β alloys, the strain is not distributed equally between the two phases, and that this effect is influenced by the primary α morphology. The β phase generally accommodates more strain than the α phase, but this effect is exacerbated as primary α plates break up [62][121][93]. Once globularisation has occurred, the β phase accommodates almost all of the strain as the equiaxed α particles are simply carried along with it [93]. If the primary α break-up in Figure 5.32 is an indication of the strain level in the β phase, and this suppresses ω formation, this may explain the reduced ageing response. In addition, strain reversal may lower the dislocation density by introducing more dislocations of opposite sign that annihilate existing ones through dynamic recovery. This may have mitigated the effect near the edge of specimen 7 (Figure 5.48), but been offset by the reduced matrix volume fraction, resulting in the lower peak hardness instead. Finally, a larger recrystallised β grain size may have been responsible for the reduction in hardness at the centre, and a reduced β grain size could have raised the hardness of specimen 5.
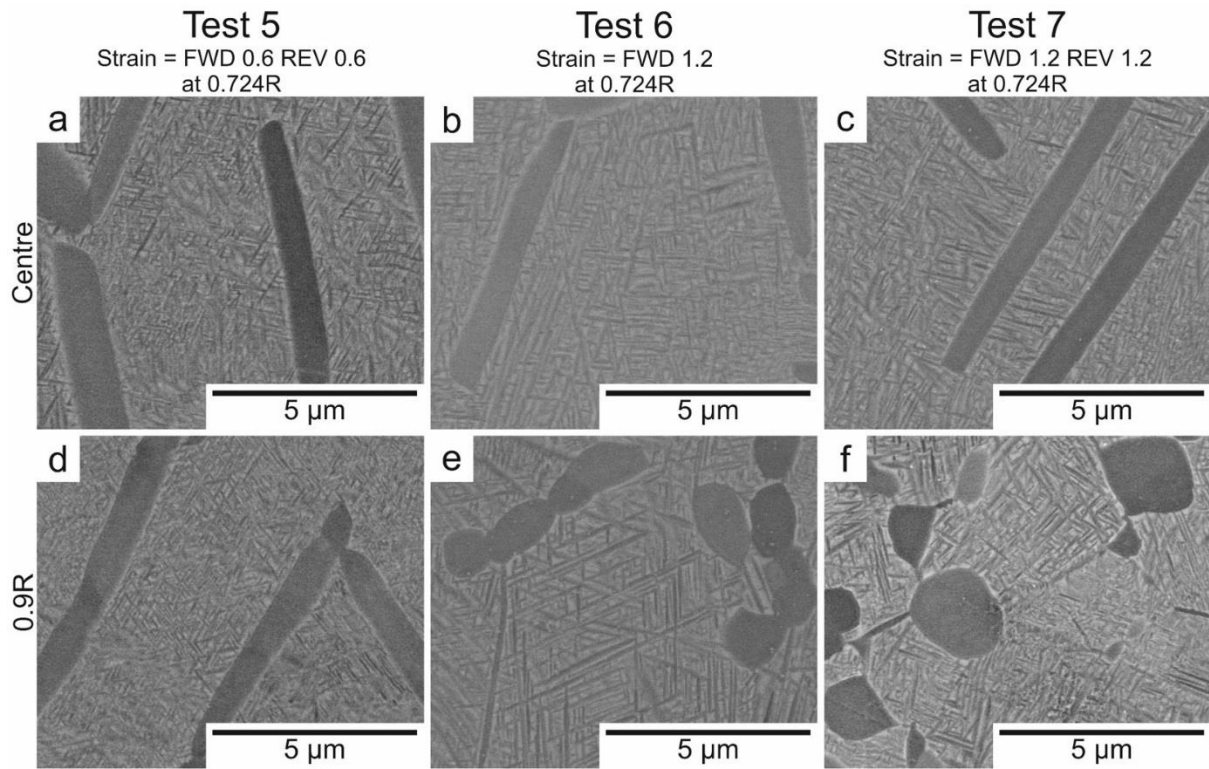
Figure 5.50: Comparison of aged microstructures at the centre and 0.9R of deformed specimens (note that quoted strain is for 0.724R).

5.6 Summary

Characterisation of Ti-10-2-3 billet revealed a microstructure of coarse 'primary' α and fine secondary α. The lack of deformation in the coarse α suggested that the billet had been forged in the β phase field. Both the coarse and fine α would then have formed during subsequent thermal treatments and/or cooling. This means the coarse α does not fit the true definition of 'primary' α since it was not present at the forging temperature. However, it is referred to as such here given that it was still present during the subtransus forging carried out in this study. The secondary α dissolves rapidly upon heating to 760 °C, accompanied by a significant reduction in the primary α volume fraction. Construction of a β approach curve indicated a β transus of around 805 °C.

Subtransus thermomechanical compression displayed a peak flow stress at low strain followed by extensive flow softening. Both the peak flow stress and magnitude of softening increase with strain rate. This behaviour cannot be explained solely via adiabatic heating, although it is likely to play a greater role at higher strain rates. Analysis of microstructural evolution during torsion tests would suggest that break up of the acicular α plates into a more globular morphology is at least partially responsible for the observed softening. Globularisation proceeds more readily at higher temperature. In spite of the higher total strain, the process of strain reversal (during torsion) did little to further globularise the primary α.

The Burger's Orientation Relationship (BOR) broke down at around 0.5 forward (FWD) strain, although it could be partially restored up to a FWD strain of about 0.8 through strain reversal. Deformation led to continuous dynamic recrystallisation (CDRX) of the β matrix, producing a new structure of small, high angle grains. Although the hardness increased in the STA condition, this effect was reduced at higher strains and was not adequately explained by the β volume fraction. However, the secondary α formed during ageing may have been slightly coarser in the more highly strained regions. This might explain the lower hardness in these areas. An exception to this general trend were the specimen centres. This deviation may have been the result of a larger β grain size.

Chapter 6 Conclusions

The work undertaken in the course of this project reaffirms the importance of microstructural control during processing of metastable β titanium alloys. The Ti-5553 forgings exhibited a significant degree of microstructural variation within them. This manifested itself as a concurrent variation in mechanical properties. The secondary α particle spacing (d) and retained β volume fraction (β_{vf}) appeared to heavily influence the strength and ductility. With the use of regression analysis, equations were fitted to the data, offering the potential to predict such properties based on these variables. However, other microstructural features represented confounding variables and weakened these correlations, limiting their applicability. The influence of β grain morphology and orientation is likely to be a major source of this deviation. Consequently, the two orientations (axial and tangential) had to be treated separately during analysis. This highlighted the difference in 'responsiveness' to heat treatment between the two orientations. The axial UTS and ductility were both significantly affected by heat treatment, whereas the tangential orientation was not.

Since the axial ductility was already superior to the tangential ductility, this only exacerbated the difference between the two, particularly near the component wall. This lacklustre response to heat treatment in the tangential specimens is likely due to limiting microstructural features that have more influence in this orientation. The fracture properties of metastable β alloys in the aged condition are heavily influenced by the preferential deformation at β grain boundaries [6]. The tangential orientation is perpendicular to the elongated direction of the β grains, which may have imposed limits on the maximum achievable ductility in this orientation. This would explain why alterations in the microstructure brought about through heat treatment (in terms of d and β_{vf}) improved the ductility of the axial orientation but failed to do so in the tangential orientation.

It would also explain why the observed correlations between the measured microstructural parameters were weaker in the tangential data (since there were more variables unaccounted for and/or these were more significant in the latter orientation). The proof stress did exhibit some improvement in the tangential orientation in response to heat treatment. This improvement was brought about largely through changes in work hardening behaviour, leaving the UTS relatively unaffected. It may be that the proof stress was less influenced by the β grain orientation as it is a better indication of a material's resistance to plastic deformation. For the same reason, the Vickers hardness correlated reasonably well with d and β_{vf}. However, although the proof stress in the tangential orientation was improved through heat treatment, the issue of ductility remains. The most effective way to improve matters is therefore likely to involve altering the β grain structure and/or texture. Unfortunately, this is liable to reduce ductility in the axial orientation. Ultimately then, the optimisation of ductility is likely to require a compromise between the two competing orientations.

A reliable description of the texture could not be obtained through EBSD due to the β grain size. However, it was possible to confirm adherence to the Burger's Orientation Relationship (BOR) throughout the forging. Acquisition of reliable texture information by sampling a larger area/volume (through EBSD, XRD or neutron diffraction) may still face problems due to the large β grain size combined with the microstructural variation that is possible over relatively short distances. This last point was most clearly illustrated by the hardness maps of forging 1. These revealed an unexpected band of soft material situated approximately 15 mm from the forging edge in the as-received condition. The magnitude of the variation in hardness and the distance over which it occurred (about 20 mm) is remarkable. This fluctuation now appears to be the result of an abrupt change in the secondary α particle size/spacing. The cause of this short range microstructural variation is unclear, but believed to be thermal in nature. It would appear that the secondary α size and morphology can fluctuate more rapidly than the primary α. The fine scale of secondary α makes it more susceptible to minor fluctuations in temperature, leading to localised variation.

Long range variation in mechanical properties is caused by the net effect of both secondary α and other, less responsive features (for example, $β_{vf}$ which exhibits a more gradual variation within the forging). The result is a general increase in hardness towards the forging edge, with a sudden drop where the secondary α unexpectedly coarsens. This abrupt and significant change in mechanical properties may well have taken place within the gauge length of the edge tensile specimens. This could be another source of error that distorted the correlations mentioned earlier. The change in unrecrystallised β grain structure throughout the forging is most likely caused by the non-uniform strain distribution that closed die forging induces. Although it is unlikely to vary as rapidly as the secondary α, attempts to correlate texture with mechanical properties may face issues if the test specimens incorporate material in the gauge length that varies wildly in other respects. It should be noted though, that the fluctuations in secondary α size/morphology were removed by heat treatment. This would suggest that the final component should also be free from such abrupt changes in microstructure and mechanical properties.

Nevertheless, this example aptly demonstrates the need to exercise great care during processing to avoid unintended consequences. The primary α morphology also exhibited variation within the forging, adopting a more globular shape near the forging edge. This was undoubtedly intentional as a globular morphology is known to enhance ductility [17]. However, this improvement in ductility comes at the expense of fracture toughness, which is higher for microstructures exhibiting more acicular α plates [8]. The final microstructure presumably represents a balance between these two competing properties that is specific to the application (in this case, a main landing gear inner cylinder). It is worth noting that the material near the forging edge is significantly harder in the as-received condition than the heat treated condition.

If the forging is rough machined in the as-received condition, the tool life may be significantly reduced near the edge. Thus, somewhat counterintuitively, tooling costs may actually be lower if this machining was carried out in the heat treated condition instead of as-received.

Initial characterisation of billet condition Ti-10-2-3 revealed a number of similarities to the forged Ti-5553 in addition to some notable differences. Both microstructures consisted of coarse primary α with a fine distribution of secondary α platelets within the retained β matrix. However, the primary α in the Ti-10-2-3 billet appeared undeformed, existing as coarse, high aspect ratio plates. This implied that the Ti-10-2-3 billet had been β forged, with both the coarse and fine α forming during subsequent thermal treatments and/or cooling (as mentioned earlier, this 'coarse α' is not technically 'primary α', but is referred to as such since it was present during the subtransus forging carried out in this study). This contrasts with the α+β forging of the Ti-5553 workpiece. Heating the Ti-10-2-3 to the industrial forging temperature of 760 °C resulted in rapid dissolution of the secondary α and a significant reduction in the primary α volume fraction.

Comparison of the β approach curve with that determined by Jones for Ti-5553 confirmed the steeper slope of the Ti-10-2-3 curve [93]. As a result, Ti-10-2-3 requires more care when forged to prevent unacceptable fluctuations in the α volume fraction [25]. From the approach curve, the β transus was found to be approximately 805 °C, about 40 °C below that reported for the Ti-5553 forgings (843 °C and 848 °C). Subtransus thermomechanical compression of Ti-10-2-3 reveals a peak flow stress at low strain followed by extensive flow softening. This softening cannot be explained by adiabatic heating alone. The peak flow stress and magnitude of flow softening both increase with increasing strain rate, although adiabatic heating is likely to play an increasing role at higher strain rates. Flow softening is also observed in subtransus torsion tests. Analysis of the primary α feret diameter would suggest that the softening is related to fragmentation of acicular α particles. The high aspect ratio plates initially offer greater resistance to deformation, before breaking up and globularising. In doing so, the flow stress falls as the globular α particles are carried by the deforming β matrix, which now accommodates far more of the strain.

The process of globularisation occurs more rapidly as the forging temperature increases. This is presumably because the α plates narrow as the β volume fraction rises with increasing temperature. These thinner plates are then easier to deform and break up at lower strain. The process of strain reversal does little to further globularise the primary α despite the higher total strain. This raises the possibility that industrial forging operations may include redundant work that achieves very little in further refining the microstructure. EBSD analysis revealed that the consistency of the Burger's Orientation Relationship (BOR) dropped to a minimum at around 0.5 forward (FWD) strain. However, it could be at least partially restored through strain reversal up to a FWD strain of about 0.8. The β matrix also exhibited continuous dynamic

recrystallization (CDRX), creating a new structure of small grains with high angle boundaries. Although solution treatment and ageing increased the hardness, this effect was less at higher strains. This variation could not be explained by the β_{vf} although there may be a slight coarsening of the secondary α in the high strain regions. It is hypothesised that deformation of the β phase suppressed ω formation and resulted in a coarser distribution of secondary α (since ω particles are believed to serve as nucleation sites for secondary α). It is also possible that the process of strain reversal may have reduced this effect. It is postulated that strain reversal may have lowered the dislocation density by introducing more dislocations of opposite sign. These would then annihilate one another during dynamic recovery, lowering the overall density. If dislocations were suppressing ω formation, this might reverse that effect and lead to a finer distribution of secondary α. This hypothesis is however in its infancy, and further work will be needed to verify it. There was also a minor but consistent drop in the aged hardness at very low strain. This deviation from the general trend may be due to a larger β grain size at the specimen centres.

Chapter 7 Further Work

Given the broad scope of this project, there are a number of areas that warrant further investigation. In terms of characterisation of the Ti-5553 forgings, the existence of the band of coarse secondary α raises questions as to how it was formed and the prevalence of such heterogeneities in other processes. This requires detailed knowledge of the processing route, and may therefore be commercially sensitive information. Given that the process route was changed between delivery of the forgings, the presence of this 'soft band' in the second forging is still uncertain, as the 'intermediate' data points are missing. It may therefore be prudent to confirm this by hardness mapping forging 2. In light of the time consuming nature of this process, a more efficient approach may be to carry out a number of hardness traverses in lieu of a full map. Given what is now known about the microstructural variation within the forging, it may also be advisable to remove a second set of microscopy specimens that more accurately reflect the positioning of the tangential tests (instead of relying on the adjacent axial specimens for microstructural information). This may improve the correlation between quantified microstructural variables and the reported mechanical properties.

However, there is still the issue of possible microstructural variation within the gauge length of tensile specimens. One solution would be to first identify the microstructural/hardness variation in another forging before positioning the tensile specimens to avoid such fluctuations (this would have been the ideal approach in the first instance). Effectively repeating the study will be time consuming, but offers other potential advantages. For instance, a slight discrepancy was noted between the β_{vf} measured in each of the two tangential orientations. In principle this should not have been the case, as the area fraction should be independent of orientation. However, the methodology itself may have introduced some variation between orientations. It would perhaps have been more appropriate to examine the axial plane as it is shared by both the flash line and centre line. Although this lesson was heeded for the secondary α measurements, the influence of interparticle spacing is also likely to vary depending upon orientation. It might therefore be advisable to measure the interparticle spacing on multiple planes to account for this, or choose a specific direction (perhaps 45° from the tensile axis).

There is also the matter of morphology. Although the hardening effect of undeformable particles should be proportional to d^{-1}, the extent of this effect is also related to the shape of the particles. The hardening effect of plates or rods can be an order of magnitude greater than spheres [82]. Despite the lack of quantitative measurements, the aspect ratio of the secondary α precipitates did appear to vary. This adds a further complication to quantification. One approach may be to use a program such as ImageJ to provide shape descriptors such as feret diameter and aspect ratio. However, this presents a similar problem to that experienced when attempting to distinguish between the primary and secondary α. The particles are often in contact, and therefore individual precipitates are indistinguishable. Some form of pattern

recognition software would be needed, which presents a major obstacle if it requires bespoke programming. It might also be useful to attempt quantification of other microstructural variables such as the thickness or continuity of grain boundary α. As mentioned earlier, correlation of the mechanical properties with texture may be difficult since the area/volume required to provide a reliable description of the texture may incorporate significant variation in other microstructural parameters that distort the results. One option could be to heat treat samples such that the β grain structure and texture is unaffected (or minimally effected), and homogenise the β volume fraction and secondary α across all samples. The mechanical properties should therefore illustrate the effect of texture more accurately.

Concerning the fitted equations for % elongation, an obvious drawback is their limited applicability to other specimen geometries and testing equipment. It would therefore be useful to obtain the reduction in area (RA) values in order to allow comparison across different studies. This was originally omitted to allow fractography, but investigation of alternatives might be useful (e.g. area measurements made through microscopy). Fractographic analysis is also an area that requires further work. Examination of the fracture surfaces, both parallel and perpendicular to the tensile axis may shed some light on the underlying mechanisms that govern the observed microstructure-property relationships. Ultimately though, with so many variables changing simultaneously, the need arises for a parametric study in order to isolate the influence of separate microstructural variables. This is particularly important given the degree of scatter present in ductility data, requiring a larger data set to reduce the uncertainty in measured properties/features [17]. This is of course easier said than done, given the difficulty in changing one microstructural variable while holding all others constant. In certain cases this may even be impossible given the interdependence of some microstructural features.

The investigation of thermomechanical processing of Ti-10-2-3 has also raised many questions. Beginning with the billet itself, the compositional homogeneity may be worth checking, as this could alter the β transus between specimens. Assuming this were uniform though, further study is required in order to confirm and corroborate the original findings. A possible change to the existing methodology would be to carry out the microstructural characterisation and hardness testing in a sequential manner for each condition (rather than remove multiple samples from each torsion specimen and heat treat them separately). If the strain distribution were non-uniform, the effect of this would be minimised between the as-deformed, solution treated and aged condition. Given the unavoidable strain rate variation across the radius of a torsion specimen, corroboration could include axisymmetric compression up to 0.8 strain. This would maintain a constant (macroscopic) strain rate and allow study of the BOR. In the course of such a study, it might be useful to look into the effects of β orientation on preservation of BOR, as this may be responsible for spurious results in the earlier investigation (see Section 5.5.3). Alternatively, to reduce the number of tests required, axisymmetric compression of double

truncated cones could be employed. This testing methodology maintains a near constant strain rate across the specimen cross section, while simultaneously covering a strain range of 0.4-1.8 depending upon the height reduction [95]. However, both compression tests are incapable of 'strain reversal' and will therefore be unable to confirm the possible restoration of BOR. Heat treatment will still offer the possibility of confirming the unusual ageing response at higher strains. There is also a need for quantitative measurements of the secondary α in the aged torsion specimens, as well as any compression tests that are carried out. Transmission Electron Microscopy (TEM) may be necessary to provide the required resolution for such analysis. The use of TEM may require ion milling to avoid the formation of martensite through stress relaxation.

Alternatively, ageing at a higher temperature may permit analysis via SEM, as with the Ti-5553 forgings. If the α precipitation is found to be coarser at higher strain, this may explain the lower aged hardness. In this case, it would then be advisable to investigate ω phase formation to see if this is responsible. Quantitative analysis of the β grain size may also be useful, although the area available at each strain level may be insufficient to produce reliable data (multiple tests would help here). Finally, it would ultimately be useful if these phenomena could be reliably modelled so that lessons learned may be applied in practice. Software such as DEFORM can be used to model torsion tests and compare outputs, in terms of flow behaviour and microstructural evolution. However, such models are often empirical in nature, and a more fundamental understanding will be required to predict the effect of non-linear strain paths on microstructure development.

References

[1]   M. Peters, J. Hemptenmacher, J. Kumpfert, and C. Leyens, *Titanium and Titanium Alloys*. Weinheim: Wiley-VCH, 2003.

[2]   G. Lutjering and J. C. Williams, *Titanium*, 2nd ed. pp. 1-77, Berlin: Springer-Verlag, 2007.

[3]   "USGS Titanium End-use statistics," 2006.

[4]   D. Banerjee and J. C. Williams, "Perspectives on Titanium Science and Technology," *Acta Mater.*, vol. 61, pp. 844–879, 2013.

[5]   R. R. Boyer, "An overview on the use of titanium in the aerospace industry," *Mater. Sci. Eng. A*, vol. 213, pp. 103–114, 1996.

[6]   G. Lutjering and J. C. Williams, *Titanium*, 2nd ed. pp. 283-386, Berlin: Springer-Verlag, 2007.

[7]   E. H. Kraft, "Summary of Emerging Titanium Cost Reduction Technologies," 2004.

[8]   J. D. Cotton, R. D. Briggs, R. R. Boyer, S. Tamirisakandala, P. Russo, N. Shchetnikov, and J. C. Fanning, "State of the Art in Beta Titanium Alloys for Airframe Applications," *Jom*, vol. 67, no. 6, pp. 1281–1303, 2015.

[9]   J. D. Cotton and M. Jackson, "Private communication between Boeing and UoS," 2010.

[10]   W. D. Callister, *Materials Science and Engineering: An Introduction*, 7th ed. pp. 54-59, New York: John Wiley & Sons Inc, 2006.

[11]   P. G. Partridge, "The crystallog raphy and deformation modes of hexagonal close-packed metals," *Metall. Rev.*, vol. 12, pp. 169–194, 1967.

[12]   I. P. Jones and W. B. Hutchinson, "Stress-state dependence of slip in Titanium-6Al-4V and other H.C.P. metals," *Acta Metall.*, vol. 29, no. 6, pp. 951–968, 1981.

[13]   N. E. Paton and J. C. Williams, "The Deformation of Body-Centred-Cubic Titanium-Vanadium Single Crystals," in *Second International Conference on the Strength of Metals and Alloys*, 1970, p. 108.

[14]   G. Lutjering and J. C. Williams, *Titanium*, 2nd ed. pp. 210-272, Berlin: Springer-Verlag, 2007.

[15]   I. Lonardelli, N. Gey, H.-R. Wenk, M. Humbert, S. C. Vogel, and L. Lutterotti, "In situ observation of texture evolution during α→β and β→α phase transformations in titanium alloys investigated by neutron diffraction," *Acta Mater.*, vol. 55, no. 17, pp. 5718–5727, 2007.

[16]   D. Qiu, R. Shi, D. Zhang, W. Lu, and Y. Wang, "Variant selection by dislocations during α precipitation in α/β titanium alloys," *Acta Mater.*, vol. 88, pp. 218–231, 2015.

[17]   T. W. Duerig and J. C. Williams, "Overview: microstructure and properties of beta titanium alloys," in *Beta Titanium Alloys in the 1980's, TMS*, 1984, pp. 19–67.

[18]   J. L. Murray, "ASM Cr-Ti Phase Diagram," 1990.

[19] H. W. Rosenberg, "Titanium Alloying in Theory and Practice," in *The Science, technology and Application of Titanium*, 1970, pp. 851–859.

[20] H. M. Flower, "Microstructural development in relation to hot working of titanium alloys," *Mater. Sci. Technol.*, vol. 6, no. 11, pp. 1082–1092, 1990.

[21] I. Polmear, *Light Alloys*, 4th ed. Oxford: Elsevier, 1981.

[22] G. Lutjering and J. C. Williams, *Titanium*, 2nd ed. pp. 174-201, Berlin: Springer-Verlag, 2007.

[23] TIMET, "Timetal 834 Data Sheet." 2000.

[24] R. R. Boyer and R. D. Briggs, "The Use of β Titanium Alloys in the Aerospace Industry," *J. Mater. Eng. Perform.*, vol. 14, no. 6, pp. 681–685, 2005.

[25] S. L. Nyakana, J. C. Fanning, and R. R. Boyer, "Quick Reference Guide for β Titanium Alloys in the 00s," *J. Mater. Eng. Perform.*, vol. 14, no. 6, pp. 799–811, 2005.

[26] R. Boyer, G. Welsch, and E. W. Collings, *Materials Properties Handbook: Titanium Alloys*. pp. 1-11, ASM International, 1994.

[27] W. G. Burgers, "On the process of transition of the cubic-body-centered modification into the hexagonal-close-packed modification of zirconium," *Physica*, vol. 1, no. 7–12, pp. 561–586, 1934.

[28] J. B. Newkirk and A. H. Geisler, "Crystallographic aspects of the beta to alpha transformation in titanium," *Acta Metall.*, vol. 1, no. 111, pp. 370–374, 1953.

[29] H. M. Otte, "Mechanism of the Martensite Transformation in Titanium and its Alloys," in *The Science, Technology and Application of Titanium*, 1970, pp. 645–657.

[30] R. Bott, "The Decomposition of Hexagonal Martensite in a Titanium-Copper Alloy," *Scr. Metall.*, vol. 19, no. 3, pp. 319–322, 1985.

[31] S. Nag, A. Devaraj, R. Srinivasan, R. E. a Williams, N. Gupta, G. B. Viswanathan, J. S. Tiley, S. Banerjee, S. G. Srinivasan, H. L. Fraser, and R. Banerjee, "Novel Mixed-Mode Phase Transition Involving a Composition-Dependent Displacive Component," *Phys. Rev. Lett.*, vol. 106, no. 24, p. 245701, 2011.

[32] S. K. Sikka, Y. K. Vohra, and R. Chidambaram, *Omega phase in materials*, vol. 27, no. 3–4. 1982.

[33] J. C. Williams and M. J. Blackburn, "Influence of Misfit on the Morphology and Stability of the Omega Phase in Titanium-Transition Metal Alloys," *Met Soc. AIME-Transactions*, pp. 2352–2355, 1969.

[34] G. H. Narayanan, T. . Luhman, T. . Archbold, R. Taggart, and D. . Polonis, "A phase separation reaction in a binary titanium-chromium alloy," *Metallography*, vol. 4, no. 4, pp. 343–358, 1971.

[35] S. Nag, R. Banerjee, R. Srinivasan, J. Y. Hwang, M. Harper, and H. L. Fraser, "Omega-Assisted nucleation and growth of alpha precipitates in the Ti-5Al-5Mo-5V-3Cr-0.5Fe beta titanium alloy," *Acta Mater.*, vol. 57, no. 7, pp. 2136–2147, 2009.

[36] V. Chandrasekaran, R. Taggart, and D. H. Polonis, "Fracture Modes in a Binary

Titanium Alloy," *Metallo*, vol. 5, pp. 235–250, 1972.

[37] J. M. Silcock, "An X-ray examination of the omega phase in TiV, TiMo and TiCr alloys," *Acta Metall.*, vol. 6, no. 411, pp. 481–493, 1958.

[38] G. The, F. V. Los, V. A. T. Legierungen, A. T. Durcis, and P. a R. Die, "Deformation Behaviour of Age-Hardened Ti-Mo Alloys," *Acta Metall.*, vol. 22, pp. 901–909, 1974.

[39] P. Laheurte, a. Eberhardt, and M. J. Philippe, "Influence of the microstructure on the pseudoelasticity of a metastable beta titanium alloy," *Mater. Sci. Eng. A*, vol. 396, pp. 223–230, 2005.

[40] A. W. Bowen, "Omega phase embrittlement in aged Ti-15%Mo," *Scr. Metall.*, vol. 5, pp. 709–716, 1971.

[41] D. J. Lin, J. H. Chern Lin, and C. P. Ju, "Effect of omega phase on deformation behavior of Ti-7.5Mo-xFe alloys," *Mater. Chem. Phys.*, vol. 76, no. 2, pp. 191–197, 2002.

[42] J. C. Williams, B. S. Hickman, and H. L. Marcus, "The Effect of Omega Phase on the Mechanical Properties of Titanium Alloys," *Metall. Trans.*, 1971.

[43] G. T. Terlinde, T. W. Duerig, and J. C. Williams, "Microstructure, Tensile Deformation, and Fracture in Aged Ti-10V-2Fe-3Al," *Metall. Trans. A*, vol. 14A, no. October, pp. 2101–2115, 1983.

[44] D. Eylon, R. R. Boyer, and D. A. Koss, "Microstructural Instabilities in Beta Titanium Alloys," in *Beta Titanium Alloy's in the 1990's*, A. Vassel, Ed. Warrendale: TMS, 1993, pp. 173–185.

[45] J. Coakley, V. A. Vorontsov, N. G. Jones, A. Radecka, P. A. J. Bagot, K. C. Littrell, R. K. Heenan, F. Hu, A. P. Magyar, D. C. Bell, and D. Dye, "Precipitation processes in the Beta-Titanium alloy Ti–5Al–5Mo–5V–3Cr," *J. Alloys Compd.*, vol. 646, pp. 946–953, 2015.

[46] N. G. Jones, R. J. Dashwood, M. Jackson, and D. Dye, "β Phase decomposition in Ti–5Al–5Mo–5V–3Cr," *Acta Mater.*, vol. 57, no. 13, pp. 3830–3839, 2009.

[47] Y. Ohmori, T. Ogo, K. Nakai, and S. Kobayashi, "Effects of ω-phase precipitation on β→α, α″ transformations in a metastable β titanium alloy," *Mater. Sci. Eng. A*, vol. 312, no. 1–2, pp. 182–188, 2001.

[48] F. Busongo, TU Hamburg-Harburg, 2005.

[49] M. A. Imam and C. R. Feng, "TTT curve for Beta21S," in *Titanium '95, Science and Technology*, 1995, p. 2361.

[50] C. R. M. Afonso, P. L. Ferrandini, A. J. Ramirez, and R. Caram, "High resolution transmission electron microscopy study of the hardening mechanism through phase separation in a β-Ti–35Nb–7Zr–5Ta alloy for implant applications," *Acta Biomater.*, vol. 6, pp. 1625–1629, 2010.

[51] L. Wagner and J. K. Gregory, "Improvement of Mechanical Behaviour in Ti-3Al-8V-6Cr-4Mo-4Zr," in *Beta Titanium Alloys in the 1990's*, D. Eylon, R. R. Boyer, and D. A. Koss, Eds. Warrendale: TMS, 1993, pp. 199–209.

[52] V. N. Moiseev, É. V Polyak, and A. Y. Sokolova, "Martensite strengthening of

titanium alloys," *Met. Sci. Heat Treat.*, vol. 17, no. 8, pp. 687–691, 1975.

[53] S. G. Fedotov, *Titanium Science and Technology*. pp. 871, Plenum Press, 1973.

[54] R. R. Boyer, G. Welsch, and E. W. Collings, *Materials Properties Handbook: Titanium Alloys*. pp. 36, ASM International, 1994.

[55] T. Grosdidier and M. J. Philippe, "Deformation induced martensite and superelasticity in a beta-metastable titanium alloy," *Mater. Sci. Eng. A*, vol. 291, no. 1, pp. 218–223, 2000.

[56] W. Chen, Q. Sun, L. Xiao, and J. Sun, "Deformation-induced microstructure refinement in primary α phase-containing Ti–10V–2Fe–3Al alloy," *Mater. Sci. Eng. A*, vol. 527, no. 27–28, pp. 7225–7234, 2010.

[57] T. W. Duerig, J. Albrecht, D. Richter, and P. Fischer, "Formation and reversion of stress induced martensite in Ti-10V-2Fe-3Al," *Acta Metall.*, vol. 30, no. 12, pp. 2161–2172, 1982.

[58] N. B. D'yakonova, I. V. Lyasotskii, and Y. L. Rodionov, "Orthorhombic martensite and the ω phase in quenched and deformed titanium alloys with 20–24 at % Nb," *Russ. Metall.*, vol. 2007, no. 1, pp. 51–58, 2007.

[59] R. P. Kolli, W. J. Joost, and S. Ankem, "Phase Stability and Stress-Induced Transformations in Beta Titanium Alloys," *Jom*, vol. 67, no. 6, pp. 1273–1280, 2015.

[60] P. Laheurte, F. Prima, A. Eberhardt, T. Gloriant, M. Wary, and E. Patoor, "Mechanical properties of low modulus beta titanium alloys designed from the electronic approach," *J. Mech. Behav. Biomed. Mater.*, vol. 3, no. 8, pp. 565–573, 2010.

[61] E. S. N. Lopes, A. Cremasco, C. R. M. Afonso, and R. Caram, "Effects of double aging heat treatment on the microstructure, Vickers hardness and elastic modulus of Ti–Nb alloys," *Mater. Charact.*, vol. 62, no. 7, pp. 673–680, 2011.

[62] I. Weiss and S. L. Semiatin, "Thermomechanical processing of beta titanium alloys— an overview," *Mater. Sci. Eng. A*, vol. 243, no. 1–2, pp. 46–65, 1998.

[63] I. Mellor, I. Grainger, K. Rao, J. Deane, and M. Conti, "Titanium Powder Production via the Metalysis Process," in *Titanium Powder Metallurgy: Science, technology and Applications*, M. Qian and F. H. Froes, Eds. 2015, pp. 51–67.

[64] S. L. Semiatin, V. Seetharaman, and I. Weiss, "The thermomechanical processing of alpha/beta titanium alloys," *Jom*, vol. 49, no. 6, pp. 33–39, 1997.

[65] I. Weiss and S. L. Semiatin, "Thermomechanical processing of alpha titanium alloys - an overview," *Mater. Sci. Eng. A*, vol. 263, pp. 243–256, 1999.

[66] M. Jackson, "Microstructural Evolution of Titanium Alloys During Isothermal Subtransus Forging," University of London, 2002.

[67] P. S. Davies, "An investigation of microstructure and texture evolution in the near-alpha Titanium alloy Timetal 834," The University of Sheffield, 2009.

[68] N. Nasseri, "Microstructure and Texture Evolution of Titanium 6246," The University of Sheffield, 2009.

[69] P. Crawforth, "Towards a Micromechanistic Understanding of Imparted Subsurface

Deformation During Machining of Titanium Alloys," The University of Sheffield, 2014.

[70] L. Li, M. Q. Li, and J. Luo, "Mechanism in the β phase evolution during hot deformation of Ti–5Al–2Sn–2Zr–4Mo–4Cr with a transformed microstructure," *Acta Mater.*, vol. 94, pp. 36–45, 2015.

[71] J. W. Brooks, P. J. Bridges, and D. Stephen, "Titanium - a Review of Current Forming and Fabrication Techniques," in *Titanium 1992: Science and Technology*, 1992, pp. 1319–1330.

[72] J. C. Williams, "Titanium Alloys: production, behaviour and application," in *High Performance Materials for Aerospace*, Springer Science & Business Media, 1995, pp. 85–134.

[73] G. Lutjering and J. C. Williams, *Titanium*, 2nd ed. pp. 81-92, Berlin: Springer-Verlag, 2007.

[74] F. Busongo, *Ti-2003, Science and Technology*, 2004, p. 1855.

[75] B. Prandi, J. F. Wadier, F. Schwartz, P. E. Mosser, and A. Vassel, "No Title," in *Titanium 1990, Products and Applications*, 1990, p. 150.

[76] Y. Combres and B. Champin, "Beta-CEZ Properties," in *Beta Titanium Alloy's in the 1990's*, D. Eylon, R. R. Boyer, and D. A. Koss, Eds. Warrendale: TMS, 1993, pp. 199–209.

[77] J. O. Peters, G. Lütjering, M. Koren, H. Puschnik, and R. R. Boyer, "Processing, microstructure, and properties of β-CEZ," *Mater. Sci. Eng. A*, vol. 213, pp. 71–80, 1996.

[78] K. S. Chan, C. C. Wojcik, and D. A. Koss, "Deformation of an Alloy with a Lamellar Microstructure: Experimental Behaviour of Individual Widmanstatten Colonies of an alpha-beta Titanium alloy," *Met Trans A*, vol. 12, no. 11, pp. 1899–1907, 1981.

[79] M. Young, E. Levine, and H. Margolin, "Age Hardening of alpha-beta Ti-6Al-2Sn-4Zr-6Mo," *Met Trans A*, vol. 10, no. 3, pp. 359–365, 1979.

[80] T. Hamijima, G. Lutjering, and S. Weissmann, "Importance of Slip Mode for Dispersion-Hardened Veta-Titanium Alloys," *Met Trans*, vol. 4, pp. 847–856, 1973.

[81] F. H. Froes and H. B. Bomberger, "The Beta Titanium Alloys," *J. Met.*, vol. 37, no. 7, pp. 28–37, 1985.

[82] G. E. Dieter and G. Ellwood, *Mechanical Metallurgy*. London: McGraw-Hill, 1988.

[83] R. Sarkar, P. Ghosal, K. Muraleedharan, T. K. Nandy, and K. K. Ray, "Effect of boron and carbon addition on microstructure and mechanical properties of metastable beta titanium alloys," *Mater. Des.*, vol. 67, pp. 50–63, 2015.

[84] R. R. Boyer, G. Welsch, and E. W. Collings, *Materials Properties Handbook: Titanium Alloys*. pp. 829-865, ASM International, 1994.

[85] J. Fan, J. Li, H. Kou, K. Hua, B. Tang, and Y. Zhang, "Influence of solution treatment on microstructure and mechanical properties of a near β titanium alloy Ti-7333," *Mater. Des.*, vol. 83, pp. 499–507, 2015.

[86]   E. A. Starke and J. C. Williams, "Microstructure and the Mechanics of Fatigue Crack Propagation," in *Fracture Mechanics: Perspectives and Directions*, 1989, pp. 184–207.

[87]   N. Clément, A. Lenain, and P. J. Jacques, "Mechanical property optimization via microstructural control of new metastable beta titanium alloys," *JOM*, vol. 59, no. January, pp. 50–53, 2007.

[88]   TIMET, "TIMETAL 10-2-3 Datasheet," 2000.

[89]   TIMET, "TIMETAL 6-4 Datasheet," 2000.

[90]   M. Jackson, N. G. Jones, D. Dye, and R. J. Dashwood, "Effect of initial microstructure on plastic flow behaviour during isothermal forging of Ti–10V–2Fe–3Al," *Mater. Sci. Eng. A*, vol. 501, no. 1–2, pp. 248–254, 2009.

[91]   S. L. Raghunathan, R. J. Dashwood, M. Jackson, S. C. Vogel, and D. Dye, "The evolution of microtexture and macrotexture during subtransus forging of Ti–10V–2Fe–3Al," *Mater. Sci. Eng. A*, vol. 488, no. 1–2, pp. 8–15, 2008.

[92]   N. Jones, M. Jackson, D. Dye, and R. Dashwood, "Comparing the hot working behaviour of high strength beta alloys Ti-5Al-5Mo-5V- 3Cr with that of Ti-10V-2Fe-3Al," in *Ti-2007*, 2007.

[93]   N. G. Jones, "Microstructural evolution of Ti-5Al-5Mo-5v-3Cr," Imperial College London, 2008.

[94]   R. L. Higginson, L. Rebecca, and C. M. Sellars, *Worked Examples in Quantitative Metallography*. London: Maney, 2003.

[95]   M. Jackson, R. Dashwood, L. Christodoulou, and H. Flower, "The Microstructural Evolution of Near Beta Alloy Ti-10V-2Fe-3Al during Subtransus Forging," *Metall. Mater. Trans. A*, vol. 36A, no. May, pp. 1317–1327, 2005.

[96]   ImageJ, *ImageJ User Guide*. 2003.

[97]   O. Engler and V. Randle, *Introduction to Texture Analysis*, 2nd ed. London: CRC Press, 2008.

[98]   Oxford Instruments, *Oxford Instruments CHANNEL 5*. Oxford Instruments, 2010.

[99]   U. F. Kocks, C. N. Tome, and H. R. Wenk, *Texture and Anisotropy: Preferred Orientations in Polycrystals and their Effect on Materials Properties*. Cambridge: Cambridge University Press, 2000.

[100]   BSI, "BS EN ISO 6507-1:2005 Metallic materials – Vickers hardness test," 2005.

[101]   S. Andrieu, F. Soniak, and S. Harris, "Private communication with MBD." Gloucester, 2011.

[102]   L. Germain, N. Gey, M. Humbert, P. Vo, M. Jahazi, and P. Bocher, "Texture heterogeneities induced by subtransus processing of near alpha titanium alloys," *Acta Mater.*, vol. 56, pp. 4298–4308 ST – Texture heterogeneities induced by, 2008.

[103]   W. D. Callister, *Materials Science and Engineering: An Introduction*, 7th ed. pp. 160, New York: John Wiley & Sons Inc, 2006.

[104]   "Internal communication with B. Wynne (UoS)." Sheffield, 2015.

[105] B. Roebuck, J. D. Lord, and M. Brooks, "Measurement Good Practice Guide No 3 Measuring Flow Stress in Hot Axisymmetric Compression Tests," 2002.

[106] L. Sun, "PhD Thesis: The Effects of Strain Path Reversal on Austenite Grain Subdivision , Recrystallisation and Phase Transformations in Microalloyed Steel," The University of Sheffield, 2012.

[107] D. R. Barraclough, H. J. Whittaker, K. D. Nair, and C. M. Sellars, "Effect of Specimen Geometry on Hot Torsion Test Results for Solid and Tubular Specimens," *J. Test. Eval.*, vol. 1, no. 3, pp. 220–226, 1973.

[108] D. F. Fields and W. A. Backofen, "Determination of Strain-Hardening Characteristics by Torsion Testing," in *ASTM Proceedings of the 60th Annual Meeting*, 1957, pp. 1259–1272.

[109] K. Muszka, M. Lopez-Pedrosa, K. Raszka, M. Thomas, W. M. Rainforth, and B. P. Wynne, "The Impact of Strain Reversal on Microstructure Evolution and Orientation Relationships in Ti-6Al-4V with an Initial Alpha Colony Microstructure," *Metall. Mater. Trans. A*, vol. 45, no. December, pp. 5997–6007, 2014.

[110] L. Sun, K. Muszka, B. P. Wynne, and E. J. Palmiere, "Effect of strain path on dynamic strain-induced transformation in a microalloyed steel," *Acta Mater.*, vol. 66, no. 0, pp. 132–149, 2014.

[111] E. B. Shell and S. L. Semiatin, "Effect of initial microstructure on plastic flow and dynamic globularization during hot working of Ti-6Al-4V," *Metall. Mater. Trans. A*, vol. 30, no. December, pp. 3219–3229, 1999.

[112] S. I. Oh, S. L. Semiatin, and J. J. Jonas, "An analysis of the isothermal hot compression test," *Met Trans A*, vol. 23, no. 3, pp. 963–975, 1992.

[113] S. Gourdet and F. Montheillet, "A model of continuous dynamic recrystallization," *Acta Mater.*, vol. 51, no. 9, pp. 2685–2699, 2003.

[114] T. Sakai, H. Miura, a. Goloborodko, and O. Sitdikov, "Continuous dynamic recrystallization during the transient severe deformation of aluminum alloy 7475," *Acta Mater.*, vol. 57, no. 1, pp. 153–162, 2009.

[115] N. Gey and M. Humbert, "Characterization of the variant selection occurring during the alpha-beta-alpha phase transformations of a cold rolled titanium sheet," *Acta Mater.*, vol. 50, no. 2, pp. 277–287, 2002.

[116] N. Gey and M. Humbert, "Journal of Materials Science, Volume 38, Number 6 - SpringerLink," *J. Mater. Sci.*, vol. 38, no. 6, pp. 1289–1294, 2003.

[117] L. Germain, S. R. Dey, M. Humbert, and N. Gey, "Determination of parent orientation maps in advanced titanium-based alloys.," *J. Microsc.*, vol. 227, no. Pt 3, pp. 284–91, 2007.

[118] Y. Hu and V. Randle, "An electron backscatter diffraction analysis of misorientation distributions in titanium alloys," *Scr. Mater.*, vol. 56, no. 12, pp. 1051–1054, 2007.

[119] J. C. Williams, F. H. Froes, C. F. Yolton, and I. M. Bernstein, "The Influence of Thermomechanical Processing on the Microstructure of Metastable beta-Ti Alloys," Pittsburgh, 1976.

[120] S. Guo, B. Chen, Q. Meng, R. Zhao, and X. Zhao, "Peculiar aging response of near beta Ti-25 Nb-2Mo-4Sn alloy for biomedical applications," *Prog. Nat. Sci. Mater. Int.*, vol. 23, no. 1, pp. 1–6, 2013.

[121] F. Montheillet, D. Dajno, N. Come, E. Gautier, A. Simon, P. Audrerie, A. Chaze, and C. Levaillant, "Hot Deformation of the High Strength BetaCEZ Titanium Alloy," in *Titanium 1992: Science and Technology*, 1992, pp. 1347–1354.

Appendix

Figure A. 1: Forging 2, with specimen locations marked for removal via EDM.

Figure A. 2: Unedited scan of centre line macro-etch.

Figure A. 3: Unedited scan of flash line macro-etch.

Figure A. 4: Unedited scan of quarter cross-section macro-etch
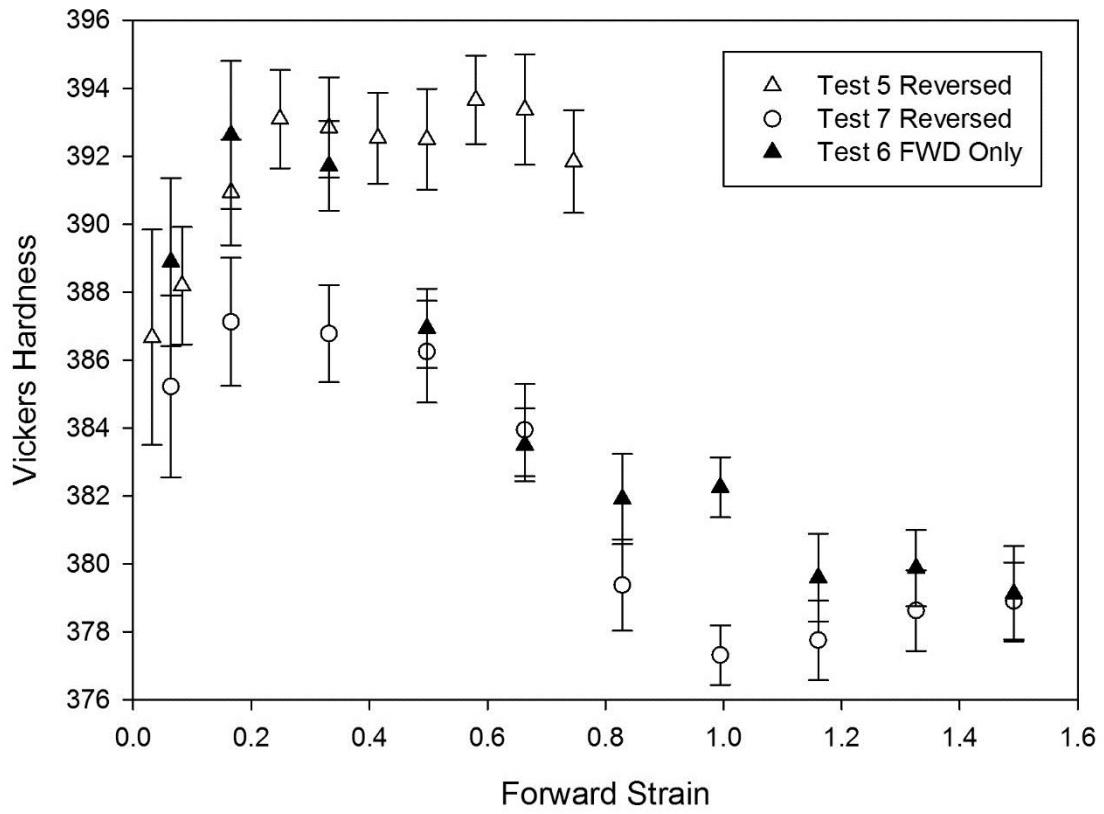
Figure A. 5: Effect of ageing on deformed Ti-10-2-3 specimens as a function of forward strain. Error bars illustrate 95% confidence limit.